BRNO UNIVERSITY OF TECHNOLOGY

VYSOKÉ UČENÍ TECHNICKÉ V BRNĚ

FACULTY OF ELECTRICAL ENGINEERING AND COMMUNICATION

FAKULTA ELEKTROTECHNIKY
A KOMUNIKAČNÍCH TECHNOLOGIÍ

DEPARTMENT OF CONTROL AND INSTRUMENTATION

ÚSTAV AUTOMATIZACE A MĚŘICÍ TECHNIKY

IONIZING RADIATION MEASUREMENT IN FIELD ROBOTICS

MĚŘENÍ IONIZUJÍCÍHO ZÁŘENÍ V MOBILNÍ ROBOTICE

DOCTORAL THESIS
DIZERTAČNÍ PRÁCE

AUTHOR   Ing. Tomáš Lázna
AUTOR PRÁCE

SUPERVISOR   prof. Ing. Luděk Žalud, Ph.D.
ŠKOLITEL

BRNO 2023

ABSTRACT

This thesis discusses ionizing radiation measurements conducted by autonomous robotic platforms, namely, unmanned ground vehicles and unmanned aircraft systems. The research comprises two fundamental tasks: radiation mapping and the localization of radioactive sources. The author introduces various radiation detection systems and explores their integrability into terrestrial and aerial robots. The experimentation is designed to develop methods for retrieving the positions of radiation emitters. The actual effort to produce such techniques embraces both systematic pre-planned surveys and active adjustment of the measurement trajectories to accelerate the process. Notably, this type of adjustment also involves directionally sensitive sensors. The thesis investigates the benefits of collaboration between ground and aerial platforms in detailed radiation mapping, exposing a practical application scenario. Furthermore, a possible use case rests in three-dimensional radiological characterization of a building via an unmanned aircraft. The majority of the proposed algorithms have been validated through real-world experiments that have confirmed their robustness and practicality.

KEYWORDS

Radiation mapping, radiation source search, mobile robotics, cooperative robots, environmental monitoring.

ABSTRAKT

Tato disertační práce se věnuje oblasti měření ionizujícího záření prostřednictvím autonomních robotických platforem, konkrétně pozemních robotů a bezpilotních leteckých systémů. Zaměřuje se na dva hlavní cíle, a to na radiační mapování a lokalizaci radioaktivních zdrojů. Autor představuje různé systémy pro detekci radiace a zabývá se jejich integrací na pozemní i vzdušné roboty. Nedílnou součástí výzkumu je vývoj metod pro zjištění pozic zářičů, a to nejen pomocí systematického průzkumu podél předem naplánované trasy, ale také s využitím aktivního upravování měřicí trajektorie za účelem zrychlení tohoto procesu. V rámci aktivní lokalizace jsou prověřovány také směrově citlivé senzory. Tato práce zkoumá i výhody spolupráce mezi pozemními a leteckými platformami, čímž demonstruje praktickou využitelnost prezentovaných postupů. Další oblastí využití robotů je trojrozměrné radiační mapování budov prostřednictvím bezpilotního letadla. Většina navržených algoritmů byla experimentálně ověřena v terénu.

KLÍČOVÁ SLOVA

Radiační mapování, vyhledávání zdrojů radiace, mobilní robotika, kooperativní roboti, monitorování prostředí.

Author's Declaration

Author:	Ing. Tomáš Lázna
Author's ID:	155192
Paper type:	Doctoral thesis
Academic year:	2023/24
Topic:	Ionizing Radiation Measurement in Field Robotics

I declare that I have written this paper independently, under the guidance of the advisor and using exclusively the technical references and other sources of information cited in the paper and listed in the comprehensive bibliography at the end of the paper.

As the author, I furthermore declare that, with respect to the creation of this paper, I have not infringed any copyright or violated anyone's personal and/or ownership rights. In this context, I am fully aware of the consequences of breaking Regulation §11 of the Copyright Act No. 121/2000 Coll. of the Czech Republic, as amended, and of any breach of rights related to intellectual property or introduced within amendments to relevant Acts such as the Intellectual Property Act or the Criminal Code, Act No. 40/2009 Coll. of the Czech Republic, Section 2, Head VI, Part 4.

Brno . . . .
author's signature*

---

*The author signs only in the printed version.

ACKNOWLEDGEMENT

Contents

Part I

Preamble

1 Introduction

This thesis explores robotic platforms and methods for ionizing radiation measurements, with a particular emphasis on radiation mapping and the localization of radioactive sources. The author is affiliated with the Robotics and AI research group at Brno University of Technology, which collaborates extensively with various organizations committed to the mitigation of chemical, biological, radiological, and nuclear (CBRN) threats. The partnerships encompass both local institutions such as the Brno-based University of Defence (and the National Radiation Protection Institute of Prague) and worldwide bodies including, for example, the International Atomic Energy Agency. Through these collaborative efforts, it has become increasingly evident that the intersection of robotics and radiation protection holds significant potential for enhancing our capacity to reduce relevant complex hazards. This work has been conceived to expose the critical aspects of nuclear security and to examine the application of robotic systems, with a strong focus on autonomous operations.

Ionizing radiation plays an important role in present-day human lives, as the effect can be encountered in a variety of fields where it serves to our benefit. In medicine, the radiation facilitates both diagnostics and therapy; the former involves X-ray radiography, computer tomography (CT) scans, and positron emission tomography (PET) scans, while the latter allows specialists to destroy cancer cells. The radiation is inseparably connected with the electricity generation in nuclear power plants. Further, it is employed in inspecting the integrity of welds, pipelines, and industrial structures in general; however, the effect finds use also in sterilizing medical equipment, pharmaceuticals, and food. Another target domain lies in research, namely, in fields like particle physics and material science. Weak sources are embedded even in smoke detectors, which can be easily found in common hotel rooms.

In many of the applications above, the source of radiation rests in radionuclides, and these substances can slip out of control during incidents or accidents. Such uncontrolled sources may pose a risk to human health; therefore, we need to monitor the radiation situation via spatially distributed measurements, and sometimes it is even necessary to retrieve the precise position of the sources. As ionizing radiation is invisible, a multitude of detection systems of different types have been developed over the past century since the time radioactivity became an object of interest.

Ionizing radiation occurs in three primary forms, each characterized by distinct properties and interaction mechanisms. Alpha particles are helium-4 nuclei, meaning that they exhibit a large mass and a positive charge; thus, they can be easily stopped and remain relatively safe if not inhaled or ingested. Conversely, beta particles are high speed electrons or positrons and possess greater penetration capabilities, potentially posing a risk to tissues upon contact. However, as these particles are also charged, they can still be efficiently stopped by certain shielding materials. Gamma rays are electromagnetic waves and the most penetrating form of natural radiation. The rays cannot be completely disabled, only exponentially attenuated; such an outcome is achievable with dense materials such as lead and tungsten. All the radiation forms share the capacity to ionize atoms, disrupting their electron structures and affecting a range of biological and molecular effects. The ionizing particles are released either immediately, during radioactive decay processes, or later, through the resulting nuclear transitions. Yet another distinct form of ionizing radiation rests in neutron radiation, which relates primarily to nuclear fission and nuclear fusion. The research presented herein centers solely on gamma radiation due to its high penetration capabilities, relevance in typical applications, and also the fact that it is emitted by commonly appearing isotopes such as caesium-137.

Gamma radiation interacts with matter through several fundamental processes. First, let us mention Compton scattering, during which the photon transfers a part of its energy to an interacting electron; as a result, the photon's direction changes. Note that the process follows the scattering formula, which can be exploited to estimate the angle of the incident gamma ray. In the case that the gamma photon is fully absorbed by an electron, the interaction is called the photoelectric effect. These two phenomena dominate at lower energies; once the transferred energy has exceeded the level of 1022 keV, a pair production is enabled, yielding the emission of an electron and a positron. The principal interactions are schematically depicted in Fig. 1.1. These processes form the basis of the detection principles, and they have to be understood properly in order to explain the radiation propagation in the environment. The radiation follows the inverse square law, i.e., the intensity is inversely proportional to the square of distance. Further, the radiation is also exponentially attenuated in mass at a rate given by the linear attenuation coefficient, which depends on the material and the photon energy.

The set of radiation detection principles involves various techniques that utilize the fundamental interactions to give rise to measurable signals, providing crucial insights into the presence, type, and energy of the radiation. The detectors are classified into three principal categories, namely, gas-filled, scintillation, and semiconductor devices. The first category comprises ionizing chambers and Geiger-Müller (GM) counters; the former operate via measuring the electrical charge generated
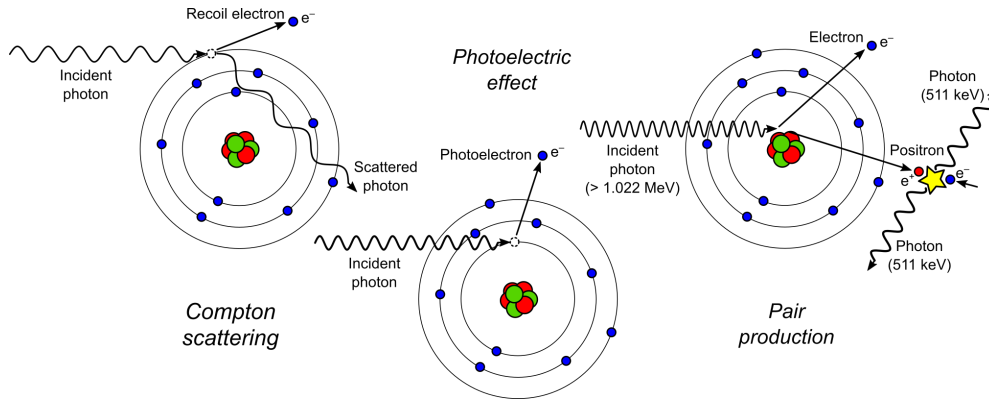
Figure 1.1: Common gamma radiation interactions with matter.

by gas ionization within the chamber. This charge is proportional to the energy of the incident radiation, allowing the spectrometry. A spectrum is essentially an energy histogram of registered interactions, typically containing features such as the so-called Compton edge (related to the scattering) and photopeaks (related to the photoelectric effect), which allow us to identify the isotope that emitted the detected radiation. Conversely, the GM counters lack the ability to provide energy information because the original charge is amplified via the Townsend discharge (avalanche); this amplification, however, offers high sensitivity, simple operation, and the capability of detecting single radiation events. Importantly, the set of gaseous detectors includes a further type, in addition to the above ones; the relevant device is called the proportional counter and combines the principles of the other two approaches. The counter exploits the avalanche concept but is still able to measure the spectra.

Scintillation detectors exploit the ability of certain materials (scintillators) to emit flashes of light when irradiated. These flashes are converted to electric signals by means of photodetectors, namely, either the conventional photomultiplier tubes or the recently broadly available semiconductor devices. The amplitude of such signals is proportional to the energy of the original interaction; scintillators thus exhibit spectrometric capabilities. This commonly used detection principle plays an essential role in the thesis and is illustrated in Fig. 1.2.

Finally, semiconductor detectors are based on the electrical charge generated by the gamma radiation interacting with the semiconductor lattice. Again, the magnitude of such a charge depends on the energy of the incident radiation. These detectors are made from, e.g., silicon or germanium and provide excellent energy resolution, making them highly suitable for precise radionuclide identification. The choice of a proper detector always depends on factors such as the type of the radiation being measured, the desired energy resolution, the required sensitivity, and the application domain. A comprehensive insight into the radiation measurement domain is provided in reference [1].
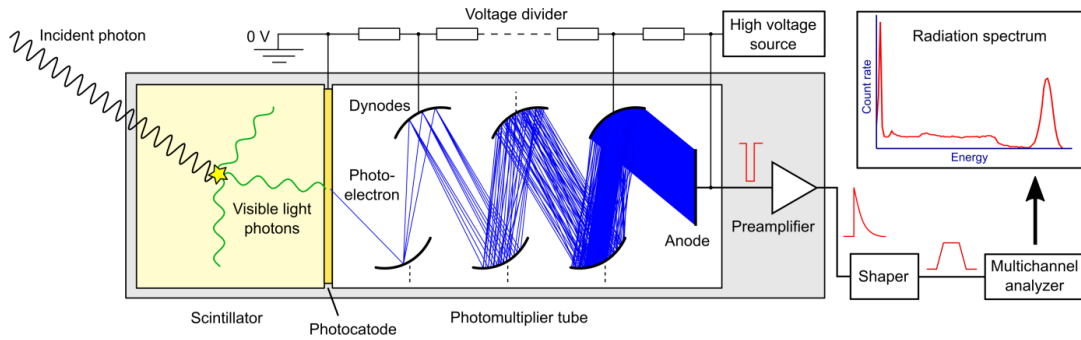
Figure 1.2: The scintillation detector principle.

Once the mission objectives are established and a convenient detection system is selected for the purpose, the detectors have to be transported to the points of interest, typically denoted as sampling points. Traditionally, this task is carried out by radiation operatives; examples of airborne (airplane or helicopter), carborne, and even walking surveys are available in the literature [2, 3, 4]. However, the devices can be also mounted on robotic platforms, introducing several benefits into the task. The robots are able to access environments overly dangerous or inaccessible to humans. The unmanned vehicles are either remotely operated or work autonomously, allowing the radiation specialists to stay outside of potentially contaminated regions. In the autonomous mode, the robots manage to perform measurements consistently and repeatedly, reducing possible variability in the results. Moreover, under proper conditions, the robotically acquired datasets tend to exhibit more prominent precision and accuracy. Nonetheless, the robotic platforms also exhibit certain disadvantages. First, it may be technically challenging to fully integrate radiation detection systems into robots; this holds true especially of off-the-shelf systems designed to be used by humans. Second, traditional measurement procedures and calibration models may not be directly applicable; therefore, the methodology needs to be adapted and validated, and sometimes reference data acquired by conventional means are needed. Finally, the robotic systems have limitations in terms of the power supply and mobility; they are usually not designed to fit a variety of different environments. Further, there may be a problem with susceptibility to radiation damage in high-intensity scenarios; radiation-hardened devices may be required instead of common commercial platforms.

Principally, two field robotics domains are relevant to radiation monitoring, and these include ground and aerial robots. Each category finds use in specific applications, possessing inherent attributes given by its character. The terrestrial platforms provide stability, i.e., the detector can easily dwell in a fixed position. They can operate close to the obstacles without a significant risk of collision and are capable of carrying detection systems at a constant height above the ground, which is benefi-

cial for precise absolute radiation mapping. The ground robots also grant a superior proximity to radiation sources distributed on the surface, compared to the aerial vehicles.

Conversely, the drones exhibit exceptional speed and mobility to rapidly perform large-scale surveys and can avoid ground-level obstacles, e.g., dense vegetation, by flying over them. In general terms, aerial platforms ensure a bird's eye perspective and can simultaneously collect image data or laser scans to reconstruct an up-to-date model of the examined scene. Finally, the measurements are not limited to a single plane, having a potential to be carried out in three dimensions to acquire more comprehensive radiation maps. Regrettably, unlike the ground platforms in the same weight category, the aerial vehicles typically exhibit smaller payload capacities, a drawback preventing them from being equipped with heavy tools such as gamma cameras. Similarly to the detection system, the choice of a fitting robotic platform should always depend on specific conditions related to the environment and mission objectives.

1.1 Motivation

Several real-world events advocate the utilization of robotic systems in situations where uncontrolled radiation sources or radioactive contamination occurred. Following the explosion at the Chernobyl nuclear power plant (NPP) in 1986, robots were applied to assess reactor conditions, clear up debris, and monitor radiation levels. In addition to other devices, the Soviet lunar rovers Lunokhod facilitated the designing and development of state-of-the-art robots for this task, as these pioneering vehicles had already been partially radiation-hardened to operate in space; in practice, however, both of the units employed at Chernobyl eventually failed because the radiation levels had become extremely high (Fig. 1.3a).

Another large-scale nuclear disaster took place in 2011 at Fukushima, where multiple reactor meltdowns resulted in a release of radioactive materials. Unmanned ground vehicles like the PackBot and Quince were utilized to explore the reactor building (Fig. 1.3b). During the subsequent years, other platforms were developed, e.g., snake-like robots to inspect the pipes leading into the containment vessels, and surface boats to operate in the pools that had formed due to the need to cool down the damaged cores. Robots equipped with manipulators are essential in specific decommissioning chores. The contamination generated by the Fukushima event is spread across Japan, and the radioactive waste needs to be stored. Such hazardous sites require periodical monitoring to assess the risks and to help with the remediation; unmanned aircraft systems (UASs), or drones, have therefore been exploited to do so in multiple cases (Fig. 1.3c).

(a)

(b)

(c)

(d)

(e)

(f)
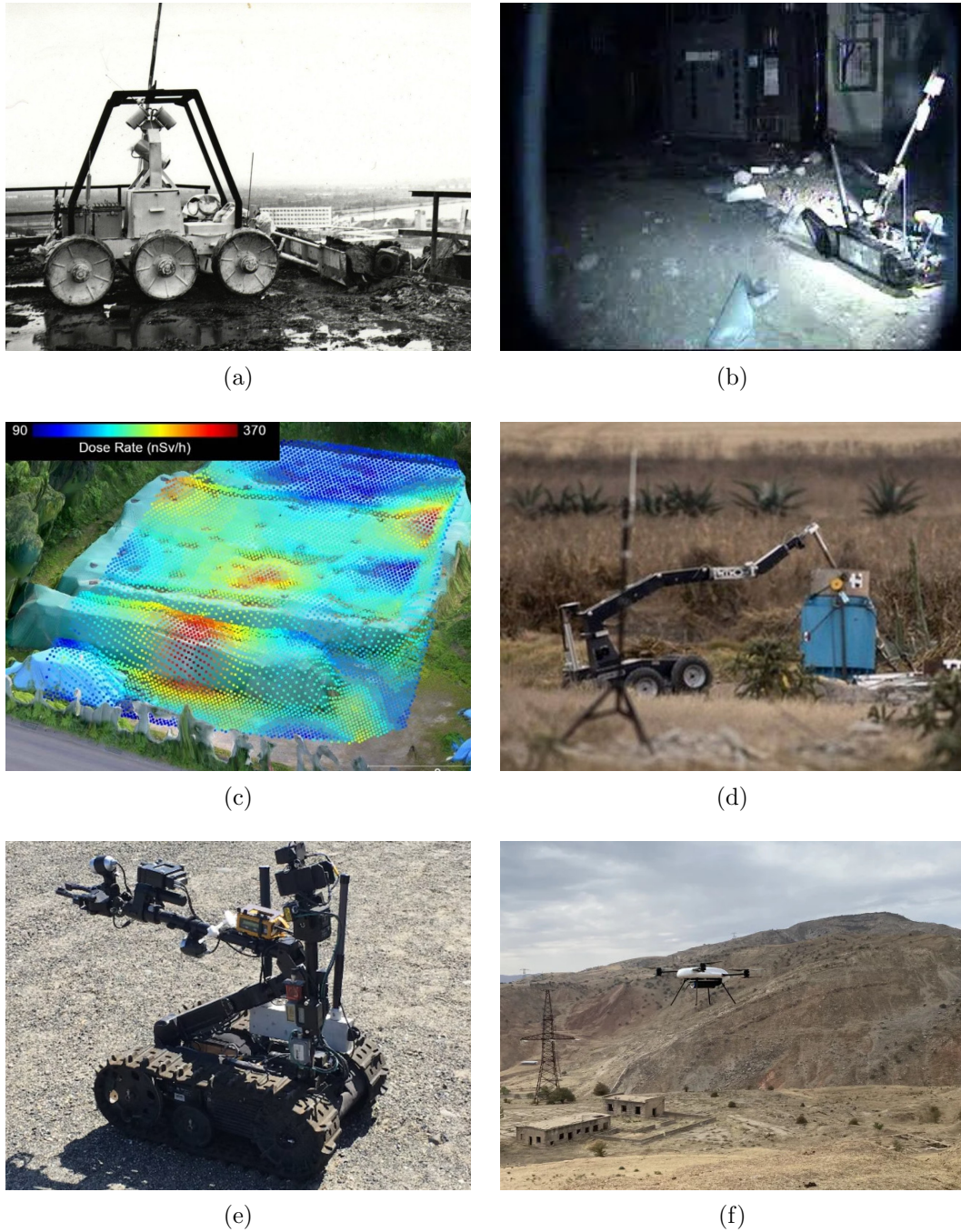
Figure 1.3: Examples of real-world scenarios where the robotic systems were applied to measure radiation or perform related tasks: cleaning the debris at the Chernobyl NPP [5] (a); exploring the reactor building at the Fukushima Dai-ichi NPP [6] (b); a UAS-based radiation map of the nuclear waste temporary storage site in Kawamata, Japan [7] (c); securing a lost radioactive source in Mexico [8] (d); a robot exploring the collapsed tunnel at Henford, Washington, the US [9] (e); surveying a uranium legacy site in Kyrgyzstan via a UAS [10] (f).

However, other risks have to be considered too. In Mexico, for example, it is rather common that radioactive sources get stolen during transportation; the thieves usually claim that they were targeting the vehicle, not its content. A prominent incident of 2013 involved the application of a remotely controlled robot to secure the lost source (Fig. 1.3d); similar events nevertheless happen almost every year in the region. In the USA, by extension, a tunnel collapsed in 2017 at a major nuclear facility near Hanford, Washington, creating a potentially dangerous situation. The authorities deployed a TALON robot, or, more concretely, the Hazmat model, to survey the area, acquire the radiation data, and capture relevant videos (Fig. 1.3e). Drones are being increasingly used to survey and map both operational and abandoned uranium mines, where the natural radioactivity occurs in extensive volumes. The relevant application sites are spread across, e.g., Australia, the United Kingdom, and Central Asia (Fig. 1.3f).

1.2 Aims and Objectives

The aim of the research herein is to probe various aspects, the practical ones in particular, of the robotic measurements of gamma radiation, with an emphasis on two principal tasks: the radiation mapping and the localization of sources. In order to be able to test the proposed methods through real-world experiments, it is necessary to establish the scope of possible scenarios and to select suitable radiation detection systems accordingly. An inevitable step, then, is to equip the robots operating in the studied domains (ground and aerial) with these sensors.

The state-of-the-art techniques often lack the ability to automatically estimate the parameters of the sources, such as their position, mainly in the case that the amount of the sources is not known in advance. The goal lies in introducing a robust method that is able to process data collected during a traditional systematic survey to retrieve the number and location of the radionuclides present in the mapped region of interest. A related aim is to shorten the localization time by altering the robot trajectory dynamically, exploiting the actual measurements; these techniques may take advantage of, for instance, the directional sensitivity of the applied detection system or the on-line source estimates acquired via Bayesian inference.

The research has been conceived to focus on utilizing multiple unmanned vehicle at a time, as the cooperation between the vehicles can combine the advantages of the different types of robots. The aerial photogrammetry executed by the drones has the capacity to build a 3D model of the surveyed area, which can be exploited in autonomous navigation or even enable the production of three-dimensional radiation maps.

The main objectives of the thesis can be defined as follows:

Aim 1: Integrating various radiation detection systems into both the terrestrial and the aerial robotic platforms to enable data collection and comprehensive field testing of radiation mapping and localization algorithms.

Aim 2: Developing algorithms for localizing radioactive point sources on the basis of scattered sampling points and exploring the possibilities of information-driven localization.

Aim 3: Examining applications which expand the capabilities of straightforward radiation mapping, namely, the cooperation between the terrestrial and the aerial robots and three-dimensional mapping; this aim is closely related to verifying the usability of the applications in real-world conditions.

1.3 Outline

This thesis explores the primary outcomes of the author's research, presenting a compilation of the key publications that cover the relevant results. The text is structured into two distinctive segments: *Preamble* and *Publications*. The former part defines the aims and goals while providing a comprehensive overview of the current knowledge in the specific research topics; in this sense, the focus is on the radiation mapping and source localization via ground and aerial robots (*State of the Art*). Additionally, the central chapters, above all *Research Summary*, offer an insight into the author's most significant achievements and published research articles; the *Discussion* section then interrelates the past efforts and the objectives set out in the thesis.

The latter segment, conveniently called *Publications*, centers on the author's main published results, accommodating five pre-prints of the articles that address the above-presented research topics. Four of these items, comprising a proceedings and three journal articles, have already undergone the peer-review process. The remaining part, a manuscript, is currently being considered for publication, as of October 2023. Each item indicates the fundamental details, including the bibliographical information, abstract, author's contribution, funding, and copyright notice.

An exhaustive index of the author's publications, encompassing both those closely aligned with the examined domain and those concerning other radiation-related subjects, is offered in the *Appendices* under the section *List of Author's Publications*.

2 State of the Art

The broad area of measuring ionizing radiation via robotic systems can be divided into three principal domains, namely, radiation mapping, the localization of hotspots, and the tracking of radioactive plumes [11]. The first field is centered on finding the spatial distribution of the radioactive contamination or ambient dose rate in a pre-defined region of interest (ROI). The tasks are usually carried out by sampling the relevant values in a relatively regular grid and ensuring their subsequent interpolation. The yielded radiation map may advise the first responders and radiation authorities whether it is safe to employ human personnel in certain areas. The following activity, localization, seeks to establish the coordinates (and, possibly, other relevant parameters) of the hotspots, or the regions of increased radiation intensity, usually produced by point sources in this context. Such an outcome is typically useful in the so-called search for uncontrolled radiological sources. The common localization algorithms presented below are not able to handle more complex types of sources, e.g., contamination dispersed over an area or a volume, and the mapping is required to quantify such sources. Note that the radiation map may yield the positions of the point sources, thus performing the localization task; however, this does not hold true in the opposite direction. The mapping is typically performed via measuring the radiation levels along the pre-planned trajectories; however, there are known cases when the surveying is information-driven (e.g., [12]). Below, the former approach will be denoted as passive exploration, while the latter will be referred to as active. In the localization domain, active algorithms are more common than in the mapping.

The last assignment concerns the radioactive plumes which occur after severe radiological accidents. This thesis does not address such large-scale issues, and therefore plume tracking is omitted from the literature overview.

2.1 Radiation Mapping

For the purpose of this section, let us consider, in a very general sense, radiation mapping to be any concept that leads to revealing radiation distribution in the context of the studied scene; this then means that the mapping does not necessarily embed the data into a specific coordinate frame. The provision of the sources'

positions is not expected. The section is structured as follows: First, the articles which discuss aerial platforms, or unmanned aircraft systems, are presented; then, the terrestrial domain is explored through unmanned ground vehicles; and, finally, miscellaneous approaches are supplemented, including those applying cooperation between different robotic assets.

2.1.1 Unmanned Aircraft Systems

A comprehensive study on the use of aerial systems in airborne radiation mapping is delivered by the authors of [13]. The researchers compare various hardware platforms and methodologies to complete both the mapping and the localization tasks. The article advocates utilizing UASs in contrast to static and mobile ground measurements and piloted airborne surveys, the criteria being the relevant advantages and disadvantages, such as that the drones enable rapid data collection over vast areas while not having to negotiate obstacles and that the operators may maintain a safe distance from contaminated zones. The available platforms include, on the one hand, fixed-wing vehicles which operate at high speeds, thus providing a greater coverage but inferior spatial resolution, and, on the other, helicopters and multirotors able to work at lower altitudes and speeds. Generally, the spatial resolution is affected by the flight speed, the integration period of the detection system, and the flight altitude. During the mission planning, it is necessary to establish the main objectives of the measurement and to consider the size of the surveyed area as well as the required spatial resolution and the maximal allowed data collection time. In many cases, the exploration can be divided into multiple stages with different parameters (Fig. 2.1). Unmanned aircraft systems usually carry scintillation and semiconductor detectors, as these provide a sufficient sensitivity. Typical scintillation materials include sodium iodide (NaI), cesium iodide (CsI), and lanthanum(III) bromide (LaBr$_3$), which offers a better energy resolution; despite such a benefit, the bromide is nevertheless not suitable for detecting low-level radiation anomalies. In semiconductor detectors, the most prominent material lies in cadmium zinc telluride (CZT), whose crystals can be manufactured up to a volume of 1 cm^3 and merged into pixel detectors. Aerial radiation mapping generally includes three steps, namely, establishing a calibration model, measuring and normalizing the data, and presenting the data. The first phase is indispensable, as the radiation measured at typical flight altitudes is affected by not only the inverse square law but also the attenuation; the model can be acquired via hover surveys. Further, the calibration is required to convert raw data to, e.g., a dose rate that possesses a clear physical meaning. The data are then collected along parallel lines whose spacing needs to be selected as a compromise between the coverage and the time efficiency. The data are usually
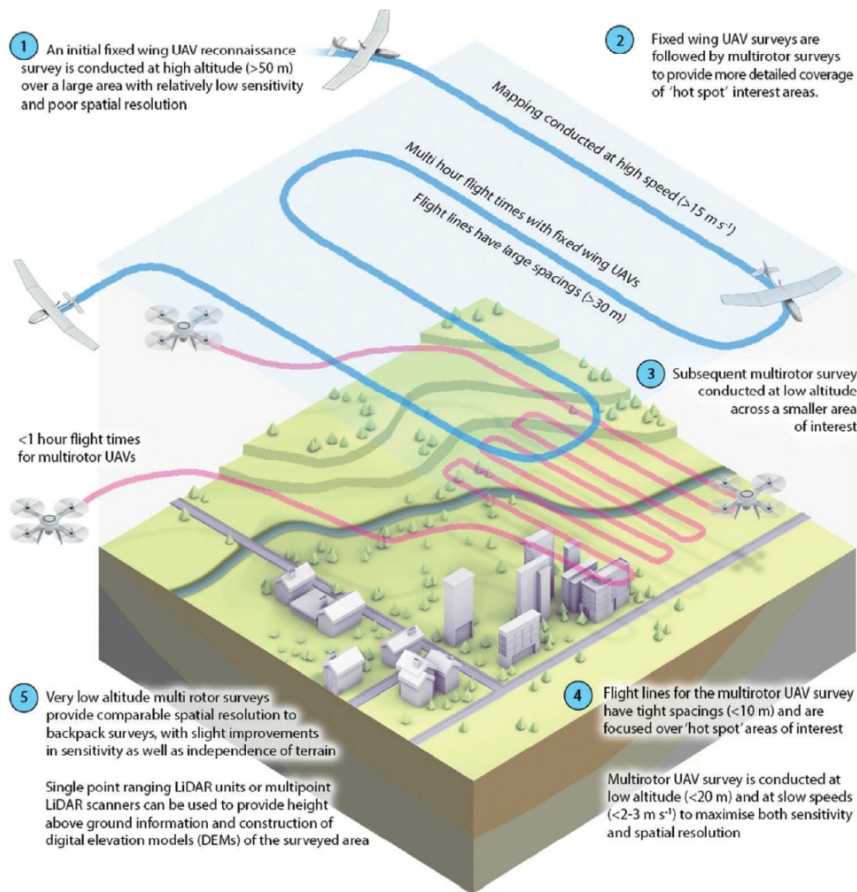
Figure 2.1: The concept of multi-phase radiation mapping via distinct aerial platforms [13].

normalized to the height of 1 meter above the ground level (AGL) and then interpolated to be ready for presentation. The resulting map can be simply laid over an orthophoto of the surveyed area; however, a 3D model is sometimes used to provide a context with the environment features. It is possible to acquire the model via either photogrammetry or lidar scans.

To discuss the literature in concrete terms, we can present diverse research reports and articles on the problems outlined in the thesis; all of the items are included in the references section.

In article [14], a real-world post-disaster scenario in Fukushima Prefecture is outlined, following from the notorious nuclear power plant accident. The experiment relies on a custom UAS carrying a CZT detector and a laser rangefinder stabilized on a gimbal. The rangefinder allows reconstructing a 3D model of a sample farm with a stepped vertical profile. An automatic waypoint navigation ensures data collection at a speed of 1 m/s, at a minimal safe altitude and with a line spacing of 2 meters. The terrain data are processed using a custom software based on the Delaunay triangulation.

The authors of [15] discuss, above all, practical considerations of airborne measurements, emphasizing the situation in developing countries. The spatial resolution is studied with respect to various flight and detector parameters; however, the article proposes that a superior spatial resolution is not required in the case of uranium legacy sites. One of the novel solutions introduced is an inequality that ensures distinguishing a point source from the radiation background; the detecting capabilities are influenced by several factors, including the source activity, detector sensitivity and integration period, background intensity, and flight altitude. By extension, two different detection systems are compared to determine if a high-volume detector delivers any significant advantages. The surveys are carried out at an altitude of 10 m and a speed of 3 m/s, with the line spacing of 10 m; the achieved coverage is 2.7 ha per mission lasting 15-20 minutes. To facilitate the data interpolation, splines are utilized; according to the researchers, a good visual interpretation is a major aspect having an impact on the utility of the results.

Another example of a real-world application is embodied in article [16], which focuses on the Chernobyl exclusion zone. A fixed-wing aircraft equipped with a pair of CsI(Tl) detectors and a Global Navigation Satellite System (GNSS) receiver is designed to explore an area of 2.4 km^2. The data are collected at speeds and altitudes ranging from 14 to 18 m/s and 40 to 60 m, respectively. The processing includes the correction of various factors – the components of the background radiation in particular – and normalization to height of 1 m AGL. To allow the interpolation, a rather simple algorithm called inverse distance weighting (IDW) is employed.

The project characterized in [17] is focused on three-phase radiation surveying. The first phase is carried out at a high altitude, using a UAS equipped with a lidar; as a result, a 3D map of the area is yielded via simultaneous localization and mapping (SLAM). The second phase takes place at a low altitude (1 m) and speed (0.2 m/s), exploiting a Geiger-Müller (GM) detector to build a radiation map. Although the authors suggest that this task could be performed autonomously via the on-board anticollision systems, the UAS is controlled by a pilot. The last phase rests in visiting the hotspots revealed previously to acquire more detailed information and to execute other steps, such as identifying the present radionuclides; the step involves solving the traveling salesman problem to find the optimum sequence of the hotspots to inspect. An interesting algorithm is presented, enabling the vegetation segmentation from the 3D model; the resulting radiation map is projected on the ground layer.

The approach set out in article [18] introduces a drone carrying a depth camera and a GM detector to explore a compact indoor area. The data from the sensors are collected simultaneously, but the processing involves two stages, as follows: First, a 3D model is reconstructed via SLAM; second, the radiation layer is computed. It is
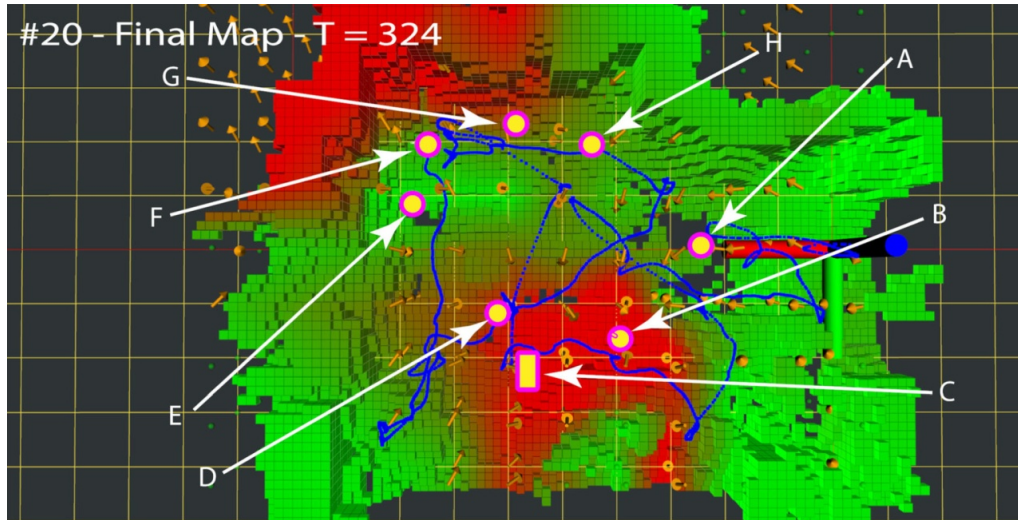
Figure 2.2: The active mapping approach presented by [12]; the true positions of the sources are labeled with the letters A through H.

assumed that every item in the point cloud embodies a source having an unknown intensity, and the measured radiation constitutes a superposition of all of the sources' contributions governed by the inverse square law. The problem formulation results in a system of equations that can be solved if the area has been covered sufficiently and, therefore, the system is not underdetermined. The algorithm is verified on a real scene, albeit with simulated radiation data only.

In [19], yet another real-world issue is addressed, namely, monitoring the soil contamination around the Fukushima Dai-ichi NPP during three consecutive years. The researchers employ an unmanned helicopter and three types of scintillation detectors. The flight parameters are set to an altitude and line spacing of 80 m, and the speed equals 8 m/s; the automatic waypoint navigation is ensured by an RTK-GNSS receiver. The explored zone exhibits an area of 52 km², and a single mission covered merely 2 km²; the complete survey thus took approximately a month, requiring the authors to consider also the radioactive decay in the data processing. The data are normalized to a height of 1 m AGL and interpolated via Kriging; it is confirmed that the values conform to the reference measurements acquired on the ground.

A different set of procedures is presented in [20], a source dedicated to developing and testing a modular radiation monitoring system ready to be deployed on various UASs in dose rate measurements, air sampling, and the acquisition of a radiation map. The system was practically demonstrated during field trials at the NPP Jaslovske Bohunice, Slovakia, the aim being to keep the devices low-cost to facilitate their use on multiple drones simultaneously and, moreover, to distribute them as static monitoring nodes. The module integrates a GM detector, an air sampler, and a GNSS receiver to ensure georeferencing.

The project in [12] is designed to use drones operating in a GNSS-denied environment. The studied space is divided into voxels, and the radiation intensity and the gradient are estimated in the explored cells; the related information and the estimation uncertainty then propagate into the neighboring voxels. The applied path planning is active and divided into the global and the local planner; the former brings the UAS into radiologically more interesting parts of the space, while the latter ensures a sufficient sampling in each visited cell. The environment is unknown and is continuously mapped via an optical SLAM. The algorithms are practically tested using a custom aerial platform comprising a lightweight scintillation detector coupled with a silicon photomultiplier (SiPM). To view an example of the yielded map, refer to Fig. 2.2.

2.1.2 Unmanned Ground Vehicles

Involving a ground robot, the experiments in [21] address the problem of the complete coverage of a structured area. The explored region is subjected to an approximate cell decomposition; the size of the cells is deduced from the parameters of the detection system on the one hand and from the required map resolution on the other, invariably via computing a minimum detectable amount (MDA). The neighboring cells' centroids are then connected, and their optimal sequence is found via depth-first search to ensure that each cell is visited. The algorithms were verified in real-world experiments, with the measured data subsequently interpolated via IDW.

The project presented in [22] ranges within a slightly different domain, as the robot operates on a water surface. The authors employ a commercial platform equipped with a GM detector, claiming that a spiral trajectory is more suitable than the typical boustrophedon-style type of path. The ROI borders are defined manually, but the subsequent measurement within them is automatic. Again, the IDW is applied to interpolate the collected data.

The authors of [23] introduce a robotic platform that, as a matter of fact, is employed in dismantling and decommissioning nuclear facilities in France; therefore, even radiation hardening needs to be addressed. The unmanned ground vehicle (UGV) can carry either a manipulator to collect the samples or a detection unit composed of a spectrometer, a gamma camera, and a dose rate meter. The rugged steel structure with belts enables the vehicle to move at the maximum speed of 10 meters per minute. The gamma camera localizes the hotspots and is accompanied with a laser rangefinder and an RGB camera to allow the fusion of images and a radiation layer. The report also summarizes several types of mission where the robot is applicable.

In the experiments presented through [24], a vehicle is deployed at the Fukushima Dai-ichi NPP, facilitating safe search with a heavily shielded box for human operators to control the radiation monitoring in the area. The truck maps the radiation by means of a gamma camera and a lidar assisting to adjust the camera's 'focal length'. It also carries a TALON, a remotely operated robot to expand the inspection capabilities; a pan-tilt-zoom camera and a thermal imager are available too.

A robot with autonomous navigation and detection abilities is discussed in [25]. The platform comprises a Husky UGV carrying an off-the-shelf localization stack and a dose rate meter. The mapping proceeds along user-defined waypoints, the navigation relying on SLAM; further, the navigation is extended to involve a radiation costmap to keep the vehicle away from high-intensity areas, protecting it from potential radiation damage. This mapping approach was experimentally verified in a semi-structured environment containing two sources; the robot managed to maintain safe clearance from these sources after recording the relevant data.

The authors of [26] present a novel method for interpolating robot-collected radiation data that are irregularly spaced, noisy, and of low intensity. The method exploits Gaussian process regression (GPR), with the suitability of the chosen kernel verified using Monte Carlo N-Particle (MCNP) simulations. The assets of such an approach include the possibility of directly establishing the interpolation uncertainty, which may assist in future exploration planning. The algorithm resembles Kriging; however, applying GPR in robotics has proved beneficial, and research articles are available on utilizing the procedure to improve the autonomous behavior. To perform the experimental testing, a Jackal UGV having an RGB camera, a pair of lidars, and a scintillation detector are used. The authors demonstrate on a simple single source scenario that their method provides better results than other commonly applied algorithms, namely, linear and thin-plate spline interpolation. Several kernels are considered and compared to establish that the Matérn 3/2 embodies the most suitable option for the studied cases.

The concept presented in [27] does not yield any actual radiation map; however, it is mentioned here, as it relates to the topic. A mobile robot carries an RGB camera and a detector mounted in a lead collimator, enabling the directional sensitivity of the device. The vehicle sweeps through the explored area to construct a panoramic image and to identify the directions in which the sources can be found.

In article [28], robotic systems are deployed in real-world nuclear scenarios via competitions., the idea being heavily promoted by the authors. According to the text, only few opportunities are available to test these systems, and the topic has encountered a lack of interest by the scientific community. The International Atomic Energy Agency (IAEA) hosted a demonstration of robots for special applications in

2017 to yield the conclusion that none of the vehicles could be immediately applied in real missions.

2.1.3 Other Approaches

A methodology centered on data processing algorithms is outlined in [11]. Usually, a sequence of corrections is applied to raw measurements in order to either reveal the actual amount of particles emitted by the sources (i.e., true count processing) or enable isotope identification (i.e., spectrum processing). The former procedure typically comprises altitude correction addressing the exponential attenuation, solid angle correction when the terrain shape deviates from the ideal plane, and radiation background subtraction. The last of the tasks is the most difficult one because the relevant methods need to consider a variety of environmental factors; however, the entire set of steps can be made somewhat easier by using machine learning approaches. To facilitate the spectrum processing, a common option is to perform the Compton correction by subtracting the estimate of the Compton continuum, the noise reduction via spectral deconvolution, and also the stripping ratio correction that reduces the contribution of the higher-energy isotopes in the lower energy channels.

The research in [29] comprises the concept of scene-data fusion (SDF), i.e., fusing the data from the contextual sensors (cameras, lidars) and radiation detectors or cameras. The presented platform-independent device executes simultaneously the 3D model reconstruction via SLAM and the radiation layer measurements. The module integrates an omnidirectional lidar, a GNSS receiver, an inertial measurement unit (IMU), and a Compton camera based on high purity germanium (HPGe). To reconstruct the radiation image, a list-mode maximum-likelihood expectation-maximization algorithm is utilized. The authors claim that the method can be used even with commercial omnidirectional detectors. The device is experimentally tested in various real-world scenes, including Chernobyl (Fig. 2.3) and Fukushima.

Another device for 3D radiation mapping is discussed in [30], especially as regards the development and testing. The system consists of a depth camera, a GM detector, a CZT spectrometer, and a tablet, and can be either carried manually or mounted on a robot. The SLAM-based mapping yields a point cloud, reprocessed to remove the outliers; the radiation measurements are then projected onto the 3D model and also interpolated. The software is capable of filtering out different isotopes via the spectral data.

The potential of cooperation between the terrestrial and the aerial vehicles is exposed in [31]. The UAS provides a photogrammetry-based terrain map, i.e., an orthophoto and a digital elevation model (DEM), and also delivers a coarse radi-
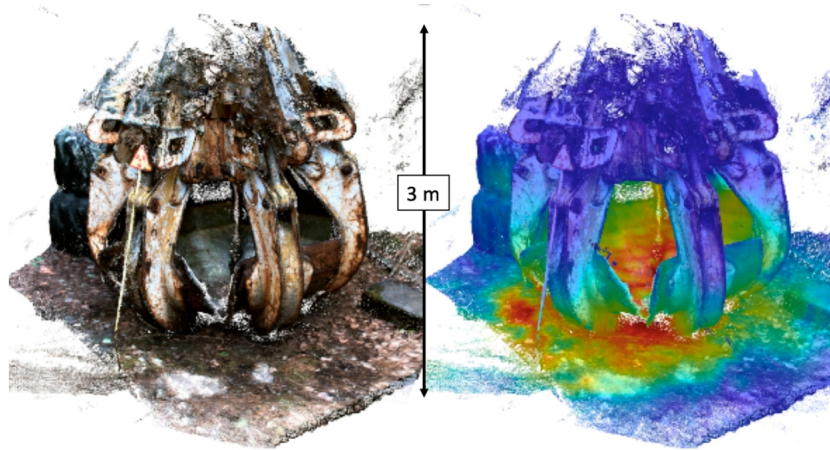
Figure 2.3: A model and a radiation map of the crane claw located at Chernobyl, acquired via scene-data fusion [29].

ation map. The discovered hotspots can then be inspected in detail by the UGV, which is, in addition to a detector, equipped with a lidar for dynamic obstacle avoidance. The path planning for the ground robot is carried out via A*, with the cost function preferring road traveling; the information on the terrain type is yielded by a ROI model subjected to segmentation. Interestingly, the UGV did not perform localization but only confirmed the presence of a radioactive source.

In article [32], the researchers set out innovative achievements in the field of UAS-UGV cooperation within radiation mapping. Similarly to the previous reference, the aircraft allows acquiring the DEM of the area, which is further utilized in constructing a costmap of the ROIs to enable the UGV to navigate safely. The Jackal UGV is equipped with an accurate RTK-GNSS receiver for self-localization and a 2-inch NaI spectrometric detector with the sampling period of 1 s. A set of rather sophisticated algorithms are utilized to extract useful information from the measured spectra, namely, the Fourier scattering transform and the Laplacian eigenmap. The spectra are classified into those corresponding to a source being present and those that embody background radiation only; the former are then subjected to iterative k-mean clustering by means of a modified Kolmogorov-Smirnov value as the metrics. As a result, the radiation hotspots produced by the point sources are segmented. The article also introduces an algorithm for the active localization of a single source. The proposed methods are thoroughly tested in field trials.

The authors of [33] compare different approaches to interpolating the radiation data from ground measurement stations scattered over a large area (approximately 7,500 km^2). The methods are based mostly on artificial neural networks of different types and structures, but fuzzy logic – the Mamdani system in particular – is applied too. The data arrive from 204 detection units, 70 % of them being used for training;

the rest then facilitate the accuracy evaluation. The authors conclude that the suggested methods yield fairly similar results, which are precise enough for practical applications.

In article [34], the examined problem lies in the directional sensitivity of a triplet of NaI scintillation detectors connected to a custom-made counting electronics. When the count rate is sufficient, the detectors establish the direction of the incident radiation at an error rate of 5°; however, the technique was practically verified only on low-activity sources in close proximity to the device. The method can handle multiple sources if these comprise different isotopes, the reason being that net counts in the photopeak area are relied on.

2.2 Localizing Radiation Hotspots

This section introduces various procedures to identify point sources of ionizing radiation. The emphasis is mainly on algorithms that enable such an activity, but related findings are also mentioned to provide a broader context. The literature overview focuses on the localization algorithms rather than the physical platforms applied. The section is structured to characterize, after a brief reference to previous work on operator-driven concepts, various passive and active localization schemes.

The project discussed in [35] involves a field experiment performed on a site with a partially collapsed hospital building which comprises a high activity source (1.5 GBq) to be localized. The actual search exploits a teleoperated Packbot UGV carrying a dose rate meter; the seeking strategy is based on following the radiation intensity gradient. The operator was unable to localize the source accurately until they changed the robot movement direction, resulting in a reduced shielding by the vehicle's body.

According to the experiments in [36], not all scenarios allow utilizing an autonomous UAS; therefore, the researchers suggest applying a teleoperated drone with a haptic interface. The aerial platform carries a custom CZT spectrometer, which enables the system to estimate the radiation gradient; the operator's controller then provides a force feedback to guide the pilot in the proper direction.

2.2.1 Passive Methods

A method for the passive localization of radioactive sources via a particle filter (PF) is outlined in [37]. The emphasis is on selecting the sampling points properly, as the source is supposed to lie in a region inaccessible to the robot; the iterative k-means clustering technique is employed to optimize the task.

In article [38], an iterative Markov chain Monte Carlo (MCMC) algorithm processes a sequence of manually selected sampling points. The procedure can be generalized to localize multiple sources; their amount, however, needs to be determined in advance, and the efficiency is significantly reduced.

Another method from the MCMC family finds use in [39]. The relevant algorithm is referred to as component-wise random walk with Metropolis-Hastings acceptance testing, and it addresses the uncertain self-localization of a robot. The authors also demonstrate the technique's capability of estimating the radiation intensity in unsampled parts of the ROI via the forward Monte Carlo analysis. Notably, the amount of sources has to be provided by the operator.

In article [40], the radiation field is modeled parametrically as a weighted sum of Gaussians. Two Bayesian estimators based on the progressive correction principle are compared: one employs the Gaussian approximation, and the other utilizes the Monte Carlo approximation. In the simulations, the former approach, which resembles the extended Kalman filter (EKF), delivers better results; importantly, this option is also less computationally intensive.

The authors of [41] exploit maximum likelihood estimation (MLE) combined with the hill-climbing algorithm. The method depends on the initial estimate, obtained in the discussed case via identifying the isodoses from the searched source.

In the project of [42], an unknown amount of sources is localizable using the data collected from a static sensor network. The applied algorithm is a hybrid PF enhanced via the mean-shift technique to increase the robustness of the procedure. The method can also consider the attenuation in unknown obstacles present in the ROI. The overall localization performance is significantly influenced by a proper choice of the bandwidth parameter.

Some of the experiments employ Compton cameras instead of the common omnidirectional detectors; see, for example, [43, 44, 45]. The methods used therein to extract the positional information from the radiation imaging devices include maximum likelihood expectation maximization (ML-EM), Kalman filter (KF), and customized additive point source localization (i.e., a sparse parametric image reconstruction algorithm); the last-mentioned option is proposed in [46].

Finally, worth mentioning are also the efforts summarized in [47], although the project does not focus strictly on radioactive sources. The proposed method processes the data from a static sensor network and localizes and even tracks an unknown number of moving sources. The advantages of the PF approach are discussed, including the unnecessity of both knowing the model order in advance and ensuring that the problem is stationary. The loss of statistical diversity in the particle set is addressed through a novel form of resampling, namely, the reversible jump MCMC algorithm.

2.2.2 Active Methods

Certain information-driven localization methods are based on contour following, i.e., establishing an isodose around a group of sources. Presumably, the sources yield spherical isodoses, which form circles in the survey plane, and they can be subsequently localized via tools such as the Hough transform. In article [48], an unmanned helicopter approaches the center of the ROI along an Archimedean spiral until the requested radiation level is encountered; the contour is then followed exploiting a PID controller. The authors also introduce an alternative in the form of a grid-based Bayesian estimator. In this case, the dynamic path planning rests in pursuing a direction perpendicular to the anticipated source-detector vector. Further, article [49] is dedicated to the development of a lightweight CZT-based detection system deployable to a circular swarm of three small drones. The measured data are processed to acquire the mean intensity in the circle, and also the gradient. The swarm then moves either in the direction of (source seeking) or perpendicularly to (contour following) the gradient. It is shown that, by making the swarm spin around its axis, the gradient estimate becomes more accurate. Next, let us mention the referenced study [50], whose authors propose a multi-phase localization procedure. At the initial stage, prominent radiation levels are identified using a log gradient classifier, and then the corresponding contours are mapped. It has to be specified if the contours are concentric (single source) or their shape varies (distributed sources); in the latter case, an optimum contour is selected for detailed sampling, and the sources are eventually localized via a variational Bayesian algorithm.

In article [51], the scenario relies on a presupposed single source in an obstacle-free ROI. The localization exploits a PF enhanced with an MCMC algorithm. To construct an optimum measurement trajectory, the partially observable Markov decision process (POMDP) is employed, with the reward function based on information entropy. The entropy reduction can be encountered also in [52]; here, the results are compared to a traditional pre-planned survey. In this context, by extension, the authors of [53] developed a method embodied in an unscented particle filter, being a hybrid between the PF and the unscented Kalman filter (UKF). To prevent particle degeneracy, the divide-and-conquer strategy is employed. The robot keeps moving towards the instantaneous estimate of the source's position until the filter converges, meaning that only a single radioactive item can be handled.

The approach from [54] rests in estimating the sources' parameters via a regularized PF enhanced with the progressive correction principle. The amount of localized items does not need to be known in advance, as it is one of the retrieved parameters. The presented active motion control utilizes the Rényi divergence expectation maximization to select the most suitable action from a set of possible candidates.
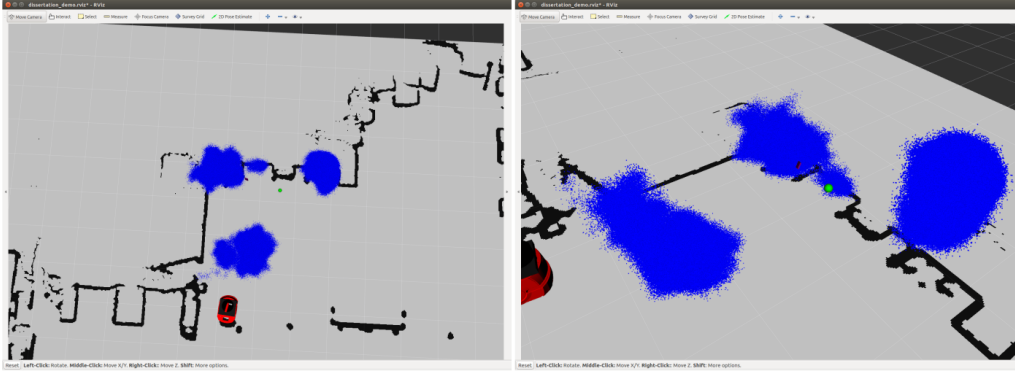
Figure 2.4: The particle filter-based active localization: the final distribution of the particles from two angles [55].

The method is verified both through simulation and on a real-world dataset, demonstrating its ability to find up to two sources.

The concept presented in [55] employs a PF for the localization and introduces three different active exploration strategies. The first option is denoted as a variance of the distances, maximizing the variance of the particle distances to the candidate sampling point; this leads to sampling near the boundaries of the particle set, which gradually shrinks. The second strategy, namely, previous measurements avoidance, maximizes the sum of the distances between the candidate sampling point and its predecessors. The third and final approach then maximizes the information gain quantified by the Fischer information matrix (FIM). After each iteration, the particles are clustered, resampled, and regularized; the variance of the Gaussian regularization kernel is deduced from the maximum deviation of all the clusters. The methods are verified via simulations based on real-world surveys; the testing emphasizes particle convergence under individual planning strategies. The localization algorithm's outputs are shown in Fig. 2.4.

Again, there are several examples of experiments relying on directional Compton detectors, such as those exposed in articles [56] and [57]. In these cases, the decision-making strategies for active exploration can rely on diverse procedures, including maximizing the FIM traces, behavior-based exploration, multi-criteria decision-making, and principal component analysis. However, it is also worth mentioning that the possibility of retrieving multiple sources is not enabled in the active autonomous mode.

3 Research Summary

The candidate's initial experience in ionizing radiation measurements arose from his activities within a research project dedicated to developing a radiation monitoring system based on a directionally sensitive detection head mountable on mobile robots. The system eventually comprised a pair of scintillation detectors, of which one was shielded by a massive lead cylinder with an aperture. The collimator had been designed as rotable to measure the directional characteristics of the incident radiation; regrettably, the sampling proved to be rather lengthy. Importantly, the author of this thesis did not participate in developing the hardware setup; rather than that, he focused on integrating the system in a robotic platform and proposing the control algorithms for predefined radiation monitoring tasks.

The candidate learned the basic principles of robotic radiation mapping by equipping the unmanned vehicle Orpheus-X4 with a commercial dose rate meter and performing a simple single-source mission; the robot had been built at the Robotics and AI group headed by Prof. Ludek Zalud at Brno University of Technology. These initial results formed the actual basis of the author's Bachelor's thesis (available in Czech) [58].

Subsequently, as the collimator-based detection system was still being developed at the time, the author started to examine a different principle, namely, partial directional sensitivity, which exploited a pair of fixed scintillation detectors. Thanks to both the inverse square law and the mutual shielding of the scintillation crystals, the system has exhibited distinctive angular characteristics. The effect can be further amplified by inserting a lead layer between the detectors. This approach eliminates the major disadvantages of the lead collimator, above all, the large mass, problematic dynamic properties, and sampling time required; however, the provided angular resolution is markedly lower. Upon completion of the experiments (the year 2017), the detection system was integrated in the Orpheus-X4 robot to allow field testing (Fig. 3.1a), and selected results were presented at local conferences.

The cooperation between the terrestrial and the aerial robots, whose procedural details were co-designed by the author, was first demonstrated on a UAS providing a photogrammetry-based map to define the region of interest and to visualize the data

(Fig. 3.2a). The experimental results were presented at the HoloMAS[1] conference through article [59]. The study also involved an early simplistic active localization approach capable of handling a single radionuclide. The method rested in estimating the direction to the source from the data points acquired along the conventional parallel lines from the radiation mapping.

More sophisticated localization schemes based on circular trajectories and the directional sensitivity provided by the detectors were proposed and verified in the candidate's Master's thesis, [60]. The sampling points arranged in a circle allowed estimating the directions to multiple sources (both inside and outside the circle) under the assumption that the radiation origins have a sufficient angular separation; in this condition, each of the source estimates is then approached while correcting the direction via a P controller. When more circles are employed simultaneously and the directional rays intersect, the sources' positions are estimable directly, without requiring the robot to drive towards them. The method nevertheless exhibits important drawbacks, the inability to address the obstacles and the need to define the circles manually in particular.

The cooperation with the UAS and several of the active localization options were eventually joined together to be published in the *International Journal of Advanced Robotic Systems*[2] through article *Cooperation between an unmanned aerial vehicle and an unmanned ground vehicle in highly accurate localization of gamma radiation hotspots* [61] in 2018. In this case, the aerial data were also utilized to construct an occupancy grid of the zone, enabling the robot to automatically navigate from the deployment site to the selected ROI.

The above-mentioned localization approaches yielded only a gross position estimate; therefore, the author developed an algorithm exploiting the Gauss-Newton method to increase the localization accuracy. The achievements were summarized in a paper presented at the ELEKTRO[3] conference in 2018 [62]. In the same year, the candidate also began to explore the capabilities and limitations of aerial radiation measurements carried out by UASs. The impact of the flight altitude in multiple scenarios was discussed through the simulations set out in a PdES[4] conference paper [63]. The research also involved the idea to follow the terrain shape via altering the altitude to maintain an approximately constant height above the ground level.

---

[1]Industrial Applications of Holonic and Multi-Agent Systems – 8th International Conference, HoloMAS 2017, Lyon, France, August 28–30, 2017

[2]AIS 0.225, Q4 in the *Robotics* category, special issue titled *Mobile Robots*

[3]12th International Conference ELEKTRO 2018, Mikulov, Czech Republic, May 21–23, 2018

[4]15th IFAC Conference on Programmable Devices and Embedded Systems, Ostrava, Czech Republic, May 23–25, 2018

Figure 3.1: The UGV Orpheus-X4 equipped with a pair of scintillation detectors (a) and a collimator-based detection system (b).

In 2019, the project dedicated to the collimator-based detection system was completed, resulting in the article *Localization of ionizing radiation sources via an autonomous robotic system*; this output was published in the *Radiation Protection Dosimetry*[5] journal. The UGV carrying the device (Fig. 3.1b) had the capacity to operate in three distinct modes, as follows: First, the conventional radiation mapping, where the directional sensitivity was not needed. Second, the localization of the point sources, with the robot following a base trajectory until the direction towards a source was identified; the source was then approached and localized, allowing the vehicle to return to the original trajectory. The research within this mode comprised developing a novel algorithm for two-phase survey planning. Third, the inspection to periodically repeat a manually defined measurement sequence and indicate any changes.

At the next stage, preliminary work to contribute towards the UAS-based 3D radiation mapping of buildings was outlined in a paper presented at the MESAS[6] conference [64]. The concept involved a real-world building model and simulated radiation data, and a method to process the data was proposed.

In 2020, the author benefited from participating in a three-month internship as a consultant at the International Atomic Energy Agency; more concretely, he spent the allocated time at the Nuclear Science and Instrumentation Laboratory, Seibersdorf, Austria, under the guidance of Assoc. Prof. Petr Sladek. This experience enabled the author to gain a deeper insight into the radiation detection principles, especially

---

[5]AIS 0.206, Q3 in the *Nuclear Science and Technology* category, special issue titled *40th Days of Radiation Protection*

[6]Modelling and Simulation for Autonomous Systems, 6th International Conference, MESAS 2019, Palermo, Italy, October 29–31, 2019
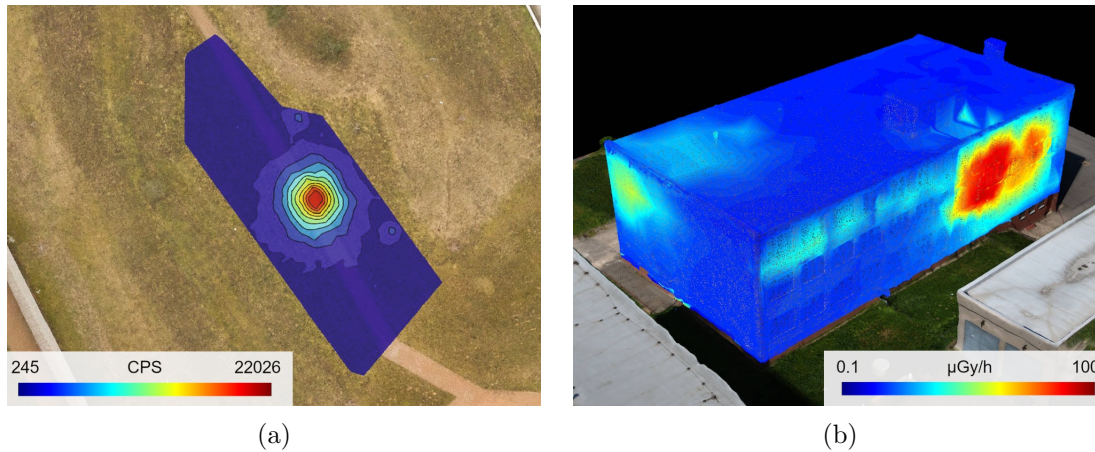
33

Figure 3.2: A common radiation map acquired with a UGV (a), and a 3D radiation map measured via a UAS (b).

as he helped to develop a methodology for using unmanned aircraft systems within the radiation mapping domain. The performed tasks also included assessing various spatial interpolation methods and processing the data acquired in the Fukushima Prefecture.

The activities relating to the cooperation between UGVs and UASs culminated in 2021, when the comprehensive results were released through the *Journal of Field Robotics*[7], in article *An automated heterogeneous robotic system for radiation surveys: Design and field testing* [65]. The research involved a three-phase survey, covering the aerial photogrammetry, aerial radiation mapping with terrain tracking to identify the hotspots, and a detailed ground measurement to enable a highly accurate source localization. The complete pipeline required only very few interventions by the human operator, as the majority of the tasks had been fully automated. In this case, the localization procedure was merely passive; the robot nevertheless had the capacity to avoid static obstacles occurring in the ROI.

The follow-up research in the radiation mapping of buildings was eventually presented at the *IROS 2022 – IEEE/RJS International Conference on Intelligent Robots and Systems*, with paper *Unmanned Aircraft System-Based Radiological Mapping of Buildings* [66]. The study embodied a proof-of-concept experimental report formed under real-world conditions. At the time of the project, the UAS responsible for the data collection was piloted manually, as a close proximity to the building walls was required. The experiment yielded a 3D radiation map (Fig. 3.2b) and demonstrated the possibility of roughly localizing the sources inside buildings.

---

[7]AIS 1.253, Q1 in the *Robotics* category

At present, the candidate focuses on the active localization while relaxing the previously introduced constraints. His new approach exploits, on the one hand, a particle filter capable of estimating the amount of sources and their parameters on the fly, and, on the other, an entropy-based motion planner which optimizes the measurement trajectory while ensuring that the obstacles are avoided. A scenario with multiple sources has thus far been verified only through simulations formed from a previously acquired real-world dataset. The up-to-date results are summarized in article *Localizing Multiple Radiation Sources Actively with a Particle Filter* [67], which is being peer reviewed as of October 2023. The achievements have already been presented at the ICRA[8] conference via a *late breaking results* poster. The real-world outcomes obtained in a single source scenario are presented in a relevant video, [68].

The timeline of the principal research results can be seen in Table 3.1.

---

[8]IEEE International Conference on Robotics and Automation 2023, London, United Kingdom, 29 May – 2 June, 2023

2015–2017 • **Prior work**

Integrating the detection systems in robots; performing basic radiation mapping tasks; developing the elementary active localization algorithms; and publishing the preliminary results at local conferences.

2018 • **Cooperation Between an Unmanned Aerial Vehicle ...**
Journal article

Designing and verifying the scheme to exploit a map acquired via aerial photogrammetry in the ground radiation mapping.

2019 • **Localization of Ionizing Radiation Sources via an ...**
Journal article

Introducing the directional detection system based on the lead collimator, and showcasing the capabilities of the device.

2020 • **Consultant with the IAEA**

Processing the data from contaminated regions in Fukushima Pref., and enhancing the methodology for UAS-based radiation mapping.

2021 • **An Automated Heterogeneous Robotic System for ...**
Journal article

Improving the cooperation between the aerial and the terrestrial robots in multi-phase surveying, and a highly accurate localization of radiation sources.

2022 • **Unmanned Aircraft System-Based Radiological ...**
Conference paper

Demonstrating the possibility of acquiring a 3D radiation map of a building, and exposing the ability to roughly localize the sources inside.

2023 • **Localizing Multiple Radiation Sources Actively ...**
Submitted manuscript

Presenting a novel paradigm for the active localization of an unknown amount of radioactive sources, utilizing the particle filter and the two-component trajectory planner.

Table 3.1: The timeline of the selected publications and related activities.

4 Discussion

The research results presented within this Ph.D. thesis can be categorized into three segments corresponding to the original goals defined above in the *Aims and Objectives* section. All of the preset aims and objectives appear to have been met; thus, in this chapter, they will be covered in greater detail to assess the achievements as well as potential deficiencies.

The first aim rested in designing physical platforms to deliver various radiation measurement-related algorithms in real-world conditions rather than through simulation studies only. This procedure, not having been conceived to primarily bring scientific innovations, embodied a cornerstone which allowed fulfilling the challenging follow-up tasks. A major part of the research activities was carried out using the Orhpeus-X4 terrestrial platform and the scintillation detector dual sensor system. The integration of the setup required not only mechanical mounting but also software development to adjust the devices, read and process the radiation spectra, and fuse the spectra with the positional data from the RTK-GNSS receiver. Comparable efforts were made in relation to the collimation-based detection system, which, additionally, required the control of the collimator rotation. The smooth operation of the detectors was ensured via custom software developed by the author of the thesis. Regarding the UASs, two different self-contained radiation detection systems, independent from the aerial platform, were utilized: One was a commercial device used in the cooperative exercise (Fig. 4.1a), and the other, applied in the building mapping, was an experimental module offering more flexibility (Fig. 4.1b). In both cases, the system stored the measurements using a data logger which allowed only post-processing, eliminating the possibility of active localization. Aerial vehicle capabilities similar to those of the ground unit discussed herein are currently under development.

The second goal addressed the problem of point source localization, focusing on the post-processing algorithms and the information-driven control. The ultimate pipeline to facilitate inputting scattered datapoints to yield the amount of the sources along with their intensities and positions was successfully designed, tested, and published. The actual procedure involves interpolating the datapoints; to execute the task, natural neighbor interpolation based on the Delaunay triangulation is applied. This method consistently delivered satisfactory outcomes and was also

<div align="center">(a)   (b)</div>

Figure 4.1: The radiation detection systems integrated onboard the photographed UASs: the DRONES-G carried by the BRUS drone (a), and the experimental module mounted on the Matrice 300 (b).

evaluated as the best option in an analysis performed jointly with the International Atomic Energy Agency. The hotspots are then separated from the radiation background via an adaptive thresholding algorithm structured by the candidate; this tool is able to determine the amount and approximate locations of the sources. The approach exhibits superior robustness, being applicable with correct results to both the terrestrial and the aerial data, where the dynamic range may differ by several orders of magnitude. Finally, the gross estimates are fine-tuned by means of the Gauss-Newton method, achieving an accuracy resembling that of the data georeferencing error. The principal advantage of the proposed pipeline, in contrast to other state-of-the-art approaches such as MLE, rests in its very simple implementability and low computational requirements. The design was also thoroughly verified in field tests under various scenarios, using ground and aerial robots.

Regarding the active (or information-driven) localization, different concepts have been explored and compared. The earlier projects focused on estimating the vector towards a source, exploiting directionally sensitive sensor equipment. The author then showed through several experiments that such an approach has the capacity to reduce the time required to retrieve the sources; the algorithms, however, exhibited serious deficiencies in terms of the generality and usability in real-world conditions. Two distinct schemes with a potential to resolve the direction of the incident radiation were studied, and it may be positively concluded that the dual detector surpasses the collimator-based system thanks to a greater versatility. To improve the universality and robustness, the directional approach was eventually abandoned to be substituted with Bayesian methods, the particle filter in particular; this filter estimates the source positions on-line. Notably, knowing the instantaneous mutual

Figure 4.2: The decontaminable terrestrial robot Orpheus-AC3.

positions of the robot and the source indirectly reveals the vector too. However, instead of following the direction, the motion planner operates to reduce the Shannon entropy by driving the robot towards points of a greater information value. Although the particle filter-based radioactive source localization is well known in the literature, the author believes that it has not been combined to date with the novel planner, which introduces important benefits in terms of the complexity.

The third aim lay in reaching beyond the scope of the conventional radiation mapping, the plan being to identify the advantages of combining robotic platforms of different kinds and expanding the mapping to include the third dimension. The experiments with the cooperation between ground and aerial robots managed to emphasize and exploit the positive features of both platforms. As is expectable, the drones have the capacity to rapidly explore vast areas and are not limited by ground-level obstacles or steep terrain; however, they offer only a meager spatial resolution and do not facilitate localizing the sources very accurately. In one of the published scenarios, an areal contamination was simulated using a number of point sources; the fact that multiple sources are involved can be only revealed by a follow-up survey carried out in the region by a terrestrial robot. Generally, a UGV can explore only compact places selected by a UAS to deliver a detailed radiation map in a time-efficient manner. The key assets of the research consist in designing a highly automated pipeline that has proved beneficial in comprehensive experimentation involving actual radiological sources. Utilizing airborne detection systems then facilitated the production of a 3D radiation maps. The field exercise showed that the pre-designed approach is viable, and the preliminary results were satisfactory. The views from the three dimensions allow revealing information and context not accessible via traditional methods; however, further research on the autonomy is required to ultimately eliminate the pilot from the pipeline.

In the author's opinion, the scientific merit of this thesis rests in providing a thorough insight into robotic radiation measurements, covering multiple detection principles, data processing algorithms, and unmanned platforms. Several methods were adopted and novel techniques designed to achieve the preset goals. Except for the newly developed active localization scheme, all of the conclusions are supported by elaborate empirical research. Obviously, the addressed topic is very wide and has become a subject of greater interest to the expert community in recent years, meaning that there still remain diverse complex tasks to focus on. The future efforts are supposed to increase the degree of autonomy and to eliminate the dependence on GNSS receivers, as these are not applicable in all environments. The experimental platforms need to employ SLAM instead and are planned to incorporate dynamic obstacle avoidance too. By extension, some real-world scenarios may involve radioactive dust-contaminated environments, and any convenient ground platform must therefore be readily decontaminable; a model robot for such a purpose, an Orpheus-AC3 designed by the group of Prof. Zalud (BUT), is visualized in Fig. 4.2. Currently, the most prominent assignment is to assess the particle filter performance in real-world conditions.

Bibliography

[1] Glenn F. Knoll. *Radiation Detection and Measurement*. John Wiley & Sons, Hoboken, New Jersey, 3rd edition edition, August 2010. ISBN: 978-0-470-13148-0.

[2] I Winkelmann, M Thomas, and K Vogl. Aerial measurements on uranium ore mining, milling and processing areas in Germany. *Journal of Environmental Radioactivity*, 53(3):301–311, April 2001. `doi:10.1016/S0265-931X(00)00138-7`.

[3] Masaki Andoh, Yukio Nakahara, Shuichi Tsuda, Tadayoshi Yoshida, Norihiro Matsuda, Fumiaki Takahashi, Satoshi Mikami, Nobuyuki Kinouchi, Tetsuro Sato, Minoru Tanigaki, Koichi Takamiya, Nobuhiro Sato, Ryo Okumura, Yukio Uchihori, and Kimiaki Saito. Measurement of air dose rates over a wide area around the Fukushima Dai-ichi Nuclear Power Plant through a series of car-borne surveys. *Journal of Environmental Radioactivity*, 139:266–280, January 2015. `doi:10.1016/j.jenvrad.2014.05.014`.

[4] Nuclear Decommissioning Authority. Particles in the Environment Annual Report for 2017 and forward Programme. *Sellafield Ltd.*, 2018. URL: `https://assets.publishing.service.gov.uk/government/uploads/system/uploads/attachment_data/file/730071/Particles_in_the_Environment_Annual_Report_for_2017.pdf`.

[5] Chernobyl Robots. *Chernobyl X*, 2021. URL: `https://chernobylx.com/chernobyl-robots/`.

[6] Erico Guizzo. Robots Enter Fukushima Reactors, Detect High Radiation. *IEEE Spectrum*, 2011. URL: `https://spectrum.ieee.org/robots-enter-fukushima-reactors-detect-high-radiation`.

[7] Aleksandra Peeva. Now Available: New Drone Technology for Radiological Monitoring in Emergency Situations. *International Atomic Energy Agency*, 2021. URL: `https://www.iaea.org/newscenter/news/now-available-new-drone-technology-for-radiological-monitoring-in-emergency-situations`.

[8] 'Dangerous' radioactive material stolen in Mexico. *BBC News*, 2015. URL: `https://www.bbc.com/news/world-latin-america-32332271`.

[9] Graham Templeton. Hanford Nuclear Site Tunnel Collapse: Send in the Robot. *Inverse*, 2017. URL: `https://www.inverse.com/article/31384-hanford-nuclear-power-station-emergency-robot-cleanup-robotics`.

[10] Kelsey D. Atherton. How drones are helping monitor Kyrgyzstan's radioactive legacy. *Popular Science*, 2022. URL: `https://www.popsci.com/technology/kyrgyzstan-drone-radiation-monitoring/`.

[11] K. A. Pradeep Kumar, G. A. Shanmugha Sundaram, and R. Thiruvengadathan. Advances in detection algorithms for radiation monitoring. *Journal of Environmental Radioactivity*, 217:106216, June 2020. `doi:10.1016/j.jenvrad.2020.106216`.

[12] Frank Mascarich, Mihir Kulkarni, Paolo De Petris, Taylor Wilson, and Kostas Alexis. Autonomous mapping and spectroscopic analysis of distributed radiation fields using aerial robots. *Autonomous Robots*, November 2022. `doi:10.1007/s10514-022-10064-7`.

[13] D. Connor, P. G. Martin, and T. B. Scott. Airborne radiation mapping: overview and application of current and future aerial systems. *International Journal of Remote Sensing*, 37(24):5953–5987, December 2016. `doi:10.1080/01431161.2016.1252474`.

[14] P. G. Martin, S. Kwong, N. T. Smith, Y. Yamashiki, O. D. Payton, F. S. Russell-Pavier, J. S. Fardoulis, D. A. Richards, and T. B. Scott. 3D unmanned aerial vehicle radiation mapping for assessing contaminant distribution and mobility. *International Journal of Applied Earth Observation and Geoinformation*, 52:12–19, October 2016. `doi:10.1016/j.jag.2016.05.007`.

[15] Christian Kunze, Benedikt Preugschat, Robert Arndt, Felix Kandzia, Benjamin Wiens, and Sven Altfelder. Development of a UAV-Based Gamma Spectrometry System for Natural Radionuclides and Field Tests at Central Asian Uranium Legacy Sites. *Remote Sensing*, 14(9):2147, January 2022. `doi:10.3390/rs14092147`.

[16] Dean T. Connor, Kieran Wood, Peter G. Martin, Sevda Goren, David Megson-Smith, Yannick Verbelen, Igor Chyzhevskyi, Serhii Kirieiev, Nick T. Smith, Tom Richardson, and Thomas B. Scott. Radiological Mapping of Post-Disaster Nuclear Environments Using Fixed-Wing Unmanned Aerial Systems: A Study From Chornobyl. *Frontiers in Robotics and AI*, 6, 2020. `doi:10.3389/frobt.2019.00149`.

[17] Luis Ramos Pinto, Alberto Vale, Yoeri Brouwer, Jorge Borbinha, Jose Corisco, Rodrigo Ventura, Ana Margarida Silva, Andre Mourato, Goncalo Marques, Yuri Romanets, Susana Sargento, and Bruno Goncalves. Radiological Scouting, Monitoring and Inspection Using Drones. *Sensors*, 21(9):3143, January 2021. `doi:10.3390/s21093143`.

[18] Henrique Carvalho, Alberto Vale, Ruben Marques, Rodrigo Ventura, Yoeri Brouwer, and Bruno Goncalves. Remote inspection with multi-copters, radiological sensors and SLAM techniques. *EPJ Web of Conferences*, 170:07014, 2018. `doi:10.1051/epjconf/201817007014`.

[19] Yukihisa Sanada, Tadashi Orita, and Tatsuo Torii. Temporal variation of dose rate distribution around the Fukushima Daiichi nuclear power station using unmanned helicopter. *Applied Radiation and Isotopes*, 118:308–316, December 2016. `doi:10.1016/j.apradiso.2016.09.008`.

[20] Stefan Cerba, Jakub Luley, Branislav Vrban, Filip Osusky, and Vladimir Necas. Unmanned Radiation-Monitoring System. *IEEE Transactions on Nuclear Science*, 67(4):636–643, April 2020. Conference Name: IEEE Transactions on Nuclear Science. `doi:10.1109/TNS.2020.2970782`.

[21] Nur Aira Abd Rahman, Khairul Salleh Mohamed Sahari, Nasri A Hamid, and Yew Cheong Hou. A coverage path planning approach for autonomous radiation mapping with a mobile robot. *International Journal of Advanced Robotic Systems*, 19(4):172988062211164, July 2022. `doi:10.1177/17298806221116483`.

[22] G. A. Wilde, R. R. Murphy, D. A. Shell, and C. M. Marianno. A man-packable unmanned surface vehicle for radiation localization and forensics. In *2015 IEEE International Symposium on Safety, Security, and Rescue Robotics (SSRR)*, pages 1–6, October 2015. `doi:10.1109/SSRR.2015.7442944`.

[23] Christian Ducros, Gerard Hauser, Najib Mahjoubi, Philippe Girones, Laurence Boisset, Antoine Sorin, Eric Jonquet, Jean Michel Falciola, and Albert Benhamou. RICA: A Tracked Robot for Sampling and Radiological Characterization in the Nuclear Field: A Tracked Robot for Sampling. *Journal of Field Robotics*, 34(3):583–599, May 2017. `doi:10.1002/rob.21650`.

[24] K. Ohno, S. Kawatsuma, T. Okada, E. Takeuchi, K. Higashi, and S. Tadokoro. Robotic control vehicle for measuring radiation in Fukushima Daiichi Nuclear Power Plant. In *2011 IEEE International Symposium on Safety, Security, and Rescue Robotics*, pages 38–43, November 2011. `doi:10.1109/SSRR.2011.6106792`.

[25] Keir Groves, Emili Hernandez, Andrew West, Thomas Wright, and Barry Lennox. Robotic Exploration of an Unknown Nuclear Environment Using Radiation Informed Autonomous Navigation. *Robotics*, 10(2):78, June 2021. `doi:10.3390/robotics10020078`.

[26] Andrew West, Ioannis Tsitsimpelis, Mauro Licata, Anze Jazbec, Luka Snoj, Malcolm J. Joyce, and Barry Lennox. Use of Gaussian process regression for radiation mapping of a nuclear reactor with a mobile robot. *Scientific Reports*, 11(1):13975, July 2021. `doi:10.1038/s41598-021-93474-4`.

[27] A. Miller, R. Machrafi, and A. Mohany. Development of a semi-autonomous directional and spectroscopic radiation detection mobile platform. *Radiation Measurements*, 72:53–59, January 2015. `doi:10.1016/j.radmeas.2014.11.009`.

[28] Frank E. Schneider and Dennis Wildermuth. Real-World Robotic Competitions for Radiological and Nuclear Inspection Tasks. In *2019 20th International Carpathian Control Conference (ICCC)*, May 2019. `doi:10.1109/CarpathianCC.2019.8765680`.

[29] Kai Vetter, Ross Barnowski, Joshua W. Cates, Andrew Haefner, Tenzing H. Y. Joshi, Ryan Pavlovsky, and Brian J. Quiter. Advances in Nuclear Radiation Sensing: Enabling 3-D Gamma-Ray Vision. *Sensors*, 19(11):2541, January 2019. `doi:10.3390/s19112541`.

[30] F. Hautot, P. Dubart, R. Abou-Khalil, and M. Morichi. Novel real-time 3D radiological mapping solution for ALARA maximization, D D assessments and radiological management. In *2015 4th International Conference on Advancements in Nuclear Instrumentation Measurement Methods and their Applications (ANIMMA)*, April 2015. `doi:10.1109/ANIMMA.2015.7465648`.

[31] Gordon Christie, Adam Shoemaker, Kevin Kochersberger, Pratap Tokekar, Lance McLean, and Alexander Leonessa. Radiation search operations using scene understanding with autonomous UAV and UGV. *Journal of Field Robotics*, 34(8):1450–1468, May 2017. `doi:10.1002/rob.21723`.

[32] John Peterson, Weilin Li, Brian Cesar-Tondreau, John Bird, Kevin Kochersberger, Wojciech Czaja, and Morgan McLean. Experiments in unmanned aerial vehicle/unmanned ground vehicle radiation search. *Journal of Field Robotics*, 2019. `doi:10.1002/rob.21867`.

[33] Cafer Mert Yesilkanat, Yasar Kobya, Halim Taskın, and Ugur Cevik. Spatial interpolation and radiological mapping of ambient gamma dose rate by using artificial neural networks and fuzzy logic methods. *Journal of Environmental Radioactivity*, 175-176:78–93, September 2017. `doi:10.1016/j.jenvrad.2017.04.015`.

[34] C. Schrage, N. Schemm, S. Balkir, M. W. Hoffman, and M. Bauer. A Low-Power Directional Gamma-Ray Sensor System for Long-Term Radiation Monitoring. *IEEE Sensors Journal*, 13(7):2610–2618, July 2013. `doi:10.1109/JSEN.2013.2258009`.

[35] D. Duckworth, B. Shrewsbury, and R. Murphy. Run the robot backward. In *2013 IEEE International Symposium on Safety, Security, and Rescue Robotics (SSRR)*, October 2013. `doi:10.1109/SSRR.2013.6719372`.

[36] Jacopo Aleotti, Giorgio Micconi, Stefano Caselli, Giacomo Benassi, Nicola Zambelli, Manuele Bettelli, Davide Calestani, and Andrea Zappettini. Haptic Teleoperation of UAV Equipped with Gamma-Ray Spectrometer for Detection and Identification of Radio-Active Materials in Industrial Plants. In Tullio Tolio, Giacomo Copani, and Walter Terkaj, editors, *Factories of the Future: The Italian Flagship Initiative*, pages 197–214. Springer International Publishing, Cham, 2019. `doi:10.1007/978-3-319-94358-9_9`.

[37] Nur Aira Abd Rahman, Khairul Salleh Mohamed Sahari, and Nasri A. Hamid. An Autonomous Clutter Inspection Approach for Radiological Survey Using Mobile Robot. *IEEE Transactions on Automation Science and Engineering*, 20(2):1212–1225, April 2023. `doi:10.1109/TASE.2022.3180345`.

[38] Yufeng Xiao, Cheng Zhang, Jia Luo, Chuan Yang, and Cheng Liu. Integrating the radiation source position into a grid map of the environment using a mobile robot. *Nuclear Instruments and Methods in Physics Research Section A: Accelerators, Spectrometers, Detectors and Associated Equipment*, 976:164253, October 2020. `doi:10.1016/j.nima.2020.164253`.

[39] Robin McDougall, Scott B. Nokleby, and Ed Waller. Probabilistic-Based Robotic Radiation Mapping Using Sparse Data. *Journal of Nuclear Engineering and Radiation Science*, 4(021009), March 2018. `doi:10.1115/1.4038185`.

[40] M. R. Morelande and A. Skvortsov. Radiation field estimation using a Gaussian mixture. In *2009 12th International Conference on Information Fusion*, pages 2247–2254, July 2009. ISBN: 978-0-9824-4380-4.

[41] Wei Tan, Jianbin Zhou, Fang Fang, Xiaozhe Li, and Xu Hong. A fast gamma-ray source localization method for mobile robots. *Applied Radiation and Isotopes*, 188:110377, October 2022. `doi:10.1016/j.apradiso.2022.110377`.

[42] Jren-Chit Chin, David K.Y. Yau, and Nageswara S.V. Rao. Efficient and Robust Localization of Multiple Radiation Sources in Complex Environments. In *2011 31st International Conference on Distributed Computing Systems*, pages 780–789, June 2011. `doi:10.1109/ICDCS.2011.94`.

[43] Doyeon Kim, Hanwool Woo, Yonghoon Ji, Yusuke Tamura, Atsushi Yamashita, and Hajime Asama. 3D radiation imaging using mobile robot equipped with radiation detector. In *2017 IEEE/SICE International Symposium on System Integration (SII)*, pages 444–449, December 2017. `doi:10.1109/SII.2017.8279253`.

[44] Petr Stibinger, Tomas Baca, and Martin Saska. Localization of Ionizing Radiation Sources by Cooperating Micro Aerial Vehicles With Pixel Detectors in Real-Time. *IEEE Robotics and Automation Letters*, 5(2):3634–3641, April 2020. `doi:10.1109/LRA.2020.2978456`.

[45] Jayson R. Vavrek, Daniel Hellfeld, Mark S. Bandstra, Victor Negut, Kathryn Meehan, William Joe Vanderlip, Joshua W. Cates, Ryan Pavlovsky, Brian J. Quiter, Reynold J. Cooper, and Tenzing H. Y. Joshi. Reconstructing the Position and Intensity of Multiple Gamma-Ray Point Sources With a Sparse Parametric Algorithm. *IEEE Transactions on Nuclear Science*, 67(11):2421–2430, November 2020. `doi:10.1109/TNS.2020.3024735`.

[46] Daniel Hellfeld, Tenzing H. Y. Joshi, Mark S. Bandstra, Reynold J. Cooper, Brian J. Quiter, and Kai Vetter. Gamma-Ray Point-Source Localization and Sparse Image Reconstruction Using Poisson Likelihood. *IEEE Transactions on Nuclear Science*, 66(9):2088–2099, September 2019. `doi:10.1109/TNS.2019.2930294`.

[47] J. R. Larocque, J. P. Reilly, and W. Ng. Particle filters for tracking an unknown number of sources. *IEEE Transactions on Signal Processing*, 50(12):2926–2937, December 2002. `doi:10.1109/TSP.2002.805251`.

[48] Jerry Towler, Bryan Krawiec, and Kevin Kochersberger. Radiation Mapping in Post-Disaster Environments Using an Autonomous Helicopter. *Remote Sensing*, 4(7):1995–2015, July 2012. `doi:10.3390/rs4071995`.

[49] Zachary Cook, Monia Kazemeini, Alexander Barzilov, and Woosoon Yim. Low-altitude contour mapping of radiation fields using UAS swarm. *Intelligent Service Robotics*, 12(3):219–230, 2019. `doi:10.1007/s11370-019-00277-8`.

[50] Abdullah Al Redwan Newaz, Sungmoon Jeong, Hosun Lee, Hyejeong Ryu, and Nak Young Chong. UAV-based multiple source localization and contour mapping of radiation fields. *Robotics and Autonomous Systems*, 85:12–25, November 2016. `doi:10.1016/j.robot.2016.08.002`.

[51] Jianwen Huo, Manlu Liu, Konstantin A. Neusypin, Haojie Liu, Mingming Guo, and Yufeng Xiao. Autonomous Search of Radioactive Sources through Mobile Robots. *Sensors*, 20(12):3461, January 2020. `doi:10.3390/s20123461`.

[52] Nantawat Pinkam, Armagan Elibol, and Nak Young Chong. Informative Mobile Robot Exploration for Radiation Source Localization with a Particle Filter. In *2020 Fourth IEEE International Conference on Robotic Computing (IRC)*, pages 107–112, November 2020. `doi:10.1109/IRC.2020.00024`.

[53] Yizhou Liu, Yike Xuan, De Zhang, and Shuliang Zou. Localizing unknown radiation sources by unscented particle filtering based on divide-and-conquer sampling. *Journal of Nuclear Science and Technology*, 59(9):1149–1161, September 2022. `doi:10.1080/00223131.2022.2032858`.

[54] Branko Ristic, Mark Morelande, and Ajith Gunatilaka. Information driven search for point sources of gamma radiation. *Signal Processing*, 90(4):1225–1239, April 2010. `doi:10.1016/j.sigpro.2009.10.006`.

[55] Robert Blake Anderson, Mitch Pryor, Adrian Abeyta, and Sheldon Landsberger. Mobile Robotic Radiation Surveying With Recursive Bayesian Estimation and Attenuation Modeling. *IEEE Transactions on Automation Science and Engineering*, 19(1):410–424, January 2022. `doi:10.1109/TASE.2020.3036808`.

[56] Michael S. Lee, Daniel Shy, William Red Whittaker, and Nathan Michael. Active Range and Bearing-based Radiation Source Localization. In *2018 IEEE/RSJ International Conference on Intelligent Robots and Systems (IROS)*, pages 1389–1394, October 2018. `doi:10.1109/IROS.2018.8593625`.

[57] Hadi Ardiny, Stefan Witwicki, and Francesco Mondada. Autonomous Exploration for Radioactive Hotspots Localization Taking Account of Sensor Limitations. *Sensors*, 19(2):292, January 2019. `doi:10.3390/s19020292`.

[58] Tomas Lazna. *Mereni zareni gama*. Brno University of Technology, 2015. Bachelor's thesis, supervised by Ludek Zalud; in Czech. URL: `http://dspace.vutbr.cz/handle/11012/39234`.

[59] Tomas Lazna, Tomas Jilek, Petr Gabrlik, and Ludek Zalud. Multi-robotic Area Exploration for Environmental Protection. In Vladimir Marik, Wolfgang Wahlster, Thomas Strasser, and Petr Kadera, editors, *Industrial Applications of Holonic and Multi-Agent Systems*, Lecture Notes in Computer Science, pages 240–254, Cham, 2017. Springer International Publishing. `doi:10.1007/978-3-319-64635-0_18`.

[60] Tomas Lazna. *Autonomous Robotic Gamma Radiation Measurement*. Brno University of Technology, 2017. Master's thesis, supervised by Ludek Zalud. URL: `https://dspace.vutbr.cz/handle/11012/65112?locale-attribute=en`.

[61] Tomas Lazna, Petr Gabrlik, Tomas Jilek, and Ludek Zalud. Cooperation between an unmanned aerial vehicle and an unmanned ground vehicle in highly accurate localization of gamma radiation hotspots. *International Journal of Advanced Robotic Systems*, 15(1), January 2018. `doi:10.1177/1729881417750787`.

[62] Tomas Lazna. Optimizing the localization of gamma radiation point sources using a UGV. In *2018 ELEKTRO*, May 2018. `doi:10.1109/ELEKTRO.2018.8398368`.

[63] Petr Gabrlik and Tomas Lazna. Simulation of Gamma Radiation Mapping Using an Unmanned Aerial System. *IFAC-PapersOnLine*, 51(6):256–262, January 2018. `doi:10.1016/j.ifacol.2018.07.163`.

[64] Tomas Lazna, Petr Gabrlik, Tomas Jilek, and Frantisek Burian. Simulating UAS-Based Radiation Mapping on a Building Surface. In Jan Mazal, Adriano Fagiolini, and Petr Vasik, editors, *Modelling and Simulation for Autonomous Systems*, Lecture Notes in Computer Science, pages 130–147, Cham, 2020. Springer International Publishing. `doi:10.1007/978-3-030-43890-6_11`.

[65] Petr Gabrlik, Tomas Lazna, Tomas Jilek, Petr Sladek, and Ludek Zalud. An automated heterogeneous robotic system for radiation surveys: Design and field testing. *Journal of Field Robotics*, 38(5):657–683, 2021. `doi:10.1002/rob.22010`.

[66] Tomas Lazna, Petr Gabrlik, Petr Sladek, Tomas Jilek, and Ludek Zalud. Unmanned Aircraft System-Based Radiological Mapping of Buildings. In *2022 IEEE/RSJ International Conference on Intelligent Robots and Systems (IROS)*, pages 1794–1801, October 2022. `doi:10.1109/IROS47612.2022.9981415`.

[67] Tomas Lazna and Ludek Zalud. Localizing Multiple Radiation Sources Actively with a Particle Filter, May 2023. Preprint at arXiv. `doi:10.48550/arXiv.2305.15240`.

[68] Robotics and AI Research Group. Autonomous Radiation Source Localization Using a Particle Filter, 2021. URL: `https://youtu.be/0x4J_Jov2XE`.

Part II

Publications

A Cooperation between an Unmanned Aerial Vehicle and an Unmanned Ground Vehicle in Highly Accurate Localization of Gamma Radiation Hotspots

Outline

Bibliographic Information

Abstract

The paper discusses the highly autonomous robotic search and localization of radiation sources in outdoor environments. The cooperation between a human operator, an unmanned aerial vehicle (UAV), and an unmanned ground vehicle (UGV) is used

to render the given mission highly effective, in accordance with the idea that the search for potential radiation sources should be fast, precise, and reliable. Each of the components assumes its own role in the mission; the UAV (in our case, a multi-rotor) is responsible for fast data acquisition to create an accurate orthophoto and terrain map of the zone of interest. Aerial imagery is georeferenced directly, using an onboard sensor system, and no ground markers are required. The UAV can also perform rough radiation measurement, if necessary. Since the map contains 3D information about the environment, algorithms to compute the spatial gradient, which represents the rideability, can be designed. Based on the primary aerial map, the human operator defines the area of interest to be examined by the applied UGV carrying highly sensitive gamma-radiation probe/probes. As the actual survey typically embodies the most time-consuming problem within the mission, major emphasis is put on optimizing the UGV trajectory planning; however, the dual-probe (differential) approach to facilitate directional sensitivity also finds use in the given context. The UGV path planning from the pre-mission position to the center of the area of interest is carried out in the automated mode, similarly to the previously mentioned steps. Although the human operator remains indispensable, most of the tasks are performed autonomously, thus substantially reducing the load on the operator to enable them to focus on other actions during the search mission. Although gamma radiation is used as the demonstrator, most of the proposed algorithms and tasks are applicable on a markedly wider basis, including, for example, chemical, biological, radiological, and nuclear missions and environmental measurement tasks.

Author's Contribution

The author was responsible primarily for performing the tasks related to the radiation measurements, namely, the deployment of the detection system on the terrestrial platform, development of the radiation mapping and the localization algorithms, radiation data acquisition, and relevant processing. Moreover, he was involved in designing the method and discussing the results; thus, he wrote the sections *Methods for Path Planning and Field Mapping* and *Radiation Sources Localization*, and significantly contributed to the chapters *Introduction*, *UGV*, *Discussion*, and *Conclusion*.

Author contribution: 30 %

Acknowledgement

Copyright and Version Notice

A.1 Introduction

At present, new security challenges appear within multiple related fields and disciplines. In this connection, the advancement in modern warfare suggests that chemical, biological, radiological, and nuclear (CBRN) defense will assume increasing importance. The U. S. Department of Health and Human Services defines several types of terrorist attacks involving sources of ionizing radiation [1]; the perpetrators of such acts may rely on 'dirty bombs', devices having the potential to disperse radioactive material in urban zones. As radiological sources are commonly present in medical or scientific facilities, they appear rather vulnerable in terms of becoming a target or an instrument of criminal practices [2]. In any case of such misuse, it would be vital to localize and dispose of the dangerous sources without unnecessary delay.

Current scientific literature outlines various methods to perform the actual retrieval and elimination operations; for instance, one of the conventional techniques relies on airborne spectrometry, where the detectors are carried by a helicopter through the region of interest (ROI) along a regular trajectory. An example of this approach is found in paper [3]. The advantage of such a procedure consists in the possibility of quickly exploring a relatively large region, while the main drawback is the low accuracy of estimating the hotspot locations. However, a detector can also be attached to an unmanned aerial vehicle (UAV), as presented in research reports [4, 5]. The benefits and disadvantages are similar to those characterizing the use of a helicopter; in this connection, UAVs nevertheless exhibit smaller payloads and shorter flying ranges, although they also feature lower initial costs.

If a high localization accuracy is required, ground-based assets have to be employed. The actual localization should not be performed by humans due to health risks, and as an unmanned ground vehicle (UGV) is less prone to radiation damage, it finds application in such reconnaissance tasks. Using UGVs in the discussed domain is demonstrated in articles [6, 7, 8, 9, 10]. A custom solution offering a high accuracy of the localization of gamma radiation hotspots is introduced within the present paper.

The proposed solution consists of an aerial and a ground platform, both working in the semi-autonomous mode. A UAV is utilized to acquire a three-dimensional map of the ROI via photogrammetric techniques. The map assists a UGV to plan a trajectory along which the hotspots are searched. In addition, the UAV may carry a detector to provide general information related to the positions of the radiation hotspots. A central advantage of our approach lies in the fact that no prior environmental map is needed, and the goal rests in identifying a solution that overcomes the state-of-the-art methods in certain particular aspects.
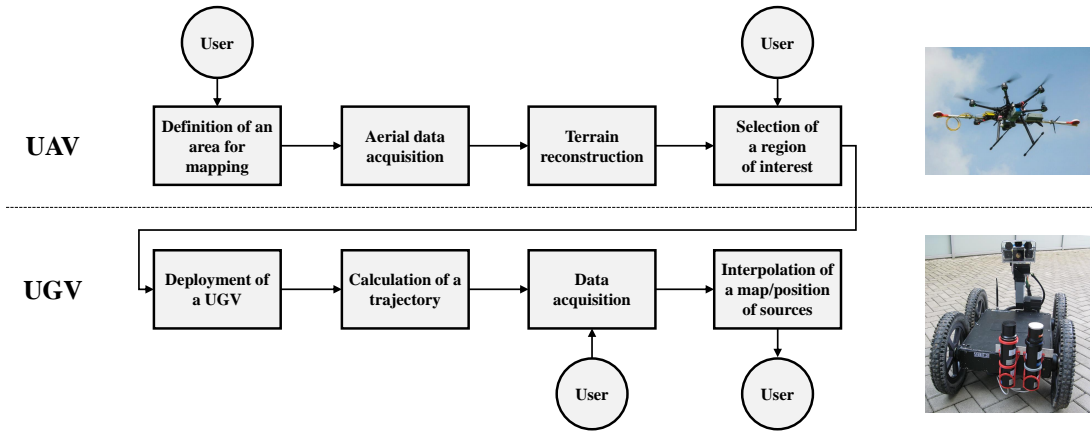
Figure A.1: The sequence of the operations forming the entire process.

The article is organized as follows: Section 'Methods' discusses the methods and equipment employed, together with several localization algorithms; chapter 'Results' offers an overview of the results achieved, including the performance, time efficiency, and accuracy typical of the individual maps and methods; and section 'Discussion' compares the results with those outlined in the referenced literature, introducing the relevant advantages and disadvantages.

A.2 Methods

The following chapter presents the working scheme of the proposed system; both the UAV and the UGV are described in detail. The final part of this section introduces the algorithms used.

A.2.1 Process Description

The sequence of steps to ensure information related to the gamma radiation hotspots is illustrated in Figure A.1. The entire process is controlled by a human operator (user).

At the initial stage, the operator has to plan a flight trajectory for the UAV to cover the potentially affected area; then, the UAV acquires images along the defined trajectory, and these are used to reconstruct the 3D model of the area. The model assists the operator in selecting the proper region of interest rideable for the UGV, considering the presence of possible radiation hotspots. The ROI is a polygon defined by a sequence of vertices.

The UGV is deployed near the border of the mapped area. First, the trajectory from the deployment position to the edge of the ROI is calculated to avoid the obstacles and slopes found by the UAV; subsequently, the operator chooses the

Figure A.2: The DJI S800 UAV equipped with the multi-sensor system for direct georeferencing.

UGV working mode. In general terms, two modes are available: mapping and localization. While the former procedure yields a map of the radiation distribution in the area, the latter one enables us to localize the radiation sources as quickly as possible; the corresponding data are then acquired in a suitable manner. Finally, the measurement is interpolated in order to provide either a map or a set of the sources' coordinates, and the results are communicated to the operator.

A.2.2 UAV

In aerial mapping, the benefit of unmanned aerial vehicles consists in their fast and safe operation at a very reasonable price, especially when compared to manned aircraft. For this reason, UAVs are convenient primarily for the mapping of local areas as their operational time is rather limited; conversely, however, the vehicles can produce a refreshed map on a daily basis, thus significantly reducing the product cycle known from traditional mapping. UAVs have already proven useful in fields and disciplines such as agriculture, civil engineering, archaelogy, or environmental and radiation mapping. Currently, projects are being executed which focus on direct radiation mapping via onboard sensors [4, 11] and combine radiation mapping with UAV photogrammetry to facilitate 3D surface reconstruction [12]; this paper nevertheless aims to explore the potential for cooperation between UAVs and UGVs.

To perform the aerial mapping, we used a six-rotor DJI S800 Spreading Wings UAV fitted with a DJI Wookong M flight controller supporting an autonomous flight according to a given trajectory. As regards the experimental aicraft, the most important utility parameter was the payload limit of about 3 kg, which allowed us to carry the required equipment (see Table A.1 for more parameters). The UAV comprises a custom-built multi-sensor system facilitating the direct georeferencing (DG)

Table A.1: The parameters of the UAV DJI S800 and the UGV Orpheus-X3 [13, 14].

Parameter	UAV	UGV
Dimensions	$1.0 \times 1.2 \times 0.5$ m	$1.0 \times 0.6 \times 0.4$ m
Weight	8 kg	51 kg
Operational time	10 mins	120 mins
Drive type	multi-rotor	wheel-differential
Operating speed	5 m·s^{-1}	0.6 m·s^{-1}
Maximum speed	26 m·s^{-1}	4.2 m·s^{-1}

Table A.2: The parameters of the custom-built multi-sensor system for UAVs to enable the direct georeferencing of aerial imagery.

Parameter	Value
Position accuracy (BD982)[a]	horizontal: 8 mm, vertical: 15 mm
Attitude accuracy (Ellipse-E)[b]	roll/pitch: 0.1°, heading: 0.4°
Camera resolution	$6,000 \times 4,000$ px
Camera lens	15 mm
Operational time	120 mins
Distance from base	1,000 m
Dimensions	$1.5 \times 0.2 \times 0.2$ m
Weight	2.6 kg

[a]1σ error in the RTK mode, according to the manufacturer's specification.

[b]The RTK mode in the airborne applications, according to the manufacturer's specification.

of aerial imagery (Figure A.2), an operation that enables us to create a georeferenced orthophoto, point cloud, or digital elevation model (DEM) without requiring ground control points (GCP).

The multi-sensor system comprises a digital camera Sony Alpha A7, a global navigation satellite system (GNSS) receiver Trimble BD982, an inertial navigation system (INS) SBG Ellipse-E, and a single board computer Banana Pi R1 (Figure A.3). The GNSS receiver measures the position with centimeter-level accuracy when real time kinematic (RTK) correction data are transmitted, and as it is equipped with two antennas for vector measurement, the device also measures the orientation around two axes. The position and orientation data are used as an auxiliary input for the INS, which provides data output at a frequency of up to 200 Hz. Since all the sensors are precisely synchronized, once an image has been captured, the position and orientation data are saved into the onboard SSD data storage (more
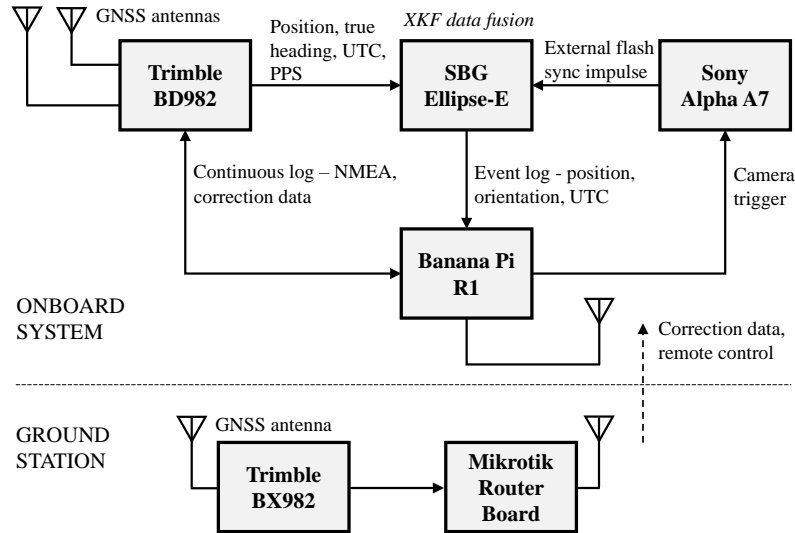
Figure A.3: The multi-sensor system for the UAV and ground station.

parameters are contained in Table A.2). The multi-sensor system mounted on the UAV is shown in Figure A.2 and described in more detail within [15].

Both the position and the image data from the onboard sensors are processed using photogrammetric software Agisoft Photoscan Professional. This SW integrates computer vision-based algorithms performing structure from motion (SfM) to allow the surface reconstruction, and it offers two georeferencing options: indirect (IG), using GCPs, and direct, utilizing onboard data. We may benefit from DG as the only approach to produce accurately georeferenced maps of areas inaccessible for humans (which is the case with radiation mapping). To achieve centimeter-level object accuracy, a method for calibrating the designed system was developed [16]. The calibration process involves the field estimation of the lever arms and the synchronization delay between the camera shutter and the INS unit; these steps significantly increase the accuracy of the position measurement of the camera perspective center.

In our experiment, the UAV is used only for the aerial photogrammetry, enabling us to create a highly detailed, up-to-date orthophoto and DEM. These products are applicable for both the localization of the ROI and the UGV navigation. If the UAV were equipped also with radiation detectors, it would locate the ROI more reliably.

A.2.3 UGV

The UGV is an Orpheus-X3 civil reconnaissance robot, a four-wheeled mid-size vehicle equipped with a sensor head carrying cameras. The robot has the ability to carry all the equipment needed for this type of mission, namely, devices to facilitate self-localization, gamma detectors with counting electronics, and a control module with the designed algorithms. The whole system, namely, the robot carrying the equip-

Figure A.4: The Orpheus-X3 carrying the equipment.

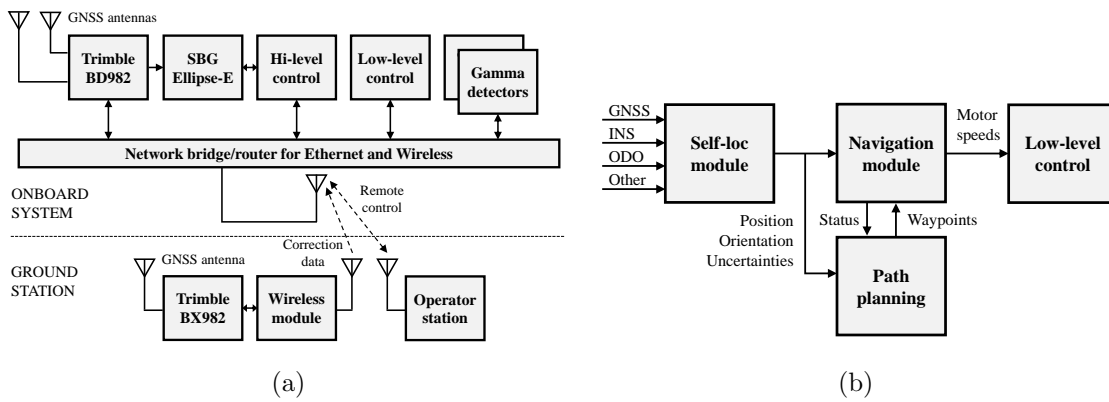(a)   (b)

Figure A.5: The interconnection of the components (a), and the control diagram of
the simplified robot drive (b).

ment, is represented in Figure A.4. The basic parameters of the robot are shown
in Table A.1. The interconnection between the main components of Orpheus-X3 is
shown in Figure A.5a. The robot is capable of autonomous driving. A simplified
block scheme of all major modules for the robot motion control is drawn in Figure
A.5b; all the blocks of this scheme will be described in detail within the following
paragraphs.

In applications that require the autonomous motion control of a mobile robot, the
self-localization task must be solved in real time. The self-localization module of the
Orpheus-X3 mobile robot is designed exploiting the modular concept with real-time
data output; such an approach allows the quick and easy integration of localization
data from different sources. The data fusion is based on uncertainties of the input
data. In standard missions, the self-localization module includes solutions from
an RTK GNSS (Trimble BD982), a MEMS-based INS (SBG Ellipse-E), and wheel
odometry (data from the motor drivers). One of the central advantages of an RTK
GNSS is the high accuracy without any drift caused by the length of the measuring
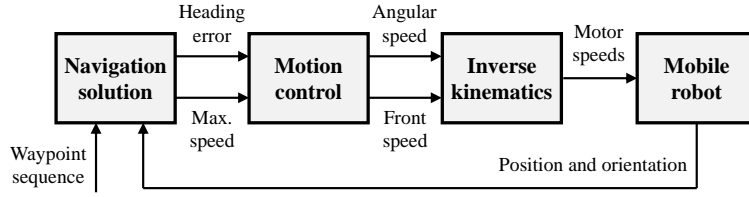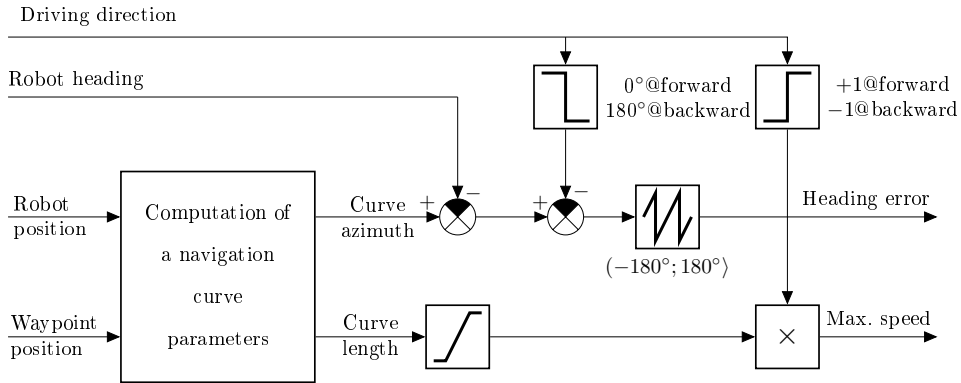
Figure A.6: The block scheme of the module.

Figure A.7: The scheme of the navigation solution solver.

period or traveled distance. The applied RTK GNSS receiver can be connected to two antennas, allowing drift-less heading measurement from the position vector between the two antennas. The localization data from special methods (including, for example, SLAM) can be also integrated if the uncertainties of the values are known. In environments with a good open sky view, an RTK GNSS is usable as the only solution. To increase the robustness of the entire self-localization module, we may also employ some relative methods to bypass the time when the RTK solution is unavailable due to reasons such as reinitialization. The position estimation accuracy reaches the level of centimeters, and the orientation (azimuth) is better than 0.5 deg if the RTK solutions are fixed. As regards accuracy, more results are obtainable from the PhD thesis [17].

The Orpheus-X3 also integrates a navigation module (Figure A.6) to control the robot motion, utilizing an externally computed requested trajectory. The trajectory is defined as a sequence of waypoints in the WGS-84 coordinate system. The internal computational scheme of the navigation solution (block No. 1 in Figure A.6) is presented in Figure A.7. The robot motion parameters, such as the turning radius and maximum speeds, can be dynamically adjusted during a mission via an integrated application interface from the related hi-level control module. The sequence of waypoints is also dynamically modifiable from the path planner module during a mission. More information about the navigation algorithms is outlined within paper [14] and PhD thesis [17].
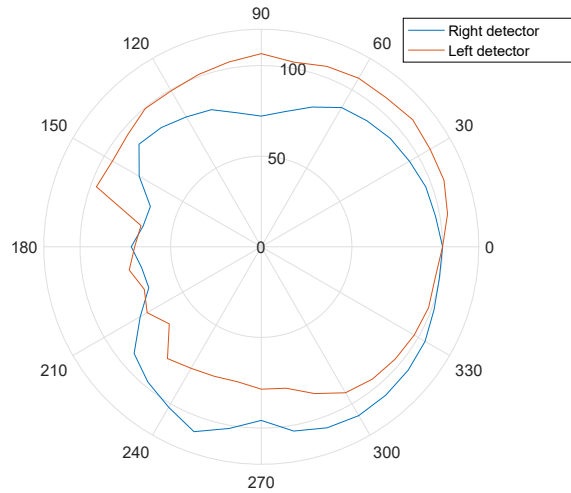
Figure A.8: The directional characteristics of the detection system.

The gamma radiation detection system comprises scintillation detectors and measuring electronics. A pair of 2-inch sodium iodide doped with thallium (NaI(Tl)) detectors are used as scintillators. The detectors are integrated with photomultiplier tubes having a standard 14-pin base. Multichannel analyzers NuNA MCB3 manufactured by NUVIA are used as the electronics; the analyzers ensure a high voltage source, a preamplifier, and ADC sampling and processing. The detector tubes are equipped with lead shielding, and one half of each spherical detector is covered with a 2 mm layer of lead facing the other detector. The reason for such a configuration is to intensify the directional sensitivity of the resulting detection system. The directional characteristics of the detectors placed on the robot are introduced in Figure A.8; however, these remain valid only if the distance between the detector centers equals 106 mm.

A.2.4 Optimal Path to the Area of Interest

The terrain negotiability of a UGV is markedly affected by its actual slope pattern. In this context, it appears very helpful if the entire system can assist the operator in finding the shortest possible path to the target area from places accessible using the regular transport infrastructure. The main obstacles for a UGV are areas where the slope of the terrain exceeds the limit value of the given UGV. The slope map is computed from a DEM, which constitutes a product of UAV photogrammetry. The paths from the starting positions to the requested target are obtained using an A* algorithm [18] in a binarized and down-sampled slope map; the down-sampling of the map is needed due to a significant reduction of the computational demands. The size of a cell in a down-sampled obstacle map should be slightly higher than the width of the applied UGV. Lowering this size below this limit has no effect because
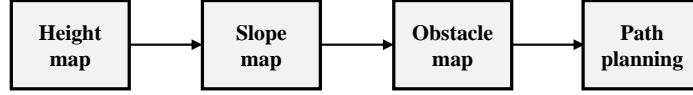
Figure A.9: The procedure for planning the path to the ROI.

of the impossibility to pass through a corridor with the width of one pixel, whereas increasing it worsens the resolution and may cause the loss of the trajectory. The down-sampling algorithm must preserve the thin lines that represent high slopes in the terrain.

Another approach to reduce the computational demands consists in using lossless compression algorithms (e. g., quadtree [29]) on a primary hi-resolution binary map. These algorithms can also be employed in lossy compression applications, where the cell size of a leaf (the last level of the tree) is larger than in the original map. In the given case, however, the workflow must be changed, with the primary binary map packed using a quadtree algorithm at the start of the data processing. Further, the path planning algorithm must be modified to natively handle the compressed data without fully expanding to an equidistant grid. Compared to the basic down-sampling, this procedure significantly reduces the number of points needed to travel through a path planning algorithm while keeping the same resolution of the map. Such an optimization then markedly affects the computational demands. Due to the negligible duration (only several seconds) of the trajectory planning operation as opposed to the DEM calculation time (which amounts to several hours if a computing grid is not utilized), the benefits of more advanced obstacle map compression techniques are unimportant in the described application.

Yet another option for diminishing the computational demands of the path planning process is to employ an optimized method to find the shortest trajectory instead of the fundamental variant of the A* algorithm. A good candidate can be seen in the *Jump Point Search* [30] algorithm, which is capable of reducing the running time by an order of magnitude. Due to both the planned ranges of the areas where the trajectories are searched and the applied map resolutions, the trajectory planning time is not critical in the context of the DEM generation time. When large areas (exceeding ~ 1 km^2) are considered, it is suitable to ensure the time optimization of the path planning process by means of a better performing algorithm or to compress the map, thus reducing the number of points into which the objects in the map are divided.

The starting position securing the shortest path to the target spot is preferred. The whole sequence of tasks is shown in Figure A.9.
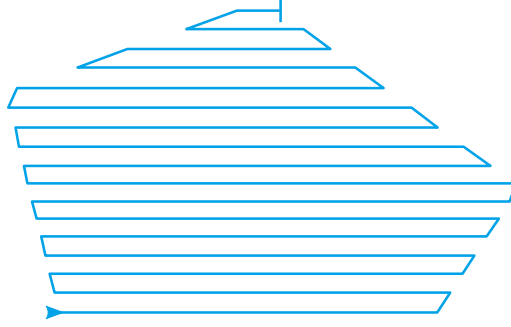
Figure A.10: A schematic example of the mapping trajectory.

A.2.5 Methods for Path Planning and Field Mapping

An algorithm specified by the adjective *m*apping constitutes an elementary algorithm to measure environmental quantities such as the dose rate in the region of interest. The idea is to pass the entire area along the parallel equidistant lines and to measure the dose or count rate periodically. If the line spacing and the robot's speed are small enough, even subtle changes in the radiation field can be noticed; thus, even weak sources can be found. This is apparently a significant advantage of the mapping operation. The drawback then rests in that the time requirements increase rapidly with the size of the measured area. A schematic example of a mapping trajectory in a pentagonal ROI is shown in Figure A.10.

The waypoints for the navigation module are generated on parallel lines inside the polygon which defines the boundaries of the ROI. It is convenient to make the lines parallel to one of the polygon's longer edges in a manner where all the lines intersect the polygon at not more than two points. When such conditions have been satisfied, the resulting trajectory becomes more efficient for the robot because the number of the turns required is minimized.

The parallel lines are separated by pre-defined spacing, a critical parameter related to the algorithm's capability of finding low-activity point radiation sources in the area. The lower the spacing, the weaker the sources localizable and the longer the timespan needed to acquire the data. Given that we know the intensity of the weakest source to be found, the optimal value of the parameter is computable. In the worst case, the source is located exactly halfway between two trajectory lines. The dose rate generated by the source should be at least three times higher than the background one, $\dot{D}_B$. Since the background may rise above the normal level in the stricken area, it is necessary to measure its value once the robot has been deployed. The spacing parameter is then given by the following equation:

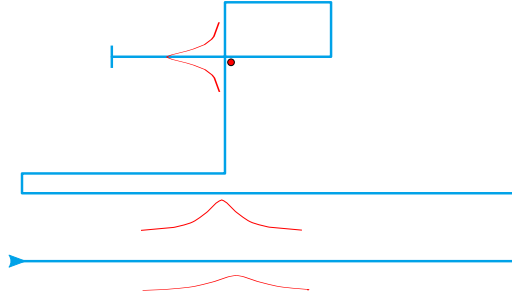$$d = 2\sqrt{\frac{\dot{D}_1}{3 \cdot \dot{D}_B}} \tag{A.1}$$

Figure A.11: A schematic example of the strong source search trajectory.

where $\dot{D}_1$ stands for the dose rate generated by the weakest source to be searched for at the distance of 1 meter. If a particular radionuclide is to be found, this value may be computed from its activity.

The mapping yields a set of scattered data points. Each of such points comprises the coordinates and spectra acquired by both detectors during a measurement period. The data points are not very suitable for visualization and further map processing, namely, the conversion to a 3D point cloud. Thus, the calculation of the radiation intensity (either the total count or the dose rate) at points in a regular grid is needed. This step can be carried out through a Delaunay triangulation [19]. After the interpolation has been performed, the data become visualizable and interpretable by the operator. If any point source is present in the mapped ROI, its position may be computed automatically, as will be described later.

In any situation where finding only one strong source is required and timing is important, the mapping algorithm may be extended as outlined below. The extension exploits the dynamic change of the trajectory in accordance with the measured data.

First, the robot follows a basic mapping trajectory. Once the end of the line has been reached, the data are examined to yield a significant peak in the radiation intensity. If peaks are found in two neighboring lines and their positions correlate, the trajectory is altered, and the robot continues in a direction perpendicular to the mapping lines passing through the center of the peak projections to the current line. The new direction is maintained until another significant peak in the measured radiation intensity appears. Afterwards, the final part of the trajectory denoted as a *l*oop is planned, and its purpose consists in acquiring a sufficient amount of data points in the vicinity of the anticipated source position in order to determine that position more accurately. A schematic example of the measurement trajectory is shown in Figure A.11

A disadvantage of the above-described algorithm is the dependence of the result on the initial mutual position of the robot and the source. The algorithm presented below exploits the directional characteristics of the detectors, meaning that its per-

formance should not depend excessively on the initial conditions and, under some circumstances, multiple sources can be found.

As the difference between the detectors' directional characteristics is rather indistinctive, we have to find a more effective way to acquire data in order to gain relevant information about the direction in which a source is present. A measurement cycle along a closed loop seems promising because all possible angles between the detectors and the sources are assumed. For a certain azimuth of the robot, an extremal ratio of the detectors' responses should be measured if a source is present within the detectable range. This is a principle similar to that found in the peaks measured by the authors of paper [20]. Obviously, the robot can simply rotate in place, but it may be convenient to choose a circular trajectory instead because the range has increased and the extremum is anticipated also in the count rate values due to the inverse square law. Since the sum of the count rates is burdened by a statistical error lower than that of the rates' ratio, this should lead to better estimation of the direction.

Assuming the robot maintains a constant speed once it has reached the circle, a cyclic dataset with equidistant data points will result from the measurement. If there are multiple sources adequately separated by an angle, more than one dominant peak can be present, and it does not suffice to only find the maximum. Real data are very noisy, requiring a robust peak detector. A simple peak is defined as a point having a value greater than its two neighboring points; the peaks are then compared to the reference levels evaluated for each peak in the following manner:

1. The nearest point with a greater or equal value is found to the left of the examined peak.

2. The point exhibiting the lowest value is found in the interval bounded by the peak and the point from step 1.

3. Steps 1 and 2 are repeated to the right of the peak.

4. The higher of the two interval minima specifies the reference level.

If the peak amplitude is greater than or equal to the reference level multiplied by the desired relative prominence, the peak is accepted. Once the peaks have been identified, it is convenient to fit their neighborhood using an appropriate function. This procedure is performed for several reasons, including that, due to the dead time, the point in the correct direction may not exhibit the maximum count rate. In the given context, we can also assume that the actual maximum is somewhere between the samples. The interpolation then provides the subsample precision. A quadratic polynomial ensures sufficient results, and its parameters are computable via the least squares method.
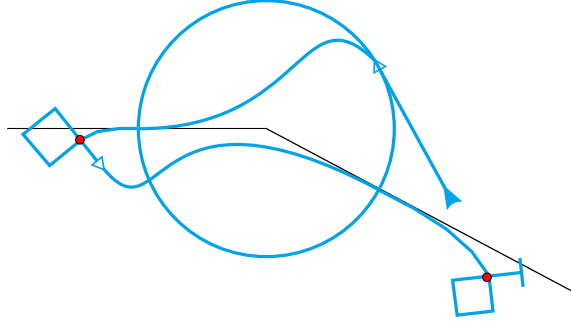
Figure A.12: A schematic example of the circular algorithm trajectory.

One detector is pointed outwards and the other inwards. By comparing the count rates in the peak, we can then determine whether the source is located outside or inside the circle.

Due to multiple effects, such as an overlap of the radiation fields, the initial direction estimation may not be accurate; however, taking advantage of the directional sensitivity, the error can be compensated. The detection system is arranged in such a manner that the difference of the count rates measured by both detectors converges to zero if the source lies in the axis of the robot. Thus, the effort is to minimize the difference by changing the azimuth of the robot while the vehicle is approaching the source. The value by which the azimuth is altered should depend on both the present and the past measured differences. Given the current readings from the detectors on the right-hand and left-hand sides, $R(t)$ and $L(t)$, and considering the previous readings, $R(t-1)$ and $L(t-1)$, the desired azimuth change may be expressed as

$$
\begin{aligned}
\Delta\phi = K_1 \frac{R(t) - L(t)}{R(t) + L(t)} &+ K_2 \frac{R(t-1) - L(t-1)}{R(t-1) + L(t-1)} + \\
&+ K_3 \frac{R(t)}{L(t)} - \frac{R(t-1)}{L(t-1)},
\end{aligned}
\tag{A.2}
$$

where K_1, K_2, and K_3 are conveniently chosen constants. Note that whenever the robot heads left from the source, the count rate measured by the right-hand detector increases while the other one decreases; as a consequence, the change of the azimuth is positive – in other words, the robot starts to head more to the right.

When the total count rate drops during three or more sampling periods in a row, it can be assumed that the robot has already passed around the source. In that case, the final part of the trajectory, or the loop, as presented previously, can be planned. Once the source has been localized, the robot may proceed in another direction where a source is anticipated. The schematic example of such a measurement trajectory is shown in Figure A.12; the actual location of the source is marked by the red point, and the black lines represent the initial direction estimation.

Table A.3: The object accuracy (RMS error) achieved with the direct and indirect georeferencing methods in UAV photogrammetry.

Method	GCP/TP	X [mm]	Y [mm]	Z [mm]
DG	0/30	19	27	25
IG	6/24	9	9	20

An obvious disadvantage of the presented algorithm rests in the limited exploration range provided by one circle. However, it is possible to cover a larger area using a set of complementary circles, applying the algorithm to each one of them.

Each of the three above-presented strategies allows us to find point radiation sources. As proposed earlier, the process of determining the sources' coordinates can be automated: First, a data point denoted as $m$aximum, which is as close as possible to the source, has to be chosen; in the latter two algorithms, the data point should be one acquired along the final loop and having the largest total count rate. Regarding the mapping, the interpolated map has to be searched for two-dimensional prominent peaks, which should correspond to the centers of the individual hotspots. Afterwards, the data points measured within the defined radius around each maximum are selected for further processing; the radius should be proportional to the total count rate in a given maximum. The points are then fitted with a suitable function. If the selected radius corresponds well to the source intensity, the paraboloid of revolution secures sufficient interpolation, and its parameters are simply computable via the least squares method. Better interpolation can be achieved using a two-dimensional Gaussian function.

A.3 Results

This section summarizes the achieved results; the outcomes of the aerial mapping, path planning, and localization of radiation sources are presented graphically.

A.3.1 Aerial Mapping

A region of approximately 30,000 m^2 accommodating a potential radiation source was mapped by a UAV carrying a multi-sensor system for direct georeferencing. During an 8-minute automatic flight, 137 photographs were taken. The flight trajectory and image capture period had been set to meet the requirement of 80 % side and 80 % forward overlap. As the applied full-frame camera was fitted with a 15 mm lens and the flight altitude corresponded to 50 meters above the ground level (AGL), the ground resolution of the images is about 2 cm/px.
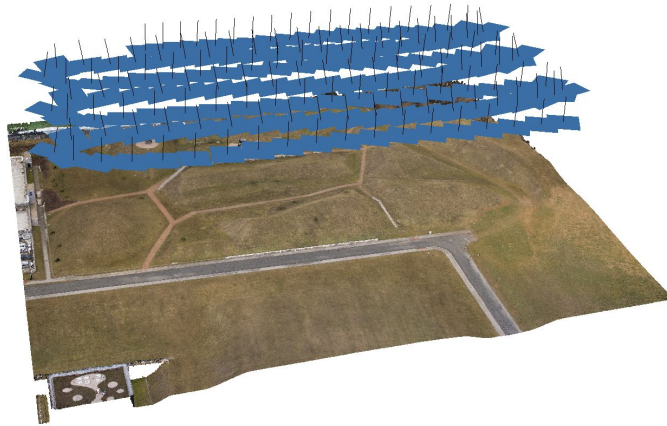
Figure A.13: The textured point cloud containing 29 million points; the blue rectangles represent the image planes, whose positions were measured using the onboard system.
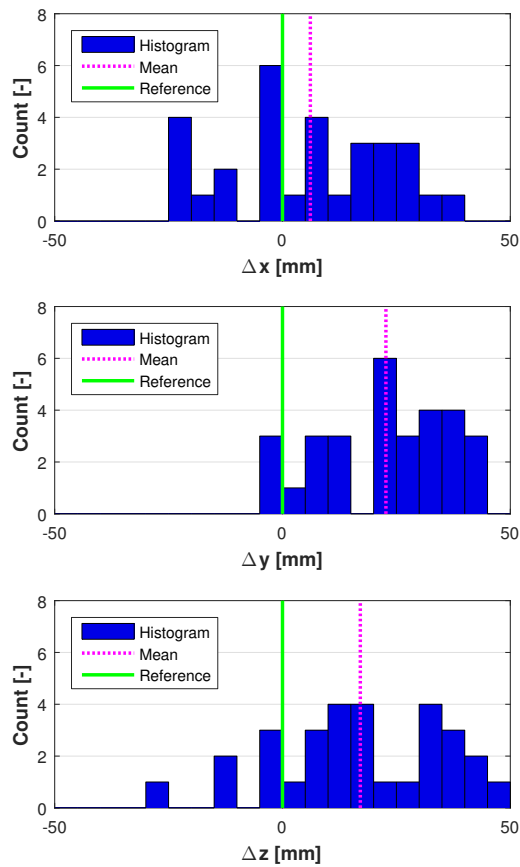

Figure A.14: The position error distribution in the terrain model generated using the UAV, without the GCPs (determined on 30 TPs).
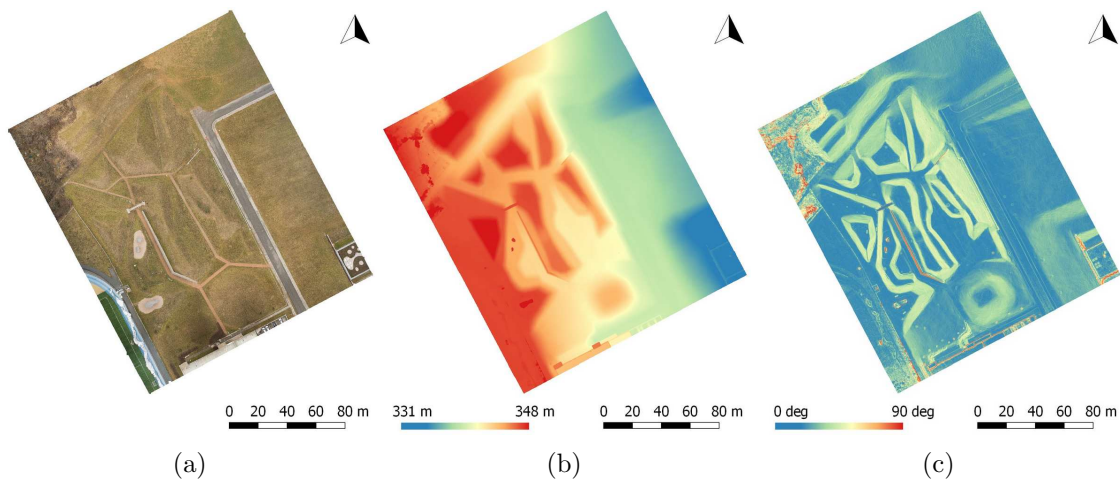
0 20 40 60 80 m   331 m   348 m   0 20 40 60 80 m   0 deg   90 deg   0 20 40 60 80 m

(a)   (b)   (c)

Figure A.15: The georeferenced ortophoto (a), digital elevation model (b), and gradient map (c), all generated using UAV photogrammetry without the GCPs.

Once the onboard position data have been refined using custom calibration, we employed them for terrain reconstruction together with the image data. Photoscan was used to generate a dense point cloud with a density of about 800 points/m^2 (Figure A.13); although the point cloud was georeferenced directly, without any GCP, thirty markers were distributed across the area due to accuracy assessment. The positions of these markers were measured with a survey-grade GNSS receiver just before and after the flight. Table A.3 presents the RMS error of the object position determined in all the 30 markers, or test points (TP). The RMS error did not exceed 3 cm for each axis, and the spatial error equalled 4.1 cm RMS. The histograms in Figure A.14 present the error distribution within the measurement, assessed using the TPs.

The same set of image data was exploited in testing the performance of indirect georeferencing, which is a techique widely used in UAV photogrammetry. Six markers were used as the georeferencing GCPs, and the remaining 24 ones assumed the role of TPs. As presented in Table A.3, the RMS error did not exceed 1 cm in the X and Y axes and 2 cm in the Z axis. The spatial RMS error of 2.4 cm was about twice smaller compared to that found in DG. Despite this excellent result, IG requires GCPs to enable georeferencing, and the technique thus cannot be utilized in situations where the area of interest is inaccessible to humans, as is the case with radiation contamination.

The georeferenced point cloud is then employed for the creation of other products, namely, a true orthophoto and a digital elevation model (Figure A.15a and A.15b). These two map layers can significantly simplify the process of localizing a source
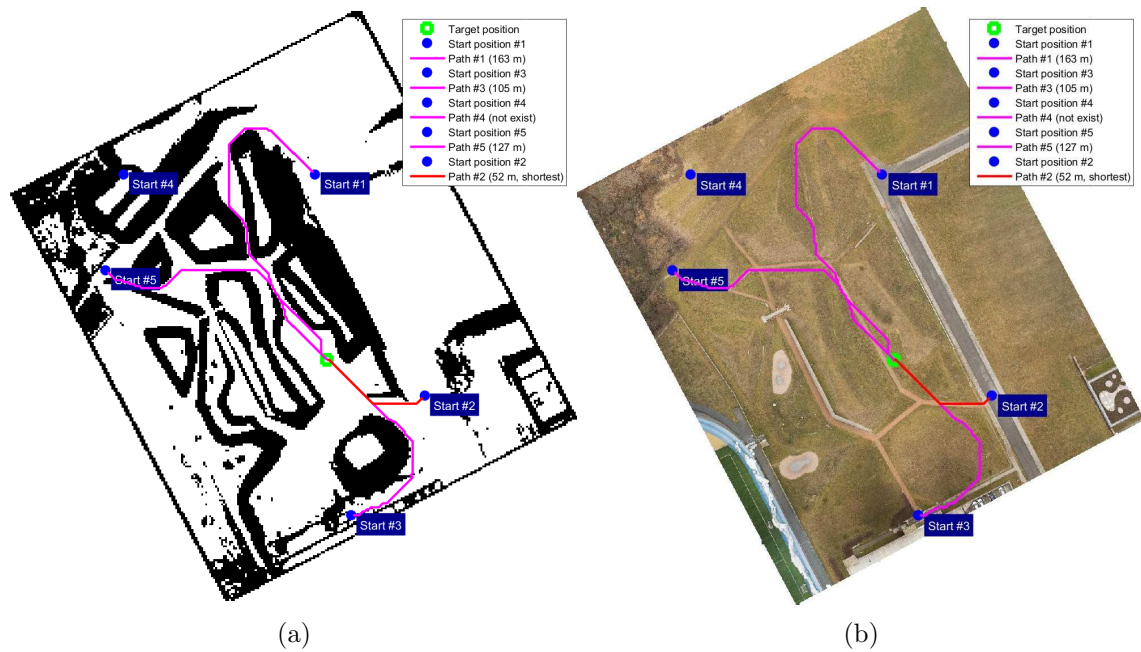
Figure A.16: The obstacle (a) and orthophoto (b) maps with possible trajectories to the target.

of radiation (if a visible damage is observable) and, above all, help us to navigate the UGV across the area. Because the applied UGV is not capable of operating on steep slopes, a gradient map layer (Figure A.15c) constitutes an instrument towards finding an appropriate trajectory to ROI.

A.3.2 Path to the Area of Interest

A binary obstacle map is obtained from the successfully formed DEM to retrieve the shortest path to the ROI. The slope threshold limit to mark a relevant cell in the map as an obstacle for the UGV is 15 degrees. The cell size in the down-sampled obstacle map was set to 150 % of the robot width, yielding a map with 300 x 285 pixels (0.9 m/pixel). Such a resolution allows us to find one path within seconds on a common PC unit. The possible mission starting positions were manually selected in the orthophoto map. The identified trajectories to the target spot are shown in Figures A.16a and A.16b. The point at which the robot was unloaded from the car was chosen from among the starting positions offering the shortest paths (with the most advantageous one being 83 m long). The final path was planned using also the A* algorithm, and it ran between the unloading point and the first waypoint of the polygon where the mapping had been performed.
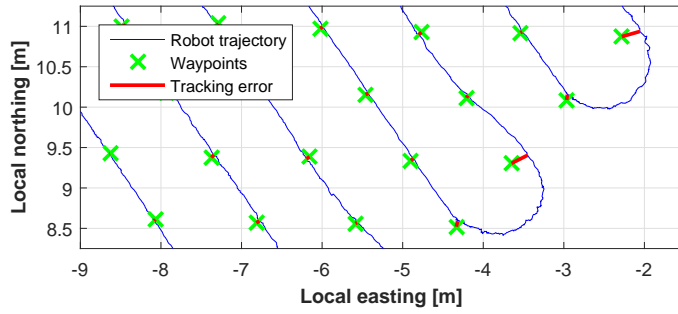
Figure A.17: The errors in waypoint tracking on the trajectory.
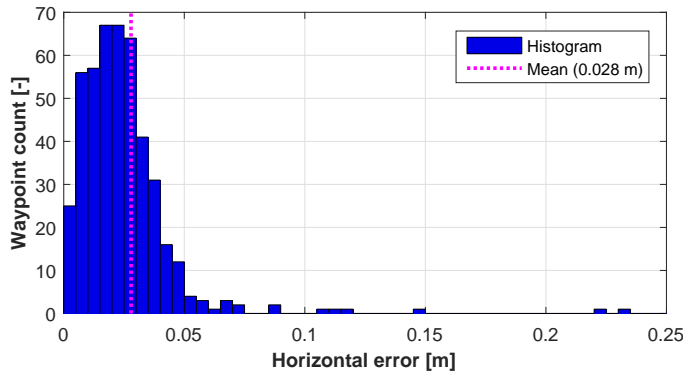
Figure A.18: The errors in waypoint tracking on the trajectory.

A.3.3 Robot Navigation Accuracy

The robot navigation accuracy was determined as the waypoint tracking accuracy. The relevant value was estimated from the real trajectory of the mobile robot and the positions of the waypoints to be passed around. The error distance between the robot trajectory and a waypoint embodies the closest distance between a waypoint and the real robot trajectory, as demonstrated in Figure A.17. The histogram of the error distance related to the waypoint tracking along the entire trajectory applied within the standard mapping method is presented in Figure A.18. The error distances are evaluated on the horizontal plane (east-north). The average error equals 2.8 cm.

A.3.4 Radiation Sources Localization

The proposed methods to localize gamma radiation sources were first simulated and then tested with actual radionuclides. There are two main reasons to run the simulations: a) The behavior of the algorithms is influenced by several parameters to be set prior to any experiment, e. g., the peak prominence and azimuth change constants; and b) it is vital to set up the experiments in a manner that enables the algorithms to work as expected, meaning that when the experiments are prepared using simulation, the time needed on site can be reduced.

The radioactive decay of a source is a process describable with the Poisson distribution. The probability of the emission of x photons is expressed as [21]

$$p(x = X) = \mathcal{P}(x; \lambda) = \frac{e^{-\lambda}\lambda^x}{x!}, \tag{A.3}$$

where λ denotes the mean emission of photons and its value is proportional to the source's activity. On the short-term basis, this activity is approximately constant in the employed radionuclides. In the long-term run, it decays following the equation [21]

$$A = A_0 e^{-\frac{t}{T_{1/2}\ln(2)}}, \tag{A.4}$$

where $T_{1/2}$ is the half-time of the radionuclide, and A_0 represents its original activity (usually stated in the calibration protocol).

Since the λ values are typically in the order of thousands and the Poisson distribution is numerically stable within the order of tens at most, the sources were approximately modeled using the normal distribution. The radiation background was modeled with the uniform distribution. The detectors were assumed to exhibit 100% conversion efficiency, and only their directional characteristics were considered. The dependence of the registered counts on the distance from a source is given by the inverse square law. Given the parameters of the sources, it is possible to calculate the counts registered in a measurement period by the detectors at any point. The total count detected by the detector k can be obtained from the equation

$$C_k = c_B + \sum_{r=1}^{R} c_{k,r}, \tag{A.5}$$

where $c_B \leftarrow \mathcal{U}([c_{B,min}; c_{B,max}])$ is the contribution of the background, and $c_{k,r}$ denotes the count rate due to the source r. The relevant value is given as

$$c_{k,r} = \frac{K_k(\phi_{k,r})a_r}{||\boldsymbol{x}_k - \boldsymbol{x}_r||^2 + h_k^2}, \tag{A.6}$$

where $K_k(\phi)$ is the sensitivity in the direction ϕ; $\phi_{k,r}$ is the angular coordinate of the source r in the coordinate system of the detector k; $a_r \leftarrow \mathcal{P}(\lambda_r)$ stands for the number of emitted photons; $\boldsymbol{x}_k$ and $\boldsymbol{x}_r$ are the coordinates of the detector and the source, respectively; and h_k is the height of the detector k above the ground. The simulations were run for multiple values of each parameter within the relevant possible range, with the parameter values set according to a convenient optimality criterion.

The radionuclides used for the experimenting are summarized in Table A.4, together with their actual activities. All the experiments took place in the same polygon that had been defined using the map acquired by the UAV. The positions of the

Table A.4: The parameters of the radionuclides.

Label	Radionuclide	Activity [MBq]
S_1	^{60}Co	8.0
S_2	^{60}Co	40.0
S_3	^{137}Cs	65.6
S_4	^{137}Cs	0.22
S_5	^{60}Co	0.35
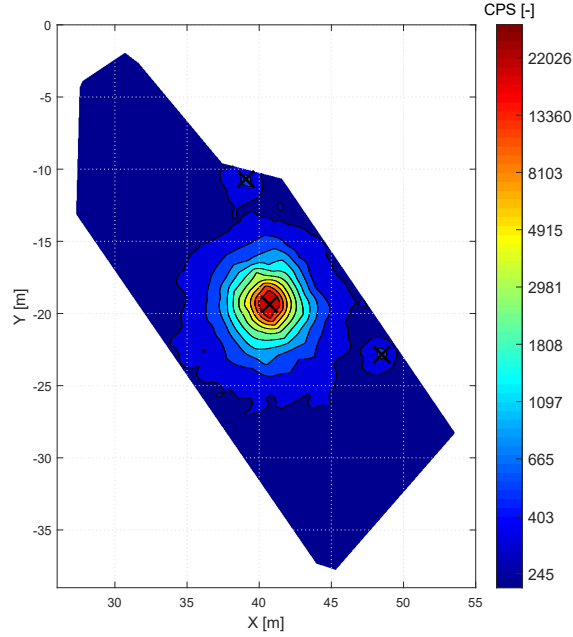
Figure A.19: The result of the mapping algorithm.

sources were measured prior to the experiments in order to provide the reference data.

To test the mapping algorithm, sources S_1, S_4, and S_5 were placed in the ROI, with the spacing sufficient to facilitate their differentiation. The distance between the parallel lines was set to 1 meter. The data acquisition took 15 minutes and 3 seconds. The map resulting from the application of a Delaunay triangulation is shown in Figure A.19, where the black crosses mark the positions of the sources gained through the interpolation. The mean error of the computed positions corresponded to 0.06 meters.

The next algorithm, strong source search, was tested using source S_3. After the passage of the first two lines, we localized the direction in which the source had been estimated. The whole localization process lasted 2 minutes and 53 seconds, including the final loop around the source. The resulting trajectory consisting of data points is visualized in Figure A.20a. The achieved position error equals 0.04 meters (the
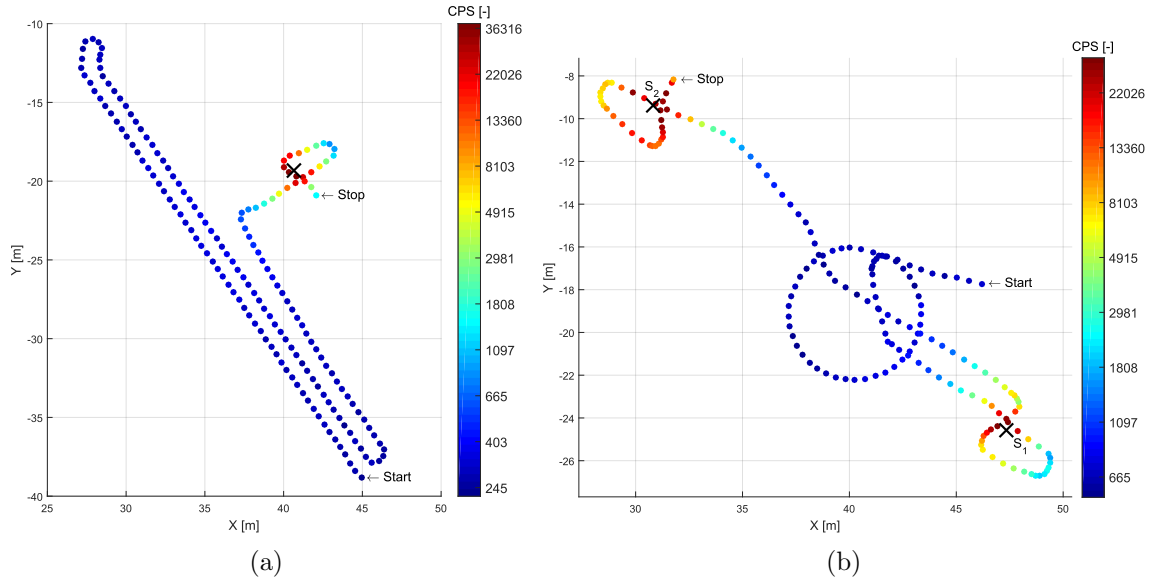
Figure A.20: The result obtained with the strong source search algorithm.

same order as in the mapping). The experiment was repeated using source S_2, where the achieved error corresponded to 0.94 meters. Since the azimuth was not corrected while approaching the source, the result strongly depended on the accuracy of the initial estimation.

First of all, the circular algorithm was verified with one source (S_2); the source was located after 1 minute and 28 seconds, with the position error of 0.52 meters. After the actual completion, another experiment was set up, using two sources (S_1 and S_2) placed inside the area in such a manner that the circular trajectory lay between them. The resulting trajectory can be seen in Figure A.20b; apparently, the initial estimation of the direction in which source S_2 can be found is rather inaccurate. However, thanks to the proposed continuous correction of the azimuth, both the sources were eventually located, and the mean position error corresponded to 0.40 meters. The entire experiment took 2 minutes and 54 seconds.

A.4 Discussion

The UAV has proven to embody a very effective tool for fast and accurate aerial mapping. The presented custom-built multi-sensor system to facilitate direct georeferencing can be carried by any UAV that exhibits a sufficient payload capacity, thus enabling the actual photogrammetry to be performed without using GCPs. This is essential when mapping areas inaccessible or dangerous to humans, including, for example, those characteristic of natural disasters or radiation mapping. The elimi-

nation of GCPs also allows us to automate the entire mapping process, resulting in no need of human interaction during the data acquisition processing.

The spatial ground accuracy of the multi-sensor system related to the above flight mission is 4.1 cm RMS, a sufficient accuracy rate for UGV navigation. This is a result surpassing those achieved within similar projects. Turner et al. [22] obtained the spatial accuracy of 11 cm using a multicopter carrying a DSLR camera synchronized with a positioning system based on a Differential GPS receiver. Fazeli et al. [23] then used a low-cost RTK GPS module to perform DG; however, they generated a spatial error of 29 cm RMS due to inaccurate time synchronization. A system similar to the one presented in this research report is characterized in a related paper by Eling et al. [24], who also used a multicopter UAV equipped with a dual antenna RTK GPS receiver, paying special attention to the calibration and time synchronization. The experiment yielded very accurate results, namely, 1.4 cm RMS for the XYZ axes, but these were achieved with a very low altitude and flight speed (20 m AGL, 2 m/s).

If we compare the accuracies of DG with those of IG, the former are typically slightly worse but remain comparable in selected cases. The object accuracy of a model georeferenced using IG mainly depends on the quality of the ground markers (GCPs), but it also reflects the flight altitude and ground resolution. The spatial error of the IG technique is normally within centimeters, as presented in, for example, the corresponding papers by Fazeli et al. [23], Barry et al. [25], and Panayotov [26]. But, as already mentioned, this approach is not suitable for our application due to the need of ground markers.

In the present article, the UAV was employed for optical mapping only; nevertheless, if a higher payload capacity were available, a detector of ionizing radiation could also be carried. In such a case, the orthophoto would be expanded to include the radiation intensity layer an outcome very beneficial for localizing the ROI. Yet this type of radiation maps cannot be as accurate and detailed as that produced by ground mapping (UGVs), because a typical flight altitude of a UAV is within tens of meters AGL. Ionizing radiation mapping via UAV is discussed in, for example, papers by Kaiser et al. [12], Torii et al. [27] or Martin et al. [28].

Since the UGV does not possess the ability to avoid obstacles autonomously, the digital elevation model is a valuable aid for the operator to define the region where the UGV can operate safely.

In this paper, three different strategies to survey the ROI are introduced and tested in real conditions. The basic surveying method consists in a mapping algorithm which provides reference of the time costs and localization accuracy for the other algorithms. Mapping the selected ROI with the area of 438 m^2 took approximately 15 minutes, with the line spacing corresponding to 1 meter. Since the trajectory was

planned evenly inside the ROI, the dependence of the time intensity on the region's area is rather linear. This fact embodies the major disadvantage of the mapping: the given operating time of the UGV equalled 120 minutes, and the maximum region that can be surveyed within a single action is limited to an area of roughly 3,500 m^2. Conversely, the advantages include the ability to negotiate radiation hotspots other than isotropic point sources – for example, area or directional sources (such as a radionuclide in an open lead container). Both the sensitivity and the accuracy of the method may be increased by setting smaller line spacing and lower forward speed of the robot; the survey, however, is then likely to be more time-consuming.

The methods based on a dynamic change of the trajectory in accordance with the information provided by the detectors reduce the time consumption while ensuring a similar accuracy. Together with the time saving feature, the strong source search algorithm provides two considerable benefits: First, if no source is found or present, the operator still gains the data allowing them to reconstruct the radiation map; second, the method is independent from the applied detection system and thus can be employed with other types of detectors, even the non-spectrometric ones. A disadvantage rests in the marked dependence of the result on the position of the source with respect to the initial position of the robot.

The circular algorithm, however, remains unaffected by this drawback and was discussed in the present paper as an alternative to the strong source search algorithm, which can beneficially exploit a direction-sensitive detection system. The relevant experiment proved that, under certain conditions, more than one source is localizable. The central importance of the algorithm nevertheless consists in its being a fundamental block for a more advanced localization algorithm to explore larger areas. Considering sources detectable at the distance of 4 meters (in the case of the detection system outlined in this paper, such sources consist in radionuclides ^{60}Co or ^{137}Cs, showing activity in the order of tens of megabecquerels), one circle covers the area of approximately 200 m^2. Within the experiments, such a circular trajectory was completed during 48 seconds. But assuming also the time consumption associated with the movement between the circles, a primary survey of the ROI chosen in this paper would last roughly 2 minutes – a major reduction of the time cost compared to the mapping.

The mapping algorithm provides localization accuracy in the order of centimeters. Johsi et al. [3] present a helicopter-borne radiation detection system and discuss the localization of a source having an intensity similar to that exhibited by the sources in our experiments. The obtained localization accuracy is within the order of meters, embodying a result expectable with respect the character of the method. More interesting, however, appears to be a comparison with the achievements of UGVs. Lin et al. [6] proposed a method for localizing a radiological source via a

mobile robot; the technique exploits an artificial potential field and a particle filter which, respectively, can negotiate the obstacles and simplify the localization. The method was verified by means of a simulation only with one source, with the achieved estimation error amounting to 0.02 meters. Ristic et al. [7] then presented an information-driven source search method. The concept was tested using Monte Carlo simulations in a square area (100 × 100 m) accommodating one source, with the results comprising an average search that took 90 seconds and yielded an accuracy in the order of tenths of meters. The relevant simulation cycles were verified using two datasets measured in real conditions. Although the method appears to be promising in terms of the time efficiency, it is still awaiting practical application. Other innovative surveying strategies were introduced by Cortez et al. [9], who nevertheless verified their research only in an area of 60 × 60 cm, insufficiently for the discussed scenarios. The localization accuracy of the method is limited to 4 cm. A rather different scheme is described by Duckworth et al. [10]; their source is localized inside a collapsed building, and the process strongly depends on the assistance from an operator. Eventually, it took a minute to localize the source inside a 6 × 6 m space.

The results within the present article are outlined using CPS values because the detectors were not properly calibrated prior to the experiments. Regarding the pursued goal, namely, the localization of radiation hotspots, the information value of the count rate is sufficient. The human operator may decide on the severity of the situation by comparing the values measured inside the ROI and the background value acquired after the deployment of the UGV. As the measured spectra are stored, they can be later approximately converted to dosimetric quantities if desirable – for example, as information for the operative team charged with the elimination of the given risk.

Although the radiation map is acquirable via the UGV alone, there are several reasons for choosing the proposed cooperation with the UAV. The main advantage consists in the possibility of using the DEM, which allows the UGV to navigate between terrain obstacles and can be beneficial for the operative team as well. Furthermore, if the radiation layer is measured during the aerial data acquisition, the area to be searched by the UGV can be reduced to save time and energy. In general, the cooperative approach combines the advantages of UAV and UGV-based solutions, minimizing the disadvantages related to the stand-alone operation of each of these systems.
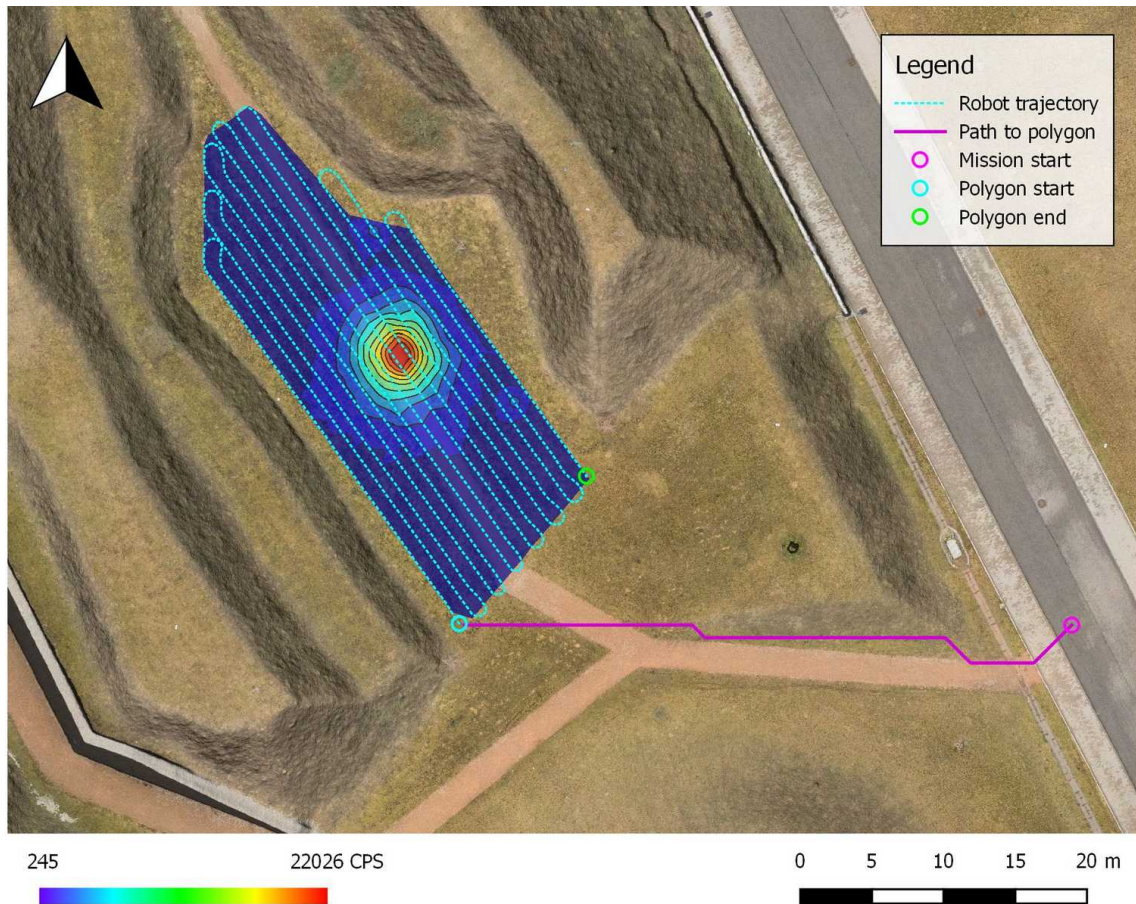
Figure A.21: Georeferenced map containing orthophoto layer with hill shading created using UAV photogrammetry complemented by the gama radiation intensity layer created by UGV.

A.5 Conclusion

This paper outlined the process of localizing ionization radiation sources via cooperation between a UAV and a UGV. All the presented methods were duly implemented, and special attention was paid to verifying the theoretical assumptions via a real mission as many similar projects rely on simulated data only. A UAV equipped with a custom-built multi-sensor system was employed to acquire the aerial data, and since this system had been designed for direct georeferencing, the technique does not require ground markers. The object accuracy obtained through photogrammetry corresponded to 4 cm RMS, and both an orthophoto and a DEM were used for the UGV trajectory planning.

An Orpheus-X3 UGV equipped with a purpose-designed gamma radiation detection system was used to test several strategies facilitating radiation source localization. Regarding the general mapping method, the localization accuracy of 6 cm was achieved in the strong and weak sources placed simultaneously inside the selected

ROI. Subsequently, an information-driven method based on the data acquired by an omnidirectional detector was designed and tested, enabling us to localize a single source at a rate approximately five times faster than that achievable with the mapping algorithm. Further, a pair of radiation detectors were utilized to assemble a detection system with considerable directional sensitivity. A modified algorithm exploiting such sensitivity, however, may ensure even better time efficiency; under certain conditions, the method allows us to localize a single source ten times faster compared to the basic method. When confronted with the common approaches in terms of the localization accuracy, the improved procedure performs worse by an order of magnitude; yet the resulting information suffices for neutralizing a source. Figure A.21 illustrates the composition of both the aerial and the ground mapping processes.

In the future, UAVs equipped with gamma detectors will likely be usable in rough radiation mapping, allowing the automatic detection of ROIs. This, along with implementing obstacle avoidance in UGVs, would lead to the more autonomous localization of radiation sources.

Bibliography

[1] Radiological Dispersal Device Playbook. *Public Health Emergancy*. Washington, DC: U. S. Department of Health and Human Services, 2015. [cit. 2017-3-12] URL: `https://www.phe.gov/preparedness/planning/playbooks/rdd/Pages/default.aspx`

[2] Ferguson C. D., Kazi T. and Perera J. *Commercial Radioactive Sources: Surveying the Security Risks*. Occasional paper No. 11. Monterey, California: Monterey Institute of International Studies, Center for Nonproliferation Studies, 2003. ISBN: 1-885350-06-6. URL: `https://www.nonproliferation.org/wp-content/uploads/2016/09/op11.pdf`

[3] Johsi T., Quiter B., Maltz J., et al. Measurement of the Energy-Dependent Angular Response of the ARES Detector System and Application to Aerial Imaging. *IEEE Transactions on Nuclear Science*, 64(7), 2015. DOI: 10.1109/TNS.2017.2693988. URL: `https://ieeexplore.ieee.org/document/7898808`

[4] Hartman J., Barzilov A. and Novikov I. Remote sensing of neutron and gamma radiation using aerial unmanned autonomous system. In *2015 IEEE Nuclear Science Symposium and Medical Imaging Conference (NSS/MIC)*, 2015. DOI: 10.1109/NSSMIC.2015.7581763. URL: `https://ieeexplore.ieee.org/document/7581763`

[5] Aleotti J., Micconi G., Caselli S., et al. Unmanned aerial vehicle equipped with spectroscopic CdZnTe detector for detection and identification of radiological and nuclear material. In *2015 IEEE Nuclear Science Symposium and Medical Imaging Conference (NSS/MIC)*, 2015. DOI: 10.1109/NSSMIC.2015.7582264. URL: `https://ieeexplore.ieee.org/document/7582264`

[6] Lin H. I., Tzeng H. J. Searching a radiological source by a mobile robot. In *2015 International Conference on Fuzzy Theory and Its Applications (iFUZZY)*, 2015. DOI: 10.1109/iFUZZY.2015.7391884. URL: `https://ieeexplore.ieee.org/abstract/document/7391884`

[7] Ristic B., Morelande M., Gunatilaka A. Information driven search for point sources of gamma radiation. *Signal Processing*, 2010, 90(4):1225–39. DOI: 10.1016/j.sigpro.2009.10.006. URL: `https://www.sciencedirect.com/science/article/pii/S0165168409004277`

[8] Wilde G. A., Murphy R. R., Shell D. A., Marianno C. M. A man-packable unmanned surface vehicle for radiation localization and forensics. In *2015 IEEE International Symposium on Safety, Security, and Rescue Robotics (SSRR)*, 2015. DOI: 10.1109/SSRR.2015.7442944. URL: `https://ieeexplore.ieee.org/document/7442944`

[9] Cortez R. A., Papageorgiou X., Tanner H. G., Klimenko A. V., Borozdin K. N., Lumia R., et al. Smart radiation sensor management. *IEEE Robotics Automation Magazine*, 2008, 15(3):85–93. DOI: 10.1109/MRA.2008.928590. URL: `https://ieeexplore.ieee.org/document/4624587`

[10] Duckworth D., Shrewsbury B., Murphy R. Run the robot backward. In *2013 IEEE International Symposium on Safety, Security, and Rescue Robotics (SSRR)*, 2013. DOI: 10.1109/SSRR.2013.6719372. URL: `https://ieeexplore.ieee.org/document/6719372`

[11] Martin P. G., Payton O. D., Fardoulisi J. S., et al. The use of unmanned aerial systems for the mapping of legacy uranium mines. *Journal of Environmental Radioactivity*, 2015, vol. 143, 135-140. DOI: 10.1016/j.jenvrad.2015.02.004. URL: `https://www.sciencedirect.com/science/article/pii/S0265931X15000314`

[12] Kaiser R., Darby I., Matos M., et al. UAV-based Mobile Gamma Spectrometry. In *CTBT Science and Technology 2017 Conference*, 2017. [cit. 2020-8-25] URL: `http://www.physics.adelaide.edu.au/cssm/workshops/inpc2016/talks/Kaiser_Thu_R1_1605.pdf`

[13] Zalud L. and Kocmanova P. Multispectral Stereoscopic Robotic Head Calibration and Evaluation. In *International Workshop on Modelling and Simulation for Autonomous Systems*, 2015, 173-184, DOI: 10.1007/978-3-319-22383-4_13. URL: `https://link.springer.com/chapter/10.1007/978-3-319-22383-4_13`

[14] Jilek T., Radiation intensity mapping in outdoor environments using a mobile robot with RTK GNSS. In *International Conference on Military Technologies (ICMT) 2015*, 2015. DOI: 10.1109/MILTECHS.2015.7153755. URL: `https://ieeexplore.ieee.org/abstract/document/7153755`

[15] Gabrlik P., Jelinek A., Janata P. Precise Multi-Sensor Georeferencing System for Micro UAVs. In *14th IFAC Conference on Programmable Devices and Embedded Systems (PDES)*, 2016, 49(25): 170-175. DOI: 10.1016/j.ifacol.2016.12.029. URL: `https://www.sciencedirect.com/science/article/pii/S2405896316326659`

[16] Gabrlik P., la Cour-Harbo A., Kalvodova P., Zalud L., and Janata P. Calibration and Accuracy Assessment in a Direct Georeferencing System for UAS Photogrammetry. *International Journal of Remote Sensing*. 2018, 39(15-16), 4931-4959. DOI: 10.1080/01431161.2018.1434331. URL: `https://www.tandfonline.com/doi/full/10.1080/01431161.2018.1434331`

[17] Jilek T., Advanced navigation in heterogeneous multi-robot systems in outdoor environment. *PhD thesis*, Brno, 2015. URL: `https://dspace.vutbr.cz/handle/11012/51783`

[18] Hart P. E., Nilsson N. J., Raphael B. A Formal Basis for the Heuristic Determination of Minimum Cost Paths. *IEEE Transactions on Systems Science and Cybernetics*, 4(2): 100-107. DOI: 10.1109/TSSC.1968.300136. URL: `https://ieeexplore.ieee.org/document/4082128`

[19] Amidror I. Scattered data interpolation methods for electronic imaging systems: a survey. *Journal of Electronic Imaging*, 2002, 11(2), 157-176. URL: `http://molly.magic.rit.edu/~mac/test/paper_pdf.pdf`

[20] Miller A., Machrafi R., Mohany A. Development of a semi-autonomous directional and spectroscopic radiation detection mobile platform. *Radiation Measurements*, 2015, vol. 72, 53-59. DOI: 10.1016/j.radmeas.2014.11.009. URL: `https://www.sciencedirect.com/science/article/pii/S1350448714003229`

[21] Ahmed S. N. Physics and Engineering of Radiation Detection. Elsevier Science Limited, 2007. ISBN: 978-0-12-045581-2.

[22] Turner D., Lucieer A. and Wallace L. Direct Georeferencing of Ultrahigh-Resolution UAV Imagery. *IEEE Transactions on Geoscience and Remote Sensing*, 2014, 52(5): 2738-2745. DOI: 10.1109/TGRS.2013.2265295. URL: `https://ieeexplore.ieee.org/document/6553130`

[23] Fazeli H., Samadzadegan F and Dadrasjavan F. Evaluation the Potential of RTK-UAV for Automatic Point Cloud Generation in 3D Rapid Mapping. In *ISPRS - International Archives of the Photogrammetry, Remote Sensing and Spatial Information Sciences*, 2016, XLI(B6): 221-226. DOI: 10.5194/isprs-archives-XLI-B6-221-2016. URL: `https://www.int-arch-photogramm-remote-sens-spatial-inf-sci.net/XLI-B6/221/2016/`

[24] Eling C., Wieland M., Hess C. et al. Development and Evaluation of a UAV Based Mapping System for Remote Sensing and Surveying Applications. In *ISPRS - International Archives of the Photogrammetry, Remote Sensing and Spatial Information Sciences*, 2015, XL-1(W4): 233-239. DOI: 10.5194/isprsarchives-XL-1-W4-233-2015. URL: `https://www.int-arch-photogramm-remote-sens-spatial-inf-sci.net/XL-1-W4/233/2015/`

[25] Barry P. and Coakley R. Field Accuracy Test of RPAS Photogrammetry. In *ISPRS - International Archives of the Photogrammetry, Remote Sensing and Spatial Information Sciences* , 2013, XL-1(W2): 27-31. DOI: 10.5194/isprsarchives-XL-1-W2-27-2013. URL: `https://www.int-arch-photogramm-remote-sens-spatial-inf-sci.net/XL-1-W2/27/2013/`

[26] Panayotov A. Photogrammetric Accuracy of Real Time Kinematic Enabled Unmanned Aerial Vehicle Systems. *Study conducted by the University of Colorado, Denver and Juniper Unmanned Aerial Systems for the United States Geological Survey*, 2015. [cit. 2016-7-26]. URL: `http://uas.usgs.gov/pdf/Reports/USGS_FINAL_REPORT_10212015.pdf`

[27] Torii T. and Sanada Y. Radiation measurement by unmanned aircraft after Fukushima Daiichi nuclear power plant accident. In *Remotely Piloted Aircraft Systems Symposium ICAO Headquarters*, Montreal, 2015. [cit. 2016-8-23]. URL: `https://www.icao.int/Meetings/RPAS/RPASSymposiumPresentation/Day%201%20Session%202%20Massaki%20Nakadate.pdf`

[28] Martin P. G., Payton O. D., Fardoulis J. S.. The use of unmanned aerial systems for the mapping of legacy uranium mines. *Journal of Environmental Radioactivity*, 2015, vol. 143, 135-140. DOI: 10.1016/j.jenvrad.2015.02.004. URL: `https://www.sciencedirect.com/science/article/pii/S0265931X15000314`

[29] Finkel R. A., Bentley J. L. Quad trees a data structure for retrieval on composite keys. *Acta Informatica*, 1974, vol. 4, 1-9 DOI: 10.1007/BF00288933. URL: `https://link.springer.com/article/10.1007/BF00288933`

[30] Harabor D., Grastien A. The JPS Pathfinding System. In *Proceedings of the Fifth Annual Symposium on Combinatorial Search*, 2012. ISBN: 9781577355847. URL: `https://research.monash.edu/en/publications/the-jps-pathfinding-system`

B Localization of Ionizing Radiation Sources via an Autonomous Robotic System

Outline

Bibliographic Information

Abstract

The article discusses an autonomous and flexible robotic system for radiation monitoring. The detection part of the system comprises two NaI(Tl) scintillation detectors; one of these is collimated to allow directionally sensitive measurements, and the other is used to calculate the dose rate and provides sufficient sensitivity. Special algorithms for autonomous operation of an unmanned ground vehicle were developed, utilizing radiation characteristics acquired by the implemented detection system. The system was designed to operate in three modes: radiation mapping, localization of discrete sources, and inspection of a region of interest. All of the modes were verified experimentally. In the localization mode, the time required

to localize ionizing radiation sources was reduced by a half compared to the field mapping mode exploiting parallel trajectories; the localization accuracy remained the same. In the inspection mode, the desired functionality was achieved, and the changes in the sources arrangement were detected reliably in the experiments.

Author's Contribution

The author performed primarily the tasks related to the robotic platform, namely, designing and implementing the control algorithms, conducting the fieldwork, and processing the results. He wrote the sections *Robotic system*, *Control algorithms*, *Experimental setup*, and *Discussion and Conclusion*. Moreover, to a large extent, he co-designed the other chapters, *Introduction* and *Results* in particular. The author is also credited with finalizing the manuscript.

<div align="right">Author contribution: 50 %</div>

Acknowledgement

Copyright and Version Notice

B.1 Introduction

There are many reasons to be prepared for radiation situation reconnaissance of a region of interest (ROI). Accidents in transportation or handling a radioactive material pose a risk of losing control over the source of ionizing radiation (IR) [1], [2]. A similar problem consists in the intentional misuse of an IR source as a radiological exposure device (RED); the worst case scenarios comprise potential threats arising from a radiological dispersal device (RDD) ([3], [4]) or nuclear power plant accidents (Chernobyl, Fukushima). The affected area can be of various sizes and different degrees of danger. To take proper radiation protection measures, we first need to identify the area contaminated with radioactive substances and to localize the 'hot spots' or radiation sources quickly and efficiently. To prevent people from entering a high risk area, remote sensing and manned or unmanned robotic systems are widely studied. The aim of our research is to satisfy the requirements for a modern, autonomous, and flexible robotic detection system that provides comprehensive data on the radiation situation at the deployment site. The monitoring of a radiation situation using unmanned aerial or ground vehicles is also a subject of research [5], [6], [7]; however, the output of such a process is a map of ionizing radiation intensity that must be evaluated by a competent person.

The method to expand the capabilities of radiation situation reconnaissance consists in obtaining more information than solely the intensity of IR. The direction to the IR source can constitute such information. The novelty of the research lies in the development of a new, directionally sensitive detection system together with special algorithms to autonomously operate the unmanned ground vehicle (UGV) in dependence on the detected radiation characteristics. These new capabilities provide radiation mapping with new possibilities in localizing discrete IR sources, performing radiation inspection of objects, and surveying the radiation signature of regions of interest.

B.2 Methods

B.2.1 Dosimetry System

A special detection system was developed within the research procedures. The system comprises two detectors, one omnidirectional and the other directionally sensitive. Both detectors are based on a scintillation crystal of sodium iodide doped with thallium (NaI(Tl)) in the size of $2''{\times}2''$ accompanied with photomultiplier tubes (Nuvia a.s., CZE). The counting electronics was specially developed to avoid data delay and distortion usual in data processing in commercial devices. The processed
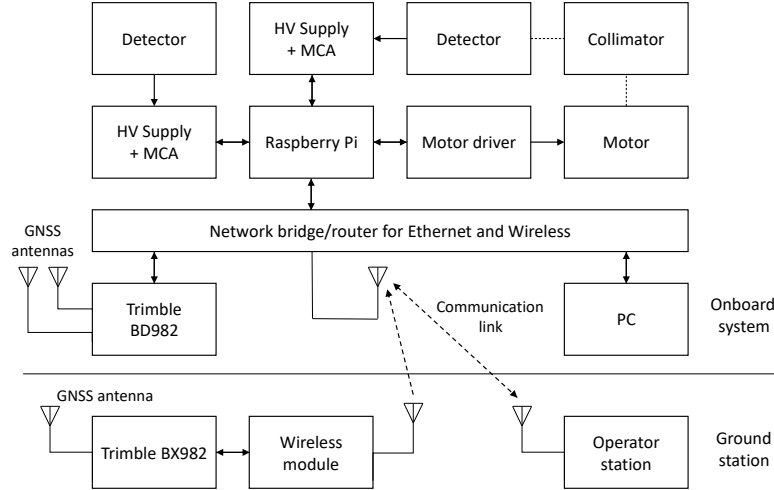
Figure B.1: A block diagram of the system.

data comprise a 256-channel spectrum of gamma radiation measured every second. Thev detectors were calibrated for the energy range from 30 keV to 2 MeV. The quantity dose equivalent rate was approximately determined by summing the spectra from the omnidirectional detector. This conversion was calibrated for the energy of 662 keV (^{137}Cs). The dynamic range of the dose equivalent rate was up to 0.6 mSv·h^{-1}.

The directionally sensitive detector was placed in a lead collimator. Shielding with the thickness of 2 cm enclosed the top and sides of the scintillating crystal. Due to the weight and volume, it was not possible to shield the whole detector. The collimator had a vertical aperture of 11 mm on its side, corresponding to the viewing angle of 15°. The collimator exhibited the weight of 7 kg, and its capabilities included rotation around the vertical axis. The sum of the gamma spectra was measured in 24 sectors during 1 turn (24 sectors × 15°= 360°). The obtained histogram was evaluated for a statistically significant increase in the detector response, which was interpolated by a triangle; subsequently, the direction to an IR source was estimated.

B.2.2 Robotic System

The detection system can be integrated in any arbitrary robotic system mechanically capable of carrying its load and is equipped with reliable self-localization and navigation modules. Within the scope of this paper, the Orpheus-X4 robotic platform developed at the Faculty of Electrical Engineering and Communication and CEITEC institute, Brno University of Technology, is employed [8], [9]. The Orpheus-X4 is a mid-size, four-wheeled reconnaissance robot with a differential drive having the payload capacity of approximately 30 kg. Importantly, the vehicle utilizes an advanced

Figure B.2: The Orpheus-X4 carrying the detection head.

module based on the Real Time Kinematic (RTK) Global Navigation Satellite System (GNSS), which ensures high-accuracy measurement of the robot's position, with the error in the order of centimeters [10]; consequently, the robot can automatically follow a pre-defined outdoor path.

The block diagram in Fig. B.1 shows the manner in which the detection system was integrated in the robotic platform. The key on-board components are connected via Ethernet, and they are embodied by a Raspberry Pi (control of detectors), a GNSS receiver, and a computer running all the control algorithms. A wirelessly connected ground station provides the correction data for the position measurement and also the remote control. An image of the complete system, namely, the robot carrying the detection head, is shown in Fig. B.2.

B.2.3 Operation Modes

For the autonomous detection system testing, three operation modes to facilitate radiation reconnaissance were designed: radiation mapping, localization of discrete sources, and inspection of objects or regions of interest.

The first operation mode uses standard ROI exploration along parallel lines by a robot carrying the radiation detector. There is no need of communication between the detector and the UGV. The results of this mode comprise a map of the ionizing radiation intensity. A subsequent evaluation is required to identify the hot spots, discrete sources, and other aspects.

The main benefit of the second mode is the ability to modify the robot trajectory in real time, exploiting the data measured by the detection system. The purpose of this mode is to reduce the time needed to accurately localize IR sources. The basic idea consists in reacting to an increased level of IR, executing the directional measurement and subsequently inspecting portions of the surveyed region where the sources have been detected. This approach causes strong sources to be reported

quickly to the operator, along with their parameters. The method is described in more detail within the following subsection.

In the third operation mode, the robotic detection system performs autonomous inspection of the specified area in terms of the presence of gamma radiation. The system must be capable of indicating a possible change in the IR intensity and subsequently specifying the character of the change (e.g., a new or a missing source). Prior to the inspection, there must be a 'learning' pass of the inspection trajectory to identify and remember the radiation signature of the ROI. During the inspection, the current radiation signature is continuously compared with the learned one. This mode is able to inform the operator about new IR sources (accident, contamination) or 'lost' sources (stolen, moved) in the region of interest, including, for example, a nuclear power plant site or a radioactive waste repository.

B.2.4 Control Algorithms

The algorithm utilized for navigating the robot along the defined path is also described in other papers, such as *Autonomous field measurement in outdoor areas using a mobile robot with RTK GNSS* [11]. This chapter emphasizes the algorithms necessary for operation in the modes described above.

The first mode is rather straightforward, with the data collected along a predefined trajectory composed of parallel lines; the trajectory is not changed during the measurement. Only one parameter, namely, the distance of parallel lines, significantly influences the result, and its choice corresponds to the desired minimum detectable activity (MDA). In order to produce a well-arranged map of the area distribution of the ionizing radiation, the scattered data are interpolated via the Delaunay triangulation [12]. The resulting map is of importance to the human operator, as it offers a quick survey of the sources' layout and intensity; moreover, it can provide an additional item of information, such as that on isodoses. Directional measurement is not employed in this mode, which serves mainly as a reference for the localization performance of the second mode.

Regarding the utilized algorithms, the second mode is more appealing; its purpose is to localize the radiation sources in a shorter time but at the same (or similar) accuracy, exploiting the directional information provided by the detection system. To perform a directional measurement, the robot has to stop for 12 seconds; thus, it is desirable to minimize the number of directional measurements to maintain the algorithm's ability to compete with the first mode. A possible approach to achieving this objective is described below.

Let us assume that the sources are present in a region with delimited borders. The region of interest should be chosen based on a primary measurement; for example,
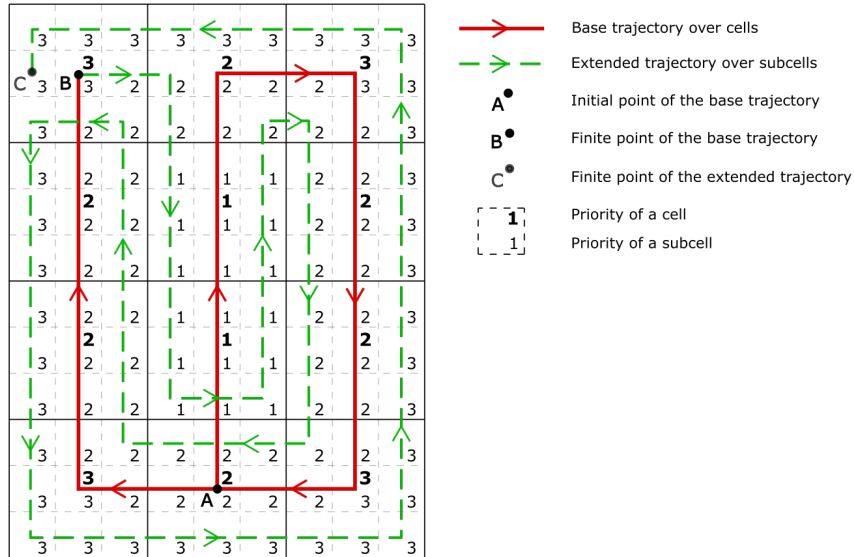
Figure B.3: An example of the two-phase survey trajectory from point A to point C; point B is a dividing spot between the primary and the secondary trajectories.

its border can be constituted by an approximate isodose. A feasible solution is to employ aerial assets [13], [14].

The exploration of the region comprises two phases, namely, a rough and a detailed one. First, the region is decomposed into cells consisting of a 3×3 matrix of subcells. The size of a subcell should ensure that any source with an MDA present in it is detectable from its center. Then, to each cell and subcell, a priority number is assigned (the lower the number, the higher the priority), having the highest value by the border. A primary trajectory is built over the cell centers, following a set of rules which prefer:

- a lower priority number,

- unvisited cells,

- constant direction.

The rules are obviously more complex; therefore, their detailed description is not discussed within this paper. A secondary trajectory over the subcell centers is built in a similar manner. An example of exploration trajectories is shown in Fig. B.3 for a region of 3×4 cells.

During the localization, the robot follows these pre-defined trajectories until the presence of a source is indicated. The indication is based on the instantaneous measured radiation intensity (represented either by a count rate or a dose rate) if its value is significantly higher than expected. Before the first source is localized,
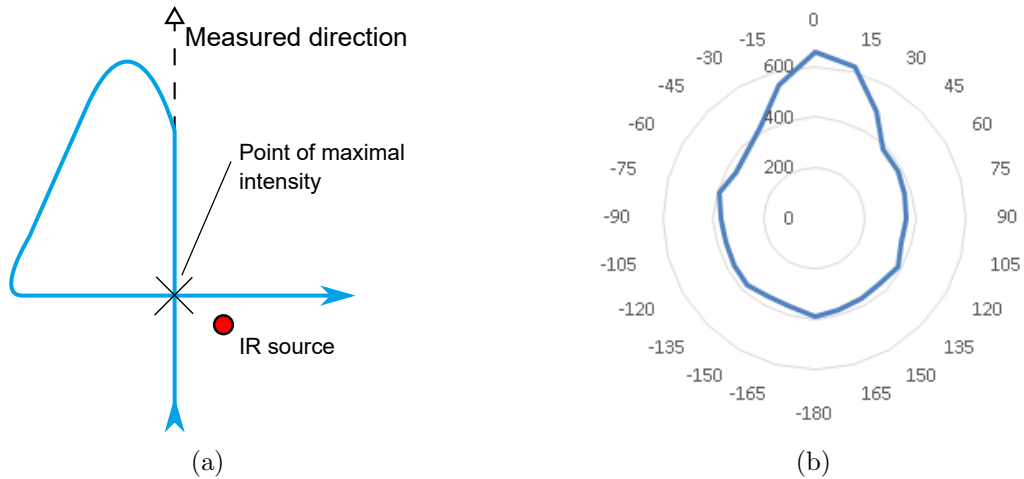
Figure B.4: A trajectory example for a better estimation of the source parameters (a). The angular dependency of the directionally sensitive detector in CPS; source of ^{137}Cs, 293.5 MBq, distance 3 m (b).

the anticipated intensity is defined solely by the radiation background, which should be measured prior to the survey, outside the stricken area (if possible). Once the indication conditions are fulfilled, the robot stops operating, and the directional measurement using the detection head is performed. If a significant direction is found, the robot will alter its trajectory in order to follow that direction. After the source is provably passed (we need to consider the dead time effect), the trajectory changes again, with the objective to collect data along a perpendicular line. The purpose consists in supplying sufficient input data into the algorithm that estimates the parameters of the source (the position and 'emission'); such a trajectory is represented in Fig. B.4a. The estimation can be performed using, e.g., the Gauss-Newton method, as described in *Optimizing the localization of gamma radiation point sources using a UGV* [15]. If multiple significant directions are found, i.e., more than one source is within the detectable range, then each of them is handled in the described manner. Afterwards, the robot returns to the base trajectory to continue the survey. However, the expected radiation intensity value does not derive from the background only but also from the established sources' radiation field. The exploration is completed when the final point of the secondary trajectory is reached.

Finally, in the third operation mode the operator needs to manually define several checkpoints that exhibit a significant radiation signature. Directional measurements are conducted in these points to provide reference for a future inspection. The course of the first inspection sequence, which is driven manually, is logged in a configuration file containing the trajectory and the distribution of the radiation intensity along it; the results of the measurements are saved. During the following autonomous

sequences, it is checked whether a change in some of the quantities oversteps the tolerance area; if such a condition is found, the anomaly is reported to the operator and can be verified by additional measurements.

B.2.5 Experimental Setup

For the experimental verification of the autonomous detection system, a rectangular region with the area of 330 m^2 was selected. Sealed radioactive sources of radionuclide ^{137}Cs with the activities of 293.5 MBq and 2.9 GBq were employed to test the first two modes of operation (the radiation mapping and localization of discrete sources). The location of sources was the same in both cases in order to compare the accuracy and time requirements of the different approaches; in the third mode, the setup included other two sources of radionuclide ^{137}Cs, whose activities equalled 14.2 MBq and 94.7 MBq. Here, the intention was to move the sources during the experiment.

B.3 Results

The detection part of the system was properly tested and calibrated. In particular, the structure and properties of the collimator for the directionally sensitive detector (i.e., the thickness of the shielding or the shape and dimension of the aperture) were investigated and estimated on the basis of Monte Carlo simulations [16] (in Czech). The real angular dependency as the main property is represented in Fig. B.4b. The Figure indicates the output of the detector in counts per second (CPS) as the function of the angle between the aperture and the source of ^{137}Cs (293.5 MBq, distance 3 m). The ratio of the CPS for 0°to that for 180°is approximately 1.7. Naturally, the ratio depends on the gamma radiation energy. A low energy radiation with a higher attenuation coefficient constitutes a higher value of the ratio.

The directionally sensitive detector is able to estimate the direction to the source very reliably within 4 to 6 meters (source of ^{60}Co, 152.5 MBq). The angle measurement accuracy equals approximately 5°.

The field experiments were performed correspondingly to the setup characterized above. For the radiation mapping (the first mode), the distance of 1 m between the parallel lines was chosen in order to provide data for sufficiently smooth interpolation. The resulting map is shown in Fig. B.5a. The area exploration took 10.5 minutes, and the localization accuracy of 10.6 cm RMS was achieved.

The experimentation in the second mode (the localization of discrete sources) necessitated the control algorithm alteration, as some of the spurious attributes of the detection system had not been anticipated; basically, several effects caused by
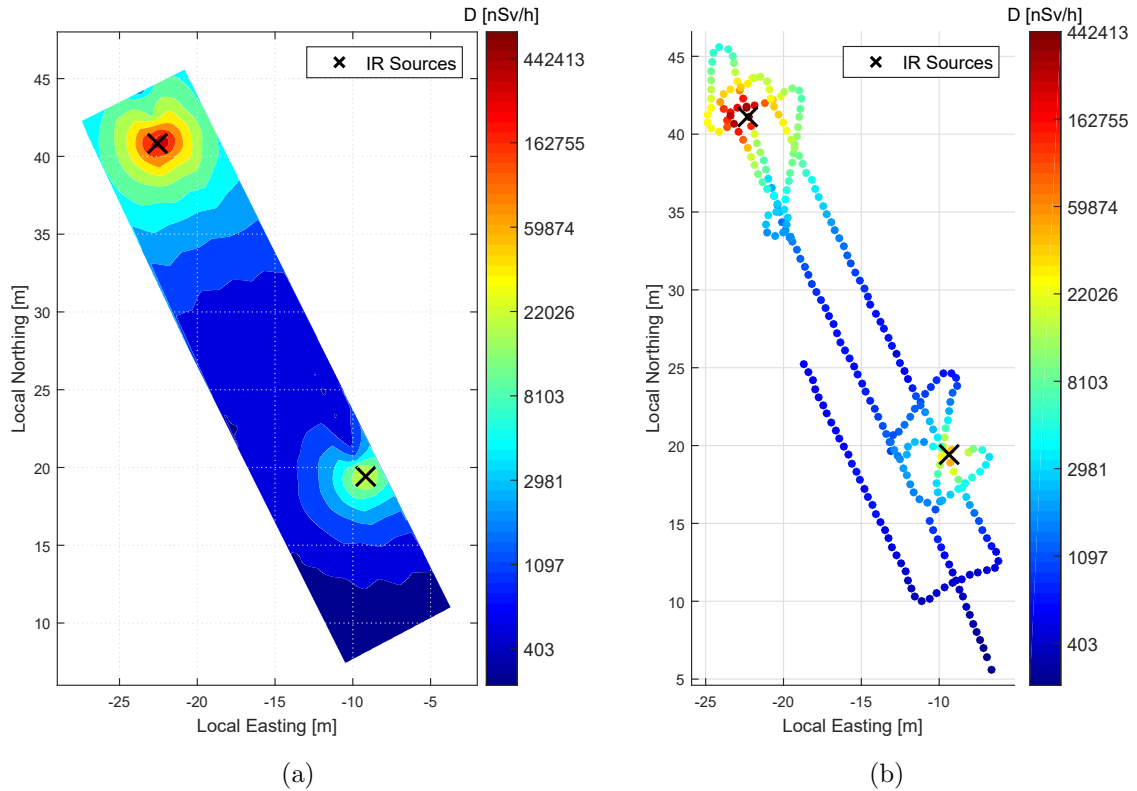
Figure B.5: The radiation mapping result related to the ^{137}Cs sources; the upper left one has the activity of 2.9 GBq, while the other exhibits 293.5 MBq (a). The source localization result related to the ^{137}Cs sources; the upper left one has the activity of 2.9 GBq, while the other exhibits 293.5 MBq (b).

the measurement geometry and the robot movement were compensated. Eventually, the sources were localized with the accuracy of 12.4 cm RMS in 5.5 minutes. The results of the experiment are visualized in Fig. B.5b. The final part of the trajectory is missing due to the data integrity corruption caused by shading of the GNSS antennas. Note that the region was decomposed to 1×4 cells; the straight line in the middle embodies the primary survey trajectory while straight lines along borders of the region represent the second one.

In the inspection mode, an approximately oval trajectory was defined manually, with two checkpoints near the IR sources where the directional measurements were carried out. The correct behavior of the system was verified by multiple passes of the inspection trajectory for each of the scenarios described below. First, the sources were kept in their initial locations; the algorithm indicated no change, as expected. Then, one of the sources was removed, and the event was correctly evaluated by the algorithm. Finally, the weaker source was placed in a new location; the system

was able to report the presence of a new source on the basis of a radiation intensity higher (compared to the background) than that detected in the initial measurement.

The described experiments were run multiple times in the same configuration (due to logistic issues) to verify the algorithms.

B.4 Discussion and Conclusion

The paper presents a custom-made, two-detector system capable of measuring both the dosimetry quantities and the direction to sources of ionizing radiation. The system was integrated in the Orpheus-X4 robotic platform and successfully tested in field experiments with real radioactive sources.

The operation mode, which enables faster localization of discrete IR sources via a directionally sensitive sensor, is introduced. Compared to the localization approach based on conventional radiation mapping, the system should offer the same accuracy within a shorter time under certain circumstances. The duration of radiation mapping in a given area is constant, and the choice of the initial measurement point is relevant in terms of the time required for the first significant item of information to arrive. Conversely, once the assumption of the sources' presence near the center of the region is correct, primary information on the situation is provided earlier, eliminating the dependence on the initial conditions even with the long directional measurement time.

Another benefit of our research consists in the inspection mode, which embodies a rather innovative technique within radiation protection. Currently, the inspection is possible merely in an outdoor environment, as it depends on the self-localization provided by the GNSS; such a scenario constitutes an apparent disadvantage. Prospectively, however, the system can be extended with an indoor self-localization module (e.g., by means of computer vision [17]). Moreover, a variable inspection trajectory of the robot is envisaged to decrease the system's predictability (to make a malevolent attack on the system more difficult).

There are several major possibilities of improving the system within future research. First, the size of the directionally sensitive part of the detection system could be reduced by employing a one-inch detector and a photodiode instead of the photomultiplier. Although such adjustment will probably reduce the detection efficiency, it could still ensure a satisfactory trade-off between the mechanical ruggedness and the accuracy of the directional measurements. Then, the system can be equipped with a detector for high dose rates, e.g., a GM tube, as the scintillators become overloaded in the vicinity of high emission sources. Finally, more general and robust localization algorithms for the robot are planned to be developed and tested.

Bibliography

[1] Danesi, P.R. *Radiological and depleted uranium weapons: environmental and health consequences*. In: Encyclopedia of Environmental Health (2011).

[2] *Nuclear security systems and measures for the detection of nuclear and other radioactive material out of regulatory control: Implementing guide*. IAEA nuclear security series no. 21, Vienna (2013).

[3] Bland, J., Potter, Ch. and Homann, S. *Radiological exposure devices (RED) technical basis for threat profile*. Sandia report SAND2018-6003. Sandia National Laboratories (2018).

[4] Curling, C. A. and Lodge, A. Review of radioisotopes as radiological weapons. Institute for Defense Analyses (2016).

[5] Schneider, F. E., Welle, J., Wildermuth, D. and Ducke, M. *Unmanned multi-robot CBRNE reconnaissance with mobile manipulation System description and technical validation*. In: Proceedings of the 13th International Carpathian Control Conference (ICCC), 637–642 (2012).

[6] Martin, P.G., Payton, O.D., Fardoulis, J.S., Richards, D.A. and Scott, T.B. *The use of unmanned aerial systems for the mapping of legacy uranium mines*. J Environ Radioact. 143, 135–140 (2015).

[7] Kim, D. et al. *3D radiation imaging using mobile robot equipped with radiation detector*. In: 2017 IEEE/SICE International Symposium on System Integration (SII), 444–449 (2017).

[8] Burian, F., Zalud, L., Kocmanova, P., Jilek, T. and Kopecny, L. *Multi-robot system for disaster area exploration*. WIT Trans Ecol Envir. 184, 263–274 (2014).

[9] Kocmanova, P. and Zalud, L. *Effective Calibration and Evaluation of Multi-Camera Robotic Head*. Int J Adv Res Comp Sci. 6, 143–152 (2015).

[10] Saghravani, S.R., Mustapha, S.b, Saghravani, S.F., Ibrahim, S.b and Yusoff, M.K.b. *Performance of Real-Time Kinematic Global Positioning System and Automatic Level Surveying for Height Determination – A Comparison*. In: 2009 International Conference on Signal Acquisition and Processing, 108–111 (2009).

[11] Jilek, T. *Autonomous field measurement in outdoor areas using a mobile robot with RTK GNSS*. IFAC PapersOnLine. 48, 480–485 (2015).

[12] Amidror, I. *Scattered data interpolation methods for electronic imaging systems: a survey*. J Electron Imaging. 11, 157–176 (2002).

[13] Lazna, T., Gabrlik, P., Jilek, T. and Zalud, L. *Cooperation between an unmanned aerial vehicle and an unmanned ground vehicle in highly accurate localization of gamma radiation hotspots*. Int J Adv Robot Syst. 15, 1–16 (2018).

[14] Gabrlik, P. and Lazna, T. *Simulation of Gamma Radiation Mapping Using an Unmanned Aerial System*. IFAC PapersOnLine. 51, 256–262 (2018).

[15] Lazna, T. *Optimizing the localization of gamma radiation point sources using a UGV*. In: 2018 ELEKTRO, 1–6 (2018).

[16] Fisera, O., Kares, J., Cuda, P. and Tomek, M. *Development of intelligent system for automatic localization of ionizing radiation sources*. In: Proceeding of conference CBRN PROTECT (2017).

[17] Chiang, S., Guo, X. and Hu, H. *Real time self-localization of omni-vision robot by pattern match system*. In: 2014 International Conference on Advanced Robotics and Intelligent Systems (ARIS), 46–50 (2014).

C An Automated Heterogeneous Robotic System for Radiation Surveys: Design and Field Testing

Outline

Bibliographic Information

Abstract

During missions involving radiation exposure, unmanned robotic platforms may embody a valuable tool, especially thanks to their capability of replacing human operators in certain tasks to eliminate the health risks associated with such an environment. Moreover, rapid development of the technology allows us to increase the automation rate, making the human operator generally less important within the entire process. This article presents a multi-robotic system designed for highly au-

tomated radiation mapping and source localization. Our approach includes a three-phase procedure comprising sequential deployment of two diverse platforms, namely, an unmanned aircraft system (UAS) and an unmanned ground vehicle (UGV), to perform aerial photogrammetry, aerial radiation mapping, and terrestrial radiation mapping. The central idea is to produce a sparse dose rate map of the entire study site via the UAS and, subsequently, to perform detailed UGV-based mapping in limited radiation-contaminated regions. To accomplish these tasks, we designed numerous methods and data processing algorithms to facilitate, for example, digital elevation model (DEM)-based terrain following for the UAS, automatic selection of the regions of interest, obstacle map-based UGV trajectory planning, and source localization. The overall usability of the multi-robotic system was demonstrated by means of a one-day, authentic experiment, namely, a fictitious car accident including the loss of several radiation sources. The ability of the system to localize radiation hotspots and individual sources has been verified.

Author's Contribution

The author was responsible primarily for the tasks related to the radiation measurements and data processing, namely, the automated selection of the regions of interest, the coverage path planning for the terrestrial robot, and the source localization. Further, he substantially participated in the overall method designing, analyzing the related work, and performing the field study. The author also wrote prominent parts of the manuscript, above all, sections *Source Localization Methods*, *Possible Applications*, *Automatic Selection of the Terrestrial Mapping Areas*, and *Radiation Data Processing and Source Localization*. He markedly contributed to the other major chapters: *Introduction*, *Results*, *Discussion*, and *Conclusion*.

Author contribution: 35 %

Acknowledgement

Copyright and Version Notice

C.1 Introduction

Any radiation mapping, namely, measurement that provides knowledge of the distribution of ionizing radiation in space and time, finds use in various applications related to common activities. In this context, we can mention, for example, geophysical surveys, environmental monitoring of nuclear sites, post-disaster responses, localization of lost radiation sources, and everyday operation of nuclear power plants (NPP). Advantageously, such tasks are often carried out by utilizing unmanned robotic systems, mainly to protect human health; however, robots are also capable of reducing the time and increasing the accuracy thanks to semi- or fully autonomous operation. To improve the efficiency, different assets and techniques may be combined. Thus, for example, one of the oldest and most commonly applied radiation survey methods is helicopter-based airborne spectrometry enabling us to quickly cover square kilometres of land, but only at the expense of inadequate accuracy and very high cost. Unmanned ground vehicles (UGVs), by comparison, may ensure superb accuracy, but their operational ranges are mostly limited to several hundreds of square meters; in the same context, unmanned aircraft systems (UASs) offer adequate accuracy and survey range. Therefore, to recognize the radiological situation in medium-sized areas, a multi-platform system seems to be a promising option.

The paper aims to present the options and perspectives of using a multi-robot system to perform highly automated radiation mapping and source localization in an outdoor environment; these tasks embody a common response to radiological incidents and nuclear accidents. The goal of the mapping, in general terms, rests in assessing the severity of the situation and providing as many data as possible to the authorities responsible for restoring the locality (these usually involve relevant national agencies and fire rescue services). The areas to be surveyed and mapped are commonly sized in the order of thousands of square meters, with the dimensions reaching up to 500×500 m; however, considering the point radiological sources, the desired localization accuracy is within decimeters to allow the sources to be collected by the human operators and validated using a hand-held device. Nevertheless, our research does not comprise scenarios with severe nuclear accidents involving serious health risks and possibly requiring the robots to be radiation-hardened.

To perform the aforementioned tasks, we designed a comprehensive mapping method that relies mainly on available technologies and algorithms combined together to solve the problem completely, i.e., from area definition to source localization. Regarding the hardware, the approach employs two unmanned platforms, namely, an aerial and a terrestrial one; each of these then has a particular role. In the paper, we cover the necessary theory to enable effective deployment of the robots, including trajectory planning aspects and choosing proper data collection

parameters; furthermore, considerable attention is allocated to automating as many steps as possible to minimize human intervention. In this context, for example, we survey techniques enabling automatic extraction of radiation hotspots from a sparse dataset and discuss deterministic estimation of a source's locations.

A major portion of the paper is centered on the practical verification of the designed process; to fulfill this step, we prepared a comprehensive experiment resembling a real-world scenario to a high degree. The setup encompassed an area of 20,000 m^2 featuring considerable height differences, artificial objects, and multiple radiation sources. Consecutively, we deployed a UAS and a UGV and performed indispensable processing cycles, as originally planned; moreover, to increase the authenticity, the entire operation was completed within a single day. Although the results obtained from the single experiment are not statistically plausible enough to be generalized, we can propose some valuable conclusions that may help to direct the future research activities in a convenient manner. Thus, for instance, the outcomes illustrate the benefits and drawbacks of the individual robotic platforms within the radiation mapping context, responding to the question of whether the aerial mapping suffices to distinguish between the individual isotopes and sources concentrated on a small area.

The paper is organized as follows: Section C.2 discusses related work in robotic radiation mapping and source localization, whilst also outlining our long-term research activities within this domain. In the next chapter (Section C.3), we provide an overview of the mapping process, followed by a thorough description of the relevant theory, designed algorithms, and applied equipment. The experiment setup, acquired data, and processing outputs are characterized in Section C.4, chronologically and according to reality. Finally, the Section C.5 compares the achieved results with both our originally planned targets and the outcomes outlined in the referenced literature. As this paper constitutes a part of a comprehensive research concept, we also address tasks to be potentially solved in the future.

C.2 Related Work

C.2.1 Robot Deployment

The necessity to employ remotely operated machines in radiation-contaminated environments appeared with the expansion of NPPs during the second half of the 20th century. Such machines were mostly used to perform inspection, manipulation, and maintenance; however, nuclear accidents shifted the interest towards the development of terrestrial mobile robots intended for disaster response applications [1]. These systems are principally applicable in reconnaissance, data gathering, and

object manipulation; due to the complexity of the environment, remote control is generally employed as the most convenient approach [2, 3, 4]. A teleoperated robot was successfully utilized, for example, to inspect the damage after the Fukushima Daiichi NPP accident in 2011 [5].

The deployment of robots with autonomous functions in post-disaster environments, especially inside or close to collapsed buildings, remains a major challenge; however, various other applications comprising radiation exposure are available. Ground robots enabling autonomous or semi-autonomous operation can be employed in radioactive waste storage facilities; areas affected by radiation as a result of an accident; uranium mines; and to localize uncontrolled radiation sources. [6] present a six-wheeled unmanned ground vehicle (UGV) specially designed for chemical, biological, radiological, nuclear, and explosive-related (CBRNE) tasks to solve some local navigation problems automatically, e.g. laser scanner-based obstacle avoidance. Autonomous radiation mapping inside pre-defined polygons was discussed by [7]. In this case, precise navigation is enabled thanks to a real-time kinematics (RTK) GPS receiver, and the data from onboard NaI detector are utilized for particle swarm optimization-based source localization. The presented solution is, however, suitable for obstacle-free areas only. The same UGV platform was deployed in a nuclear storage facility to perform inspections [8]. In such a GPS-denied environment, localization embodies the essential task; thus, a light detection and ranging (LiDAR) sensor is utilized to execute simultaneous localization and mapping (SLAM), facilitating navigation inside an unknown territory. As is apparent, the above-mentioned studies principally examine localization, navigation, and mapping problems.

Flying robots, compared to UGVs, enable quick radiation data collection over a large area thanks to a higher speed; additionally, they operate in a free space, typically facing none or only a very small number of obstacles (considering safe distance from the ground). A UAS as a means to assist in solving nuclear emergency cases was proposed already in 2008, when a 100 kg unmanned helicopter equipped with an 8 kg scintillating detector was employed to estimate dose-rate distribution automatically [9]. A similarly sized unmanned system proved to be beneficial after the Fukushima Daiichi accident, where it provided information about the deposition of radioactive cesium around the site [10, 11]; importantly, this was a case when a detailed radiation map of this type was compiled for the first time. Unlike ground robots, UASs operate at certain distances from the source, and thus they require a sensitive radiation detection system, which embodies considerable payload. For this reason, micro-unmanned vehicles, a category popular thanks to its flexibility, low price, and safe operation, must operate as close to the ground as possible to collect radiation data even with less sensitive detectors [12, 13]. Flying robots, moreover, are applicable in producing digital elevation models (DEM) thanks to the LiDAR or

photogrammetry techniques to supplement the radiation data layer [14]. [15] present a complex, multi-sensor system for both UASs and UGVs, which integrates various sensors and approaches to present radiation data in 3D and real time. The drawback of low-altitude mapping rests in potential collisions with obstacles, a problem discussed within [16], where the flight height during legacy uranium mines mapping had to be manually adjusted. UASs can operate even indoors, in GPS-denied environments [17], and novel, lightweight radiation sensors may allow the use of even smaller vehicles, possibly operated in swarms [18].

The advantages of both ground and aerial robots may be combined within a multi-robotic radiation mapping system. Such an idea was introduced by [19], whose unconventional solution comprises an unmanned helicopter carrying a small UGV. In this case, the UAS is intended to localize potential radiation-contaminated area via an onboard detector and to produce a DEM. A UGV, by contrast, is deployed with a winch system, facilitating comprehensive ground inspection and sample collection. However, the practical capabilities of the system have not been confirmed sufficiently. A similar method was introduced and verified by [20], whose aerial platform yielded a georeferenced orthophoto and a DEM, while also performing measurements with an onboard scintillation detector. A ground robot was then automatically navigated to locations exhibiting a maximal counts per second (CPS) value, and a classified map based on the orthophoto as well as the DEM enabled the choice of an energy-effective path; real-time obstacle avoidance was ensured by a LiDAR. The experiment verified the system's ability to localize an unknown source; however, the simple localization technique detects one maximum only, thus being unsuitable for multi-source or areal contamination scenarios. A promising concept to exploit different robotic platforms is described within the study [21], where the key idea rests in using an aerial imagery-based DEM to divide the study site into sub-areas according to their suitability for individual robots. Ground radiation measurements are carried out in UGV-passable regions only; a UAS is employed in the rest of the target zone. Moreover, various algorithms exploiting radiation spectra are tested to find the sources. Despite the advantages, the system has not yet been fully prepared to operate in real-world conditions without operator intervention.

C.2.2 Source Localization Methods

One of the common tasks addressed in the literature is the localization, which consists in identifying the parameters of the point sources present in the studied region of interest. The methods usually work with a series of discrete measurements that are assumed to have been taken at known positions; these measurements are per-

formed by either a robotic platform or static sensors. In many cases, the methods are verified only by simulation.

The paper [22] utilizes maximum likelihood estimation (MLE) to find the coordinates of a single source via measurements from multiple locations, reducing the problem to two dimensions to acquire a coarse estimate that is improved by using a gradient method. In [23], the artificial potential field approach is adopted to localize a source by navigating a robot towards it; the attractive force is derived from the source's position estimated via the particle filter (PF) technique, while the repulsive one allows the robot to avoid obstacles. Another example of PF application can be found in [24]; the advantage of the interpretation proposed within the article consists in that it is not necessary to know the number of sources a priori. The algorithm works with a network of detectors measuring at multiple places simultaneously and is thus unsuitable for single-robot scenarios. An array of directional sensitive detectors can be employed for tracking a moving source as well [25]. Fast hotspot localization is characterized by [26], where the proposed algorithm dynamically adopts the UAS trajectory to move towards the hotspot. Localization methods utilizing a UAS to collect data are examined in paper [27]. A method exploiting the radiation contour is outlined; the related analysis managed via the Hough transform is able to find multiple sources, whose contours may overlap. Surveying the region of interest with more UGVs enabling us to localize multiple sources is covered in [28]; the presented strategy prefers short paths having higher radiation intensity gradients. The parameter estimation utilizes the PF method with disperse resampling to prevent particle degeneration.

Over the last decade, the localization algorithms have been studied by B. Ristic and his research group, who partially verified the methods by using real data acquired during a field test. The paper [29] compares three approaches to single source localization; the techniques are based on the MLE, the extended Kalman filter (EKF), and the unscented Kalman filter (UKF). The authors also analyzed the theoretical minimum estimation error with a Cramér-Rao bound, indicating that sequential Bayesian estimators (the EKF and the UKF) provide better performance than the MLE. The radiation field can be modeled as a weighted sum of 2D Gaussians, or a Gaussian mixture [30]. To find the Gaussians' parameters, two estimators, namely, a Gaussian and a Monte Carlo approximation, are employed, with the former yielding better results in both the simulations and the real data application. The algorithm is rather robust, and exact a priori knowledge of the number of sources is not required. In [31], up to three sources are localized, with binary and continuous genetic algorithms constituting alternative implementations of the MLE algorithm and negative-log likelihood being the objective function. The number of sources present in the area can be found by applying the minimum de-

scription length (MDL) principle. This method is based on minimizing the function that takes the parameter matrix as the input; this matrix needs to be estimated for every considered number of sources [32]. An information-driven search altering the measurement trajectory during the data acquisition process is outlined in the article [33]. The number of sources is assumed to be unknown; the source are tracked by one or more mobile observers, and their parameters are estimated via a multi-target, track-before-detect particle filter. The particles are initialized with different amounts of sources; at the end of each update step, some of the particles acquire a source while some others lose it. The observer motion control maximizes the estimation of the reward function. The simulations have shown that the information-driven search yields results more accurate than those obtained from the survey along a pre-defined uniform trajectory. The method was also verified by using field data.

C.2.3 Possible Applications

Potential missions for multi-robot systems involve several applications that beneficially combine quick, flexible operation and a large range of aerial assets with the versatility and better radiation measurement conditions ensured by terrestrial robots. A combination of UASs and UGVs provides a synergy of benefits for radiological mapping, bringing both global information from the territory and accurate dosimetry or spectroscopy data from the points of interest. Nuclear safety, radiation and environmental protection, remediation, and decommissioning then embody some of the target fields. Generally, prior knowledge of the character of the post-accident radiological situation is not available, i.e., it is not known whether the sources are solid, liquid, sealed, leaking, or the contamination is dispersed in the soil. Despite this, the mapping strategy mostly remains the same, and its goal is to acquire gridded data. Different types of algorithms are employed, e.g., when tracking a radioactive cloud; however, such an example is a very special and ranges outside the scope of our research. Common incidents involve uncontrolled sources used in non-destructive testing, medicine, or geology; typically, these sources are sealed. Even when the nature of the contamination does not allow the sources to be localized, the mapping is still important in delimiting the safe zones.

Regarding UGVs, a major advantage rests in the possibility of applying semiconductor high-purity germanium (HPGe) detectors with high resolution (radionuclide identification) capabilities; in UASs, conversely, the resolution is still limited by vibrations and the microphonic effect [34], and the onboard heavy sensitive detectors restrain the operation time. Although some HPGe detection systems are not susceptible to vibrations, their weight often exceeds 18 kg [35], making them inconvenient for the category of UASs utilized in our research. In general terms, the aircraft are

suitable for light-weight detectors like GM tubes and plastic scintillators; considering the purpose, we can also employ inorganic (crystal) scintillators or CdZnTe solid-state detectors to acquire basic spectroscopy capabilities. In the given context, a UGV is significantly more flexible and can carry diverse detection systems, including continuously working dose rate meters with high dynamic range coverages, accurate solid-state spectrometers, neutron detectors and beta contamination meters for occasional static measurements, and alpha contamination indicators. The devices mounted on a UGV may support the monitoring with measurements at a height of 1 m above the ground, which corresponds to the dosimetry standard for radiological mapping [36]. Comprehensive radiation surveys necessarily involve detailed, laboratory-based analyses of the samples, and the use of UASs/UGVs can improve the applied sampling strategy. Moreover, a ground robot is capable of assisting in remote sample collection if equipped appropriately.

C.2.4 Authors' Previous Work

CBRNE robotics and multi-robot systems have for almost two decades embodied the research focus of the Robotics and AI group headed by Prof. Zalud at Brno University of Technology. The Orpheus reconnaissance robot family [37], a central project pursuing the development of four-wheel skid-driving portable CBRNE robots (Figure C.1), is being continuously refined and has been employed in various experiments and missions, such as those devised to determine water contamination [38]. In the context of the topic, we have examined automatic radiation mapping thanks to the robot's built-in RTK global navigation satellite system (GNSS) -based navigation system, establishing that a UGV is capable of substituting for human-performed measurements effectively, more accurately, and without safety risks [39]. However, the approach was not subjected to comprehensive testing, including, for example, obstacle-accommodated environment.

To extend the usability of the terrestrial platforms, we developed a multi-sensor system for UAS photogrammetry to assemble high-resolution orthophotos and surface models [40]. Benefiting from the capability of operating without ground georeferencing targets, the solution is perfectly convenient for radiation-related tasks; the products are applicable in UGV trajectory planning under difficult conditions. Moreover, our simulations suggest that the surface model may find use in aerial radiation mapping, too [41]. In radiation detection system-equipped UASs, flying at a constant altitude above ground level (AGL) collects more consistent data compared to flying at a constant mean sea level (MSL) altitude, thus making source localization more accurate. All the above-mentioned equipment, methods, and experience enabled us to compose a comprehensive multi-platform system for automatic ra-

Figure C.1: The four-wheel Orpheus robot family and other platforms of the heterogeneous reconnaissance mobile robot system ATEROS.

diation source search. A first attempt in this field was published previously [42]; however, numerous aspects and issues still remain to be addressed to increase the reliability, credibility, robot interoperability, and overall real-world usability, i.e., the main topics dealt with in this research.

C.3 Methods

C.3.1 Method Overview

Robot-based environmental mapping in an outdoor environment generally embodies a challenging task due to the largely variable conditions that may be encountered, especially in terms of the terrain, vegetation diversity, and weather conditions. Moreover, further special requirements may arise as regards the measuring equipment and time constraints. In this context, choosing the proper robotic platform is crucial to achieve the desired results.

To perform the radiation mapping and source localization tasks, we designed a method operating two different robots, namely, a hexacopter UAS and a four-wheel, skid-steering UGV. The former platform enables us to cover a large area within a reasonable time, regardless of the terrain nature; however, the distance from the surface may limit the applicability of some sensors. Advantageously, at the initial stages of the procedure, the vehicle is employed to carry out the aerial photogrammetry and sparse radiation mapping. The latter platform is suitable for the reconnaissance and mapping of small areas (hundreds of square meters) only, due to its low operation speed; another limiting factor rests in the reduced terrain negotiability, depending on the slope pattern. Thus, the UGV finds use in
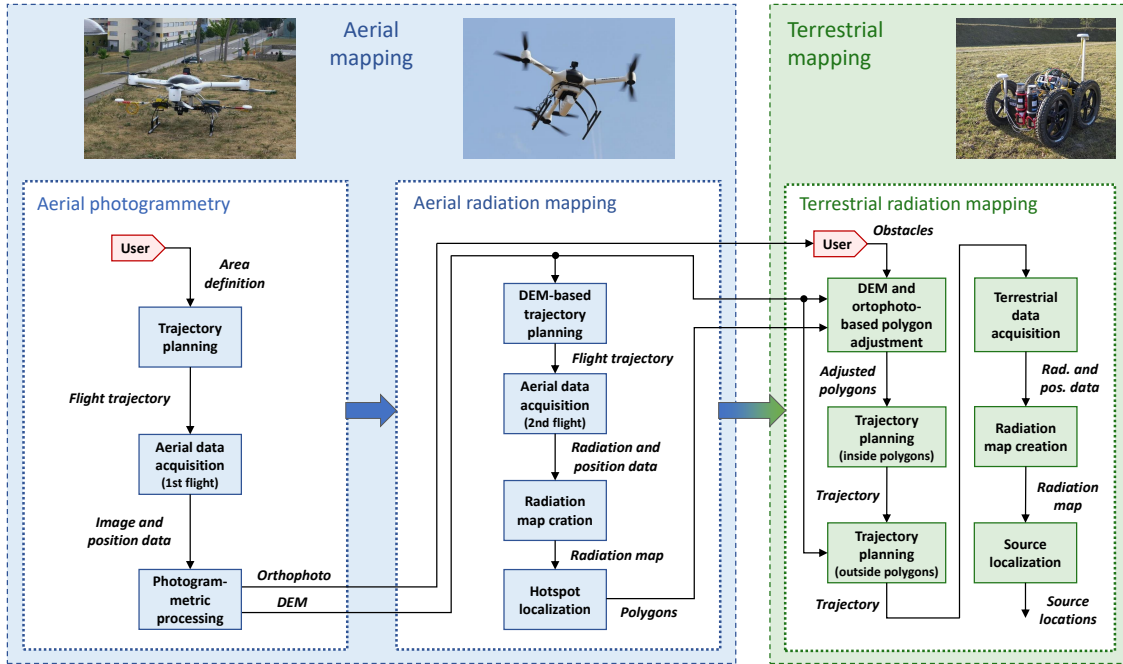
Figure C.2: The sequence of the operations that form the entire process. The actual mapping comprises the aerial (blue) and terrestrial (green) branches; the user interventions are highlighted in red.

precise radiation mapping and source localization, namely, at the final stages. Both platforms are described within Section C.3.7.

As is evident from Figure C.2, our approach comprises the following three phases: aerial photogrammetry, aerial radiation mapping, and terrestrial radiation mapping. The first phase aims to create the actual orthophoto and 3D model of the area, i.e., products to be utilized later for the trajectory planning and to help operators orientate themselves in the unknown environment. The initial step, namely, defining the area of interest, must be executed by a user considering the current situation; however, the following operations, such as the actual flight, are already fully automatic, with the UAS's trajectory designed according to the photogrammetric requirements. Yet, from the general perspective, the entire operation must still be supervised by a pilot, especially due to safety and legal concerns. The outcomes of the photogrammetric processing (Section C.3.2) and the first phase as a whole embody a georeferenced orthophoto and a DEM.

The second phase is intended to localize potential radiation hotspots by means of aerial radiation mapping of the entire area. In order to obtain credible results, the UAS trajectory design encompasses the DEM acquired within the previous phase to allow us to operate at a constant height above ground level (AGL). This procedure is described thoroughly in Section C.3.3. Once the sparse radiation map is

available, our algorithm selects the sub-areas that exhibit increased radiation levels (Section C.3.4).

The goal of the final phase consists in building detailed radiation maps of the hotspots by using the UGV; this step facilitates the potential localization of individual sources. To perform such a task, we must consider the degree to which the terrain negotiability is limited in the relevant platform, and thus the selected regions are adjusted via both the DEM-based obstacle map and the orthophoto, where other possible obstacles and impassable locations are selected by the user. The aforementioned mechanisms are addressed in Section C.3.4. The UGV trajectory planning problem can then be divided into two tasks, namely, covering the pre-specified polygons (hotspots) and executing A*-based robot navigation between the polygons (Section C.3.5). The collected data are employed to generate a detailed radiation map and to allow the source localization. This stage, described in Section C.3.6, involves utilizing the least-square method to estimate both the precise location of the individual sources and their approximate activity.

C.3.2 Aerial Photogrammetry

Aerial photogrammetry embodies the first phase of the mapping method, and its goal is to deliver the actual orthophoto and DEM, i.e., products necessary for trajectory planning during subsequent mapping phases. The stage comprises three principal steps: trajectory planning, data acquisition, and processing. In terms of the first step, the common approach involves the flight pattern with parallel strips, known from both manned and unmanned aerial photogrammetry [43, 44]. Relevant parameters, such as the flight height, image overlaps, and ground resolution, are selected with respect to the applied photographic equipment and the required quality of the final product. In the data acquisition, we consider a custom-built multi-sensor system to collect both the aerial imagery and the position data; the system is introduced in Section C.3.7.

The aerial data are typically processed via a photogrammetric pipeline tool; for example, the widely used Agisoft Photoscan software package embodies a suitable choice, as it enables us to execute all the photogrammetric processing stages. The workflow comprises estimating the camera exterior and interior orientations, generating the sparse and dense point clouds, and composing the orthophoto and the DEM (see [45] for a detailed workflow description). Assuming available position data of the locations where the individual images were captured, the software allows transforming the products into a geographic coordinate system even without GCPs; this approach is known as direct georeferencing [46, 47]. Nevertheless, several ground targets are commonly recommended to be used for accuracy assessment

purposes and to support the estimation of the camera's intrinsic parameters. The conventional procedure involving GCPs, namely, the indirect georeferencing method, is generally unsuitable in CBRNE tasks, given the health risks.

C.3.3 Aerial Radiation Mapping

Aerial radiation mapping embodies the second phase of the mapping method. The technique aims to create a sparse ionizing radiation map of the entire study site to localize possible hotspots to be mapped via the UGV. Without any prior knowledge of the hotspots, and lacking a detection system with directional sensitivity, the straightforward flight strategy comprises parallel survey lines, similarly to the previous photogrammetry flight. The main difference rests in the setting of major parameters, including the flight altitude AGL h, distance between lines n, speed v, and sampling period p. Certainly, no single correct solution is ready for choosing the parameters, but several rules can still be defined to find a setting appropriate to the actual mission. As UASs typically carry a low-weight and low-sensitivity detector, and as the dose rate decreases with the square of the distance, the h must be as small as possible to detect even weak sources. In practice, the minimum flight altitude is always limited by the actual precision of the UAS navigation system; the terrain shape and obstacles within the mapping site have to be considered, too. However, the distance d between the source and the detector is, in addition to the vertical component h, formed also by the horizontal distance. The condition $d = h$ applies when the UAS is directly above the source, and the formula (C.1) describes the marginal situation when the source is located exactly between the survey lines being n meters apart (Figure C.3).

$$d = \sqrt{\left(\frac{n}{2}\right)^2 + h^2} \tag{C.1}$$

The n, together with the $v \cdot p$ value, define the spatial density of the collected radiation data. A low n value yields data with a high density and homogeneity in the lateral axis (with respect to the flight lines); the intensity decrease in a source positioned between the flight lines is insignificant. Nevertheless, such a setting can result in a very long flight trajectory and operation time. Contrariwise, a high n value produces a shorter trajectory; however, the resulting data density can be too low to distinguish between the individual sources, and thus the hotspot localization may become ineffective. Moreover, weak sources lying between the flight lines may not be detected at all due to a considerable intensity decrease. The described effects are illustrated in Figure C.4 for $h = 15$, a realistic flight height value in micro UASs.

The data density in the longitudinal axis, determined by the speed and the sampling period, should be approximately the same as in the lateral axis, due to the
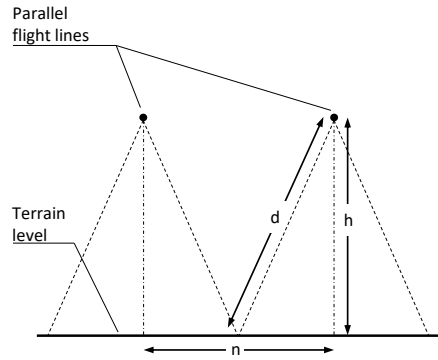
Figure C.3: The basic parameters of the UAS trajectory for the radiation mapping procedure.
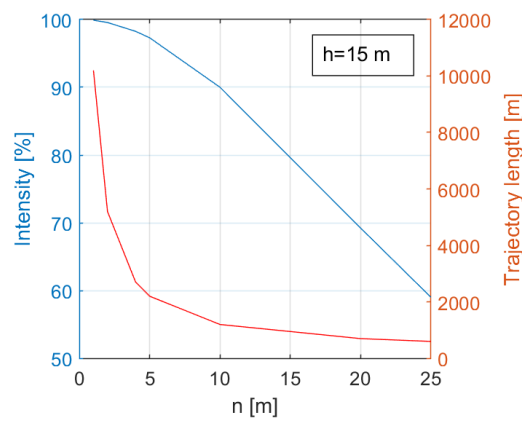
Figure C.4: The effect of the n value (the distance between the flight lines). The blue line expresses the intensity of a source located exactly between the flight lines, relative to the intensity of a source lying under the flight line; the intensity decreases due to the inverse-square law. The red line renders the flight trajectory length per 1 ha squared area.

subsequent processing. Since the maximum v is often limited to ensure safe UAS operation close to the surface, the p must be set in view of this fact (high density data may be downsampled without any information loss in the postprocessing). In addition, the speed setting directly relates to the operation time.

The flight parameters also influence the resolution of the mapping, which can be imagined as a hypothetical peak width invoked by a single point source; the narrower the peak, the better the resolution. More concretely, the resolution depends mostly on the detector's footprint, that is, the ground area that produces a majority of incident particles. With decreasing size, a higher resolution can be achieved. In a stationary detector, the footprint consists in a circle of radius approximately equal to the detector's altitude. When the measurement is performed by moving aircraft, the footprint is dilated along the trajectory portion traversed during the sampling
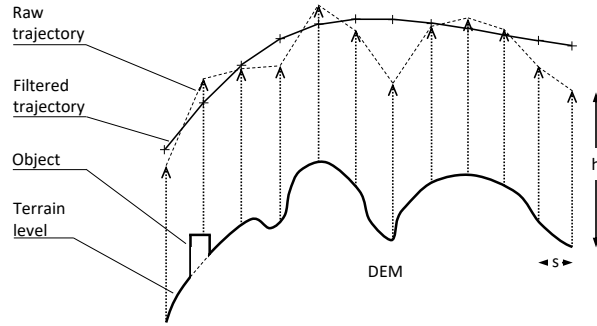
Figure C.5: The principle of the terrain-based trajectory adjustment.

period. Given these assumptions, the dependency of available scan accuracy on the altitude and speed of the UAS is quadratic and linear, respectively. In our case, the resolution is limited especially by the minimum feasible flight altitude. The mapping resolution can be improved via methods based on deconvolution, as outlined in article [48]. The authors of the referenced paper address the effect of varying height above ground as an essential issue; in our approach, however, this is solved during the trajectory planning phase. To apply deconvolution, it is necessary to have a precise model of the detector's response, the most important aspect then being its energy efficiency, which could be acquired either experimentally or via MCNP simulation.

In UAS-based radiation mapping, the common approach involves operating at a constant MSL altitude [20, 16], an option applicable at locations that lack significant height differences. As indicated within one of our previous papers [41], major variations in the flight height above ground level produce non-homogeneous and unreliable data; thus, a means to secure a constant AGL height is essential in hilly sites. The proposed method utilizes a photogrammetry-based DEM, the output of the initial UAS flight, to adjust the radiation mapping trajectory, i.e., to modify the vertical trajectory components. The procedure is described within Algorithm 1and illustrated in Figure C.5. Yet the trajectory produced by using the algorithm may contain an extensive amount of waypoints to be stored in the UAS's memory; therefore, the s value has to be chosen carefully.

Another option to maintain a constant flight height above the surface rests in utilizing a laser rangefinder; in such a case, the MSL altitude is controlled according to the measured data. This functionality, however, must be supported by the UAS's control unit and, above all, may pose a risk in unknown areas due to the inability to avoid vertical obstacles having a height higher than the actual AGL flight altitude (buildings, for example). Thus, we consider the DEM-based approach more suitable for the discussed application, although the operation must still be supervised by

an operator. To increase the robustness and safety, a combination of DEM-based planning and real-time obstacle avoidance would deliver the ideal approach.

C.3.4 Automatic Selection of the Terrestrial Mapping Areas

Aerial radiation mapping yields a set of scattered data points, each comprising the coordinates and the spectrum. For further processing and finding hotspots, calculating the radiation intensity (dose rate) at points in a regular grid is required; this step can be carried out through the interpolation based on Delaunay triangulation [49]. The density of the data points in the axis parallel to the flight direction is approximately five times higher than that in the perpendicular axis, due to the chosen flight speed, sampling period, and distance between the strips. Regrettably, such point distribution is not convenient for the interpolation, and each four subsequent spectra are thus averaged in order to achieve an even distance of points in both axes.

Once the interpolated radiation map is available, the operator can manually mark the regions of interest (ROIs); nevertheless, we believe that automatic selection, despite not being indispensable, provides a helpful auxiliary tool. The goal is to minimize the number of human interventions in the whole process. Moreover, a similar algorithm can be re-used during the source localization phase, as will be shown later. A viable approach to automatic selection rests in employing a two-

---

Algorithm 1 The DEM-based trajectory adjustment.

Input: The horizontal trajectory T (turnover points), digital elevation model D (raster), AGL height h (scalar), and segment size s (scalar).

Output: The terrain-adjusted spatial trajectory T_t (3D points).

1: **Trajectory segmentation:** Splitting the lines defined by the points T into smaller segments having a maximum size s to obtain dense trajectory points T_s will facilitate precise terrain following. The s value is chosen with respect to the character of the terrain.

2: **Find the corresponding DEM points:** For every point defined in T_s, find the nearest horizontal point of D.

3: **Compose the 3D trajectory:** Use the height values of the obtained DEM points as the height coordinates for the trajectory T_s.

4: **Compute a new altitude:** Increase the altitude of every point in T_s by the height h.

5: **Smooth the trajectory:** Apply the 7th order low-pass IIR filter to the T_s point sequence to obtain the filtered trajectory T_t. This step is taken to avoid sudden height changes; regrettably, it is not energy-efficient and can increase the operation time.

---

dimensional peak detector; such an option is unsuitable for the general case, as the data do not always represent a clear sharp peak, e.g., if

- the peak comprises contributions by multiple radiation sources;

- the magnitude of the peak is comparable to the radiation background, as the data are very noisy due to statistical laws;

- the magnitude of the peak exceeds the capacity of the detector, and the dead time is over 50 %, causing higher dose rate levels to yield a lower number of counts.

The first two cases can be certainly expected during aerial radiation mapping; thus, we adopt a different method. The basic idea is as follows: By eliminating the radiation background, a connected set will be left for each significant peak. The problem is in identifying the background, as it not only depends on the geographical location but, generally, can be increased by strong artificial sources. The unnecessary data may be assumed to lie within the three-sigma band around their mean value. To find such an *adaptive threshold*, the statistical parameters of the background must be estimated. An analytical solution to the described problem is not feasible, because we cannot anticipate the number of radiation sources or their activity relative to natural radionuclides and cosmic rays. Instead, an empirical threshold T_{bg} is derived from the statistical parameters of the complete dataset as a sum of the dataset's mean value and a half of its standard deviation:

$$T_{bg} = \mu + \frac{\sigma}{2} \tag{C.2}$$

From points having an intensity lower than T_{bg}, the threshold of the hotspots is derived:

$$T_{hotspots} = \mu_{bg} + 3 \cdot \sigma_{bg} \tag{C.3}$$

The adaptive thresholding method was verified with both simulated [41] and previously measured terrestrial data.

Once the thresholding is applied to the interpolated points arranged in a regular grid, the remaining connected sets are enclosed by contours using the marching squares algorithm [50]. Apparently, only contours having a certain minimal length should be accepted in order to eliminate random noise-induced peaks; we suggest that a valid contour should encircle at least four aerial samples. Finally, the regions are smoothed and optionally enlarged via the Minkowski addition [51] with a circle-shaped structuring element. The hotspots are eroded at first to suppress the noise; subsequently, they may be dilated again to adjust their sizes. The resulting ROIs are passed, as connected sets of points in a regular grid, on to the next stage for further processing; such a grid is then denoted as the *ROI map*.

C.3.5 Terrestrial Radiation Mapping

The first task for a UGV is to move from a safe zone to the first detected contaminated area. A system user selects in the map suitable places where the robot can be potentially unloaded. This task requires the knowledge of obstacles in the area of interest. The required obstacle map is computed from the previously created DEM.

We attempt to obtain a DEM with the highest possible resolution to acquire the best source data, allowing us to reveal as many obstacles as detactable in the real terrain. The effective resolution is limited by the capabilities of the equipment and the time allocated for the processing. The intended DEM resolution equals 10 cm/pixel, considering the parameters of the sensing and processing equipment. Regarding the path planning, the process is resource-intensive if we use a large quantity of obstacle map cells; thus, it is convenient to employ only the number of cells necessary for the given purpose. Our mission allows having an obstacle map where the pixel size approaches the width of the UGV, with a satisfactory path planning accuracy preserved. Such a procedure of creating the obstacle map involves also reducing the pixel count; this operation, however, is not implemented as separate downscaling. The input parameters to facilitate the generation of the obstacle map are as follows:

- the maximum allowed inclination of the ground (max allowed magnitude of the robot pitch and roll angle),

- the maximum height of a negotiable obstacle perpendicular to the terrain,

- the pixel size of the obstacle map.

From these parameters, we can define the obstacle function (Figure C.6) of the employed UGV. The function is used for detecting the impassable area in the group of DEM pixels that forms one pixel of the obstacle map. Each existing square sub-group of the DEM pixels for every obstacle map pixel is checked by verifying if the obstacle function has been satisfied. The algorithm starts by checking all groups of 2x2 DEM pixels, then 3x3 pixels, etc.; the process terminates at the whole group of DEM pixels, which invariably forms a pixel of the obstacle map. In the case that a sub-group of DEM pixels is found that does not meet the obstacle function, the corresponding pixel of the obstacle map is marked as the obstacle. The process produces a binary map whose pixel size equals the integer multiple of the DEM pixel size.

To find the optimal scenario of moving a UGV to the contaminated areas, the system operator must manually select the places where the robot can be potentially unloaded. From these starting points, we plan three types of trajectories: towards
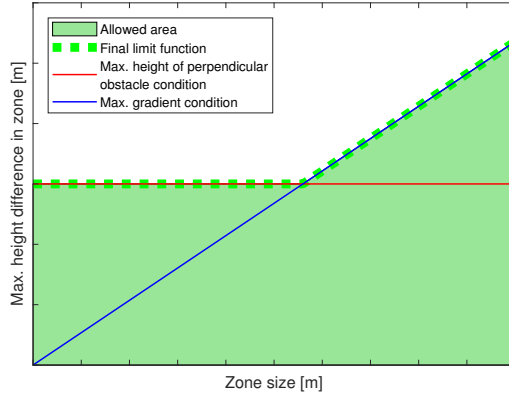
Figure C.6: The obstacle function.

the detected contaminated areas; between these zones; and back from the last area to the unloading place. To move between the contaminated areas, the starting point for the path planning is the waypoint at the end of the trajectory inside the current area, while the final point is marked by one of the endpoints of the trajectory inside the next area. These path planning tasks can be generally solved by any A* based algorithm [52]; the shortest sequence of paths from the set of all possible solutions is used. A precondition for solving the global path planning task rests in the availability of an obstacle map, which, in our case, is derived from the photogrammetry-based DEM.

To plan a trajectory inside the regions of interest, we have to describe each such region with a set of polygons, one 'envelope' representing the outer limits of the area; optionally, the description can be expanded to include multiple 'holes' that characterize obstacles not traversable by the UGV. At this point, both the coarse characterization of the terrestrial-mapped hotspots (Section C.3.4) and the obstacle map are available and need to be fused. This is also the moment when the operator should intervene to validate if all of the actual obstacles are contained in the map; alternatively, the operator inserts the missing objects manually. Note that this step can utilize the earlier acquired orthophoto to identify restrictions.

Both maps are composed of binary value cells, which can be either empty or occupied. In the ROI map, the empty cells represent the areas where the terrestrial mapping is to be performed. The maps are fused through a relatively simple intersection: If corresponding cells in the maps are empty, then the cell is empty; conversely, it is occupied when the occupancy condition has been met in at least one of the maps. An example of the fusion producing a *fused map* is shown in Figure C.7.

Generally, a single region of interest may be divided by obstacles into multiple subregions; thus, the fused map is subjected to connected-component labeling [53] to distinguish individual areas enclosed by the envelopes. Subsequently, each area

112
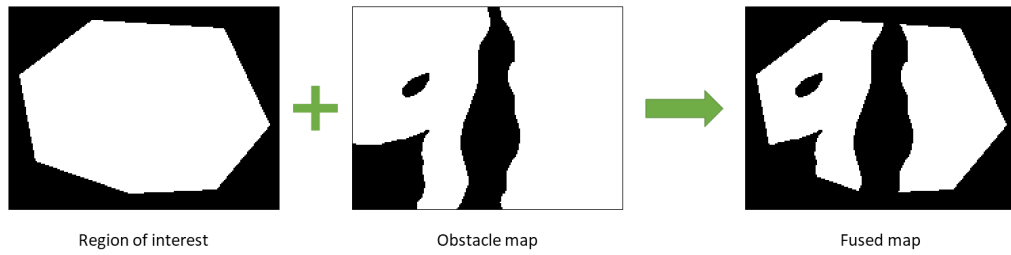
Figure C.7: An example of how a fused map is generated; the white color represents the free space.
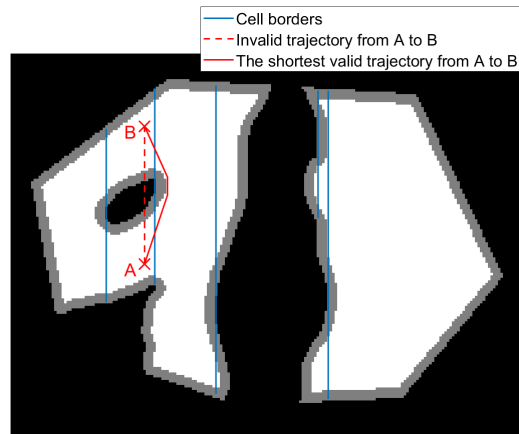
Figure C.8: An example of the Boustrophedon decomposition and interconnection of subsequent cells; the black color represents the obstacles, while their dilation is in grey.

greater than the rationally chosen threshold (the criterion being applied to exclude miniature portions of the region) is searched for contours in order to identify its envelope and holes.

Then, each mapped region is divided into a set of disjoint obstacle-free subregions by using the Boustrophedon decomposition [54], a procedure suitable for problems where obstacles are defined by polygons. The principle of this algorithm is to acquire subregions, or cells, that can be completely covered by a uniform back-and-forth trajectory; each cell has two edges parallel to the *sweep line*, which, in turn, is parallel to the survey direction. The result of the decomposition depends on the selected sweep line orientation (relative to the ROI); in general terms, it is desirable to minimize the number of cells. Finally, the region is described by a graph whose nodes represent the subregions and edges define their adjacency.

To determine the order in which the subregions are explored, the depth-first search algorithm is applied; this method guarantees that all nodes (cells) are visited and prefers transitions between adjacent ones. Trajectory planning inside the cells is rather straightforward. In some cases, when moving from one cell to another, a

direct connecting path may collide with an obstacle. Since the non-traversable zones are already described by the polygons, the visibility graph algorithm [55] is utilized to find the shortest non-colliding path; to preserve a clearance from the obstacles, the corresponding polygons are dilated. The situation is illustrated in Figure C.8.

C.3.6 Radiation Data Processing and Source Localization

Handling the terrestrial data is largely similar to the aerial radiation data processing presented in Section C.3.4. The localization of the sources can be characterized by three steps:

1. Estimating the number of sources, R.

2. Estimating the initial coarse parameters of R sources.

3. Increasing the accuracy of the parameters in accordance with the measured data.

The first step utilizes the adaptive thresholding algorithm. Although multiple sources in a single region form a sole hotspot within the primary map, they may yield more peaks inside the detailed secondary map built from the UGV data, which are acquired in a finer grid and from a closer distance than the aerial dataset. To perform the estimation, the following steps are applied:

1.a Compute the peak threshold.

1.b Interpolate the data into a regular grid.

1.c Eliminate the radiation background.

1.d Find valid contours in the map; their count equals the number of sources.

Regarding the source parameters, three items are sought for each source; these items include the emission intensity and coordinates in two axes. Let us have a source i with the vector $\boldsymbol{\theta}_i = (\alpha_i, x_i, y_i)$; all of the sources are then characterized by the parameter matrix $\boldsymbol{\theta} = (\boldsymbol{\theta}_1, \boldsymbol{\theta}_2, \ldots, \boldsymbol{\theta}_R)^\mathsf{T}$. To initiate the matrix, we suggest choosing a central point within each contour to define the coordinates and taking the greatest corresponding total count value to estimate the intensity. By filling in the matrix, the second localization step is completed.

Finally, the accuracy of the parameters is iteratively improved via the Gauss-Newton method [56], which finds use in solving non-linear least squares problems. Given a matrix of M measurements, $\boldsymbol{z} = (\boldsymbol{z}_1, \boldsymbol{z}_2, \ldots, \boldsymbol{z}_M)^\mathsf{T}$, where $\boldsymbol{z}_i = (c_i, x_i, y_i)$ to denote the total count obtained and the coordinates where the measurement has

$$\text{(a)} \qquad\qquad\qquad\qquad \text{(b)}$$

Figure C.9: The BRUS UAS configured for the experiment: with a multi-sensor system to perform the photogrammetry (a), and carrying a gamma radiation detection setup (b).

been taken, the Gauss-Newton algorithm minimizes the sum of residuals (the differences between the expected and the measured values); the residual m is expressed as:

$$r_m = c_m - \sum_{r=1}^{R} \frac{\alpha_r}{(x_m - x_r)^2 + (y_m - y_r)^2 + h^2}, \qquad \text{(C.4)}$$

where h is the height of the detectors above the terrain. The parameter matrix is updated in each step according to the equation

$$\boldsymbol{\theta}_{k+1} = \boldsymbol{\theta}_k - (\boldsymbol{J}^\mathsf{T} \boldsymbol{J})^{-1} \boldsymbol{J}^\mathsf{T} \boldsymbol{r}(\boldsymbol{\theta}_k), \qquad \text{(C.5)}$$

where $\boldsymbol{J}$ is the $M \times 3R$ Jacobi matrix of the partial derivatives of the residuals. The iterations continue until the sum of the squared residuals stops decreasing significantly.

C.3.7 Unmanned Platforms

The proposed method involves using two unmanned platforms, namely, a UAS and a UGV; the former item ensures aerial data acquisition during the initial stage of the mapping process. The system must be capable of operating automatically and carrying various sensors to perform the photogrammetry and to measure the ionizing radiation. Since the latter procedure comprises low-altitude flying, which requires high maneuverability and low-speed operation, we chose a BRUS Heavy rotary-wing UAS by the Military Technical Institute of the Czech Republic. This platform provides a sufficient payload capacity and endurance for the desired tasks (Table C.1).

Table C.1: The parameters of the unmanned platforms and equipment. RDS: radiation detection system.

Parameter	UAS	UGV
Dimensions	1.2 × 1.2 × 0.5 m	1.0 × 0.6 × 0.4 m
Weight (incl. battery, without payload)	10.7 kg	51 kg
Max payload weight	8.0 kg	30 kg
Operational time without payload	45 mins	120 mins
Drive type	multi-rotor	wheel, skid-steering
Operating speed	2.0 – 5.0 m/s	0.6 m/s
Max speed	16.7 m/s	4.2 m/s
Photogrammetry system weight	2.8 kg	—
RDS – weight	3.0 kg	2.2 kg
RDS – number of detectors	1	2
RDS – detector type	NaI(Tl)	
RDS – detector size	2×2"	
RDS – energy range	50 keV – 3 MeV	
RDS – energy resolution	7 % @ 662 keV	
RDS – channels (conversion gain)	256	1024
RDS – multichannel analyzer	NUVIA MCB3	

At the initial stage of the actual mapping, the UAS is fitted with a custom-built multi-sensor system for aerial photogrammetry, illustrated in Figure C.9a. This setup enables us to create georeferenced photogrammetric products, namely, an orthophoto or a DEM, without requiring ground control points (GCPs). The setup integrates a consumer-grade, full-frame camera; a dual-antenna RTK GNSS receiver; an inertial navigation system (INS); and other necessary components. It was previously described in more detail within article [40] and subsequently found use in, for example, UAS-based aerial snow depth mapping [57]. The existing results indicate that the system able to reach centimeter-level object accuracy. A similar concept was already utilized by other researchers, too [58, 59, 60].

The second phase of the mapping cycle comprises ionizing radiation measurement; for this purpose, the UAS is fitted with a NUVIA DRONES-G radiation detection system (Figure C.9b, Table C.1). The compact setup involves a detector and other relevant electronic components (such as a GNSS module and a laser altimeter).

For the terrestrial mapping, we chose the four-wheeled Orpheus-X4 UGV (Figure C.10, Table C.1). The robot offers an automatic navigation along the planned

Figure C.10: The Orpheus-X4 UGV equipped with a GNSS receiver and a pair of NaI(Tl) radiation detectors.

trajectory, and in the case of a good and stable GNSS RTK solution, it is possible to reach 3 cm (1σ) in stable flat surfaces [61]. However, the accuracy is generally much worse in unstable traction terrains. The self-localization function employs a dual antenna GNSS, an INS, and wheel odometry. The system relies mainly on the RTK GNSS to solve the 2D position and heading, nevertheless, the dead reckoning solutions INS and wheel odometry are used to bypass insufficient GNSS solution. Orpheus was previously described in more detail in articles [62] and [63].

To perform the robotic mapping of gamma radiation, scintillation detectors seem to make a good trade-off for the desired features. The detectors provide a high density and volume, thus have good sensitivity for gamma rays. Moreover, common inorganic scintillators possess spectrometric abilities; knowledge of the spectra enables us to identify different radionuclides and can facilitate separating useful information from the radiation background. The applied setup, summarized within Table C.1, was chosen mainly thanks to its accessibility, conventionality, and previous experience. If not stated otherwise, the presented algorithms work with the total count (TC) value, i.e., the sum of counts in all channels. An advantage of utilizing multiple detectors consists in higher sensitivity of the measurement system and better cumulative statistical attributes of the measurements.

C.4 Results

C.4.1 Experiment Setup

The method for multi-robot radiation mapping and source localization presented in the paper was evaluated by utilizing a fictitious accident at a site in close proximity to the campus of Brno University of Technology, Brno, the Czech Republic, in August
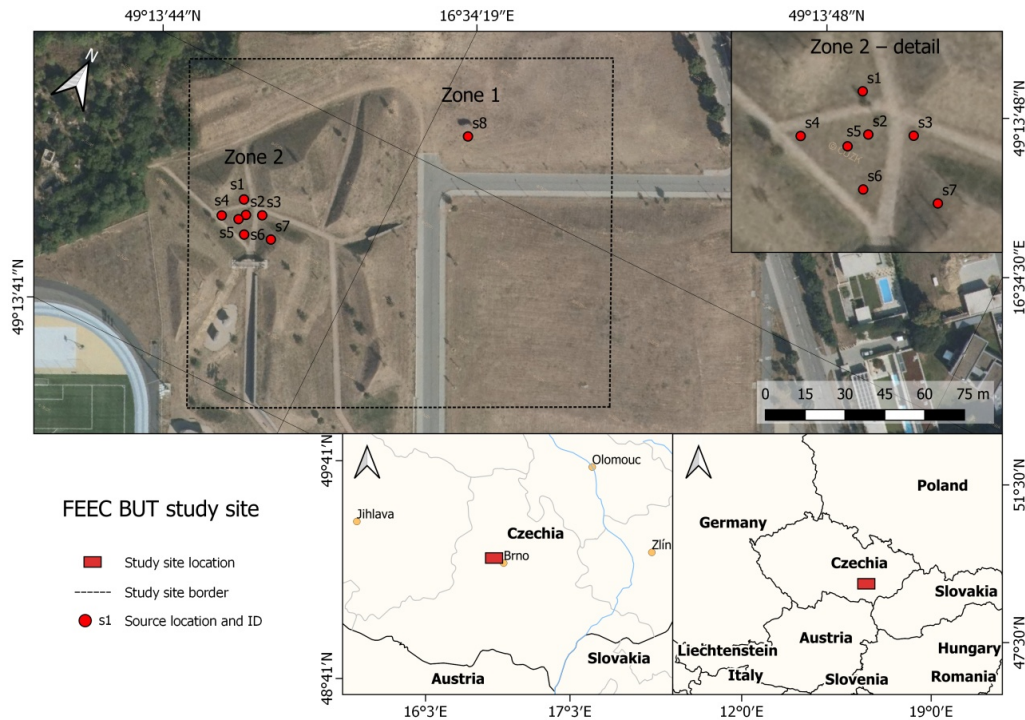
Figure C.11: The location of the study site, and the spatial distribution of the radiation sources (orthophoto courtesy of the State Administration of Land Surveying and Cadastre [64]. FEEC BUT: Faculty of Electrical Engineering and Communication at Brno University of Technology

2018 (Figure C.11). The goal was to arrange authentic conditions corresponding to a scenario with several gamma radiation sources lost in a certain area after a car accident. Regarding the parameters known to the tested method, the exact location, number, and activity were undefined; we can nevertheless assume that the sources belong to the class utilized in the civil sector, and the application options thus involve, for example, the calibration of devices for nondestructive testing, flow meters, level measurement systems, nuclear densometers, and density well-logging probes.

The experiment site occupies an area of 20,000 m^2, comprising mainly grassy terrain with various man-made objects such as a road, paths, climbing walls, and several vehicles involved in the car accident. While one half of the location is relatively flat ($< 4°$), the other includes hills with slopes up to 30° and other UGV-impassable zones.

Within the experiment site, we planted eight gamma radiation sources, namely, Co-60 and Cs-137 isotopes exhibiting the activity of 2.9–123.8 MBq (Table C.2). The strongest source can be considered category 4 (out of 5) according to the International Atomic Energy Agency's classification [65], i.e., a person is unlikely to be harmed unless directly exposed for many hours or standing close by for multiple

118

Table C.2: Radiation sources used in the experiment.

Source	Zone	Isotope	Activity [MBq]
s1	2	Co-60	2.85
s2	2	Cs-137	7.53
s3	2	Co-60	2.95
s4	2	Cs-137	7.53
s5	2	Cs-137	79.82
s6	2	Co-60	24.56
s7	2	Co-60	24.76
s8	1	Co-60	123.78

weeks. Other sources range within category 5, meaning that they are most probably not dangerous. However, possible delayed health effects are not taken into account. None of the sources is exempt, and all were handled by human operators. As is evident from Figure C.11, the sources are scattered inside two locations: Zone 1, containing a single, high-activity source, and zone 2, which includes seven sources representing the areal contamination. To ensure safety, the relevant area was closed to common access during the experiment.

C.4.2 Aerial Photogrammetry

The photogrammetry parameters, such as the image overlaps and ground resolution, were selected to yield high-resolution mapping products and to capture even the smallest details (Table C.3); the resulting trajectory is illustrated within Figure C.12. To assess the accuracy, six ground targets were deployed prior to the experiment, and their positions were acquired by a survey grade GNSS receiver (the position of the custom base station providing correction data to our robots was obtained in the same manner).

The data collected during the first, 10-minute UAS flight were processed immediately after landing; 124 relevant images from the total of 211 collected items were eventually utilized (one of the images is shown in Figure C.13a). The estimated camera location measurement accuracy (1σ spatial error) reported by the onboard GNSS-aided INS equals 0.74 m on the average and 5.3 m maximally. As is evident from Figure C.13b, a conspicuous accuracy decrease of to up to five meters occurred for a short time interval only; the reason rests in the GNSS' RTK fix solution outage caused by an insufficient quality of the signal necessary for the carrier-phase tracking.

Table C.3: The parameters of the flight trajectories and data acquisition for both
flights (one enabling the photogrammetry and the other facilitating the
radiation mapping). ATOP: above take-off point.

| Parameter	1st flight	2nd flight
Number of strips	6	14
Strip length	160 m	140 m
Distance between strips (n)	26 m	10 m
Flying altitude (h)	60 m ATOP	15 m AGL
Flying speed (v)	5 m/s	2 m/s
Sampling period (p)	2 s	1 s
Base (b)	10 m	2 m
Image forward overlap	92 %	—
Image side overlap	84 %	—
Image footprint	190 × 125 m	—
Image ground resolution	3.1 cm/px	—
Camera shutter speed	1/1,000 s	—
Camera aperture	5.6	—
Camera ISO	Auto (100–400)	—
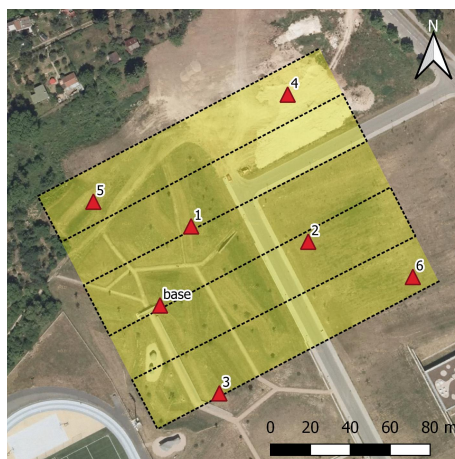
Figure C.12: The UAS trajectory planned for the photogrammetry flight. The yel-
low rectangle represents the study site (having an area of 20,000 m^2),
and the red triangles indicate the positions of the ground targets.

(a)   (b)
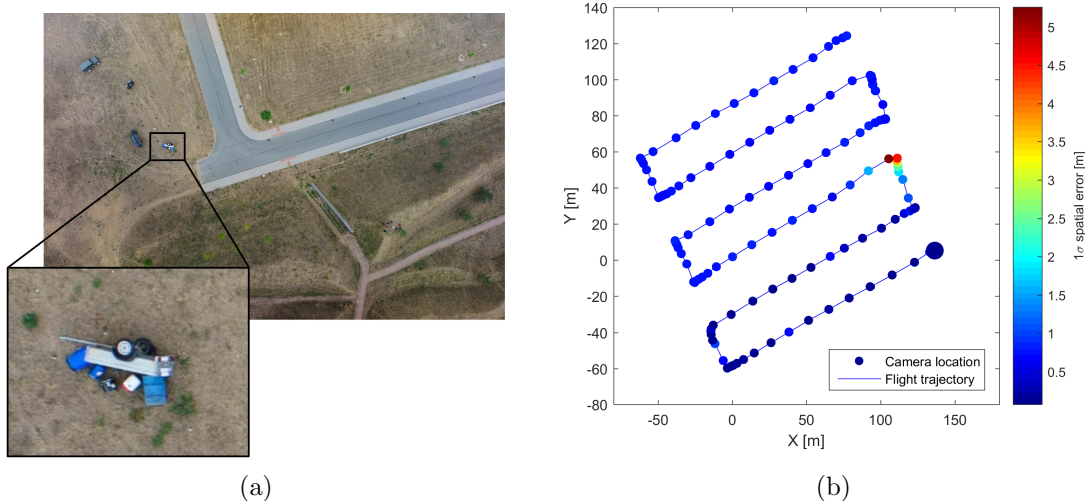
Figure C.13: A sample image captured at 60 m AGL during the initial flight. The detail shows the car accident simulated in zone 2 (a). The flight trajectory and the INS spatial error estimation at the camera locations, with the starting point highlighted. The zero coordinates correspond to the position of the base station (b).

The dataset was processed in Photoscan at a low quality in order to reduce the processing time (approximately 45 minutes), yielding a point cloud containing $\sim$200 points/m^2 and producing a DEM and an orthophoto with the resolutions of 7.4 cm/pix and 1.9 cm/pix, respectively (Figures C.14a and C.14b). The georeferencing quality was assessed by utilizing the six ground targets; the procedure reported root mean square error (RMSE) values of 0.55, 0.34, and 1.13 m for the latitude, longitude, and altitude, respectively. Despite the fact that, due to the RTK outage, these accuracies do not correspond to the capabilities of the system as outlined in our previous studies, the levels should not affect the subsequent mapping phases: The UAS is intended to fly at a safe distance from the surface (15 m AGL) during the radiation mapping, and the UGV trajectory planning algorithm comprises a clearance around the obstacles to prevent collision caused by inaccuracies in the map or navigation. In this context, it is then important to stress that an operator must supervise the operation of both platforms to abort the process in cases of an imminent accident.

C.4.3 Aerial Radiation Mapping

The aerial radiation mapping parameters described in Section C.3.3 were chosen in view of the applied hardware and with the aim to obtain data having an approximate

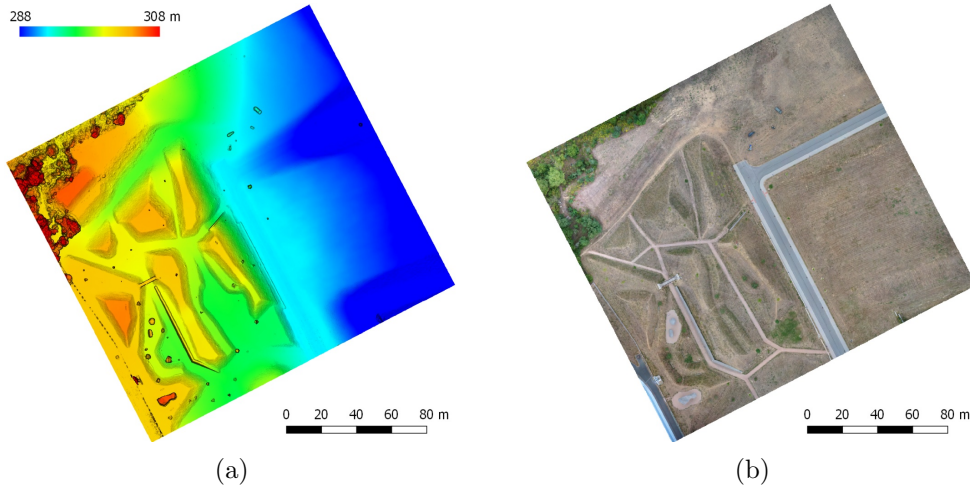Figure C.14: The UAS photogrammetry-based DEM (indicating the spectral color-scaled elevation and black-marked slopes) (a) and orthophoto (b).

spatial density of 10×10 m, a suitable value for the hotspot localization (the parameters are summarized in Table C.3). Note that these flight parameters correspond to the detector footprint size of approximately 770 m². The vertical components of the trajectory (Figure C.15) were computed employing Algorithm 1 with $s = 10$, resulting in 209 waypoints; the relevant points are represented in Figure C.16 (the red series). The upper part of the figure further displays the vertical coordinate of the actual GPS trajectory and the underlying terrain; the bottom graph shows the height above ground level. The presented data refer to the UAS flown at a relatively constant distance from the surface; at some moments, however, deviation from the desired value of 15 m is obvious. In this context, the rangefinder reports the height of 13.7 m RMSE, while the GPS-DEM derived value (GPS height minus surface height) is slightly higher, reaching 16.6 m RMSE. It should be noted that none of the sources is accurate enough for detailed assessment. The distance values measured by the rangefinder exhibit a high accuracy (usually in the order centimeters); however, the device measures incorrect data, namely, greater values, during tilting maneuvers. The GPS/DEM-derived data, by contrast, are independent from the UAS attitude; nevertheless, the typical accuracy of code-based GPS height measurement lies in the order of meters, and the low frequency error components may cause a non-negligible offset, considering a short time period. Despite these drawbacks, the presented data clearly indicate that the terrain-following method allowed us to collect radiation data at a relatively constant distance from the surface as compared to the common approach involving flying at a constant MSL height. The applied algorithm is further discussed in Section C.5.
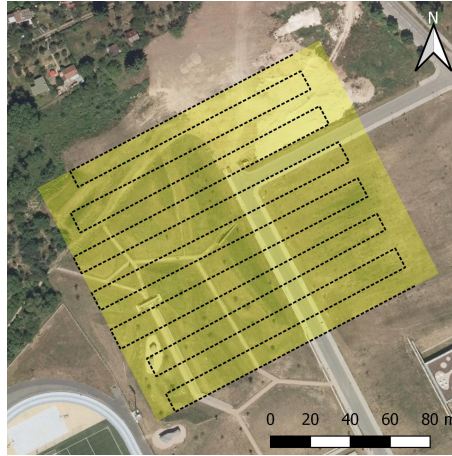
Figure C.15: The UAS trajectory planned for the radiation measurement flight (the yellow rectangle represents the study site).
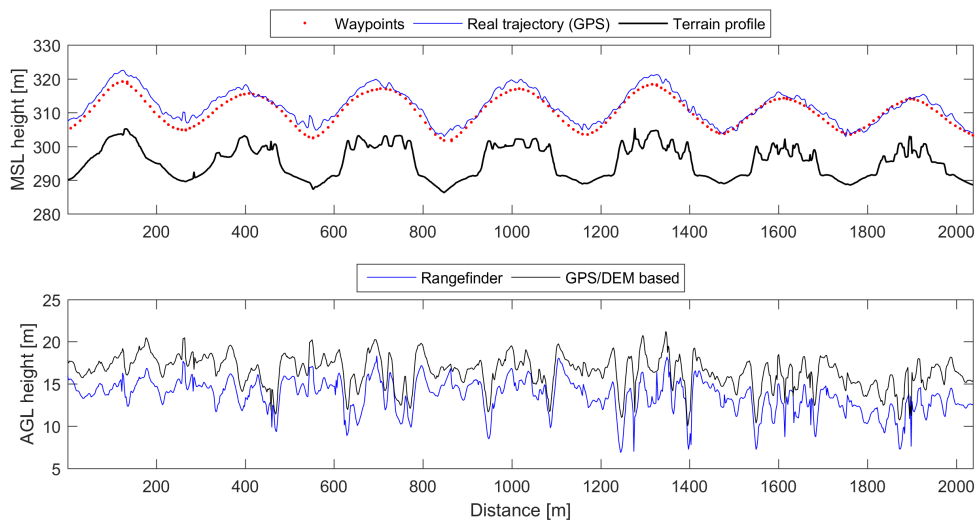
Figure C.16: The vertical profile of the UAS trajectory during the radiation-mapping phase, completed with the trajectory waypoints and underlying terrain (upper graph). The AGL flight height recorded by the rangefinger, represented together with the related GPS/DEM-based estimation (bottom graph).

The relevant portion of the collected radiation data comprises the minimum and maximum values of 0.042 and 0.207 µGy·h^{-1}, respectively, whereas the mean radiation background intensity approximately equals 0.07 µGy·h^{-1}. The scattered data, illustrated within Figure C.17a, indicate two areas with an increased radiation intensity; we can draw the same conclusion from the values interpolated to the 10 cm regular grid presented in Figure C.17b. To perform the interpolation, we downsampled the original data to achieve a comparable data density in both axes. The dataset contains, in addition to the dose rate values, also raw data allowing
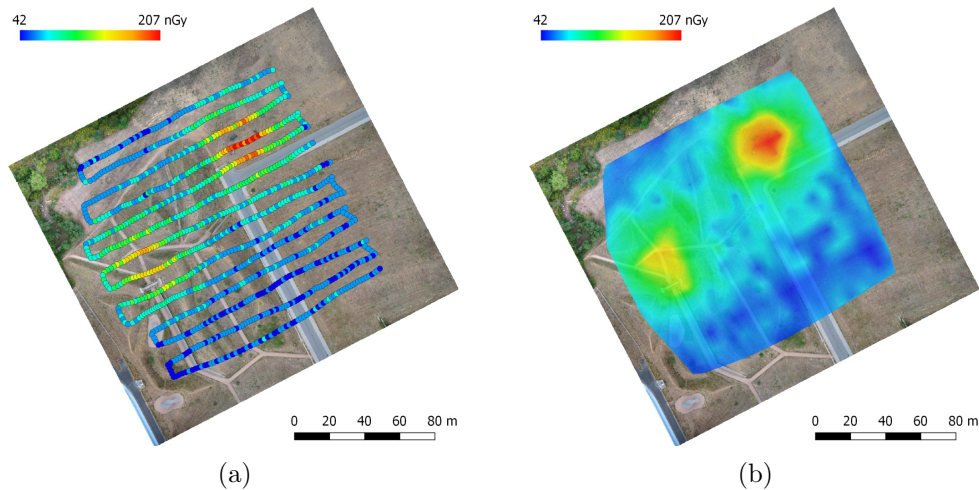
Figure C.17: The dose rates obtained during the UAS-based radiation mapping procedure (a); the acquired data were downsampled and interpolated for the subsequent processing (b).

spectral analysis and radionuclide identification; this step, however, is not necessary for hotspot localization and was thus not performed during the experiment. The spectral analysis potential is outlined in Section C.5.

C.4.4 Areas Selected for the Terrestrial Mapping

The interpolated radiation map has been subjected to the ROI selection algorithm. First, the background threshold was computed automatically, equaling $0.090\ \mu Gy \cdot h^{-1}$; such a result is in good accordance with the actual background intensity, which reached up to about $0.095\ \mu Gy \cdot h^{-1}$. Subsequently, the script was able to determine the hotspot separation threshold, attaining $0.103\ \mu Gy \cdot h^{-1}$. A 3D visualization of the thresholding process is shown in Figure C.18a. Note the small 'spikes' around the two major radiation intensity peaks, induced by the measurement noise. In order to eliminate these spikes and to smoothen the region's borders slightly, the imprint of the hotspots was morphologically eroded by a structuring element of a size corresponding to 3 meters. Finally, both of the remaining regions were roughly approximated by polygons with 7 vertices (Figure C.18b).

C.4.5 Terrestrial Radiation Mapping

The terrestrial radiation mapping is carried out by a UGV; thus, the actual procedure requires knowledge of inaccessible areas to enable proper path planning. In this concrete application, we do not need the obstacle map to have a resolution as high as that of the source DEM (74 mm), because the path planning is intended to

124
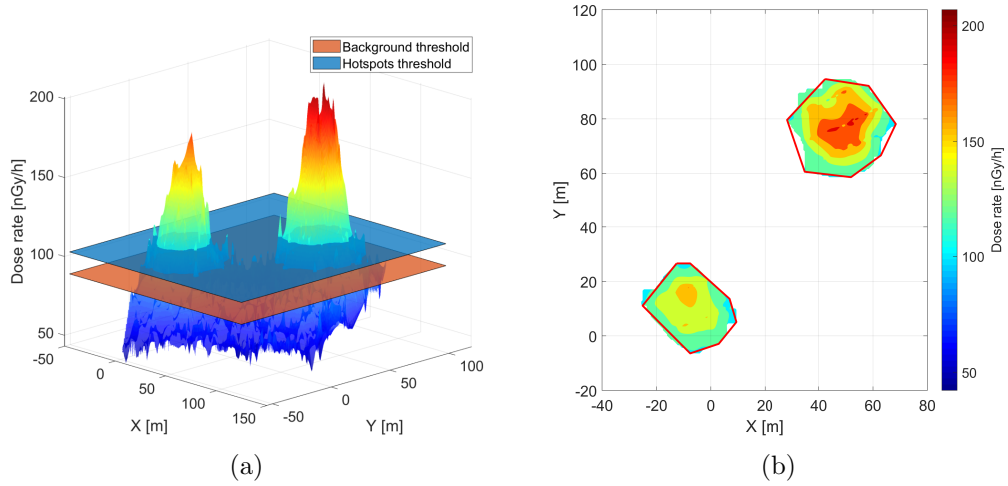
Figure C.18: The adaptive thresholding applied to the aerial radiation data (a), and polygonal approximation of the hotspots (b).

be performed at a resolution corresponding to the dimensions of the UGV, as suffices for outdoor environments; in this context, we can point out that larger pixels reduce the time of the subsequent processing operations. To deliver the planned mission, we selected the value of 0.518 m, namely, the integer multiple of the DEM pixel size which corresponds to the width of the UGV. The resulting obstacle maps (Figure C.19) computed for five different terrain limits show the terrain negotiability differences. When in the automatic navigation mode, our UGV can safely pass an outdoor terrain characterized by a gradient of 16 degrees or surmount obstacles having 0.16 m; if operated manually, however, the vehicle is capable of managing 20 degrees and 0.2 m. These values were obtained experimentally during previous missions. In certain conditions, the UGV may nevertheless be unable to negotiate areas that exhibit such parameters (e.g., when the terrain is sodden or comprises oily surfaces). The results described below are based on the obstacle map computed for the 0.16 m and 16 deg limits (the orange layer in Figure C.19).

Subsequently, the obstacle map is fused with the hotspot polygons. Prior to the processing by the automatic script, several additional obstacles, in particular a curb and plants that formed a new boundary limiting the southern side of the upper-right ROI (corresponding to zone 1), had to be defined manually. Moreover, two minor obstacles, namely, a small barrel and the remains of a tree, were added inside the lower-left ROI (zone 2). In Figure C.20a, these adjustments are marked in gray. The rough hotspot borders, modified in accordance with the obstacle map, form the 'envelopes' of the regions to be mapped and are visualized as the green polygons; the blue polygons inside the green ones then represent the 'holes' to be avoided. Note that the algorithm yielded two distinct subregions within the lower-left ROI;
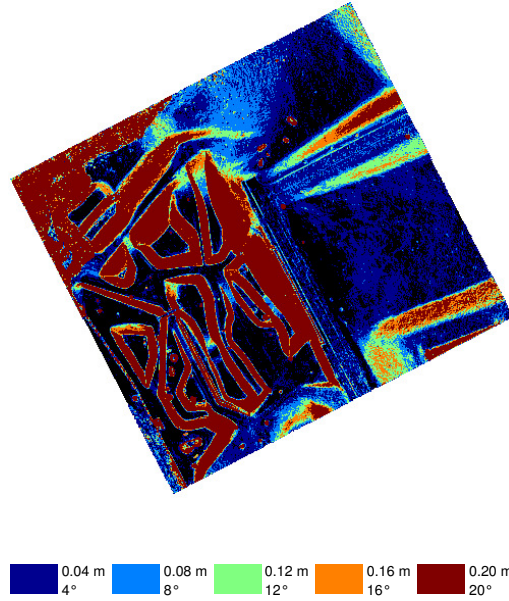
Figure C.19: The obstacle maps computed for the different UGV limits.

one of these areas, however, is inaccessible to the UGV (as can be proved via the path-planning algorithm) and will not be further examined within the article.

Both envelopes and their corresponding holes are passed to the algorithm responsible for the decomposition. Zone 1, whose area reached approximately 750 m^2, was divided into 13 cells, as shown in Figure C.21a. Note that the numerical labels of the cells refer to their indices assigned during the decomposition, i.e., the numbers correlate to the order in which the cells were initiated. The sweep line orientation was eventually chosen manually because the implementation had not been robust enough to handle an arbitrary case. In the trajectory planning, the first phase consists in selecting the initial point to start the survey; in our case, this step was performed manually. The resulting trajectory is plotted in Figure C.21b, and its theoretical length equals 448 m; note that this value applies only to holonomic robots without kinematic constraints.

The same procedure was utilized also in zone 2, where the Boustrophedon algorithm split the area of 250 m^2 into 10 distinct partitions (Figure C.22a). The complete trajectory has the length of 192 m and is shown in Figure C.22b.

The last path planning task interconnects the regions of interest and the zone most convenient for unloading the UGV. The operator selects suitable points to start the mission; we chose two spots (the green and pink circles in Figure C.20b) on the road at the edge of the mapped area, where the contamination level is within the safe limits. The start and end points of the planned trajectory inside the ROI are fixed and cannot be altered during this phase. Using the A* algorithm implemented in the project presented in [66], three paths were planned: from the unloading zone to a
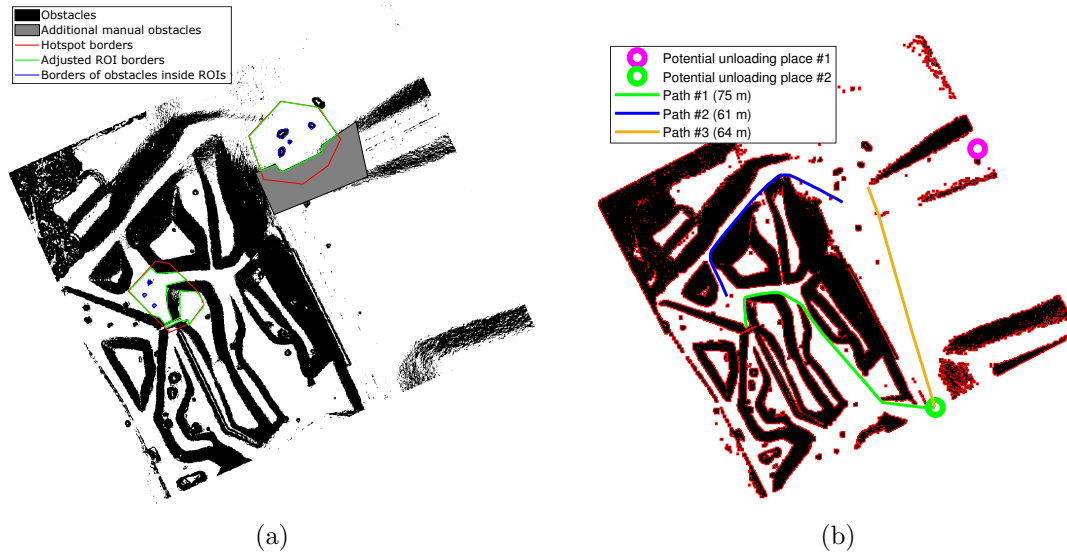
Figure C.20: The adjustment of the regions of interest via the obstacle map (a). The A* planned trajectories between the unloading zone and the regions of interest (b).
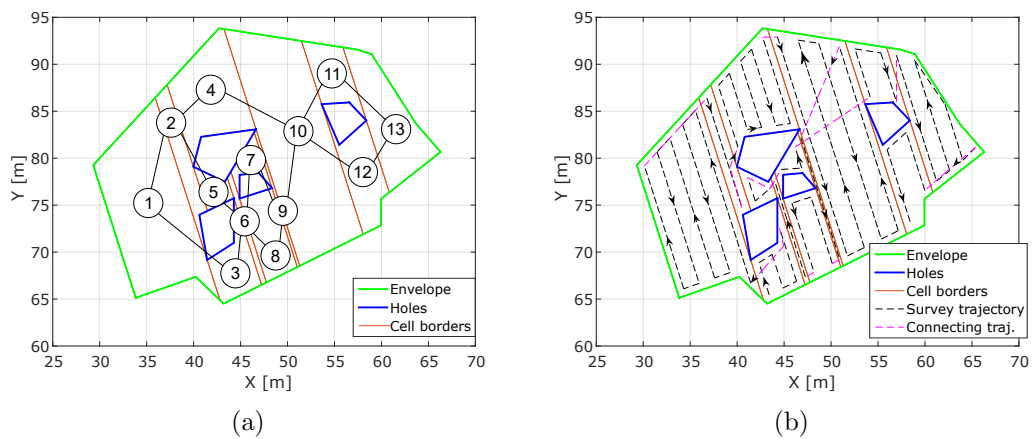
Figure C.21: The result of the Boustrophedon cell decomposition for the first ROI, complemented with a cell adjacency graph (a); the planned trajectory within the first ROI (b).

ROI, from this ROI to the next ROI, and from this last ROI back to the unloading zone. The sums of the path lengths are evaluated to select the lowest value. To reduce the UGV collision probability, all of the obstacles are expanded with an enclosing pixel (the red areas in Figure C.20b). The resulting shortest sequence of the three paths is shown in a modified obstacle map (Figure C.20b). The paths are 200 m long in total, and the UGV completed them in 6 minutes and 20 seconds (the speed varied from 0.4 to 0.6 m/s).
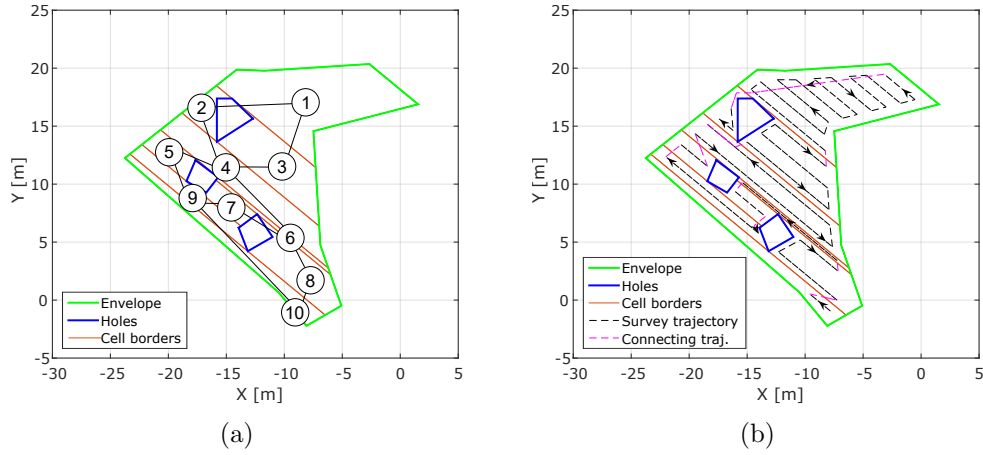
Figure C.22: The result of the Boustrophedon cell decomposition for the second ROI, complemented with a cell adjacency graph (a); the planned trajectory within the second ROI (b).

C.4.6 Radiation Data Processing and Source Localization

After completing the path planning phases, we employed the UGV to acquire the radiation data in both zones. The robot's minimal turning radius was set to 0.6 m; thus, the shape of the actual trajectory differed from that of the pre-generated one. With the maximal forward speed equaling 0.6 m/s (0.4 m/s while turning), the measurement took 15 minutes and 10 seconds in zone 1, while the time relevant to zone 2 was 7 minutes and 35 seconds.

The measurement outcomes for zone 1 are presented in Figure C.23a; the relevant path was 495 m long. Subsequently, the data were interpolated and the background removed (the background and hotspot threshold exhibited the values of 1645 CPS and 2124 CPS, respectively). As the zone included merely a single source, the thresholding left a sole peak, and the parameter matrix was initialized smoothly. The initial and the improved estimates, are indicated in Figure C.23b. The localization error equaled 0.123 m (Table C.4).

The situation was more problematic in zone 2, where we placed 7 sources in total. The individual data points captured are shown in Figure C.24a; the length of the actual trajectory corresponded to 221 m. Three sources, namely, radionuclides s1, s4, and s7, were located outside the surveyed area (discussed in Sec. C.5). The threshold levels for the background and the hotspots equaled 2707 CPS and 4684 CPS, respectively; note that the values are greater than those relating to zone 1, as the major portion of the data points lay in the vicinity of the sources. The adaptive thresholding yielded three distinct peaks, correspondingly to sources s3, s5, and s6; the last peak (s2, weak caesium 137) was overshadowed by the strong Cs-137 in its

Figure C.23: The individual data points measured along the planned trajectory; the points capture the total count in the first ROI (a). The interpolated radiation map highlighting the result of the source localization procedure (b).

close proximity. Consequently, only 3 out of the 7 sources were localized successfully, as is obvious from the detailed results in Table C.4. The average localization error in both of the zones (considering only sources whose parameters were found) equals 0.10 cm RMS.

To quantify the benefits of employing the UGV in more detailed measurement, the localization algorithm was also applied to the aerial data. The thresholding result remained the same as in the ROI selection (Figure C.18), yielding two source estimates. Clearly, the localization error in zone 2 cannot be computed, because the 7 sources present there appear as a single one in the aerial radiation map. However, we can compare the results obtained within zone 1, where the UAS localization error equals 1.28 m (Table C.4).

C.5 Discussion

Within the presented experiment, we introduced and successfully tested a multi-robot radiation mapping method consisting of numerous steps (the essential mapping outputs are summarized in Figure C.25). The entire operation lasted 24 hours; this continuous time interval comprised not only the necessary tasks, namely, the data gathering and processing, but also the site preparation and cleanup, safety-related steps, and activities not directly associated with the experiment. The time intensity of the operations relevant to the mapping and processing are summarized within the Gantt chart in Figure C.26. The individual items include the time spent on the automatic tasks (data processing, robot operation), operator interventions, and
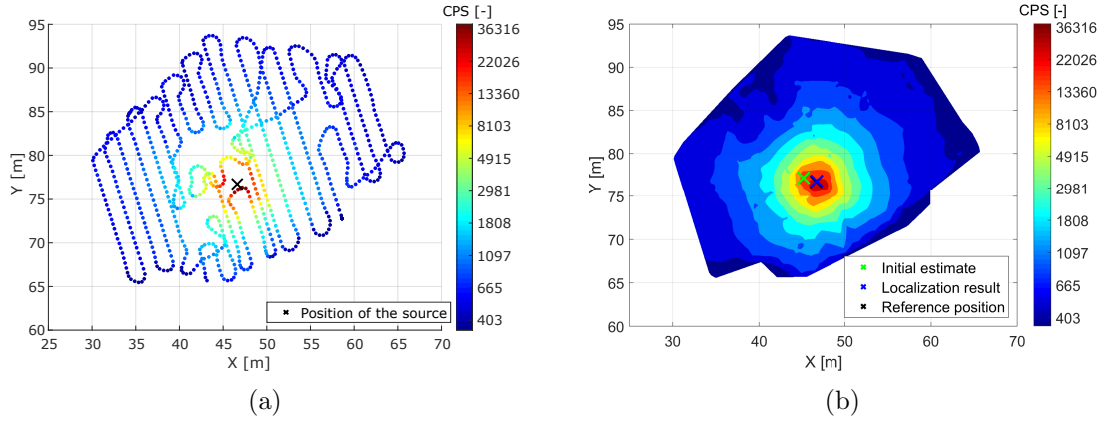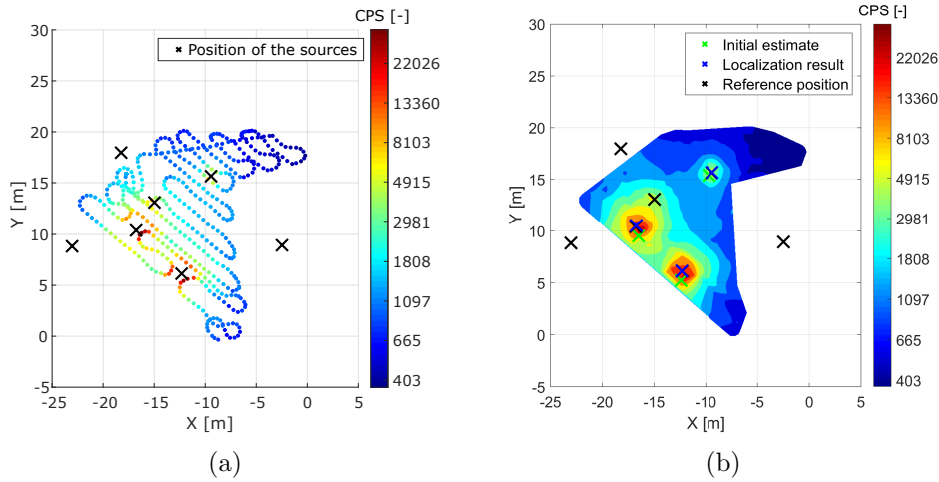
Figure C.24: The individual data points measured along the planned trajectory; the points capture the total count in the second ROI (a). The interpolated radiation map highlighting the result of the source localization procedure (b).

robot preparation and manipulation. The most time-intensive stages are the UGV operation and the photogrammetric processing. Theoretically, an ideal mission takes less than 4 hours; in reality, however, we had to face numerous minor issues that eventually prolonged the whole process, mainly as the mission marked the first time the systems were deployed together.

The UAS photogrammetry survey involved the use of our custom-built multi-sensor system and was carried out repeatedly; during the procedures, we thoroughly evaluated the achievable accuracy. Despite this, the attained values did not meet our expectations: As described in Section C.4.2, the RMS object error determined by using the six test points lay within the order of decimeters in the horizontal coordinates and rose slightly above a meter in the vertical one. According to our investigation and data analysis, all systems performed properly (including the RTK correction transmission); however, the signals on the GNSS receiver's antennas were rather weak, caused insufficient conditions for the carrier phase tracking during the entire flight. This problem resulted in RTK-fixed solution outages and made the INS exclude the GNSS data from the position and orientation estimates for a moment; the issue affected the beginning of the third survey line (Figure C.13b). Since the multi-sensor system was combined with the BRUS UAS for the first time, the problem may have been generated by interferences from the UAS's electronic systems; this assumption must nevertheless be verified through future experiments. Fortunately, the lower georeferencing quality did not manifest itself in the subsequent

Table C.4: The source localization results: N-q stands for non-quantifiable, as the UAS localization error for zone 2 cannot be expressed in the usual manner.

Source	Zone	Error UGV [m]	Error UAS [m]	Isotope	Activity [MBq]	Comment
s1	2	–		Co-60	2.85	Outside the ROI
s2	2	–		Cs-137	7.53	–
s3	2	0.067		Co-60	2.95	–
s4	2	–	N-q	Cs-137	7.53	Outside the ROI
s5	2	0.138		Cs-137	79.82	–
s6	2	0.018		Co-60	24.56	–
s7	2	–		Co-60	24.76	Inaccessible to the UGV
s8	1	0.123	1.28	Co-60	123.78	–

phases, and we still consider direct georeferencing crucial with respect to radiation-related missions.

Aerial radiation mapping proved to be a very effective tool for hotspot localization. The innovative approach involving flying at a constant AGL height regardless of the surface character allowed us to collect homogeneous data. Outside this scenario, the distance separating the ground and the detector would vary between 15 and 30 meters in a flight 15 meters above the highest location (at a fixed MSL altitude); such a diversity would certainly mean inconsistent data, and lower-positioned hotspots would be localized inaccurately or not at all. However, the DEM-based trajectory adjustment (Algorithm 1) needs to be improved in several aspects, of which the two most prominent ones are as follows: First, the method does not deliver the desired distance from the surface at high gradient locations, as it modifies the vertical coordinates of the waypoints only; another reason for the deficiency rests in the smoothing technique, which, while suppressing sudden height variations contained in the trajectory, further slows down the response to rapid slope changes. These effects are illustrated in Figure C.16, where the negative and positive peaks in the bottom part almost exclusively relate to the sudden gradient alterations. Second, the algorithm would perform better if it considered UAS vertical speed limits.

Based on the UAS-collected data, two regions of interests were automatically defined; this action reduced the original area of 20,000 square meters, to less than 10 %, with only 1,500 m^2 left for the terrestrial mapping. Nonetheless, the system can be scaled to a larger area by dividing the surveys into multiple UAS flights. As
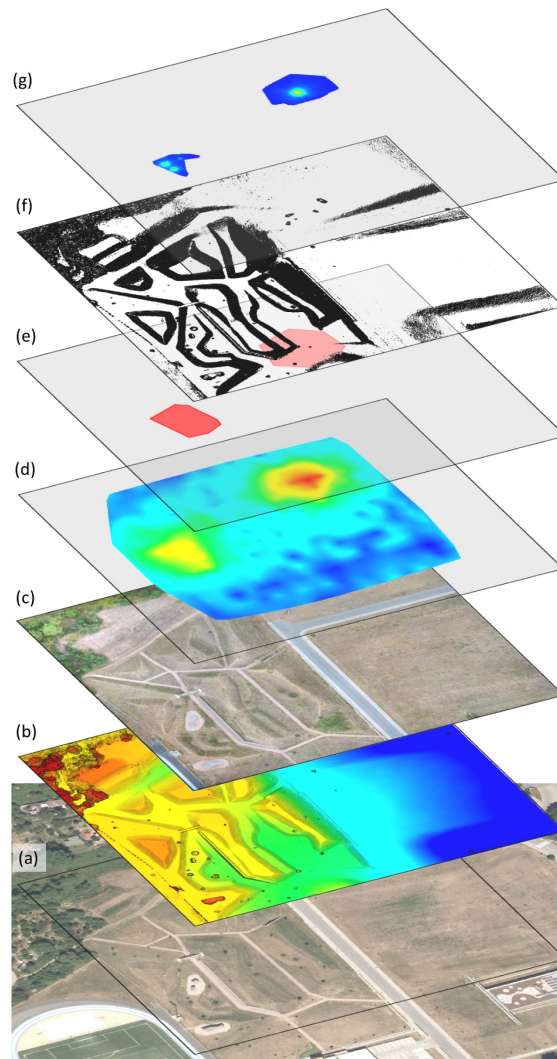
Figure C.25: The most significant map layers assembled during the mapping and processing. The layers are arranged according to their times of origin, from the bottom upwards: the primary orthophoto (a); the UAS-based, shaded DEM (b); the UAS-made orthophoto (c); the UAS-delivered radiation map (d); the detected regions of interest (e); the DEM-based UGV traversability map (f); and the UGV-made radiation map (g).

stated in the introduction, the largest region reasonably explorable via the described methodology has the size of 500×500 m. Assuming the flight parameters employed within our research, the image and radiation data acquisition missions would take two and nine flights, respectively; this scenario can be regarded as acceptable for the given purpose. By extension, the reconnaissance of such a large area probably does not require an equal spatial resolution of the measurements, meaning that the necessary number of flights can theoretically be reduced. Surveying significantly
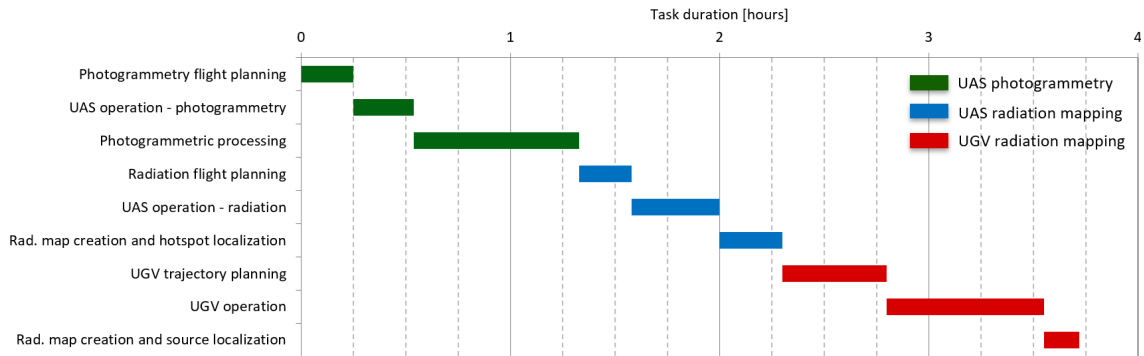
Figure C.26: The approximate times of the individual tasks during the experiment (considering an ideal case, i.e., a scenario when no issues or other activities prolong the operation; in reality, the experiment was carried out within 24 hours).

vaster regions, however, already requires helicopter-based systems to narrow down the search space.

Using only a DEM to select regions inaccessible to UGVs within the mapped area cannot yield 100% reliable outputs. Deformable objects (such as blades of grass and light bushes) satisfy the definition of an obstacle in terms of the height and gradient, despite being effectively bypassable by a UGV; moreover, such objects cannot be separated from non-deformable obstacles, because in a DEM they are represented by the same data. Although the decision-making can utilize an orthophoto (automatically or manually), this approach produces only probable bypassability, which does not constitute a reliable option. Other issues arise from the actual capabilities of a DEM, one of the main limitations being that some free spaces, such as those under bridges, are not covered by the model. If no safe path for a UGV is found, we can follow that with the highest passability rate, albeit exclusively in the operator-assisted mode.

For many reasons, autonomous UGVs designed to participate in diverse missions require real-time obstacle avoidance. In view of this parameter, the DEM-based method is markedly limited in that the model captures only the situation existing at the time the source data were acquired, and thus the technique's applicability remains solely within the representation of fixed obstacles, including hills and mountains. Another set of incorrectly evaluated obstacles comprises objects undetected due to inaccuracies stemming from either the low resolution (e.g., in thin items such as columns and fences) provided by a DEM or poor object texture (e.g., the light being outside the usable sensor range). Such collisions can be prevented by a real-time obstacle avoidance system installed on board the UGV. In the context of our mission, it is important to emphasize that objects inside the mapped area are very

likely to occur or change unexpectedly, and this type of system would significantly increase the efficiency of the entire reconnaissance process. However, operator supervision may still be applicable (and even irreplaceable in certain critical missions) thanks to its overall safety and reliability.

Considering the requirement for short overall mission time, an adequate DEM resolution has to be selected. For this purpose, we tested higher resolutions (up to 16x) to determine that while they did not improve the resulting obstacle map, the processing time and noise level increased significantly. Based on the attempts to fine-tune the whole task, we may conclude that computing a DEM with resolutions above 5 cm/pix does not bring any substantial benefits. Regarding the UAS path planning for the second flight, which also embodies the second task employing a DEM, it is possible to point out the lower sensitivity to DEM accuracy, an aspect that enables us to achieve satisfactory results even at values below 5 cm/pixel.

In terms of planning the path for the UGV, it seems beneficial to optimize the procedure, as the terrestrial survey has shown to be one the most time-consuming stages of the whole mission. The robot must markedly reduce its speed while turning, and therefore optimizing the number of turns could yield more convenient trajectories. A possible approach is presented in paper [67], the basic idea being that the sweep direction does not have to remain the same in all of the cells but should exploit the angle of the long axis of each polygon instead. Another suggestion relies on connecting the subregions in a manner which reduces the length of the traversals. Finally, the decomposition process itself can be optimized to achieve a minimum sum of cell widths. Still other enhancement concepts are outlined in article [68]; these, however, focus on aerial assets. In the case of terrestrial path planning, we cannot employ convex hulls of polygons, because otherwise obstacle avoidance could not be assured; moreover, taking the wind direction into account is not necessary.

Although all of the algorithms worked only with either the dose rate or the raw total count during the entire source localization procedure, the use of spectrometric detectors in the experiment enabled further processing of the acquired data. Figure C.27 shows the sample spectrum integrated over the period of 10 s along the trajectory between the distinct radionuclides. The graph visualizes three photopeaks, which essentially embody the 'fingerprints' of the incident photons, namely, the photons' energy that is unique for each radioactive element. The net counts in the energy windows are proportional to the contribution of the relevant isotopes towards the overall measured intensity; note that the width of a window depends on the energy resolution of the detector, usually expressed by full width at half maximum (FWHM). To compute the net value, it is necessary to subtract the average background level and also the counts yielded through the impact of the higher-energy photons (in our experiment, the cobalt 60 affects the caesium 137 window
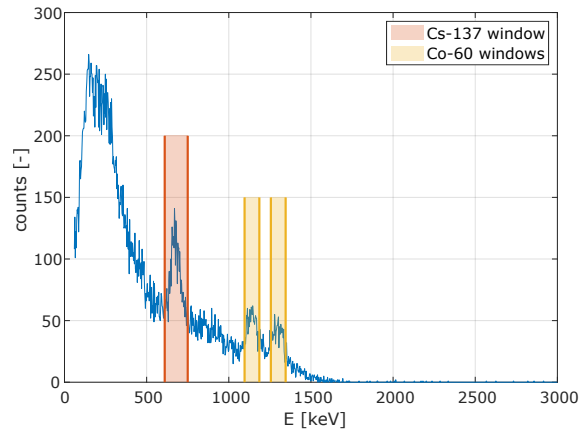
Figure C.27: A radiation spectrum measured by the UGV's on-board detector; the graph indicates the energy windows of the applied radionuclides.
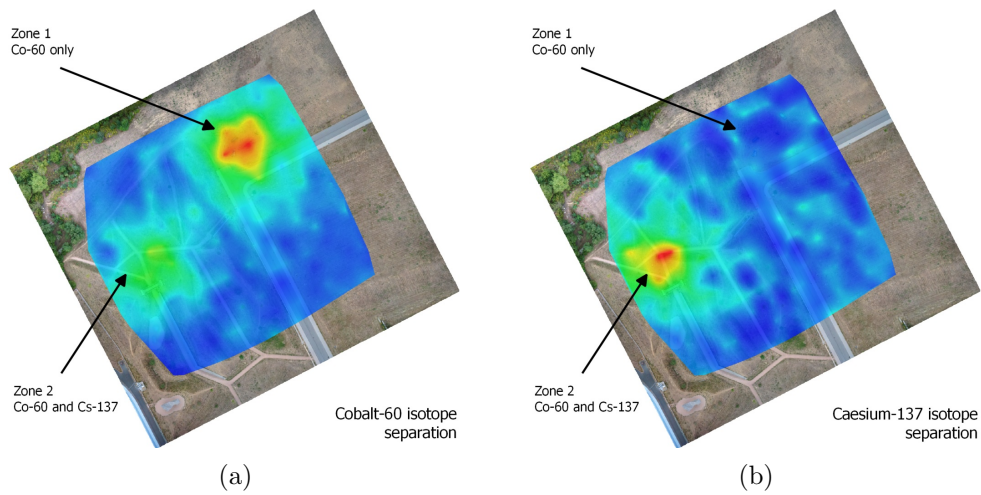
Figure C.28: The maps with separated radiation intensities for the cobalt 60 (a) and the caesium 137 (b).

via Compton scattering). The photons' influence can be quantified via the stripping coefficient, acquired from those measurements where the cobalt is present while the caesium is not; such a scenario was performed in area 1. As an example of the spectral isotope separation, maps relating to the two radionuclides are presented in Figure C.28; the images clearly show that Cs-137 sources were located in only one of the hotspots. This step was not vital for the localization of the sources via our method and was therefore supplied additionally. In a practical scenario, the maps with separated isotopes could be utilized by relevant authorities.

Another one of the procedures and outcomes executed or obtained at a later time is the estimation of the source strength and activity. These properties were estimated solely with the aerial data because the spectra measured by the terrestrial

robot had been corrupted due to an HW malfunction and could not be converted to dose rate values in a proper manner; regrettably, the problem was discovered only during the post-processing phase, when the measurements could not be repeated. For the estimation, curve fitting was utilized to find the coefficients a, b, c of the following mathematical function:

$$\dot{D} = f(d) = \frac{a}{d^2 + b^2} + c, \qquad (C.6)$$

which expresses the dependence of the measured dose rate $\dot{D}$ on the horizontal distance d from the source. The sought parameters are the dose rate at the distance of one meter (a), the vertical distance from the source (b), and the background dose rate (c). Theoretically, the measured altitude could be used instead of the second coefficient; however, the accuracy of the relevant value is not sufficient to enable a decent fit. Note that d denotes the distance from the estimated position provided by the localization algorithm. The results of the fitting for both regions of interest are introduced in Figure C.29; each zone was delimited by the radius of 35 m around the estimated source position. Although the fit error in zone 2 (where multiple radionuclides were present) is somewhat greater than that in the single-source case (zone 1), it is actually impossible to determine the number of sources from the aerial data only.

Given the curve parameters, in particular the dose rate at one meter, $\dot{D}_1$ (nGy·h^{-1}), and assuming a single source whose isotope is known, we can evaluate the activity of the source. The computation is rather straightforward and exploits the relationship between the activity, generated dose rate, and exposure rate constant, which is radionuclide-specific [69]. In zone 1, the estimated activity in Co-60 (note that the isotope can be identified from the spectra by its characteristic photopeaks) equals 105.0 MBq; the error reaches -15.2 % with respect to the reference value of 123.8 MBq. In aerial radiation mapping, such a result is comparatively accurate.

The experiment indicated that both aerial and terrestrial radiation mapping procedures involve specific drawbacks, as follows: The information density of the data acquired by the UAS suffices for localizing a single isolated source (s8), providing a result that could be accurate enough in practice; however, given the coarse aerial radiation map, it is virtually impossible to distinguish between a strong source, multiple radionuclides, and non-point areal contamination, as demonstrated in zone 2. By contrast, the UGV-based measurements characterized the actual radiological situation in a better manner, yet still not precisely enough; the reason lay in that the hypothetical 'center of radiation' (an analogy to a center of mass) in zone 2 was shifted towards the east by the relatively strong source s7, causing the weak radionuclides to be left outside the region of interest. In the future, this problem
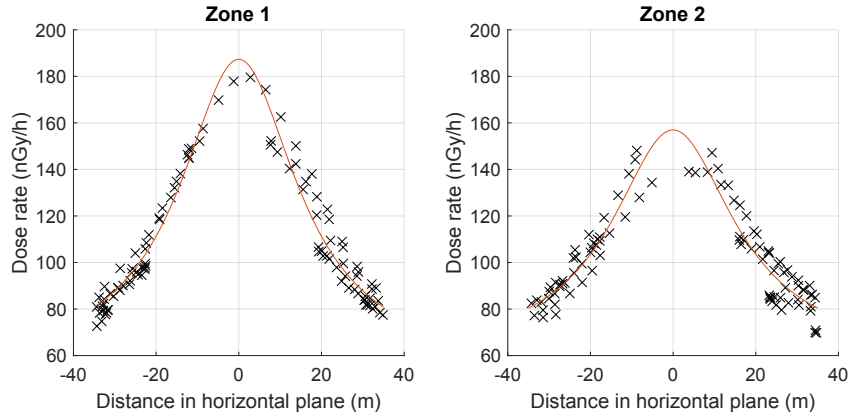
Figure C.29: The dependence of the dose rate measured by the UAS on the horizontal distance from the estimated position of a source. The data points are fitted with a curve in order to evaluate the source strength.

could be easily eliminated by enlarging the ROI prior to executing the UGV path planning phase. Although the radiation detection systems mounted on the UAS and the UGV were principally the same (the only exception being that the terrestrial robot carried two detectors instead of one), the resolution of a scan delivered by the UGV will always be superior to that obtained from the UAS, given the fundamental physics of the detection. As the aerial detector performs the measurements from an AGL altitude 30 times greater (0.5 m vs. 15 m) than the terrestrial one, it necessarily averages radiation from an area approximately 900 times larger. The ground platforms allow utilizing heavier systems, e.g., a collimated gamma camera; however, to apply such systems, we would have to alter the surveying strategy completely. The gamma camera requires a series of long stationary measurements from points elevated above the scanned area; based on our experience, we can assume that the localization process would be more time-consuming and less accurate if conducted via this technique. Obviously, a terrestrial robot is incapable of localizing sources positioned in a space classified as an obstacle (s7), and this deficiency, in general terms, requires further application of a UAS to explore such portions of the ROI that remain inaccessible to other robots. Using a UAS in this scenario nevertheless also invokes the question of safety, as the aerial vehicle needs to be brought closer to the terrain. Regarding the ground inspection, another disadvantage consisted in that the procedure failed to separate the overshadowed weak source (s2); however, performing a measurement detailed enough to localize this source would probably be more time-intensive than repeating the entire survey after other sources had been removed from the area. Yet, despite the difficulties, the UGV has proved to be a significant component of the system because it provides a more accurate overview of the radiological situation within the hotspots.

137

Contrary to our previously published research, we did not attempt to employ information driven localization, i.e., real-time UGV trajectory adaptation according to continuously acquired data. Instead, the goal was to compile a radiation map as precise as possible to cover also sources that are generally difficult to detect. With some prior information, such as that only one radionuclide is sought, we could utilize the partial directional sensitivity provided by the two-detector system to head towards the radiation source immediately after its presence has been indicated. To achieve this purpose, it would be necessary to assure obstacle avoidance, fusing the source direction estimation with the obstacle map via exploiting the potential field algorithm if feasible.

If we compare the results achieved within our research with those presented in articles focused on the same or similar topics, namely, [20] and [21], several key differences stand out. The former paper offers semantic classification of the surface type, providing useful information for navigating a terrestrial robot. Importantly, the applied UGV is equipped with an obstacle avoidance system that can be especially helpful in environments with dynamically occurring obstacles. By contrast, however, the authors do not utilize any sophisticated aerial data processing method to recognize multiple points of interest (POI) on the ground. The latter article introduces algorithms that exploit the measured spectra in selecting the POIs to perform information-driven localization of a single source; advantageously, the authors also compare multiple methods applicable for the given purpose. Considering the outcomes of these two research projects, we can stress that the novelty and benefit of our concept consist in other aspects, defined as follows: the terrain- following capability and directly georeferenced photogrammetry delivered by the UAS; automatic selection of the ROIs; and higher-accuracy, isotope-independent localization of multiple sources, performed with a UGV whose navigation and trajectory planning are fully autonomous (except for the necessity to validate the obstacle map by an operator). Finally, it is worth mentioning in the given context that the whole experiment was completed in a single day.

C.6 Conclusion

Using relevant experiments, this paper verified a concept of exploiting aerial and terrestrial robotic platforms to localize uncontrolled radiation sources in a previously unknown outdoor area. After completing the three phases of the designed survey process, we found four of the eight radionuclides (or three of the four significant ones); the achieved accuracy was below 0.2 m, a value sufficient to support subsequent steps such as the removal of the sources from the area. The experiment was implemented in 24 hours, including the elimination of various technical issues. The-

oretically, the area of 20,000 m^2 can be explored in only 4 hours, assuming conditions similar to those presented herein. To complete the entire task smoothly, however, the system would require further modifications. In this context, there remain major constraints as related to the weather, environment, radiological situation, and other relevant aspects: The systems must operate in adequate flight conditions, and satisfactory GNSS reception as well as the accessibility of a significant part of the area to the UGV need to be ensured. Moreover, the radiation intensities have to be well detectable yet not hazardous for the electronics. At this point, it is also vital to emphasize that the cooperation between aerial and terrestrial robots should be promoted because the same results cannot be achieved with one of the variants only; a UAS, for example, is incapable of ensuring either conclusive localization accuracy or differentiation between sources concentrated within an area of hundreds of square meters. By contrast, a UGV, if operated without the aerial data, has to explore the inspected area globally, and the lack of an obstacle map causes serious navigation problems, especially where the applied vehicle is not equipped with an evasion module. Our future research will be directed towards employing information-driven localization and fitting the UGV with an obstacle avoidance system.

Bibliography

[1] Ioannis Tsitsimpelis, C. James Taylor, Barry Lennox, and Malcolm J. Joyce. A review of ground-based robotic systems for the characterization of nuclear environments. *Progress in Nuclear Energy*, 111:109–124, March 2019. ISSN: 0149-1970. `doi:10.1016/j.pnucene.2018.10.023`.

[2] Kui Qian, Aiguo Song, Jiatong Bao, and Huatao Zhang. Small Teleoperated Robot for Nuclear Radiation and Chemical Leak Detection. *International Journal of Advanced Robotic Systems*, 9(3):70, 2012. ISSN: 1729-8814. `doi:10.5772/50720`.

[3] Roberto Guzman, Roman Navarro, Juan Ferre, and Miguel Moreno. RESCUER: Development of a Modular Chemical, Biological, Radiological, and Nuclear Robot for Intervention, Sampling, and Situation Awareness. *Journal of Field Robotics*, 33(7):931–945, 2016. ISSN: 1556-4967. `doi:10.1002/rob.21588`.

[4] Christian Ducros, Gerard Hauser, Najib Mahjoubi, Philippe Girones, Laurence Boisset, Antoine Sorin, Eric Jonquet, Jean Michel Falciola, and Albert Benhamou. RICA: A Tracked Robot for Sampling and Radiological Characterization in the Nuclear Field. *Journal of Field Robotics*, 34(3):583–599, 2017. ISSN: 1556-4967. `doi:10.1002/rob.21650`.

[5] Keiji Nagatani, Seiga Kiribayashi, Yoshito Okada, Kazuki Otake, Kazuya Yoshida, Satoshi Tadokoro, Takeshi Nishimura, Tomoaki Yoshida, Eiji Koyanagi, Mineo Fukushima, and Shinji Kawatsuma. Emergency response to the nuclear accident at the Fukushima Daiichi Nuclear Power Plants using mobile rescue robots. *Journal of Field Robotics*, 30(1):44–63, 2013. ISSN: 1556-4967. `doi:10.1002/rob.21439`.

[6] Frank E. Schneider and Dennis Wildermuth. An autonomous unmanned vehicle for CBRNE reconnaissance. In *2011 12th International Carpathian Control Conference (ICCC)*, pages 347–352, May 2011. `doi:10.1109/CarpathianCC.2011.5945877`.

[7] M. E. Hosmar, S. B. Nokleby, and E. Waller. Experimental Testing of an Autonomous Radiation Mapping Robot. In *2017 CCToMM M3 Symposium*, 2017. [cit. 2020-3-27]. URL: `http://www.cctomm.ca/2017/110.pdf`.

[8] Maozhen Wang, Xianchao Long, Peng Chang, and Taşkln Padlr. Autonomous Robot Navigation with Rich Information Mapping in Nuclear Storage Environments. In *2018 IEEE International Symposium on Safety, Security, and Rescue Robotics (SSRR)*, August 2018. ISSN: 2475-8426. `doi:10.1109/SSRR.2018.8468634`.

[9] Shin-ichi Okuyama, Tatsuo Torii, Akihiko Suzuki, Masanori Shibuya, and Nobuyuki Miyazaki. A Remote Radiation Monitoring System Using an Autonomous Unmanned Helicopter for Nuclear Emergencies. *Journal of Nuclear Science and Technology*, 45(sup5):414–416, June 2008. ISSN: 0022-3131. `doi:10.1080/00223131.2008.10875877`.

[10] Yukihisa Sanada and Tatsuo Torii. Aerial radiation monitoring around the Fukushima Dai-ichi nuclear power plant using an unmanned helicopter. *Journal of Environmental Radioactivity*, 139:294–299, January 2015. ISSN: 0265-931X. `doi:10.1016/j.jenvrad.2014.06.027`.

[11] Yukihisa Sanada, Tadashi Orita, and Tatsuo Torii. Temporal variation of dose rate distribution around the Fukushima Daiichi nuclear power station using unmanned helicopter. *Applied Radiation and Isotopes*, 118:308–316, December 2016. ISSN: 0969-8043. `doi:10.1016/j.apradiso.2016.09.008`.

[12] P. G. Martin, S. Kwong, N. T. Smith, Y. Yamashiki, O. D. Payton, F. S. Russell-Pavier, J. S. Fardoulis, D. A. Richards, and T. B. Scott. 3D unmanned aerial vehicle radiation mapping for assessing contaminant distribution and mobility. *International Journal of Applied Earth Observation and Geoinformation*, 52:12–19, October 2016. ISSN: 0303-2434. `doi:10.1016/j.jag.2016.05.007`.

[13] J. W. MacFarlane, O. D. Payton, A. C. Keatley, G. P. T. Scott, H. Pullin, R. A. Crane, M. Smilion, I. Popescu, V. Curlea, and T. B. Scott. Lightweight aerial vehicles for monitoring, assessment and mapping of radiation anomalies. *Journal of Environmental Radioactivity*, 136:127–130, October 2014. ISSN: 0265-931X. `doi:10.1016/j.jenvrad.2014.05.008`.

[14] D. T. Connor, P. G. Martin, N. T. Smith, L. Payne, C. Hutson, O. D. Payton, Y. Yamashiki, and T. B. Scott. Application of airborne photogrammetry for the visualisation and assessment of contamination migration arising from a Fukushima waste storage facility. *Environmental Pollution*, 234:610–619, March 2018. ISSN: 0269-7491. `doi:10.1016/j.envpol.2017.10.098`.

[15] Kai Vetter, Ross Barnowski, Joshua W. Cates, Andrew Haefner, Tenzing H. Y. Joshi, Ryan Pavlovsky, and Brian J. Quiter. Advances in Nuclear Radiation Sensing: Enabling 3-D Gamma-Ray Vision. *Sensors*, 19(11):2541, January 2019. `doi:10.3390/s19112541`.

[16] P. G. Martin, O. D. Payton, J. S. Fardoulis, D. A. Richards, and T. B. Scott. The use of unmanned aerial systems for the mapping of legacy uranium mines. *Journal of Environmental Radioactivity*, 143:135–140, May 2015. ISSN: 0265-931X. `doi:10.1016/j.jenvrad.2015.02.004`.

[17] Frank Mascarich, Taylor Wilson, Christos Papachristos, and Kostas Alexis. Radiation Source Localization in GPS-Denied Environments Using Aerial Robots. In *2018 IEEE International Conference on Robotics and Automation (ICRA)*, pages 6537–6544, 2018. ISSN: 2577-087X. `doi:10.1109/ICRA.2018.8460760`.

[18] Tomas Baca, Martin Jilek, Petr Manek, Petr Stibinger, Vladimir Linhart, Jan Jakubek, and Martin Saska. Timepix Radiation Detector for Autonomous Radiation Localization and Mapping by Micro Unmanned Vehicles. In *2019 IEEE/RSJ International Conference on Intelligent Robots and Systems (IROS)*, pages 1129–1136, November 2019. ISSN: 2153-0866. `doi:10.1109/IROS40897.2019.8968514`.

[19] Kevin Kochersberger, Kenneth Kroeger, Bryan Krawiec, Eric Brewer, and Thomas Weber. Post-disaster Remote Sensing and Sampling via an Autonomous Helicopter. *Journal of Field Robotics*, 31(4):510–521, 2014. ISSN: 1556-4967. `doi:10.1002/rob.21502`.

[20] Gordon Christie, Adam Shoemaker, Kevin Kochersberger, Pratap Tokekar, Lance McLean, and Alexander Leonessa. Radiation search operations using scene understanding with autonomous UAV and UGV. *Journal of Field Robotics*, 34(8):1450–1468, November 2017. ISSN: 1556-4959. `doi:10.1002/rob.21723`.

[21] John Peterson, Weilin Li, Brian Cesar-Tondreau, John Bird, Kevin Kochersberger, Wojciech Czaja, and Morgan McLean. Experiments in unmanned aerial vehicle/unmanned ground vehicle radiation search. *Journal of Field Robotics*, 36(4):818–845, 2019. ISSN: 1556-4967. `doi:10.1002/rob.21867`.

[22] E. Bai, K. Yosief, S. Dasgupta, and R. Mudumbai. The maximum likelihood estimate for radiation source localization: Initializing an iterative search. In *53rd IEEE Conference on Decision and Control*, pages 277–282, December 2014. `doi:10.1109/CDC.2014.7039394`.

[23] H. I. Lin and H. J. Tzeng. Searching a radiological source by a mobile robot. In *2015 International Conference on Fuzzy Theory and Its Applications (iFUZZY)*, November 2015. `doi:10.1109/iFUZZY.2015.7391884`.

[24] J. C. Chin, D. K. Y. Yau, and N. S. V. Rao. Efficient and Robust Localization of Multiple Radiation Sources in Complex Environments. In *2011 31st International Conference on Distributed Computing Systems*, pages 780–789, June 2011. `doi:10.1109/ICDCS.2011.94`.

[25] C. Liu, P. L. Drouin, G. St-Jean, M. Déziel, and D. Waller. Wireless Radiation Sensor Network with directional radiation detectors. In *2014 IEEE Nuclear Science Symposium and Medical Imaging Conference (NSS/MIC)*, November 2014. `doi:10.1109/NSSMIC.2014.7431111`.

[26] A. A. R. Newaz, S. Jeong, and N. Y. Chong. Fast radioactive hotspot localization using a UAV. In *2016 IEEE International Conference on Simulation, Modeling, and Programming for Autonomous Robots (SIMPAR)*, pages 9–15, December 2016. `doi:10.1109/SIMPAR.2016.7862348`.

[27] Jerry Towler, Bryan Krawiec, and Kevin Kochersberger. Radiation Mapping in Post-Disaster Environments Using an Autonomous Helicopter. *Remote Sensing*, 4(7):1995–2015, July 2012. `doi:10.3390/rs4071995`.

[28] N. Pinkam, S. Jeong, and N. Y. Chong. Exploration of a group of mobile robots for multiple radiation sources estimation. In *2016 IEEE International Symposium on Robotics and Intelligent Sensors (IRIS)*, pages 199–206, December 2016. `doi:10.1109/IRIS.2016.8066091`.

[29] A. Gunatilaka, B. Ristic, and R. Gailis. On Localisation of a Radiological Point Source. In *2007 Information, Decision and Control*, pages 236–241, 2007. `doi:10.1109/IDC.2007.374556`.

[30] M. R. Morelande and A. Skvortsov. Radiation field estimation using a Gaussian mixture. In *2009 12th International Conference on Information Fusion*, pages 2247–2254, July 2009. URL: `https://ieeexplore.ieee.org/abstract/document/5203720`.

[31] C. Mendis, A. Gunatilaka, B. Ristic, S. Karunasekera, and A. Skvortsov. Experimental verification of evolutionary estimation algorithms for radioactive source localisation. In *2009 International Conference on Intelligent Sensors, Sensor Networks and Information Processing (ISSNIP)*, pages 151–156, December 2009. `doi:10.1109/ISSNIP.2009.5416811`.

[32] A. Gunatilaka, B. Ristic, and M. Morelande. Experimental verification of algorithms for detection and estimation of radioactive sources. In *2010 13th International Conference on Information Fusion*, July 2010. `doi:10.1109/ICIF.2010.5711880`.

[33] Branko Ristic, Mark Morelande, and Ajith Gunatilaka. Information driven search for point sources of gamma radiation. *Signal Processing*, 90(4):1225–1239, April 2010. ISSN: 0165-1684. `doi:10.1016/j.sigpro.2009.10.006`.

[34] Sergio Zimmermann. Active microphonic noise cancellation in radiation detectors. *Nuclear Instruments and Methods in Physics Research Section A: Accelerators, Spectrometers, Detectors and Associated Equipment*, 729:404–409, November 2013. ISSN: 0168-9002. `doi:10.1016/j.nima.2013.06.060`.

[35] AMETEK ORTEC. IDM-200-V Interchangeable Detector Module, 2020. URL: `https://www.ortec-online.com/products/radiochemistry-health-physics-research-industrial/gamma-spectroscopy/all-in-one-spectrometers/idm-200-v`.

[36] I. M. G. Thompson, L. Botter-Jensen, S. Deme, F Pernicka, and J. C. Saez-Vergara. *Radiation protection 106 : technical recommendations on measurements of external environmental gamma radiation doses*. Office for Official Publication of the European Communities, Luxembourg, 1999. ISBN: 92-828-7811-2. URL: `https://ec.europa.eu/energy/sites/ener/files/documents/rp106.pdf`.

[37] F. Burian, L. Zalud, P. Kocmanova, T. Jilek, and L. Kopecny. Multi-robot system for disaster area exploration. In *WIT Transactions on Ecology and the Environment*, volume 184, pages 263–274, June 2014. `doi:10.2495/FRIAR140221`.

[38] Lukas Nejdl, Jiri Kudr, Branislav Ruttkay-Nedecky, Zbynek Heger, Lukas Zima, Ludek Zalud, Sona Krizkova, Vojtech Adam, Marketa Vaculovicova, and Rene Kizek. Remote-Controlled Robotic Platform for Electrochemical Determination of Water Contaminated by Heavy Metal Ions. *International Journal of Electrochemical Science*, 10(4):3635–3643, April 2015. ISSN: 1452-3981. `doi:10.1016/S1452-3981(23)06567-7`.

[39] Tomas Jilek. Radiation intensity mapping in outdoor environments using a mobile robot with RTK GNSS. In *International Conference on Military Technologies (ICMT) 2015*, pages 1–7, Brno, Czech Republic, 2015. IEEE. `doi:10.1109/MILTECHS.2015.7153755`.

[40] Petr Gabrlik, Anders la Cour-Harbo, Petra Kalvodova, Ludek Zalud, and Premysl Janata. Calibration and accuracy assessment in a direct georeferencing system for UAS photogrammetry. *International Journal of Remote Sensing*, 39(15-16):4931–4959, August 2018. ISSN: 0143-1161. `doi:10.1080/01431161.2018.1434331`.

[41] Petr Gabrlik and Tomas Lazna. Simulation of a Gamma Radiation Mapping Using Unmanned Aerial System. In *IFAC-PapersOnLine*, volume 51, pages 256–262, Amsterdam, May 2018. Elsevier. `doi:10.1016/j.ifacol.2018.07.163`.

[42] Tomas Lazna, Petr Gabrlik, Tomas Jilek, and Ludek Zalud. Cooperation between an unmanned aerial vehicle and an unmanned ground vehicle in highly accurate localization of gamma radiation hotspots. *International Journal of Advanced Robotic Systems*, 15(1), January 2018. ISSN: 1729-8814. `doi:10.1177/1729881417750787`.

[43] Karl Kraus. *Photogrammetry: Geometry from Images and Laser Scans*. Walter de Gruyter, 2007. ISBN: 978-3-11-019007-6.

[44] Taua M. Cabreira, Lisane B. Brisolara, and Paulo R. Ferreira Jr. Survey on Coverage Path Planning with Unmanned Aerial Vehicles. *Drones*, 3(1):4, March 2019. `doi:10.3390/drones3010004`.

[45] G. Verhoeven, M. Doneus, Ch. Briese, and F. Vermeulen. Mapping by matching: a computer vision-based approach to fast and accurate georeferencing of archaeological aerial photographs. *Journal of Archaeological Science*, 39(7):2060–2070, July 2012. `doi:10.1016/j.jas.2012.02.022`.

[46] Mozhdeh Shahbazi, Gunho Sohn, Jerome Theau, and Patrick Menard. Development and Evaluation of a UAV-Photogrammetry System for Precise 3d Environmental Modeling. *Sensors*, 15(11):27493–27524, November 2015. `doi:10.3390/s151127493`.

[47] H. Fazeli, F. Samadzadegan, and F. Dadrasjavan. Evaluating the Potential of RTK-UAV for Automatic Point Cloud Generation in 3d Rapid Mapping. In *ISPRS - International Archives of the Photogrammetry, Remote Sensing and Spatial Information Sciences*, volume XLI-B6, pages 221–226. Copernicus GmbH, June 2016. `doi:10.5194/isprs-archives-XLI-B6-221-2016`.

[48] James R. Curry, Richard J. Detry, Kristin L. Adair, and Thomas M. Weber. Improving the Quality and Spatial Resolution of Aerially-Collected Radiation Data using Spatially-Variant Deconvolution. In *Proceedings of the INMM 52nd Annual Meeting*, 2011. URL: `https://www.osti.gov/servlets/purl/1107744`.

[49] Isaac Amidror. Scattered data interpolation methods for electronic imaging systems: a survey. *Journal of Electronic Imaging*, 11(2):157–176, 2002. `doi:10.1117/1.1455013`.

[50] C. Maple. Geometric design and space planning using the marching squares and marching cube algorithms. In *2003 International Conference on Geometric Modeling and Graphics, 2003. Proceedings*, pages 90–95, July 2003. `doi:10.1109/GMAG.2003.1219671`.

[51] Jyh-Ming Lien. Covering Minkowski sum boundary using points with applications. *Computer Aided Geometric Design*, 25(8):652–666, November 2008. ISSN: 0167-8396. `doi:10.1016/j.cagd.2008.06.006`.

[52] P. E. Hart, N. J. Nilsson, and B. Raphael. A formal basis for the heuristic determination of minimum cost paths. *IEEE Transactions on Systems Science and Cybernetics*, 4(2):100–107, 1968. `doi:10.1109/TSSC.1968.300136`.

[53] Lifeng He, Yuyan Chao, Kenji Suzuki, and Kesheng Wu. Fast connected-component labeling. *Pattern Recognition*, 42(9):1977–1987, September 2009. ISSN: 0031-3203. `doi:10.1016/j.patcog.2008.10.013`.

[54] Howie Choset. Coverage of Known Spaces: The Boustrophedon Cellular Decomposition. *Autonomous Robots*, 9(3):247–253, December 2000. `doi:10.1023/A:1008958800904`.

[55] Han-Pang Huang and Shu-Yun Chung. Dynamic visibility graph for path planning. In *2004 IEEE/RSJ International Conference on Intelligent Robots and Systems (IROS) (IEEE Cat. No.04CH37566)*, volume 3, pages 2813–2818, September 2004. `doi:10.1109/IROS.2004.1389835`.

[56] Peter Deuflhard. Least Squares Problems: Gauss-Newton Methods. In *Newton Methods for Nonlinear Problems*, Springer Series in Computational Mathematics, pages 173–231. Springer, Berlin, Heidelberg, 2011. ISBN: 978-3-642-23899-4. `doi:10.1007/978-3-642-23899-4_4`.

[57] Petr Gabrlik, Premysl Janata, Ludek Zalud, and Josef Harcarik. Towards Automatic UAS-Based Snow-Field Monitoring for Microclimate Research. *Sensors*, 19(8):1945, January 2019. URL: `https://www.mdpi.com/1424-8220/19/8/1945`, `doi:10.3390/s19081945`.

[58] C. Eling, M. Wieland, C. Hess, L. Klingbeil, and H. Kuhlmann. Development and Evaluation of a UAV Based Mapping System for Remote Sensing and Surveying Applications. In *ISPRS - International Archives of the Photogrammetry, Remote Sensing and Spatial Information Sciences*, volume XL-1/W4, pages 233–239, August 2015. `doi:10.5194/isprsarchives-XL-1-W4-233-2015`.

[59] D. P. Bliakharskii, I. V. Florinsky, and T. N. Skrypitsyna. Modelling glacier topography in Antarctica using unmanned aerial survey: assessment of opportunities. *International Journal of Remote Sensing*, 40(7):2517–2541, April 2019. ISSN: 0143-1161. `doi:10.1080/01431161.2019.1584926`.

[60] Seyyed Meghdad Hasheminasab, Tian Zhou, and Ayman Habib. GNSS/INS-Assisted Structure from Motion Strategies for UAV-Based Imagery over Mechanized Agricultural Fields. *Remote Sensing*, 12(3):351, January 2020. `doi:10.3390/rs12030351`.

[61] T. Jilek. *Advanced Navigation in Heterogeneous Multi-robot Systems in Outdoor Environment*. PhD thesis, Brno University of Technology, Technicka 10, Brno, Czech Republic, 12 2015. URL: `https://dspace.vutbr.cz/handle/11012/51783`.

[62] Petra Kocmanova and Ludek Zalud. Effective Calibration and Evaluation of Multi-Camera Robotic Head. *International Journal of Advanced Computer Science and Applications*, 6, October 2015. `doi:10.14569/IJACSA.2015.061020`.

[63] Ludek Zalud, Lukas Kopecny, and Frantisek Burian. Orpheus Reconnissance Robots. In *2008 IEEE International Workshop on Safety, Security and Rescue Robotics*, pages 31–34, October 2008. ISSN: 2374-3247. `doi:10.1109/SSRR.2008.4745873`.

[64] CUZK. CUZK - Geoportal, 2010. [cit. 2017-3-15. URL: `http://geoportal.cuzk.cz`.

[65] IAEA. *Categorization of radioactive sources*. Number RS-G-1.9 in IAEA Safety Standards series. International Atomic Energy Agency, Vienna, 2005. ISBN: 92-0-103905-0.

[66] Einar S. Ueland, Roger Skjetne, and Andreas R. Dahl. Marine Autonomous Exploration Using a Lidar and SLAM. volume 6 of *International Conference on Offshore Mechanics and Arctic Engineering*, 6 2017. `doi:10.1115/OMAE2017-61880`.

[67] Yan Li, Hai Chen, Meng Joo Er, and Xinmin Wang. Coverage path planning for UAVs based on enhanced exact cellular decomposition method. *Mechatronics*, 21(5):876–885, August 2011. ISSN: 0957-4158. `doi:10.1016/j.mechatronics.2010.10.009`.

[68] Matthew Coombes, Tom Fletcher, Wen-Hua Chen, and Cunjia Liu. Decomposition-based mission planning for fixed-wing UAVs surveying in wind. *Journal of Field Robotics*, 37(3):440–465, 2020. ISSN: 1556-4967. `doi:10.1002/rob.21928`.

[69] Glenn F. Knoll. *Radiation Detection and Measurement.* John Wiley & Sons, Hoboken, New Jersey, 3rd edition edition, August 2010. ISBN: 978-0-470-13148-0.

D Unmanned Aircraft System-Based Radiological Mapping of Buildings

Outline

Bibliographic Information

Abstract

The article focuses on acquiring a 3D radiation map of a building via a two-phase survey performed with an unmanned aircraft system (UAS). First, a model of the studied building is created by means of photogrammetry. Then, radiation data are collected using a 2-inch NaI(Tl) detector in a regular grid at a distance of 2 m from all accessible surfaces of the building (i.e., the walls and the roof). The data are then georeferenced, filtered, projected to the building model, and interpolated to yield the detailed radiation map. A method to estimate the parameters of the radiation sources located inside is introduced and successfully tested, providing a localization

accuracy in the order of meters. This task is aimed to deliver the proof of concept for employing such a mapping technique within nuclear safeguards. The acquisition of the radiation data was performed via a manual flight to ensure an appropriate safety level; in this context, it should be noted that the autonomous flight mode still requires major improvements in terms of safety.

Author's Contribution

The author's key responsibilities were associated with the development of the methodology and radiation data processing; however, he also participated in designing the experiment and the field work. He wrote most of the sections *Radiation Theory*, *Processing Pipeline*, and *Results*, and markedly contributed to the *Introduction*, *Experimental Setup*, and *Conclusion* chapters. The author is also credited with finalizing the manuscript.

<div align="right">Author contribution: 40 %</div>

D.1 Introduction

The present-day society relies on nuclear technology significantly; therefore, the necessity to inspect and monitor radiation-related facilities remains a permanent factor. Tasks such as tracking illegal transportation and storage of radioactive nuclear material, searching for uncontrolled radioactive sources, securing detailed surveys of buildings and structures to detect possible contamination, and monitoring nuclear facilities (e.g., nuclear repositories) require accurate and up-to-date information on the area of interest. The traditional approaches rely on human-made measurements; such techniques may nevertheless be inefficient as regards the radiation safety and security, time requirements, and costs. Thus, the utilization of robotic platforms is becoming more frequent in this domain, as their overall availability increases. The majority of the research articles propose acquiring planar radiation maps; in some applications, however, it can be beneficial to have a 3D map of the structure being investigated. This type of map then represents the spatial distribution of the radiation intensity, covering multiple angles of view. Such scenarios comprise mainly buildings and other complex structures that exhibit a distinctive vertical profile. A 3D map can assist with identifying radiation hotspots not visible to an overhead monitoring vehicle due to various structural elements, properties, and configurations of the building. This article discusses radiological mapping that employs unmanned aircraft systems (UAS), multicopters in particular. These platforms, unlike terrestrial and other aerial robots, facilitate measuring data close to the examined buildings and at adjustable altitudes.

The efforts embodied in this article are centered on the following scenario: A building with at least two floors comprises one or more radioactive sources, placed either loosely or in a container. Let us assume that the radionuclides exhibit an activity and energy sufficient for them to be detectable from the outside. No other sources, except the radiation background, are present within a relevant distance from the structure under investigation. The building is also required to offer ample space around it to enable the operation of a UAS in the vicinity of the building's outer shell.

The actual survey involves two phases: First, a flight is conducted at a high altitude to ensure the 3D reconstruction of the relevant building via, for example, aerial photogrammetry or laser scanning. Second, a comprehensive flight is performed in a regular pattern around the building to acquire radiation data. Finally, all the data are processed to estimate the source locations and to produce a relevant 3D radiation map, i.e., a model with interpolated radiation data projected on its surface.

An overview of industry-related inspection tasks for which the application of the UAS technology can be beneficial is outlined in [1], radiological cases are covered

as well. The authors claim that UASs are capable of minimizing the survey time and the human resources; moreover, they also protect the operators by executing the hazardous tasks. The typical role of UASs in area radiation mapping is exposed in source [2]; this article describes radiation data processing in great detail. Another variant of the survey, also exploiting LiDAR readings to acquire a coarse elevation model of the explored area, can be found in [3]. The authors of [4] adopt a more conventional approach to aerial radiological monitoring, relying on a 3D model reconstruction of the studied area via photogrammetry. Two examples of data acquisition in a 3D space that are not strictly related to ionizing radiation are presented in sources [5], [6]; while the former analyzes the inspection of bridges, the latter covers an automated UAS-based assessment of buildings, thus being more relevant to our research. Radiation mapping inside buildings, utilizing SLAM based on a depth camera to reconstruct an environment map, is suggested in [7]. Article [8] describes a multiphase UAS inspection involving a LiDAR-based SLAM, identification of radiation hotspots, and characterization of radioactive sources. Applications relevant to international nuclear safeguards are provided in paper [9]. A radiological inspection of a collapsed building is discussed in article [10]; similarly to our case, the radiation data were collected at various height levels, enabling the localization of a source not stationed on the ground. Article [11] presents work that relates to our outcomes very closely, promoting a concept termed Scene-data fusion (SDF): The 3D model of a scene, obtained via LiDAR scanning and SLAM, is fused with radiation readings using the list-mode maximum-likelihood expectation-maximization (ML-EM) algorithm. Such an approach yields radiological maps with good relative localizations of the hotspots and can be scaled from small scenes and local objects up to large buildings.

This article builds on our previous work, as we already analyzed the radiological inspection of buildings; a simulation was carried out and characterized in [12]. In this context, we also partially utilize our results obtained via the co-deployment of a UAS and a terrestrial robot in a thorough examination of an area of interest [13].

D.2 Radiation Theory

Regarding radation, we consider only the gamma form because it is generated by most sources, either directly or as a by-product of various relevant interactions (e.g., those induced by neutron sources, nuclear material, and beta sources). Importantly, this type of high-energy electromagnetic radiation also exhibits a good penetrability.

A radioactive source is characterized by several parameters. These include, above all, an activity in Bq, which stands for the number of atom disintegration cycles per second. By extension, the emitted photons can have either one or multiple

energy levels (keV), and their average amount per disintegration cycle is stated as a ratio (%). The other parameters (besides activity) are defined by the type of radionuclide. Note that radioactive decay is a stochastic process and follows the Poisson distribution; all quantities describing it represent merely the mean, or the most probable cases.

The propagation of radiation in space is affected by the traveled distance and the materials passed through. The radiation intensity can be expressed as the flux of photons ($s^{-1} \cdot m^{-2}$); in practice, however, dosimetry quantities are utilized more frequently, involving either the dose rate ($Gy \cdot h^{-1}$) or the equivalent dose rate ($Sv \cdot h^{-1}$). The intensity is inversely proportional to the square of the distance. While traversing the mass, the radiation is exponentially attenuated at a rate determined by the linear attenuation coefficient μ (m^{-1}); its value depends on the material properties and the energy of the photons. When passing through N segments of multiple materials, the intensity decreases to

$$I = I_0 \frac{\exp\left(-\sum_{i=1}^{N} \mu_i d_i\right)}{\left(\sum_{i=1}^{N} d_i\right)^2} \tag{D.1}$$

where I_0 is the initial intensity. This equation, however, applies only to the ideal case of no scattering and secondary radiation in the material. In reality, such a scenario is not feasible but can be approximated in a narrow-beam geometry; conversely, in a broad-beam geometry, both scattered particles and secondary radiation reach the detector, affecting the measurement result. The geometry type is determined mostly by the mutual positioning of the source, detector, and shielding/obstacles in between. The aforementioned laws of propagation need to be considered in acquiring and interpreting radiation maps of buildings and other structures.

Both the origin and the detection of ionizing radiation comprise stochastic phenomena, which then significantly affect the detection sensitivity and energy resolution of the spectroscopic measurements (besides the number of incident photons, their energy is measured as well). The detection systems may suffer from dead time when overloaded by a high flux of photons; additionally, this undesirable effect reduces the reliability of the results acquired. However, it is possible to estimate and compensate for the dead time if digital signal processing is employed.

Finally, radiation background should be mentioned, as it introduces considerable noise into the measurements. The effect consists of two principal components, namely, terrestrial and cosmic radiation. While the former is produced by the radionuclides that are naturally present in the soil (in particular, uranium-238 and thorium-232 together with their decay products, but also potassium-40), the latter arises from stellar objects. The background does not have a constant intensity, due

to the randomness inherent in its generation, and its mean varies in time. The background embodies a severe issue when its magnitude is comparable with that of the radiation to be detected.

For more information on the principles of ionizing radiation, the reader is invited to consult the book [14].

D.3 Processing Pipeline

The proposed process of handling the measured data has three inputs and two outputs. Thus, the pipeline is entered by the radiation data (acquired by the detection system), positioning data, and building model (represented by a point cloud) to yield an interpolated radiation map projected on the model and an estimate of the sources' parameters. Both outputs are produced in two independent branches, even though they share the data pre-processing phase. The complete pipeline is illustrated in Fig. D.1; a description of the individual steps follows.
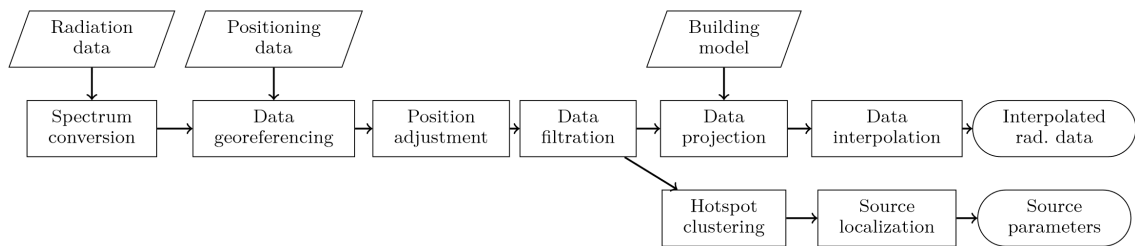
Figure D.1: The data processing pipeline with the individual steps (rectangles), input data (sloping rectangles), and outputs (rounded rectangles).

Converting the spectra

First, the raw radiation data are converted to dose rate values, which carry a clear physical meaning. Obviously, an inappropriate choice of the detection system can negatively influence the mapping results; let us therefore assume a spectrometric detector having a latency limited to the sampling period, i.e., all pulses are correctly registered during the period, with no further processing or averaging performed by the counting electronics. Commercial survey meters are usually unsuitable for our purposes. To perform the data conversion, we need to identify the relationship between the spectra (a histogram of the incident photon energies) and the dose rate for the applied detection system. This is achieved via calibration: the spectra are collected for not less than 5 minutes at diverse distances from the radioactive source (typically, Caesium-137); then, the total absorbed energy per second at each point is computed, and, finally, the dependence of the theoretical dose rate on the

absorbed energy is fitted with an appropriate curve, such as that described by a polynomial function [15]. Note that the background value, obtained from a separate measurement, must be included.

Data georeferencing

As the radiation data are to be interpreted spatially, together with the building model, georeferencing is of vital importance. In this context, utilizing a global navigation satellite system (GNSS) onboard the UAS embodies the most accessible and straightforward approach to the given task; the method, however, may comprise significant positioning errors in the vicinity of obstacles, due to a poor signal level and multipath errors. The accuracy and robustness can be increased by including in the position estimation process other sensors, such as a barometer and inertial sensors. Another technique for obtaining the absolute positions rests in tracking the flying UAS by means of a robotic total station; despite the excellent accuracy, however, the line-of-sight requirement is satisfiable only with substantial difficulty in applicable scenarios. Conversely, the radiation data may be georeferenced relatively to the building's facade by using a simultaneous localization and mapping (SLAM) algorithm. This approach not only delivers the positioning data but also creates the model, which, alternatively, is also assembled via aerial photogrammetry or laser scanning.

Position adjustment

Due to various inaccuracies in the data georeferencing, the whole dataset may include a translational error in the context of the building model. As the data are collected at approximately constant distances, it should be feasible to estimate the magnitude of such an offset and to eliminate the problem. The naive approach lies in aligning the centroids of the model and the radiation dataset; this option, however, may not yield a correct result when either the model or the dataset has a more complex shape. By contrast, exploiting point distances is potentionally functionable in a broader set of scenarios. The initial stage involves, above all, computing the mean distance between the measured points and the model; after that, the difference between the mean and the actual distances is minimized via the steepest descent algorithm by adjusting the translation of the datapoints in all three axes.

Data filtering

In order to achieve satisfactory interpolation results, it is beneficial to have similar datapoint densities in all axes. As the distance between the sampling points is usually significantly shorter than that in parallel survey line spacing, the dataset

is reduced prior to further processing. First, depending on the data noisiness, a moving mean is applied to the dose rate values of all the dataset components; then, each n subsequent points are fused into a single one. During the filtering, various data fluctuations are suppressed.

Data projection

Due to a lack of measurements inside the studied building, the aerial data must be projected onto the building's surfaces; otherwise, the interpolation algorithm would assume incorrectly that the radiation intensity on the surfaces is lower than at the locations of the measurements (which only applies if the intensity inside is zero). The selected projection method is rather straightforward: for each measurement, the closest point of the model is found and assigned the relevant dose rate value. This universal approach does not require any assumptions or prior knowledge. In terms of the accuracy, we can then claim, based on the description above, that the closer to the surface the measurements are taken, the more accurate the projection result is.

Data interpolation

Finally, the radiation data are interpolated to the outer shell of the building being investigated; the shell is represented by a point cloud delivered through, for example, the photogrammetry. The applied method is a natural neighbor interpolation based on the Delaunay triangulation [16]; this option exhibited the most accurate results in our previous research.

Hotspot clustering

The number of sources located in the building needs to be estimated prior to finding the sources' parameters. To execute this task, several algorithms are adopted. Step one rests in removing the points that likely do not form a part of the hotspots from the dataset. This is achieved by thresholding the dose rate values; the threshold is determined by the statistical parameters of the dataset, as shown in our previous work [13]. As a result, a subset of datapoints is yielded, forming clusters around the expected locations of the radiation sources. To split the clusters, a k-means algorithm [17] is employed; however, the number of the clusters is not known a priori. The parameter k is estimated by using the silhouette method [18], which computes a silhouette value for each possible k (range 1 to 10); the value specifies whether a point is similar to its own cluster or, rather than that, other clusters. The k with the greatest corresponding silhouette level is chosen. The suitability of

the output is furthermore validated via the elbow method [18]. The k value directly determines the estimated number of sources.

Source localization

The parameters of the sources, namely, their location in 3D and their intensity, are found with the iterative Gauss-Newton method in a manner analogous to our previous research [13]. As the initial position estimates, we utilize the centroids of the clusters. Regarding the sources' intensity, the maximum dose rate ten times multiplied is chosen in each cluster to constitute the initial estimate.

D.4 Experimental Setup

As already mentioned, a similar method for radiation data mapping on a building surface was previously studied and characterized within one of our papers [12]; however, the simulated radiation and positioning data exposed therein may not correspond to reality sufficiently to assess the algorithm in a thorough manner. For this reason, we conducted an experiment involving real radiation sources in a building, two UASs to collect the actual radiation data, and aerial imagery to perform the 3D reconstruction.

D.4.1 Study Site

The experiment took place at a fire rescue service training center, namely, a three-story brick building with a reinforced concrete skeleton, which proved suitable for assessing the method (Fig. D.2). The building has originally been designed as a storehouse, meaning that the individual floors are predominantly arranged as an open space including a minimum of inner walls (Fig. D.3). The building is approx-

Figure D.2: The building from the experiment (north-east view).

imately 37 m long, 28 m wide, and 11 m tall; the longer walls contain multiple windows, while the shorter ones have none.
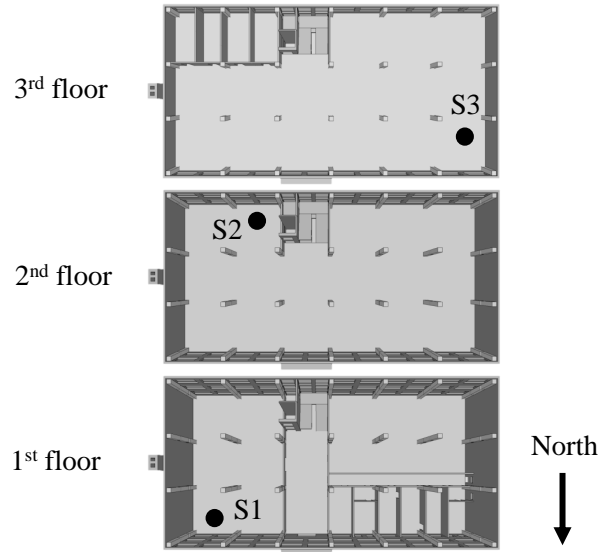
Figure D.3: The building floorplan indicating locations of the individual radiation sources (black points, see Table D.1).

The 3D model was obtained by means of aerial photogrammetry and indirect georeferencing [19]. At this stage, a DJI Mavic 2 multirotor UAS was employed to collect the aerial imagery from a height of 30 m, and a survey-grade GNSS allowed us to localize the 12 ground control points pre-distributed around the building. This reconstruction technique, assuming a similar mission setup, typically reaches a centimeter-to-decimeter georeferencing accuracy [20]. Although the accuracy was not evaluated via check points, and, in general, may vary locally due to numerous factors (such as the texture complexity or lighting conditions), the reconstruction method and the expected quality are entirely satisfactory for the intended purpose, namely, the model facilitates only visualizing the radiation data and has no impact on the source localization phase.

In the experiment, we used three different radiation sources, as summarized in Table D.1. The sources were placed on different floors, as far apart from one another as possible (Fig. D.3); this configuration allowed the radionuclides to be easily distinguished in the collected radiation data. Even the strongest source yields a dose rate of merely 1 mGy·h^{-1} in close proximity (if unshielded); to affect the UAS (the communication module and the GNSS receiver in particular), the intensity would have to be ten times greater.

Table D.1: The characteristics and locations of the radiation sources.

Source	Isotope	Activity	Shielding	Floor
S1	Cs-137	10.90 GBq	1" lead container	1st
S2	Cs-137	2.41 GBq	none	2nd
S3	Co-60	0.63 GBq	none	3rd

D.4.2 Radiation data acquisition system

To acquire the aerial radiation data, we utilized an off-the-shelf DJI M210 multirotor UAS (Fig. D.4); the vehicle provided a sufficient payload and flight time along with fair stability and controllability, enabling us to operate near obstacles in the manual control mode. The onboard radiation detection system (RDS) consisted of two components: a photomultiplier-based, $2'' \times 2''$-sized, NuDET NAI thallium-doped sodium iodide detector, and a multichannel analyzer exploiting a NuNA MCB. The former had a resolution of 7.5 % at 662 keV, and the latter ensured digital signal processing in 1,024 channels and was calibrated to an energy range from 50 keV to 3 MeV. The recommended sampling period of the RDS equaled 1 s. The radiation data georeferencing relied on the UAS's internal localization data, which had been supplied by the GNSS, barometer, inertial sensors, and other data sources. In addition, we collected the locations of the individual flights' take-off points via employing a survey-grade GNSS and shifted the recorded flight trajectories accordingly within the postprocessing stage. This step was expected to contribute towards suppressing potential long-term offsets, produced mostly by the low-accuracy onboard GNSS; thus, we possibly reached an increase in the relative accuracy of the georeferenced model and radiation measurements.

D.4.3 Data Acquisition Setup

The choice of the data acquisition parameters, namely, the spatial density, distance from the facade, and flight speed, directly influences the resulting radiation map in terms of its resolution, accuracy, and level of details. The mission setting, however, must also respect the UAS's limits, RDS parameters, and, if applicable, time constraints.

A straightforward mapping approach comprises flight lines parallel to the building facade and roof, assuming a constant spacing and distance from the structure. Considering the radiation propagation theory (section D.2), the distance should be as low as possible; otherwise, the informative impact of the measurements may degrade.

Figure D.4: The unmanned aircraft with a radiation detection system, and the live spectrum visualization.

By extension, when choosing the proper value for the given scenario, we should respect the UAS's limits and characteristics, wind speed, and pilot experience. The built-in obstacle avoidance system of the M210 UAS maintains a clearance of 3.5 m; however, taking into account all the conditions, we deactivated this feature to select a minimum safe clearance of 2 m for the mission.

The spatial density of the collected radiation data directly influences the level of details in the resultant radiation map; however, an excessively high density may lead to prolonged flight times. A straightforward mapping approach comprises flight lines parallel to the building facade and roof, with the density given by the line spacing and flight speed (at a constant sampling period). We consider 2 m line spacing, 0.5 m/s flight speed, and 1 s sampling rate the optimum values for the object being investigated; all of the parameters were verified by a mission specialist. The spatial resolution of airborne surveys was further studied in [21].

D.5 Results

The resulting dataset comprises 2,727 datapoints corresponding to a net flight time of approximately 45 minutes. Obviously, the actual flight was longer, due to factors such as stopovers and battery swaps.

The acquired spectra constituted an absorbed energy range from 30 to 3,800 MeV·s^{-1}. The radiation detection system was subsequently calibrated by using a Cs-137 source, yielding a relationship between the absorbed energy and the dose rate in the relevant range. The dependence was fitted with a quadratic function (Fig. D.5) to compensate for the deficiencies of the multichannel analyzer; all of the spectra were converted to dose rate values accordingly. Although we focus
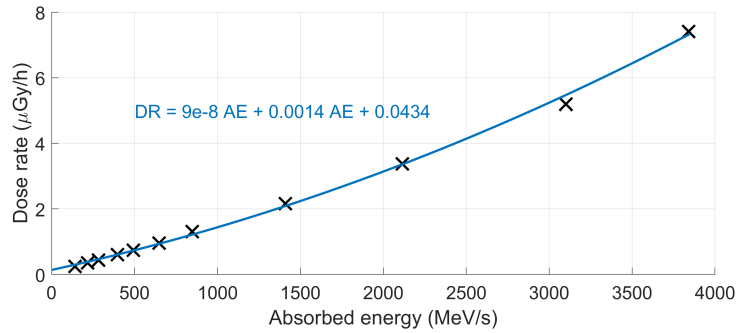
Figure D.5: The calibration of the detection system.

especially on relative mapping, not on measuring accurate dosimetry quantities, this step enables us to linearize the intensity values, resulting in improved localization of the sources. In view of the georeferencing, the data quality corresponds to our expectations: the horizontal accuracy, especially close to the ground, is strongly affected by the GNSS limitations, but the vertical components are fairly accurate thanks to the barometric data included.

The collected radiation data were shifted with respect to the model; thus, we applied the offset correction method, yielding the result $\boldsymbol{T} = (0.88, -1.58, -0.17)$ m in the x, y, and z axes, respectively. Such magnitudes, importantly, should not be neglected. The datapoints after position refinement are presented in Fig. D.6a. Their pre-processing was completed by fusing every three subsequent points, and the moving average had not been applied. The members of the reduced dataset were projected onto the building, exploiting the point cloud obtained via photogrammetry. Finally, the interpolation was carried out, producing a continuous layer on the building's shell. The resulting color-coded radiation map is shown in Fig. D.6b. This map exposes two interesting effects: First, several artefacts appeared, especially on the roof near the elevator shaft. The issue arises from the applied experimental setup and method, which caused several datapoints to be incorrectly projected on the shaft to induce a gap in the data on a portion of the roof. Second, the dependence of the radiation propagation on the building's structure and materials is clearly visible, including in particular the difference between the windows and the brick walls. The concrete columns between the windows are also distinguishable upon a closer look. The sources on the 1st and 2nd stories cannot be detected from above, due to the attenuation in the ceilings and floors; this outcome actually substantiates the need of 3D mapping (if there were no source in the 3rd story, no radiation anomaly would be detected by means of a conventional aerial survey). The density of the survey lines and the aircraft speed proved to be adequate in terms of the spatial resolution of the resulting map; the radiation distribution is captured in sufficient detail.

(a)

(b)
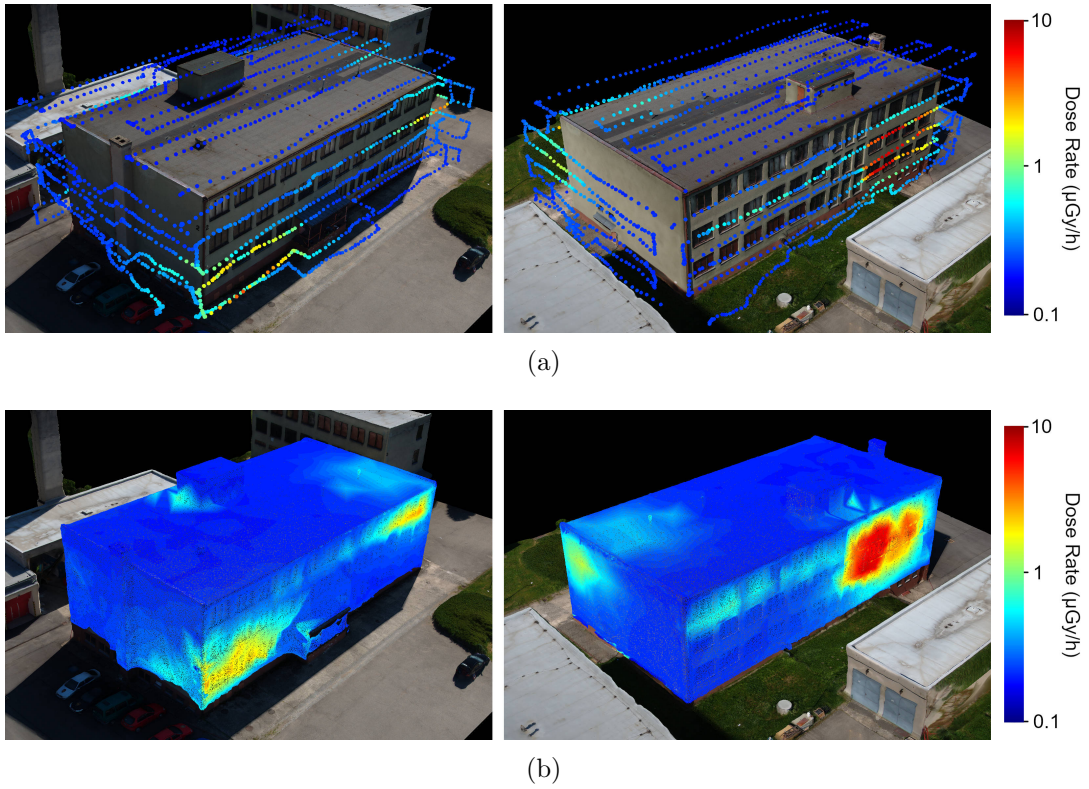
Figure D.6: The collected (a) and interpolated (b) radiation data over the 3D model obtained via aerial photogrammetry. The left-hand column captures the north-east view, while the right-hand one visualizes the south-west direction. All of the colour bars are in the log scale.

Table D.2: The localization results, supplemented with improperly expressed intensities of the sources.

Src.	True position			Estimated position			Absolute position error	Estimated dose rate in 1 m
	X [m]	Y [m]	Z [m]	X [m]	Y [m]	Z [m]	[m]	[μGy·h^{-1}]
S1	-2.97	-1.93	1.59	-1.21	2.09	3.02	4.6	6.6
S2	-8.83	-18.25	5.28	-9.87	-19.93	5.94	2.1	37.3
S3	-33.38	-8.11	8.50	-33.89	-5.52	8.05	2.7	14.3

The dataset was then thresholded and clustered by using the k-means algorithm. Both the silhouette and the elbow method indicated that the optimal number of clusters equals three, which is in accordance with the actual count of radioactive sources. The estimates of the sources' parameters were subsequently initialized and improved by means of the Gauss-Newton algorithm. The localization accuracy was assessed with respect to the approximate ground-truth positions; the results are summarized in Table D.2. To reveal their true intensity or even activity, the sources need to be unshielded; this condition, however, is not feasible in the examined scenario. The achieved magnitude of the localization error is comparable to that of the georeferencing error, which produces an inaccuracy greater than neglecting the attenuation does. Thus, for example, the data around the northeast corner in the survey lines at the level of the 1st floor are shifted away from the building, causing the source S1 to be localized outside. Generally, the algorithm tends to estimate the sources' positions closer to the measured points than they really are; this is due to the simplification of the applied radiation propagation model.

Our results can be regarded as bringing a certain degree of novelty to complete the previous research discussed in the Introduction. A comprehensive study on the complete post-disaster response procedure was proposed by Duncan and Murphy [10]; these authors' raster scan, however, was not employed at a sufficient complexity and detail. Moreover, the paper did not specify any visual results to represent the spatial distribution of the radiation. By extension, the localization method relied on manual greedy search, and the coordinates were not provided; this is in contrast to our approach, where the sources' coordinates are estimated automatically during the data processing phase. Outcomes very similar to our 3D radiological map of the building were delivered by Vetter et al. [11], whose scenario nevertheless included only one source, not enabling us to evaluate the performance of the system in a multi-source case. Further, the research did not involve localizing the source in terms of estimating its exact position. On the other hand, Vetter et al. achieved a greater relative positional accuracy in the collected datapoints, as they did not rely on absolute georeferencing but rather on a SLAM-based concept. Another difference between Vetter et al's project and our solution rests in the better spatial resolution of our map.

D.6 Conclusion

We introduced a comprehensive method to produce, by utilizing an unmanned aircraft system, a 3D radiation map of buildings and other structures. The proposed procedure requires an experienced pilot to operate the UAS at a rather small constant distance from the building's surfaces. The general purpose of this article lay

in delivering a proof of concept, namely, establishing whether the presented data collection approach is effective; the aims and objectives therefore did not involve developing an ultimate autonomous system. The UAS was characterized as a valuable asset in the discussed type of task. In this context, we can conclude that a high-energy (above 300 keV) source with an activity in the order of hundreds of megabecquerels is well detectable from the outside, even when located in a relatively subtle container; this, however, holds true if the source's distance from the edge of the structure does not significantly exceed 5 m.

A successful automatic localization of the sources was conducted to offer a complementary interpretation of the measured radiation data. Although the accuracy was not strictly superior, primarily due to problematic georeferencing of the input data, knowing the sources' parameters could help us to correct the dose rate values during the projection phase; however, the exact relationship between the parameters and the rate still remains to be investigated.

Neither the spatial accuracy nor the accuracy of the radiation measurements, however, are critical for the intended field of application. The purpose of the research was to provide complementary information to relevant authorities because real nuclear security operations still require human intervention. Generally, a 3D radiological map helps to increase the situational awareness and to reduce the operational costs in terms of the time and risks. A precise 3D model (see the map detail in Fig. D.7) allows a mission commander to see what parts of the examined structure are potentially unsafe, reflecting the current trends within the domain. In cases of searching for uncontrolled sources, UAS mapping-based localization can significantly reduce the time to be spent inside a risky environment, thus minimizing the radiation exposure.
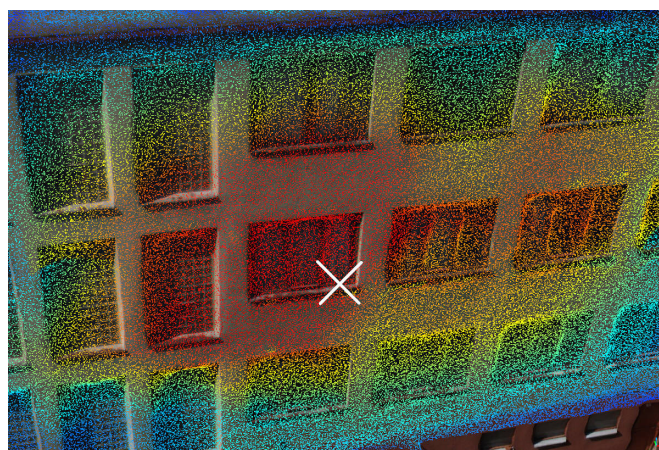

Figure D.7: A detail of the real world data-based hotspot produced by the source S2 on the building model. The approximate position of the source is marked with a white cross.

The presented mapping technique is applicable in differently sized and complex buildings; however, the data collection time may increase dramatically. In large premises, the different data acquisition parameter values, namely, those of the distance from the building, line spacing, and flight speed, may embody a factor that not only reduces the operating time but also lowers the map quality and source localization performance.

The most prominent challenge concerning further development of the mapping methodology lies in making the radiation data acquisition phase autonomous. This process, however, would require us to perform significant improvements on the UAS, including mounting proximity sensors and using advanced algorithms to perform the localization and navigation tasks autonomously even in highly complicated or GNSS-disturbed environments. State-of-the-art commercial UASs enable automatic flights or maintain a safe clearance from obstacles; such features, however, do not suffice to accomplish autonomous mapping near complex structures.

Applying LiDAR is expected to facilitate accurate radiation datapoint positioning in the coordinate system of a building (via either a pre-acquired model or SLAM). Such an improvement could significantly enhance the quality of the eventual map, as poor georeferencing previously affected the spatial resolution of the map and also the localization results. Finally, the impact of the flight parameters on various aspects of the aerial spectrometry and mapping needs to be studied comprehensively, as this issue has not been sufficiently covered in the literature to date.

Bibliography

[1] Parham Nooralishahi, Clemente Ibarra-Castanedo, Shakeb Deane, Fernando Lopez, Shashank Pant, Marc Genest, Nicolas P. Avdelidis, and Xavier P. V. Maldague. Drone-Based Non-Destructive Inspection of Industrial Sites: A Review and Case Studies. *Drones*, 5(4):106, December 2021. `doi:10.3390/drones5040106`.

[2] Stefan Cerba, Jakub Luley, Branislav Vrban, Filip Osusky, and Vladimir Necas. Unmanned Radiation-Monitoring System. *IEEE Transactions on Nuclear Science*, 67:636–643, April 2020. `doi:10.1109/TNS.2020.2970782`.

[3] P. G. Martin, S. Kwong, N. T. Smith, Y. Yamashiki, O. D. Payton, F. S. Russell-Pavier, J. S. Fardoulis, D. A. Richards, and T. B. Scott. 3D unmanned aerial vehicle radiation mapping for assessing contaminant distribution and mobility. *International Journal of Applied Earth Observation and Geoinformation*, 52:12–19, October 2016. `doi:10.1016/j.jag.2016.05.007`.

[4] John Peterson, Weilin Li, Brian Cesar-Tondreau, John Bird, Kevin Kochersberger, Wojciech Czaja, and Morgan McLean. Experiments in unmanned aerial vehicle/unmanned ground vehicle radiation search. *Journal of Field Robotics*, 2019. `doi:10.1002/rob.21867`.

[5] Guido Morgenthal, Norman Hallermann, Jens Kersten, Jakob Taraben, Paul Debus, Marcel Helmrich, and Volker Rodehorst. Framework for automated UAS-based structural condition

assessment of bridges. *Automation in Construction*, 97:77–95, January 2019. `doi:10.1016/j.autcon.2018.10.006`.

[6] Alexander Benz, Jakob Taraben, Paul Debus, Bedilu Habte, Luise Oppermann, Norman Hallermann, Conrad Voelker, Volker Rodehorst, and Guido Morgenthal. Framework for a UAS-based assessment of energy performance of buildings. *Energy and Buildings*, 250:111266, November 2021. `doi:10.1016/j.enbuild.2021.111266`.

[7] Alberto Vale, Rodrigo Ventura, and Paulo Carvalho. Application of unmanned aerial vehicles for radiological inspection. *Fusion Engineering and Design*, 124:492–495, November 2017. `doi:10.1016/j.fusengdes.2017.06.002`.

[8] Luis Ramos Pinto, Alberto Vale, Yoeri Brouwer, Jorge Borbinha, Jose Corisco, Rodrigo Ventura, Ana Margarida Silva, Andre Mourato, Goncalo Marques, Yuri Romanets, Susana Sargento, and Bruno Goncalves. Radiological Scouting, Monitoring and Inspection Using Drones. *Sensors*, 21(9):3143, January 2021. `doi:10.3390/s21093143`.

[9] Lauren Boldon, Justin K Reed, Zoe N Gastelum, John E Smart, and Jay Disser. Unmanned Aerial Systems Applications for International Nuclear Safeguards. In *Annual Meeting Proceedings of Institute of Nuclear Materials Management*, 2017.

[10] Brittany A. Duncan and Robin R. Murphy. Autonomous capabilities for small unmanned aerial systems conducting radiological response: Findings from a high-fidelity discovery experiment. *Journal of Field Robotics*, 31(4):522–536, 2014. `doi:10.1002/rob.21503`.

[11] Kai Vetter, Ross Barnowski, Joshua W. Cates, Andrew Haefner, Tenzing H. Y. Joshi, Ryan Pavlovsky, and Brian J. Quiter. Advances in Nuclear Radiation Sensing: Enabling 3-D Gamma-Ray Vision. *Sensors*, 19(11):2541, January 2019. `doi:10.3390/s19112541`.

[12] T. Lazna, P. Gabrlik, T. Jilek, and F. Burian. Simulating UAS-based radiation mapping on a building surface. In *Modelling and Simulation for Autonomous Systems (MESAS 2019)*, pages 130–147, Cham, Germany, March 2020. `doi:10.1007/978-3-030-43890-6_11`.

[13] Petr Gabrlik, Tomas Lazna, Tomas Jilek, Petr Sladek, and Ludek Zalud. An automated heterogeneous robotic system for radiation surveys: Design and field testing. *Journal of Field Robotics*, 38(5):657–683, 2021. `doi:10.1002/rob.22010`.

[14] Glenn F. Knoll. *Radiation Detection and Measurement*. John Wiley & Sons, Hoboken, New Jersey, 3rd edition edition, August 2010. ISBN: 978-0-470-13148-0.

[15] Marcel Ohera, Daniel Sas, and Petr Sladek. Calibration of spectrometric detectors for air kerma rates in environmental monitoring. *Nuclear Technology and Radiation Protection*, 35:323–330, January 2020. `doi:10.2298/NTRP20043230`.

[16] Isaac Amidror. Scattered data interpolation methods for electronic imaging systems: a survey. *Journal of Electronic Imaging*, 11(2):157–176, 2002. `doi:10.1117/1.1455013`.

[17] Khaled Alsabti, Sanjay Ranka, and Vineet Singh. An efficient k-means clustering algorithm. *Electrical Engineering and Computer Science*, January 1997. URL: `https://surface.syr.edu/eecs/43/`.

[18] Chunhui Yuan and Haitao Yang. Research on K-Value Selection Method of K-Means Clustering Algorithm. *J*, 2(2):226–235, June 2019. `doi:10.3390/j2020016`.

[19] K. Kraus. *Photogrammetry: Geometry from Images and Laser Scans*. Walter de Gruyter, Berlin, 2007. `doi:10.1515/9783110892871`.

[20] V.E. Oniga, A.I. Breaban, N. Pfeifer, and C. Chirila. Determining the suitable number of ground control points for uas images georeferencing by varying number and spatial distribution. *Remote Sensing*, 12(55):876, 2020. `doi:10.3390/rs12050876`.

[21] Christian Kunze, Benedikt Preugschat, Robert Arndt, Felix Kandzia, Benjamin Wiens, and Sven Altfelder. Development of a UAV-Based Gamma Spectrometry System for Natural Radionuclides and Field Tests at Central Asian Uranium Legacy Sites. *Remote Sensing*, 14(9):2147, January 2022. `doi:10.3390/rs14092147`.

E Localizing Multiple Radiation Sources Actively with a Particle Filter

Outline

Bibliographic Information

Abstract

We discuss the localization of radiation sources whose number and other relevant parameters are not known in advance. The data collection is ensured by an autonomous mobile robot that performs a survey in a defined region of interest populated with static obstacles. The measurement trajectory is information-driven rather than pre-planned, and the localization exploits a regularized particle filter estimating the sources' parameters continuously. Regarding the dynamic robot control, this switches between two modes, one attempting to minimize the Shannon entropy and the other aiming to reduce the variance of expected measurements in unexplored

parts of the target area; both of the modes maintain safe clearance from the obstacles. The performance of the algorithms was tested in a simulation study based on real-world data acquired previously from three radiation sources exhibiting various activities. Our approach reduces the time necessary to explore the region and to find the sources by approximately 40 %; at present, however, the method is unable to reliably localize sources that have a relatively low intensity. In this context, additional research has been planned to increase the credibility and robustness of the procedure and to improve the robotic platform autonomy.

Author's Contribution

The author reviewed the related research, proposed and developed the localization and control algorithms, carried out the simulations, and processed the results. He was also exclusively responsible for writing the manuscript, and contributed towards its finalization.

Author contribution: 95 %

Acknowledgement

Version Notice

This is a submitted version of the manuscript; the fulltext is also available at the *arXiv* preprint server: `https://arxiv.org/abs/2305.15240`.

E.1 Introduction

Radiation detection and the localization of radioactive sources are tasks of major significance in many fields and facilities, including nuclear power plants, environmental monitoring, and search for uncontrolled sources. Traditionally, these procedures have relied on human operatives, who are required to enter potentially contaminated areas; the advancement in robotics has nevertheless allowed radiation mapping with unmanned vehicles. The robots can survey hazardous environment, eliminating nuclear risk to human health, and are capable of navigating through complex terrain to locate and identify radiation sources. By using autonomous vehicles, we can also increase the efficiency and accuracy of the process. This article has been designed to present an approach for localizing multiple radiation sources without prior knowledge of their number and other relevant parameters. We propose a method that localizes sources by using a particle filter combined with an active planning strategy, increasing the task performance efficiency.

The problem of finding sources of ionizing radiation via robotic assets has been thoroughly studied in the literature. An overview of different approaches to active localization (i.e., the measurement trajectory is not pre-planned or controlled by a human operator), including their comparative analysis, is offered in [1]. Several techniques rely on pixel detectors or Compton cameras, which provide various degrees of directional information. The set of articles on mapping or passive localization comprises, for instance, reference [2], where a 3D radiation image is reconstructed to enable locating a single source. The authors of [3] introduce a comprehensive simulation tool for Timepix detectors, verifying their instrument via using a micro aerial vehicle to retrieve a source. An additive point source localization algorithm is presented in [4], demonstrating its ability to find up to four radionuclides by means of a custom handheld device. An active localization method utilizing a Compton imaging device and the maximum likelihood-expectation maximization algorithm is described in [5]; the authors exploit a Fisher information matrix (FIM) to identify an optimal sequence of dwell points. The central deficiencies of gamma cameras, namely, the long acquisition time and poor angular resolution, are addressed in [6]; here, an optimal data acquisition strategy to suit the camera's parameters is outlined through multi-criteria decision-making, delivering better results than the behavior-based approach. Article [7] applies principal component analysis to previous measurements to determine the direction of the next dwell point, the localization relying on a simple back-projection; there is the possibility of locating multiple sources, which nevertheless requires an input from a human operator.

Other articles discuss common omnidirectional detectors; at this point, we can focus on those that investigate passive localization. A method for extracting direc-

tional information from an acquired dataset and finding intersections via maximum likelihood estimation is presented in [8]. The authors of [9] then propose a platform based on the Robot Operating System (ROS) to systematically map an indoor environment in which radiation hotspots are definable. The approach characterized in [10] relies on a static network of detectors and presents a hybrid particle filter supported by a mean-shift algorithm capable of locating an unknown number of sources.

An associated cluster of articles embraces active localization; here, studies considering a single source are referred to first. The procedure set out in [11] localizes the source via a particle filter enhanced with a Markov chain Monte Carlo method; the search strategy alone adopts a partially observable Markov decision process subsuming a reward function based on the Shannon entropy. Another concept that employs the entropy is exposed in [12]. Further, article [13] proposes a combination of a particle filter and an unscented Kalman filter to estimate the source position in each axis separately; the robot is driven directly towards the point where the source is anticipated.

Finally, related work on the active localization of multiple sources is summarized. Article [14] focuses on sophisticated radiation mapping rather than source localization; the proposed framework is able to reconstruct a 3D map with an unmanned aircraft system (UAS) in a satellite navigation-denied environment, and different isotopes can be distinguished. Another UAS-based approach exploits contour following supported by sampling in a suitable region of interest [15]; the localization is performed with a variational Bayesian algorithm. The authors of [16] propose 2D localization via a particle filter involving progressive correction and apply a search strategy based on maximizing the Rényi divergence; a relevant experimental verification demonstrated the capability of retrieving up to two sources. In article [17], a particle filter is also used to localize sources in 3D; moreover, the radioactive decay and attenuation of the radiation in the obstacles can be modeled, thanks to automatic identification of the isotopes. During the search, a pre-determined number of measurements are conducted; the choice of the optimal trajectory is FIM-based. Nonetheless, the above-mentioned studies do not demonstrate the capability of retrieving multiple sources while ensuring that the entire region is explored; importantly, our research proposes an attempt to address such a deficiency.

The problems, scenarios, and preconditions in this article can be described as follows: Let us have an unknown number of radioactive sources that are concealed in a known region of interest (ROI) defined by a polygon with holes (static obstacles). A single unmanned ground vehicle (UGV) equipped to control its linear and angular velocity is available; the UGV carries an accurate self-localization system and a radiation detector which provides a counts per second (CPS) value at a constant

sampling period. The goal is to localize all of the sources as quickly as possible; the result is expected to be independent of the starting position of the robot, and the robot must not leave the ROI or cross the obstacles. The proposed algorithms are verified through simulations exploiting the real-world dataset acquired during our previous research [18].

E.2 Localization algorithm

This section characterizes the proposed localization algorithm, which exploits the importance sampling principle. The method has been designed to function independently of the data acquisition trajectory, and it should operate smoothly even in pre-planned systematic surveys. The particle filter is a Bayesian technique that approximates a posterior distribution by a set of random samples, i.e., particles [19]. Let us have a state vector $\boldsymbol{\theta}$ and a set of observations $\mathbb{Z} = \{\boldsymbol{z}_i\}_{i=1}^M$. At a time step t, the posterior probability is computed via the Bayes rule

$$p(\boldsymbol{\theta}_t|\boldsymbol{z}_t) = \frac{p(\boldsymbol{z}_t|\boldsymbol{\theta}_t) \cdot p(\boldsymbol{\theta}_t|\boldsymbol{z}_{1:t-1})}{p(\boldsymbol{z}_t|\boldsymbol{z}_{1:t-1})}. \tag{E.1}$$

As the number of sources r is unknown, it embodies one of the estimated state variables, and the length of the vector $\boldsymbol{\theta}$ varies accordingly. Let us have a set of N particles $\boldsymbol{\chi}_t = \{\boldsymbol{\theta}_t^{(i)}\}_{i=1}^N$, where $\boldsymbol{\theta}^{(i)} = (r, \lambda_B, x_1, y_1, \lambda_1, \cdots, x_r, y_r, \lambda_r)$. The mean background radiation rate is denoted as λ_B, and the tuple (x, y, λ) represents the 2D coordinates of the source, together with its mean count rate at the distance of one meter.

At the start of the localization process, the particles are initialized randomly. We then have to select the maximum number of sources, r_{max}, with the minimum assumed to equal one. Although an emitter is assumed to be present during the initialization phase, the algorithm is capable of exploiting a particle regularization to reach the hypothesis that there are no sources (see below). The prior probability of r sources being present is adopted from [16]; this probability drops linearly with the increasing r. The background radiation, λ_B, is distributed uniformly. The sources' coordinates (x, y) are drawn from the uniform distribution, and samples outside the outer boundaries $\mathcal{R}$ of the ROI are rejected. Finally, the intensity λ follows the gamma distribution $\Gamma(\alpha, \beta)$, the two parameters being the shape and the rate, respectively.

Traditionally, the particle filter involves a prediction step that reflects the state transition probability $p(\boldsymbol{\theta}_t|\boldsymbol{\theta}_{t-1}, \boldsymbol{u}_t)$ given by the previous state and the control input $\boldsymbol{u}_t$. In this case, we assume the system to be stationary, i.e., $\boldsymbol{\theta}_t = \boldsymbol{\theta}_{t-1}$. Such simplification is possible with the sources in static positions and their half-life values

markedly exceeding the duration of the localization; thus, the radioactive decay can be ignored.

A correction step follows, each particle being assigned a weight computed according to the measurement model

$$w_t^{(i)} \propto p(\boldsymbol{z}_t | \boldsymbol{\theta}_t^{(i)}) \cdot w_{t-1}^{(i)}. \tag{E.2}$$

To derive a suitable model, four effects have to be considered:

1. Both the radioactive decay and the radiation detection are stochastic processes, meaning that we need to select an appropriate probability density function (PDF) to represent adequately the relevant physical laws. The radioactive decay follows a binominal distribution, commonly replaced with a Poisson distribution having a mean λ [20]. At large rates, we can further apply an approximation by the normal distribution whose mean and variance equal λ, that is

$$\mathcal{P}(\lambda) \sim \mathcal{N}(\lambda, \lambda), \tag{E.3}$$

$$p(X = k) = \frac{\lambda^k e^{-\lambda}}{k!} \approx \frac{1}{\sqrt{\lambda 2\pi}} e^{-\frac{(k-\lambda)^2}{2\lambda}}. \tag{E.4}$$

2. Gamma radiation propagates with respect to the inverse square law and is attenuated by the mass it passes through. Ideally, with no scattering and secondary radiation, the intensity decreases to

$$I = I_0 \frac{\exp\left(-\sum_{i=1}^{S} \mu_i d_i\right)}{\left(\sum_{i=1}^{S} d_i\right)^2}, \tag{E.5}$$

where I_0 is the initial intensity, μ_i represents the linear attenuation coefficient of the i-th material, and d_i is the length of the intersection of a hypothetical radiation ray with the material [21]. Our scenario considers high-energy photons passing only through air at relatively short distances (< 20 m); therefore, the attenuation effect can be ignored, and the numerator expression in Eq. E.5 approximately equals one. Conversely, reflecting the attenuation would significantly increase the complexity of the estimation problem, as the attenuation coefficient μ is energy-dependent; thus, we cannot know its value a priori.

3. The radiation background introduces considerable noise into the measurements. The relevant components include terrestrial radiation, produced by the radionuclides that are naturally present in the soil, and galactic and solar cosmic radiation. It has to be considered that each acquired spectrum or count rate embodies a superposition of the useful signal yielded by the localized sources on the one hand and the background on the other [22].

4. The detection system may suffer from dead time when overloaded with a high flux of photons. In particular situations, above all, those where the system exhibits paralyzable behavior, the detected counts start to decrease with increasing actual photon interactions; such an effect occurs when the rates are high. This condition can be compensated for by computing the expected counts λ', using the theoretical rate λ and the detector-specific dead time constant τ [23].

Combining all of the above effects enables us to express the probability $p(\boldsymbol{z}_t|\boldsymbol{\theta}_t^{(i)})$. The measurement vector $\boldsymbol{z}_t$ is characterized by the tuple (ϕ_t, ψ_t, ν_t), that is, the coordinates in the x and y axes, and the detected count rate. First, we need to compute the theoretical count rate at the point (ϕ_t, ψ_t), yielded by $\boldsymbol{\theta}_t^{(i)}$:

$$\lambda(\boldsymbol{z}_t, \boldsymbol{\theta}_t^{(i)}) = \lambda_{\mathrm{B}}^{(i)} + \sum_{j=1}^{r^{(i)}} \frac{\lambda_j^{(i)}}{(x_j^{(i)} - \phi_t)^2 + (y_j^{(i)} - \psi_t)^2 + D^2}, \tag{E.6}$$

where D is the fixed detector height above the ground level; note that we anticipate all of the sources to be located on the ground. Subsequently, the dead time effect is applied:

$$\lambda' = \lambda(\boldsymbol{z}_t, \boldsymbol{\theta}_t^{(i)}) \cdot e^{-\tau \cdot \lambda(\boldsymbol{z}_t, \boldsymbol{\theta}_t^{(i)})}. \tag{E.7}$$

The notation has been slightly simplified, yielding the reduced equation below, which computes the unnormalized weight:

$$\hat{w}_t^{(i)} = \frac{1}{\sqrt{\kappa \lambda' 2\pi}} e^{-\frac{(\nu_t - \lambda')^2}{2\kappa \lambda'}} \cdot w_{t-1}^{(i)}, \tag{E.8}$$

where κ is the constant that helps us to tune the variance of the utilized normal PDF to respect the real-world measurements. Once the particles have been processed, the weights are normalized, and the effective sample size N_{eff} is computed. We have

$$w_t^{(i)} = \frac{\hat{w}_t^{(i)}}{\sum_{j=1}^N \hat{w}_t^{(j)}}; \quad N_{\mathrm{eff}} = \frac{1}{\sum_{i=1}^N (w_t^{(i)})^2}. \tag{E.9}$$

To prevent particle depletion, resampling is not performed in each iteration; instead, the algorithm idles until the effective sample size has dropped below the chosen threshold, $N_{\mathrm{eff}} < N_{\mathrm{thr}}$. Eventually, the resampling is executed using the low variance algorithm [24].

As each resampling operation reduces the particle set variance, this needs to be increased via regularization. Such a step also helps the localization algorithm to respond to newly discovered sources through altering their estimated count r. First, all parameters but r are regularized. The resampled set $\boldsymbol{\chi}$ is divided into subsets, $\boldsymbol{\chi}_1, \boldsymbol{\chi}_2, \cdots, \boldsymbol{\chi}_{r_{\max}}$, with respect to the number of sources. In each subset, the standard deviation $\boldsymbol{\sigma}$ of the parameters is computed, and the vector of random

numbers $\boldsymbol{G}$ is drawn from the Gaussian kernel. Then, the particles are updated to read

$$\forall \boldsymbol{\theta} \in \bar{\chi}_i : \boldsymbol{\theta} = \boldsymbol{\theta} + \frac{h_i}{\xi} \boldsymbol{\sigma}_i \boldsymbol{G}, \tag{E.10}$$

where h is the suggested bandwidth [25], and ξ denotes the tuning parameter. Whenever a source hypothesis reaches beyond $\mathcal{R}$ or its intensity drops below zero, it dissolves, and the respective r value is decremented.

Then, the number of sources is regularized according to the pre-set probabilities of 'birth', p_{B}, and 'death,' p_{D}. The latter case is straightforward: a random source hypothesis is picked and dissolved; note that the minimum allowed number of sources equals zero. When a new hypothesis is added, the corresponding parameters are sampled, respecting the posterior $p(\boldsymbol{\theta}_t | \boldsymbol{z}_t)$. Specifically, the coordinates $(x, y) \in \mathcal{R}$ are sampled from the normal distribution centered at (ϕ_t, ψ_t), while the intensity exploits

$$\lambda \sim \mathcal{P} \left(\nu_t \left[(x - \phi_t)^2 + (y - \psi_t)^2 + D^2 \right] \right). \tag{E.11}$$

The control algorithm presented in the next section requires us to use the current source estimate in some cases; to acquire one, the expected number of sources is computed first, reading

$$\hat{r}_t = \left\lfloor \sum_{i=1}^{N} w_t^{(i)} \cdot r_t^{(i)} + 0.5 \right\rfloor. \tag{E.12}$$

The source estimate is then expressed as

$$\hat{\boldsymbol{\theta}}_t = \left. \sum_{i:r^{(i)}=\hat{r}_t} w_t^{(i)} \cdot \boldsymbol{\theta}^{(i)} \middle/ \sum_{i:r^{(i)}=\hat{r}_t} w_t^{(i)}. \right. \tag{E.13}$$

E.3 Control algorithm

The control system is designed to propose a motion command on the basis of previous measurements. The suggested algorithm comprises two components, one denoted as a *local* and the other as a *global* planner; the former aims to speed up the convergence of the particle filter, while the latter ensures that the whole ROI is covered.

The region is subjected to an approximate cell decomposition, which yields a set of free square cells $\mathbb{C} = \{\mathcal{C}_i\}_{i=1}^{K}$. The cells have a dimension δ, chosen with respect to the time efficiency relative to the exhaustive exploration along a boustrophedon path. The extent of the most dense meaningful trajectory can be pre-determined for a given ROI by the parameters of the detection system and the desired spatial resolution; this limit should not be exceeded in the dynamic planning. The cell $\mathcal{C}_i$ is considered free when its center, $\boldsymbol{c}_i$, lies inside the ROI, $\mathcal{R}$, and does not appear within

any obstacle $\mathcal{O} \in \mathbb{O}$. A survey ends once every cell has been *visited*, meaning that the number of measurements acquired therein is greater than the preset threshold:

$$\forall \mathcal{C} \in \mathbb{C}: \quad \left| \{ \boldsymbol{z}_i : (\phi_i, \psi_i) \in \mathcal{C} \} \right| \geq s_{\min}. \tag{E.14}$$

The two planners introduced earlier are switched according to three conditions. In these, the global planner is applied if: 1. The current cell (i.e., that which accommodates the robot at a time t) is visited; 2. the robot is not in a free cell (as may happen near region boundaries and obstacles); 3. the relative mean unnormalized weight of the particles is above the threshold

$$\overline{\hat{w}_t} \,/\, \overline{\hat{w}_{1:t}} > \hat{w}_{\mathrm{thr}}. \tag{E.15}$$

The local planner, by contrast, finds use in all other scenarios. Both planners differ in the criterion function $f(\boldsymbol{u})$, which allows selecting the fittest member from the set of potential actions $\mathbb{U} = \left\{ \boldsymbol{u}_i = (v_i, \omega_i) \right\}_{i=1}^{L}$ (the linear and angular velocities). In each action, a new position (ϕ', ψ') is acquired with a common differential drive kinematic model.

The local planner relies on the Shannon entropy. First, the expected count rate at (ϕ', ψ') is computed with respect to the current estimate $\hat{\boldsymbol{\theta}}_t$ via Eqs. E.6 and E.7; subsequently, all particles are weighted. The entropy is then given by

$$H = -\sum_{i=1}^{N} w^{(i)} \cdot \log w^{(i)}. \tag{E.16}$$

Finally, the entropy values are rescaled so that the maximum equals one.

Conversely, the global planner's criterion exploits the Euclidean distance between the new position and the center of the next-best cell. To choose this cell, the *curiosity* value C is estimated, equaling the standard deviation of expected measurements at the center $\boldsymbol{c}_i$ of a cell, the measurements being yielded by the particles in $\boldsymbol{\chi}_t$. We have

$$C(\mathcal{C}_i) = \sqrt{\frac{1}{N} \sum_{j=1}^{N} \left(\mathbb{E}[\lambda(\boldsymbol{\theta}^{(j)}, \boldsymbol{c}_i)] - \overline{\mathbb{E}[\lambda]} \right)^2}. \tag{E.17}$$

As the most curious cell may appear on the opposite side of the ROI and the curiosity may change with every measurement, an A*-like algorithm is adopted to pick a suitable unvisited cell that is close to the robot. This algorithm searches for an optimal path from the current position to the highest-curiosity cell; however, the cost of visiting a node (cell) is not only given by the physical distance but also exhibits an inverse proportionality to the respective curiosity value. The resulting next-best cell then embodies the first unvisited node along the path. Once this sub-goal has been reached, a new one is chosen.

At the following stage, obstacles need to be considered, as we do not desire the robot to cross them. To address this requirement, another criterion function common for the planners is introduced; the function is inspired by the repulsive force used in artificial potential fields [26], reading

$$
\begin{aligned}
g(\boldsymbol{u}) = {} & (R_{\mathrm{R}} - \min \lVert (\phi', \psi') - (x, y) \in \mathcal{R} \rVert)^2 + \\
& \sum_{\mathcal{O} \in \mathbb{O}} (R_{\mathrm{O}} - \min \lVert (\phi', \psi') - (x, y) \in \mathcal{O} \rVert)^2,
\end{aligned} \tag{E.18}
$$

where R_{R} and R_{O} represent the effective radii for the region boundaries and the obstacles, respectively. Finally, the fittest action is selected by using the criterion functions (depending on the currently applied planner) and weighting factors a, b:

$$
\arg \min_{\boldsymbol{u} \in \mathbb{U}} \quad a \cdot f(\boldsymbol{u}) + b \cdot g(\boldsymbol{u}). \tag{E.19}
$$

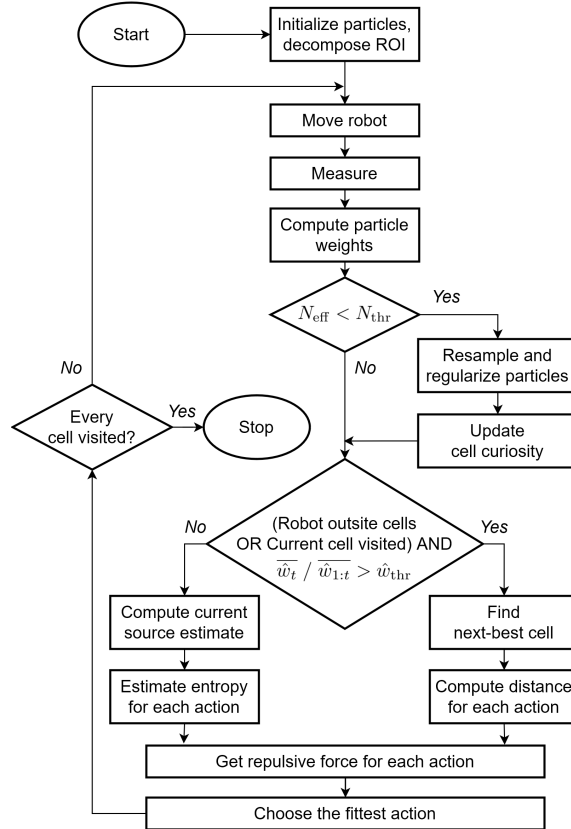The overall structure of the proposed algorithm is outlined through the flowchart in Fig. E.1.

Figure E.1: The structure of the localization and control algorithms.

E.4 Experimental setup

The performance of both the localization and the control algorithms was tested via a comprehensive simulation study utilizing real-world experimental data [18]. The region of interest captures an area of 277 m^2 and contains three static obstacles, whose areas range from 1 m^2 to 2.5 m^2 and were delimited utilizing a photogrammetric model. The obstacles in this scenario involved exclusively sparse vegetation and plastic drums, allowing them to avoid conflict with ignoring the attenuation. It is assumed that the survey can start in any vertex of the polygon $\mathcal{R}$. The ROI comprises three distinguishable radiation sources, of which one is cesium-137 and two are cobalt-60, the respective activities calculated to the measurement date being 80 MBq, 25 MBq, and 3 MBq; hereafter, the point sources are specified as S_1, S_2, and S_3. Note that the radioactive material is sealed and unshielded.

The area was decomposed to 29 cells, each having the dimension $\delta = 3$ m (Fig. E.3a). The character of the study site, i.e., a flat grass field, enables simplifying the localization algorithm into two dimensions. We can reasonably assume that any uncontrolled point source lies on the terrain surface, which is known to be flat thanks to the available digital elevation model (DEM).

The original data were acquired by an Orpheus-X4 UGV carrying a pair of $2'' \times 2''$ thallium-doped sodium iodide (NaI(Tl)) detectors that executed the sampling at the period of 1 s. The self-localization was ensured by an accurate Real-time Kinematic Global Navigation Satellite System (RTK-GNSS) receiver. With respect to the applied platform's capabilities and limitations, the set of candidate actions was populated with 5 elements: $\mathbb{U} = \{(0.6 \text{ ms}^{-1}, 0 \text{ s}^{-1}), (0.5 \text{ ms}^{-1}, \pm\pi/8 \text{ s}^{-1}), (0.4 \text{ ms}^{-1}, \pm\pi/4 \text{ s}^{-1})\}$. The remaining relevant parameters are specified in Table E.1.

Table E.1: The relevant parameters of the proposed algorithms.

N	10^4	α	2	N_{thr}	2000	s_{min}	3
r_{max}	10	β	12000	ξ	2.55	$\hat{w}_{\text{thr}}$	0.35
$\lambda_{\text{B,min}}$	250	τ	$2 \cdot 10^{-5}$	p_{B}	1/100	R_{R}	1.5 m
$\lambda_{\text{B,max}}$	750	κ	15^2	p_{D}	1/600	R_{O}	1 m

E.5 Results and Discussion

Three iterations of an example run of the proposed algorithm are presented in Fig. E.3b, E.3c, and E.3d, respectively. In this case, the survey took 229 iterations in total, and all of the three sources were localized successfully. To assess the

efficiency of the control algorithm and the robustness of the localization one, 500 simulations were run, with the initial robot position being randomly selected from the set of the ROI vertices. As a reference, the dataset acquired during the pre-planned survey was employed; this dataset consisted of 437 datapoints iteratively fed into the localization algorithm. We carried out 100 simulations for both the original and the reversed measurement orders. An overview of the results is provided in Table E.2; here, a source hypothesis is considered *valid* once the variance of coordinates in both axes has dropped below 1.5 m^2, and a source is *localized* if the corresponding hypothesis lies within a range of 1.5 meters. Valid hypotheses beyond 1.5 m from any source are labeled as *false positives*. The progress of the localization error and the occurrences of the false positives in time are displayed in Fig. E.2; note that these aspects embody the averaged results from all of the 500 simulations covered by our control algorithm. An additional series of simulations enabled us to verify how the algorithm performs in the no-source scenario; relevant results are summarized at the bottom of Table E.2. The actual radiation measurements in this case were replaced with Gaussian noise having parameters ($\mu = 500, \sigma = 70$) derived from real data.
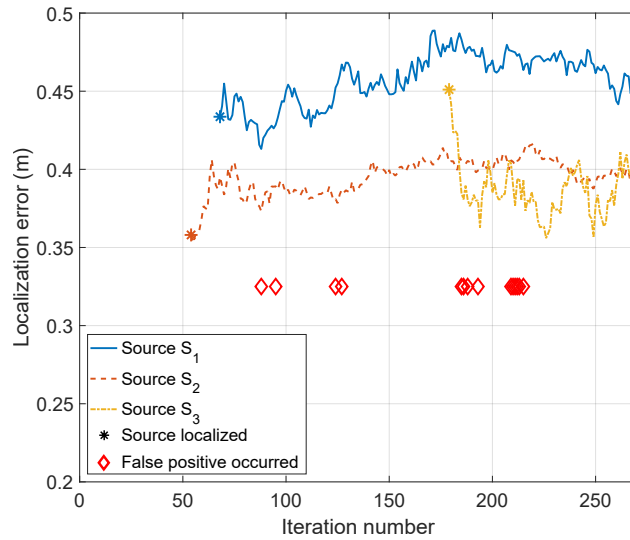
Figure E.2: The localization error pattern.

Considering the above-presented data, the localization algorithm can be characterized as robust enough, as it identifies all of the sources in each of the cases under the pre-planned exhaustive survey trajectory scenario. Such a good result, however, does not apply to source S_3 when the proposed dynamic control algorithm is employed: The source is really weak and thus detectable only from a close proximity (< 1.5 m), and, given the selected cell size, the algorithm does not always navigate the robot adequately. As determined empirically, the current algorithm setup requires approximately 9 samples per cell on average, meaning that the δ value cannot

be significantly reduced; for the studied area and the reference systematic survey, the information-driven control tends to be less efficient if $\delta < 2.3$ m. Note that the original line spacing equaled approximately 1 m, this being the value chosen to achieve the maximum possible spatial resolution with respect to the applied platform and detectors.

Table E.2: The averaged localization results: The numbers after the $\pm$ sign represent the standard deviation from all of the performed simulated experiments (where applicable).

		Proposed control algorithm	Systematic survey (original)	Systematic survey (reversed)
	Total iterations	271 ± 32	437	437
	False positive rate (%)	4.8	1.8	9.0
S_1	Localized? (% of all experiments)	99.8	100.0	100.0
	First localizing iteration	77 ± 38	64 ± 5	217 ± 31
	% of localizing iterations	58 ± 18	75 ± 11	34 ± 9
	Localization error (m)	0.45 ± 0.29	0.33 ± 0.24	0.46 ± 0.37
S_2	Localized? (% of all experiments)	100.0	100.0	100.0
	First localizing iteration	51 ± 45	22 ± 3	311 ± 35
	% of localizing iterations	74 ± 19	76 ± 16	26 ± 8
	Localization error (m)	0.39 ± 0.25	0.43 ± 0.19	0.48 ± 0.34
S_3	Localized? (% of all experiments)	62.8	99.0	100.0
	First localizing iteration	176 ± 65	301 ± 11	148 ± 4
	% of localizing iterations	24 ± 17	30 ± 5	29 ± 11
	Localization error (m)	0.47 ± 0.34	0.38 ± 0.24	0.33 ± 0.29
No sources				
	Total iterations	216 ± 22	437	437
	False positive rate (%)	0.0	0.0	0.0
	Estimated number of sources	$1e{-}5 \pm 3e{-}4$	0.012 ± 0.005	0.010 ± 0.003

Interestingly, the false positive (FP) rate is significantly greater when the order of the datapoints has been reversed in the pre-planned trajectory case; this condition may arise from the fact that essentially all of the measurements in the first third of the survey carry only a minor information value, as the count rates are situated near the radiation background. Conversely, the dynamic planner exhibits a satisfactory FP rate. In Fig. E.2, the FPs are shown to appear mostly after the source S_3 has been encountered, with the other two sources having been already localized by that

moment. Even though the algorithm may seem to encounter issues at low count rates due to an improper choice of the kernel for the particle weighting process, other functions were rejected, as they caused fast particle deprivation and overall algorithm instability: For example, the apparently suitable Poisson kernel exhibited an excessively narrow PDF in the given context. The algorithm's performance at low intensities was partially improved by progressively altering the κ parameter (instead of leaving it constant); this approach, however, produced additional issues. The problem therefore needs to be addressed in the future research to yield more sophisticated adjustment of the method; possibly, some factors such as the directional characteristics of the detection system should not be neglected.

The localization error ranges from 0.35 m to 0.5 m and is relatively stable in each source during the experiment. Such an accuracy may suffice from a practical perspective, but when really necessary, better results are achievable via post-processing, by using, for instance, the Gauss-Newton method [18]. Moreover, it was demonstrated that an absence of sources does not affect the algorithm's behavior negatively: No FPs occurred during the surveys, and the estimated number of sources converged towards zero in both the pre-planned and the dynamic trajectories.

The proposed dynamic control has met our expectations, as it indeed reduces the time required to localize the sources independently of the robot's starting position; this holds true especially of the two strong sources, S_1 and S_2. The total iterations are reduced by 39 % compared to the systematic approach, and the iterations needed to localize the three sources drop by 41 or 44 %, depending on the order of the datapoints in the reference survey. The main drawback lies in that the weakest source, S_3, is not found each time. This issue is planned to be addressed in the future experiments, by such means as enhancing the planners to reward the actions which bring the robot farther from the previously acquired datapoints; this concrete step will increase the effective coverage of the ROI for the same number of iterations.

Our current efforts were inspired mostly by Ristic et al. [16] and Mascarich et al. [14]. From the former, we adopted the regularization framework and particle structure, albeit with a slight modification: We allowed also the estimation of the mean radiation background rate (as suggested in, e.g., [8]). The latter then led us to develop the idea of dividing the control algorithm into local and global components. Our local planner exploited the Shannon entropy ([11], [12]); although we had already carried out experiments involving the FIM, applying the entropy enabled us to obtain better results.

The novelty of the research presented herein rests in the global planner design and the strategy of switching the control modes. In this context, we also modified the algorithms and tuned their parameters to reach sufficiently consistent outcomes even with noisy real-world data. Compared to Ristic et al., we demonstrated the ability
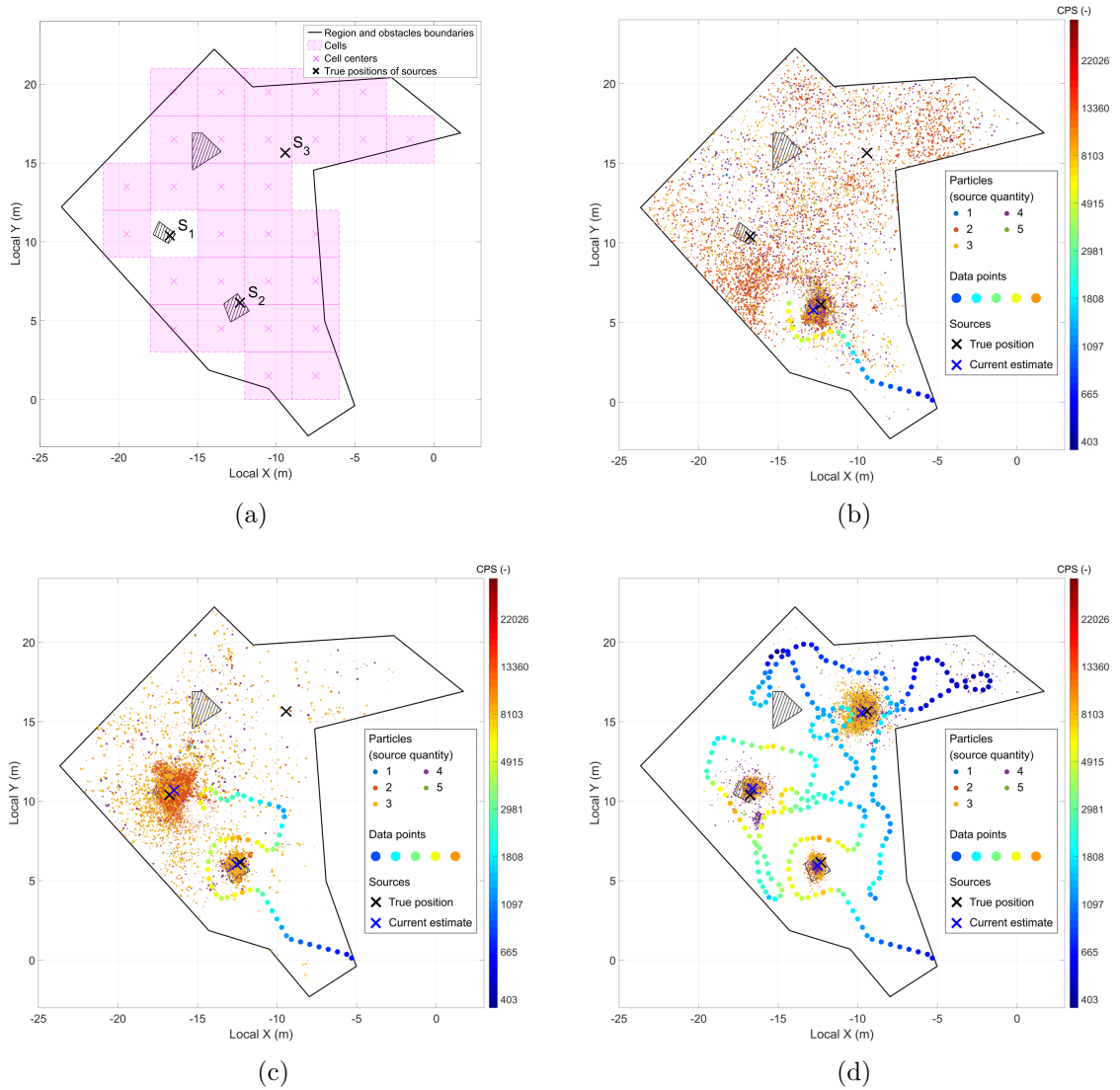
Figure E.3: The region of interest decomposed into cells, with the sources denoted alphanumerically (a). Three iterations of an example run of the proposed algorithm: Showing iterations No. 25 (b), 56 (c), and 229, namely, the final one (d). The color bars are in the log scale.

to acquire valid localization results even when the parameter r_{max} is significantly greater than the actual number of sources being sought; moreover, our approach ensures complete coverage of the target area.

In the future experimentation, we will focus on utilizing the information embedded in the measured radiation spectra; an inspiring option was presented by, for instance, Anderson et al. [17]. Regrettably, relevant datasets available to us lack reliable spectra because the detection system was damaged during the initial fieldwork. Another challenge to improve the procedures lies in exploiting the partial directional information provided by an array of measurement units; importantly,

the task may be successfully completed with only two detectors. By extension, we can also mention that the presented use case including only bare sources may not be realistic; our planned work is therefore expected to focus on more complex scenarios.

E.6 Conclusion

The article discusses a comprehensive method for localizing multiple radiation sources by means of an autonomous mobile robot in a known outdoor environment. Two principal factors, namely, a localization and a control algorithm, are relied on: The former estimates the number of the sources and their relevant parameters via a particle filter, and the latter chooses the optimal robot movement sequence to reduce the time required to find the sources while ensuring complete coverage of the region of interest. The novelty of the research rests in conveniently combining known partial algorithms into a coherent unit that delivers robust performance, as verified through extensive simulation studies based on real-world data. Our solution localizes the sources already during the measurement, i.e., earlier than the post-processing, and alters the robot trajectory accordingly to prioritize the most information-rich sectors of the target area. The method is applicable primarily within the search for uncontrolled sources but can be modified to find use in other domains too. Importantly, the algorithms will be deployed on an Orpheus-X4 platform to yield reliable functionality verification.

The drawbacks include, above all, the need to know the environment map a priori, the dependence on an accurate RTK-GNSS self-localization, the assumption that the sources are located in a 2D plane, and the inability to manage the radiation attenuation in potentially dense obstacles. To address the first two issues, we intend to enable the UGV to navigate itself with lidar-based Simultaneous localization and mapping (SLAM); however, an instrument to limit the scope of the surveyed region will still be necessary. This planned step will improve the system's overall autonomy, albeit probably at the expense of the localization algorithm's performance, which may deteriorate due to a lower accuracy of the datapoint positioning. Regarding the third problem, the difficulty is easily resolvable through expanding the particle structure and the measurement model to include another coordinate; to avoid estimating phantom sources in improbable positions (e.g., hovering in air), it may be beneficial to acquire and exploit a terrain model.

The last of the above-outlined disadvantages, however, is markedly more prominent, requiring knowledge of the radiation energy, geometry of the obstacles, and relevant attenuation coefficients. A set of possible solutions were proposed in the literature; most of the authors nevertheless assume that at least some parameters have been provided in advance to reduce the estimation problem complexity.

Bibliography

[1] Kathleen McGill and Stephen Taylor. Robot algorithms for localization of multiple emission sources. *ACM Computing Surveys*, 43(3):15:1–15:25, April 2011. `doi:10.1145/1922649.1922652`.

[2] Doyeon Kim, Hanwool Woo, Yonghoon Ji, Yusuke Tamura, Atsushi Yamashita, and Hajime Asama. 3D radiation imaging using mobile robot equipped with radiation detector. In *2017 IEEE/SICE International Symposium on System Integration (SII)*, pages 444–449, December 2017. `doi:10.1109/SII.2017.8279253`.

[3] Petr Stibinger, Tomas Baca, and Martin Saska. Localization of Ionizing Radiation Sources by Cooperating Micro Aerial Vehicles With Pixel Detectors in Real-Time. *IEEE Robotics and Automation Letters*, 5(2):3634–3641, April 2020. `doi:10.1109/LRA.2020.2978456`.

[4] Jayson R. Vavrek, Daniel Hellfeld, Mark S. Bandstra, Victor Negut, Kathryn Meehan, William Joe Vanderlip, Joshua W. Cates, Ryan Pavlovsky, Brian J. Quiter, Reynold J. Cooper, and Tenzing H. Y. Joshi. Reconstructing the Position and Intensity of Multiple Gamma-Ray Point Sources With a Sparse Parametric Algorithm. *IEEE Transactions on Nuclear Science*, 67(11):2421–2430, November 2020. `doi:10.1109/TNS.2020.3024735`.

[5] Michael S. Lee, Daniel Shy, William Red Whittaker, and Nathan Michael. Active Range and Bearing-based Radiation Source Localization. In *2018 IEEE/RSJ International Conference on Intelligent Robots and Systems (IROS)*, pages 1389–1394, October 2018. `doi:10.1109/IROS.2018.8593625`.

[6] Hadi Ardiny, Stefan Witwicki, and Francesco Mondada. Autonomous Exploration for Radioactive Hotspots Localization Taking Account of Sensor Limitations. *Sensors*, 19(2):292, January 2019. `doi:10.3390/s19020292`.

[7] Takuya Kishimoto, Hanwool Woo, Ren Komatsu, Yusuke Tamura, Hideki Tomita, Kenji Shimazoe, Atsushi Yamashita, and Hajime Asama. Path Planning for Localization of Radiation Sources Based on Principal Component Analysis. *Applied Sciences*, 11(10):4707, January 2021. `doi:10.3390/app11104707`.

[8] Wei Tan, Jianbin Zhou, Fang Fang, Xiaozhe Li, and Xu Hong. A fast gamma-ray source localization method for mobile robots. *Applied Radiation and Isotopes*, 188:110377, October 2022. `doi:10.1016/j.apradiso.2022.110377`.

[9] Benjamin Bird, Arron Griffiths, Horatio Martin, Eduardo Codres, Jennifer Jones, Alexandru Stancu, Barry Lennox, Simon Watson, and Xavier Poteau. A Robot to Monitor Nuclear Facilities: Using Autonomous Radiation-Monitoring Assistance to Reduce Risk and Cost. *IEEE Robotics & Automation Magazine*, 26(1):35–43, March 2019. `doi:10.1109/MRA.2018.2879755`.

[10] Jren-Chit Chin, David K.Y. Yau, and Nageswara S.V. Rao. Efficient and Robust Localization of Multiple Radiation Sources in Complex Environments. In *2011 31st International Conference on Distributed Computing Systems*, pages 780–789, June 2011. `doi:10.1109/ICDCS.2011.94`.

[11] Jianwen Huo, Manlu Liu, Konstantin A. Neusypin, Haojie Liu, Mingming Guo, and Yufeng Xiao. Autonomous Search of Radioactive Sources through Mobile Robots. *Sensors*, 20(12):3461, January 2020. `doi:10.3390/s20123461`.

[12] Nantawat Pinkam, Armagan Elibol, and Nak Young Chong. Informative Mobile Robot Exploration for Radiation Source Localization with a Particle Filter. In *2020 Fourth IEEE International Conference on Robotic Computing (IRC)*, pages 107–112, November 2020. `doi:10.1109/IRC.2020.00024`.

[13] Yizhou Liu, Yike Xuan, De Zhang, and Shuliang Zou. Localizing unknown radiation sources by unscented particle filtering based on divide-and-conquer sampling. *Journal of Nuclear Science and Technology*, 59(9):1149–1161, September 2022. `doi:10.1080/00223131.2022.2032858`.

[14] Frank Mascarich, Mihir Kulkarni, Paolo De Petris, Taylor Wilson, and Kostas Alexis. Autonomous mapping and spectroscopic analysis of distributed radiation fields using aerial robots. *Autonomous Robots*, November 2022. `doi:10.1007/s10514-022-10064-7`.

[15] Abdullah Al Redwan Newaz, Sungmoon Jeong, Hosun Lee, Hyejeong Ryu, and Nak Young Chong. UAV-based multiple source localization and contour mapping of radiation fields. *Robotics and Autonomous Systems*, 85:12–25, November 2016. `doi:10.1016/j.robot.2016.08.002`.

[16] Branko Ristic, Mark Morelande, and Ajith Gunatilaka. Information driven search for point sources of gamma radiation. *Signal Processing*, 90(4):1225–1239, April 2010. `doi:10.1016/j.sigpro.2009.10.006`.

[17] Robert Blake Anderson, Mitch Pryor, Adrian Abeyta, and Sheldon Landsberger. Mobile Robotic Radiation Surveying With Recursive Bayesian Estimation and Attenuation Modeling. *IEEE Transactions on Automation Science and Engineering*, 19(1):410–424, January 2022. `doi:10.1109/TASE.2020.3036808`.

[18] Petr Gabrlik, Tomas Lazna, Tomas Jilek, Petr Sladek, and Ludek Zalud. An automated heterogeneous robotic system for radiation surveys: Design and field testing. *Journal of Field Robotics*, 38(5):657–683, 2021. `doi:10.1002/rob.22010`.

[19] Sebastian Thrun, Wolfram Burgard, and Dieter Fox. *Probabilistic Robotics*. The MIT Press, Cambridge, Mass, 1st edition, August 2005. ISBN: 978-0-262-20162-9.

[20] John Foster, Kypros Kouris, Ian P. Matthews, and Nicholas M. Spyrou. Binomial vs poisson statistics in radiation studies. *Nuclear Instruments and Methods in Physics Research*, 212(1):301–305, July 1983. `doi:10.1016/0167-5087(83)90706-8`.

[21] Glenn F. Knoll. *Radiation Detection and Measurement*. John Wiley & Sons, Hoboken, New Jersey, 3rd edition, August 2010. ISBN: 978-0-470-13148-0.

[22] Daryoush Shahbazi-Gahrouei, Mehrdad Gholami, and Samaneh Setayandeh. A review on natural background radiation. *Advanced Biomedical Research*, 2:65, July 2013. `doi:10.4103/2277-9175.115821`.

[23] Shoaib Usman and Amol Patil. Radiation detector deadtime and pile up: A review of the status of science. *Nuclear Engineering and Technology*, 50(7):1006–1016, October 2018. `doi:10.1016/j.net.2018.06.014`.

[24] Jeroen D. Hol, Thomas B. Schon, and Fredrik Gustafsson. On Resampling Algorithms for Particle Filters. In *2006 IEEE Nonlinear Statistical Signal Processing Workshop*, pages 79–82, September 2006. `doi:10.1109/NSSPW.2006.4378824`.

[25] Christian Musso, Nadia Oudjane, and Francois Le Gland. Improving Regularised Particle Filters. In Arnaud Doucet, Nando de Freitas, and Neil Gordon, editors, *Sequential Monte Carlo Methods in Practice*, Statistics for Engineering and Information Science, pages 247–271. Springer, New York, NY, 2001. ISBN: 978-1-4757-3437-9. `doi:10.1007/978-1-4757-3437-9_12`.

[26] Seyyed Mohammad Hosseini Rostami, Arun Kumar Sangaiah, Jin Wang, and Xiaozhu Liu. Obstacle avoidance of mobile robots using modified artificial potential field algorithm. *EURASIP Journal on Wireless Communications and Networking*, 2019(1):70, March 2019. `doi:10.1186/s13638-019-1396-2`.

Part III

Appendices

F List of Author's Publications

Journal Articles With Impact Factor

GABRLIK, Petr; LAZNA, Tomas; JILEK, Tomas; SLADEK, Petr and ZALUD, Ludek. An automated heterogeneous robotic system for radiation surveys: Design and field testing. Online. *Journal of Field Robotics*. 2021, vol. 38, no. 5, pp. 657-683. ISSN 1556-4959. Available from: `https://doi.org/10.1002/rob.22010`. [cit. 2023-10-06].

LAZNA, Tomas; FISERA, Ota; KARES, Jaroslav and ZALUD, Ludek. Localization of Ionizing Radiation Sources via an Autonomous Robotic System. Online. *Radiation Protection Dosimetry*. 2019, vol. 186, no. 2-3, pp. 249-256. ISSN 0144-8420. Available from: `https://doi.org/10.1093/rpd/ncz213`. [cit. 2023-10-06].

LAZNA, Tomas; GABRLIK, Petr; JILEK, Tomas and ZALUD, Ludek. Cooperation between an unmanned aerial vehicle and an unmanned ground vehicle in highly accurate localization of gamma radiation hotspots. Online. *International Journal of Advanced Robotic Systems*. 2018, vol. 15, no. 1. ISSN 1729-8814. Available from: `https://doi.org/10.1177/1729881417750787`. [cit. 2023-10-06].

Scopus/WoS Indexed Articles

CIHLAR, Milos; RAICHL, Petr; GABRLIK, Petr; JANOUSEK, Jiri; MARCON, Petr et al. Simulation of Autonomous Robotic System for Intelligence and Reconnaissance Operations. Online. In: MAZAL, Jan; FAGIOLINI, Adriano; VASIK, Petr; BRUZZONE, Agostino; PICKL, Stefan et al. (ed.). *Modelling and Simulation for Autonomous Systems*. Lecture Notes in Computer Science. Cham: Springer International Publishing, 2023, pp. 64-73. ISBN 978-3-031-31267-0. Available from: `https://doi.org/10.1007/978-3-031-31268-7_4`. [cit. 2023-10-06].

LAZNA, Tomas; GABRLIK, Petr; SLADEK, Petr; JILEK, Tomas and ZALUD, Ludek. Unmanned Aircraft System-Based Radiological Mapping of Buildings. Online. In: *2022 IEEE/RSJ International Conference on Intelligent Robots and Systems (IROS)*. IEEE, 2022, pp. 1794-1801. ISBN 978-1-6654-7927-1. Available from: `https://doi.org/10.1109/IROS47612.2022.9981415`. [cit. 2023-10-06].

LAZNA, Tomas; GABRLIK, Petr; JILEK, Tomas and BURIAN, Frantisek. Simulating UAS-Based Radiation Mapping on a Building Surface. Online. In: MAZAL, Jan; FAGIOLINI, Adriano and VASIK, Petr (ed.). *Modelling and Simulation for Autonomous Systems*. Lecture Notes in Computer Science. Cham: Springer International Publishing, 2020, pp. 130-147. ISBN 978-3-030-43889-0. Available from: `https://doi.org/10.1007/978-3-030-43890-6_11`. [cit. 2023-10-06].

GABRLIK, Petr and LAZNA, Tomas. Simulation of Gamma Radiation Mapping Using an Unmanned Aerial System. Online. *IFAC-PapersOnLine*. 2018, vol. 51, no. 6, pp. 256-262. ISSN 2405-8963. Dostupné z: `https://doi.org/10.1016/j.ifacol.2018.07.163`. [cit. 2023-10-05].

LAZNA, Tomas. Optimizing the localization of gamma radiation point sources using a UGV. Online. In: *2018 ELEKTRO*. IEEE, 2018. ISBN 978-1-5386-4759-2. Available from: `https://doi.org/10.1109/ELEKTRO.2018.8398368`. [cit. 2023-10-06].

LAZNA, Tomas. The Visualization of Threats Using the Augmented Reality and a Remotely Controlled Robot. Online. *IFAC-PapersOnLine*. 2018, vol. 51, no. 6, pp. 444-449. ISSN 2405-8963. Available from: `https://doi.org/10.1016/j.ifacol.2018.07.113`. [cit. 2023-10-06].

LAZNA, Tomas; JILEK, Tomas; GABRLIK, Petr and ZALUD, Ludek. Multi-robotic Area Exploration for Environmental Protection. Online. In: MARIK, Vladimir; WAHLSTER, Wolfgang; STRASSER, Thomas and KADERA, Petr (ed.). *Industrial Applications of Holonic and Multi-Agent Systems*. Lecture Notes in Computer Science. Cham: Springer International Publishing, 2017, pp. 240-254. ISBN 978-3-319-64634-3. Available from: `https://doi.org/10.1007/978-3-319-64635-0_18`. [cit. 2023-10-06].

Other Publications

LAZNA, Tomas and ZALUD, Ludek. Localizing Multiple Radiation Sources Actively with a Particle Filter. Manuscript submitted for publication. Available from: `https://doi.org/10.48550/arXiv.2305.15240`

LAZNA, Tomas; SLADEK, Petr; GABRLIK, Petr; MATOS, Milan and RIDIKAS, Danas et al. Unmanned Aircraft Systems Based Radiological Mapping of Buildings and Objects. Online. In: *The 7th International Conference on Advancements in Nuclear Instrumentation Measurement Methods and their Applications: Book of Abstracts*. Czech Technical University in Prague, 2021, p. 116. Available from: `https://indico.utef.cvut.cz/event/23/attachments/416/1010/ANIMMA%202021%20-%20Book%20of%20Abstracts.pdf`. [cit. 2023-10-06].

LAZNA, Tomas. Localization of Gamma Radiation Sources. Online. In: *Proceedings of the 25th Conference STUDENT EEICT 2019*. Brno: Brno University of Technology, 2019, pp. 556-560. ISBN 978-80-214-5735-5. Available from: `https://www.eeict.cz/eeict_download/archiv/sborniky/EEICT_2019_sbornik.pdf`. [cit. 2023-10-06].

LAZNA, Tomas. Robotic Localization of Radiological Sources. Online. In: *Proceedings of the 24th Conference STUDENT EEICT 2018*. Brno: Brno University of Technology, 2018, pp. 373-377. ISBN 978-80-214-5614-3. Available from: `https://www.eeict.cz/eeict_download/archiv/sborniky/EEICT_2018_sbornik.pdf`. [cit. 2023-10-06].

LAZNA, Tomas. Robotic Measurement of Gamma Radiation. Online. In: *Proceedings of the 23rd Conference STUDENT EEICT 2017*. Brno: Brno University of Technology, 2017, pp. 196-198. ISBN 978-80-214-5496-5. In Czech. Available from: `https://www.eeict.cz/eeict_download/archiv/sborniky/EEICT_2017_sbornik.pdf`. [cit. 2023-10-06].

G List of Abbreviations

AGL	Above the Ground Level
AI	Artificial Intelligence
AIS	Article Influence Score
CBRN	Chemical, Biological, Radiological, and Nuclear
CBRNE	Chemical, Biological, Radiological, Nuclear, and Explosive
Co-60	Cobalt-60
CPS	Counts per Second
Cs-137	Cesium-137
CsI	Cesium Iodide
CsI(Tl)	Thallium-doped Cesium Iodide
CZT	Cadmium Zinc Telluride
DEM	Digital Elevation Model
DG	Direct Georeferencing
DSLR	Digital Single-Lens Reflex
EKF	Extended Kalman Filter
FIM	Fischer Information Matrix
FP	False Positive
GCP	Ground Control Points
GM	Geiger-Müller
GNSS	Global Navigation Satellite System
GPS	Global Positioning System
HPGe	High Purity Germanium
IAEA	International Atomic Energy Agency
IDW	Inverse Distance Weighting
IG	Indirect Georeferencing
IMU	Inertial Measurement Unit
INS	Intertial Navigation System
IR	Ionizing Radiation
KF	Kalman Filter

MCMC	Markov Chain Monte Carlo
MCNP	Monte Carlo N-Particle
MDA	Minimum Detectable Amount, Minimum Detectable Activity
MLE	Maximum Likelihood Estimation
ML-EM	Maximum Likelihood Expectation Maximization
MSL	Mean Sea Level
NaI	Sodium Iodide
NaI(Tl)	Thallium-doped Sodium Iodide
NPP	Nuclear Power Plant
P	Proportional
PDF	Probability Density Function
PF	Particle Filter
PID	Proportional-integral-derivative
POMDP	Partially Observable Markov Decision Process
RDS	Radiation Detection System
RGB	Red, Green and Blue
RMS	Root Mean Square
RMSE	Root Mean Square Error
ROI	Region of Interest
ROS	Robot Operating System
RTK	Real-time Kinematic
SLAM	Simultaneous Localization and Mapping
TC	Total Count
TP	Test Points
UAS	Unmanned Aircraft System
UAV	Unmanned Aerial Vehicle
UGV	Unmanned Ground Vehicle
UKF	Unscented Kalman Filter